

UNIVERSIDAD DE JAÉN

FACULTAD DE CIENCIAS
DEPARTAMENTO DE FÍSICA

TESIS DOCTORAL

ANALYSIS OF THE SPATIOTEMPORAL BALANCING OF SOLAR AND WIND ENERGY RESOURCES IN ANDALUSIA (SOUTHERN SPAIN): METHODS FOR REDUCING THEIR POWER FLUCTUATIONS

PRESENTADA POR:
FRANCISCO JAVIER SANTOS ALAMILLO

DIRIGIDA POR:
DR. D. DAVID POZO VÁZQUEZ
DR. D. JOAQUÍN TOVAR PESCADOR

JAÉN, 12 DE NOVIEMBRE DE 2012

ISBN 978-84-8439-688-8

Analysis of the spatiotemporal balancing of solar and wind energy resources in Andalusia (southern Spain): methods for reducing their power fluctuations

P H D T H E S I S

to obtain the degree of

Doctor of Physics

Defended by

Francisco Javier Santos Alamillos

SOLAR RADIATION AND ATMOSPHERE MODELING GROUP

DEPARTMENT OF PHYSICS

University of Jaén

Thesis Advisors:

Dr. Antonio David Pozo Vázquez and

Dr. Joaquín Tovar Pescador

September 2012

El **Dr. Joaquín Tovar Pescador**, Catedrático de Escuela Universitaria del Departamento de Física de la Universidad de Jaén, España
y el **Dr. Antonio David Pozo Vázquez**, Profesor Titular de Universidad del Departamento de Física de la Universidad de Jaén, España,

CERTIFICAN:

Que la presente memoria, titulada "**Analysis of the spatiotemporal balancing of solar and wind energy resources in Andalusia (southern Spain): methods for reducing their power fluctuations**", ha sido realizada bajo su dirección. Y considerando que representa trabajo de Tesis, autorizan su presentación y defensa para optar al grado de Doctor en Física con mención de Doctor Europeo.

Dr. A. David Pozo Vázquez
Departamento de Física
Universidad de Jaén

Dr. Joaquín Tovar Pescador
Departamento de Física
Universidad de Jaén

Memoria presentada para optar al grado de:
Doctor en Física, con mención de Doctor Europeo

Francisco Javier Santos Alamillos
Licenciado en Ciencias Físicas
Jaén, Septiembre de 2012

balancing, *n.* **1.** The action of balance. **2.** The placing of one thing over against another as in a balance, compensation; reduction to equilibrium, proportionate adjustment. **3.** Oscillation about a position of equilibrium.

Oxford English Dictionary.

AGRADECIMIENTOS

Escribir el punto y final de la presente tesis doctoral ha sido para mí un momento muy emotivo y que me ha llenado profundamente de satisfacción. En ese instante, tras esbozar una ligera sonrisa y levantar la mirada de la pantalla, pensé en todas aquellas personas que han participado de forma directa o indirecta, y sobre todo, desinteresada en la elaboración de esta tesis doctoral. Por ello, creo que la mejor forma de mostrar mi más sincero agradecimiento es dedicarles estas líneas.

En primer lugar, me gustaría agradecer a mis directores de tesis, el Dr. David Pozo Vázquez y el Dr. Joaquín Tovar Pescador, la oportunidad que me han brindado para poder trabajar junto a su lado. Su apoyo incondicional, me ha servido para dar mis primeros pasos en la investigación, y gracias a ello, madurar como científico y como persona.

Muchísimo tengo también que agradecer a mis compañeros, cuya ayuda y paciencia han sido un pilar muy importante sobre el que me he apoyado estos años. En primer lugar José Antonio, que tantísimas horas que ha empleado para guiarme por el mundo python. Sus valiosos consejos no sólo me han servido para programar de forma más ordenada y eficiente, si no también para despertar en mí la creatividad y curiosidad investigadora. Innumerables han sido los buenos momentos que he pasado trabajando con Vicente. Gracias a él, la jornada transcurría de forma mucho más amena, mientras silbaba sus bandas sonoras de cine y compilaba miles de veces el modelo WRF en Helios. Por supuesto, también agradecer al informático infiltrado en el departamento de física, Samuel, las horas que ha empleado con el desagradecido Helios para facilitarnos el trabajo. Tampoco me olvido de la ayuda y apoyo que me han prestado Álvaro, Husain y el administrador único y maestro culinario Pepe. Muchas gracias a todos.

También me gustaría agradecer a las instituciones públicas y privadas que han cooperado con el desarrollo de esta tesis, ya que este trabajo no hubiese sido posible sin la financiación de la Junta de Andalucía, y sin la cesión de datos meteorológicos por parte de la Agencia Estatal de Meteorología y de empresas como Magtel Renovables y Gamesa.

Por supuesto, no me olvido de mi familia, ni de Mila ni de mis amigos, que gracias a

su apoyo, comprensión e inyecciones de moral, me han permitido seguir trabajando para elaborar esta tesis. Espero que el tiempo que no he podido pasar con vosotros se vea recompensado con este trabajo.

Por último, y aunque no pueda leer estar líneas, quiero agradecer a mi padre todo el cariño y la dedicación que me ha prestado durante toda mi vida, y que tanto echo en falta ahora. Sé que esta tesis era tu ilusión, y por eso en momentos de flaqueza he sacado toda la fuerza para terminarla. Espero que estés orgulloso de mí. Siempre te llevaré en mi corazón.

ABSTRACT

Sustainable social and economic development requires assured and affordable access to energy resources. Moreover, continuous economic expansion and rising prosperity will cause worldwide demand for energy to grow. However, the current power system, which are mainly composed of centralized energy systems based on fossil fuels, are made questionable by the well-know depletion of these fossil fuels and the issue of climate change. To maintain both a sustainable economy capable of providing essential goods and services to citizens, and a supportive global climate system requires a major shift in how energy is produced and used. In this new promissing scenario, the replacement of fossil fuels by renewable energy sources, especially solar and wind energy, will play an essential role. Despite the evident advantages that renewable energy technologies offer, the major challenge is their integration into existing energy supply infraestructure. The difficulty comes from the fluctuating nature of wind and solar resources and their sensitivity to weather patterns, compared to the relatively stable and predictable sources of conventionally generated electricity. Several solutions have been proposed in the literature to diminish renewable power fluctuations. One of the most promising ways to reduce the power fluctuations from renewables is to take advantage of their spatial variability over a region for designing an efficient and strategic interconnections between renewable power production systems. The knowledge of this spatial variability provides areas where a below-normal production can be compensate by other zones with above-normal production, smoothing the fluctuations of the combined power production as result of their connection. In this thesis, we propose a general methodology to analyze spatiotemporal balancing of the wind energy resource alone, and between the solar and wind energy resources in the Southern Iberian Peninsula, and its implications for a reduction in wind and solar power fluctuations. The methods consisted in two steps. In a first, a Principal Component Analysis (PCA) or Canonical Correlation Analysis (CCA) is done,and resulting spatiotemporal patterns are examined. This analysis type depends on wheater the evaluation implies one resource (in this thesis wind energy), or both (wind and solar energy). In the second step, based on the former analysis, we assess optimum locations for wind farms and combination of solar plants (PV or CSP plants, depending on the type of solar resource) for stable power. Given the topographic characteristics of the study region and their enormous importance for wind speed variability and, therefore, for the existence of spatial balancing associated

with wind energy resources, we evaluated the reliability of regional wind estimates from WRF prior to the balancing analysis. In this evaluation, the first objective was to assess the relative roles of parameterization choice, terrain and surface properties representation in WRF, as related to regional wind resource assessment. The second and more important objective was to achieve an optimal setup of WRF, for obtaining the wind and solar estimates used in the balancing analysis. This study was conducted at different spatial resolutions. Finally, we evaluated the existence of wind and solar energy resource balancing associated with the North Atlantic Oscillation (NAO) cycle in the Mediterranean area.

CONTENTS

Contents **XI**

1 Introduction **1**
1.1 Renewable energy: advantages and challenges 1
1.2 Objectives 10
1.3 Specific objectives and structure 12
1.4 Thesis Summary 14

2 Sensitivity analisis of WRF wind estimates to land-cover representation and daily SST variability **19**
2.1 Introduction 19
2.2 Database and study area 23
2.3 Methods 25
2.4 Results 29
2.5 Summary and conclusions 39

3 Analysis of WRF model wind estimate sensitivity to parameterization choice and terrain representation in Andalusia (Southern Spain) **43**
3.1 Introduction 43
3.2 Study region and data 47
3.3 Methods 53
3.4 Results and discussion 57
3.5 Summary and conclusions 68

4 A methodology for evaluating the potential contribution of wind energy to baseload power: A case study in Andalusia (Southern Spain) **73**
4.1 Introduction 73
4.2 Methods and study area 77
4.3 Results 83
4.4 Summary and conclusions 101

5 Analysis of spatio-temporal balancing between wind and solar energy (GHI) resources in the southern Iberian Peninsula 105
5.1 Introduction . . . 105
5.2 Methods and study Area . . . 109
5.3 Results . . . 116
5.4 Summary and conclusions . . . 133

6 Optimum location of wind farms and CSP plants for reducing power fluctuations 135
6.1 Introduction . . . 135
6.2 Methods, data and study area . . . 140
6.3 Results and discussion . . . 148
6.4 Summary and conclusions . . . 169

7 The impact of the NAO on solar and wind energy resources in the Mediterranean Area 173
7.1 Introduction . . . 173
7.2 Data description . . . 178
7.3 Results . . . 179
7.4 Conclusions . . . 191

8 Concluding remarks and future research 195
8.1 Sensitivity of wind estimates to parameterization choice, terrain and surface representation . . . 196
8.2 Analysis of the spatio-temporal balancing between solar and wind energy resources . . . 198
8.3 Balancing between the solar and wind energy associated with the NAO cycle . . . 203
8.4 Future Research . . . 205

Bibliography 207

CHAPTER 1

INTRODUCTION

1.1 Renewable energy: advantages and challenges

1.1.1 Background

Sustainable social and economic development requires assured and affordable access to energy resources (Moomaw et al., 2011). Moreover, continuous economic expansion and rising prosperity will cause worldwide demand for energy to grow. In particular, it is expected that worldwide primary energy demand will increase by 45% and demand for electricity by 80%, between 2006 and 2030 (IEA, 2008). However, current power systems, which are mainly composed of centralized energy systems based on fossil fuels, are made questionable by the well-known depletion of these fuels and the issue of climate change. The International Panel on Climate Change (IPCC) Fourth Assessment Report (IPCC, 2007a) states that 85% of the current primary energy driving global economies comes from fossil fuel combustion, and consumption of these fuels accounts for 56.6% of all anthropogenic greenhouse gas (GHG) emissions. An increase in GHG emissions associated with the provision of energy services is a major cause of climate change, whose main effect is an increase in global average temperature since the mid-19th century (IPCC, 2007a). Despite the dramatic consequences of increasing GHG emissions, CO_2 concentrations have continued to increase, reaching values 39% greater than pre-industrial levels (IPCC, 2007b; NOAA, 2010). As a consequence, global

average temperature has increased by 0.76 °C since the preindustrial period, and the warming trend has increased significantly over the last 50 years (IPCC, 2007b).

To maintain both a sustainable economy capable of providing essential goods and services to citizens, and a supportive global climate system requires a major shift in how energy is produced and used (Nfah et al., 2007; Kankam and Boon, 2009). In a new promising energy scenario, the replacement of fossil fuels by renewable energy sources, especially solar and wind energy, will play an essential role. For example, European Union (EU) regulations set a binding target for 20% of EU total energy supply to come from renewables by 2020 (6.5% in 2007). To achieve this 20% final consumption goal in Spain, a substantial increase in the contributions of wind and solar energy to electricity production is necessary, from the current 15% to greater than 45% (Gómez et al., 2010). Similar target increases in the share of these renewables are expected in other regions (Jacobson and Delucchi, 2011). Furthermore, European regulations set a firm target of cutting 20% of their GHG emissions by 2020, relative to 1990 (*European Directives 2009/28/EC and 2009/29/EC*).

There are two main solar electricity technologies - Photovoltaic (PV) and Concentrating Solar Power (CSP). PV systems enable direct conversion of sunlight into electricity through semiconductor devices by receipt of Global Horizontal Irradiance (GHI). Today, PV provides 0.2% of total global electricity generation. Germany is the highest producing country in the world, with 17.3 GW installed capacity, followed by Spain with more than 4 GW (about 4% of the country's total installed capacity) (IEA, 2010b). While its use is small today, PV power has a promising future, as it is projected to provide around 5% of global electricity consumption by 2030, increasing to 11% by 2050 (IEA, 2010b).

The basic concept of CSP is relatively simple - CSP devices concentrate energy from the sun's rays to heat a receiver. This heat is transformed first into mechanical energy (by turbines or other engines) and then into electricity. CSP plants use Direct Normal Irradiance (DNI), which is energy received on a surface that maintains itself perpendicular to the sun's rays. CSP developers typically set a lower threshold for DNI of about 2000 $kWhm^{-2}year^{-1}$. Below that threshold, other solar electric technologies, such as PV, are assumed to have a competitive advantage. Optimal locations for installing

CSP technology are usually in arid and semi-arid areas with reliably clear skies, which are typically within latitudes between 15° and 40° north or south (IEA, 2010a). In addition, this technology is able to store solar energy in the form of heat. As of early 2011, the global stock of CSP plants neared 1.5 GW capacity, being mainly in Spain (about 1 GW). Projects now in development or under construction in more than a dozen countries (including China, India, Morocco, Spain and the United States) are expected to total 15 GW, with an expected contribution of about 5% (1500 GW) of annual global electricity production in 2050 (IEA, 2010b).

Wind energy is probably the most cost-effective of the renewable energy technologies, and is expected to play a key role in the next decades (Jacobson and Delucchi, 2011; IEA, 2009). In addition, wind energy is the renewable technology with the fastest growth rate; since 2000, cumulative installed capacity has grown at an average rate of around 30% per year (GWEC, 2007). In 2008, this energy provided nearly 20% of electricity consumption in Denmark, more than 11% in Portugal and Spain, over 4% in the entire EU, and nearly 2% in the United States (IEA, 2009). By 2030, wind power is estimated to contribute about 9% of global electricity production, growing to 12% by 2050 (IEA, 2009). In Spain, to achieve the 20% final renewable consumption goal set by EU regulations, a substantial increase in the contribution of wind electricity production is necessary, from the current 11% to about 30% (Gómez et al., 2010). Similar target increases in the share of wind energy are expected in other regions (Lund, 2007; Krajacic et al., 2011).

Despite the evident advantages that renewable energy technologies offer, the major challenge is their integration into existing energy supply infrastructure (Lund, 2005, 2006). The difficulty comes from the fluctuating nature of wind and solar resources and their sensitivity to weather patterns, compared to the relatively stable and predictable sources of conventionally generated electricity. Solar and wind energy resources have spatial and temporal variability over a wide range of scales. All time scales are relevant in renewable energy, from short-term variability (minutes to hours) to synoptic, seasonal and climate time scales. Accurate information on expected solar irradiance or wind speed on short-term and synoptic time scales can be used for management of electricity grids, scheduling of conventional power plants, and for decision making in the energy market (Holttinen, 2005). Information on monthly and seasonal scales is also of interest

for maintenance operations and strategic planning (Weisser and Foxon, 2003). Finally, information on resource variability at climate time scales (years to decades) is a key issue in the first stages of a renewable energy project. In particular, since the life span of wind farms or solar plants (both PV and CSP) is about 20 years, an economic feasibility study of the project should include adequate estimation of interannual variability of the resource.

The fluctuating nature of renewable electricity production makes the cost of renewables less competitive for power generation systems, because intermittent production creates negative externals that translate into grid integration costs. In particular, renewable power intermittency has implications for both costs of renewable integration into the electricity system (balancing costs), and costs associated with maintaining adequate system reliability (backup costs). Other technological solutions, such as energy storage, are still too immature for the large scale. Today, short-term wind and solar power forecasting is the primary requirement for efficient integration of renewables into power systems, and for reduction of grid integration costs (Saintcross et al., 2005; Kariniotakis, 2006; Lorenz et al., 2010; Lara-Fanego et al., 2011). Unfortunately, the skill of these forecasts is still limited, and unpredicted generation must be accommodated by system reserves. To sum up, as wind and solar power contributes a higher proportion of all generation, it will become increasingly difficult for electrical system operators to effectively integrate such additional fluctuating power input. Thus, solutions that reduce power fluctuations are important if wind and solar electricity is to significantly displace other electricity technologies.

There is no a clear consensus in the literature on evaluating the contribution of solar and wind power toward reducing the capacity of conventional power systems. In general, two types of metrics for describing this contribution can be distinguished - capacity credit and firm capacity.

Capacity credit is defined as the ability of a renewable power system to contribute to peak electrical demand, while maintaining the same security of supply as conventional power plants (Boyle, 2008). In this sense, capacity credit is the amount of thermal plant generation capacity that can be displaced from the power system with the same reliability. It is usually expressed as the percentage of installed power capacity.

Obtaining the capacity credit is no easy task, since full modeling of the power system is required. Several studies have analyzed the wind energy capacity credit, within individual countries and for all Europe (Giebel, 2005, 2007; Gross et al., 2008). The main conclusion was that wind power has capacity credit, but it is highly dependent on the supporting electric system, wind load factor and penetration level. On average, for a penetration around 20%, the wind energy capacity credit could approach 20% of installed power (Gross et al., 2008). For PV technology, estimates of the capacity credit range between 25% and 75% of installed power (Pelland and Abboud, 2008; Xcell Energy, 2009; GE, 2010). However, lower values are possible at high levels of solar penetration and in electricity systems where demand patterns and PV output are poorly correlated. For CSP technologies, similar capacity credit values are found for plants without thermal storage. In plants with this storage, capacity credit could be 89% to 93% of installed capacity, nearly as high as thermal plants (GE, 2010).

Firm capacity can be defined as the fraction of installed power capacity that is available at the same probability as that of a thermal plant (Giebel, 2005). With this definition, the firm capacity of a power system can be regarded as baseload power. Despite the fact that capacity credit and firm capacity are related, they account for different characteristics of renewable power systems. Firm capacity translates directly into potential fossil or nuclear baseload capacity, whereas capacity credit may reduce the need for conventional maximum capacity while not affecting baseload capacity. In addition, capacity credit could be considerably greater than firm capacity, provided that renewable production is correlated with load demand. Unlike capacity credit, firm capacity can be assessed comparatively easily from pure wind or solar data (Landberg, 1997).

1.1.2 Reduction of power fluctuations from renewables

One of the most promising ways to reduce the power fluctuation from renewables is to take advantage of their spatial variability. It is well known that spatial correlation of wind speed and (to a lesser extent) solar irradiance diminishes with distance, because of different weather and climate conditions over large regions and the effect of topographic features (mainly on wind speed variability). As a consequence, interconnection of wind farms, solar power plants, or even wind farms with solar plants across a region may

reduce fluctuations in total production. That is, a balancing effect can be achieved, because of variable weather and climate and terrain influences on wind speed and solar radiation across a region. When this balancing is present, the combined output of numerous, widely-spaced renewable energy plants, based on the same or different resources (but mainly wind and solar), would be smoother than the output of individual power plants. In addition, such disperse generation is expected to reduce forecast error, thereby reducing grid integration cost. Nevertheless, it should be realized that the balancing may be very dependent on the temporal and spatial scales considered.

There are numerous works in the literature that analyze spatiotemporal variability of the wind energy resource and its consequence for wind power integration (Kahn, 1979; Landberg, 1997; Holttinen, 2005; Heide et al., 2010). The idea is that since spatial correlation of wind speed diminishes with distance, the combined output of numerous and widely-spaced wind farms across a region should be smoother than the individual output. This smoothing effect becomes significant when weather conditions across the interconnecting region are sufficiently variable and/or terrain complexity significant. If this is the case, above-normal wind speeds at certain times and locations can compensate below-normal speeds at other locations (negative spatial correlations), producing spatial balancing of the wind energy resource. In such cases, by interconnecting advantageously-distributed wind farms, it may be possible to achieve either reduced minimum-wind output or secured peak load, eventually transforming wind energy into a reliable supply. In a recent work, Roques et al. (2010) analyzed wind power production across different European countries, obtaining an optimum combination of cross-country portfolios that minimized variance of wind production. They concluded that wind power production across Europe varies considerably, and that an optimal combination of wind production at different locations can foster a much less variable total production. The ability of wind energy to provide firm capacity (baseload) has been shown to be limited. For instance, Oswald et al. (2008) analyzed the ability of wind energy to provide reliable electricity in the United Kingdom (UK). The principal conclusion was that, although aggregation of output across the country was smoother than the output of individual wind, this aggregation does not lead to a substantial firm capacity. Similar results were found in analogous aggregation studies for Denmark (Ostergaard, 2008) and Germany (Weigt, 2009). In the latter study, it was concluded that only 0.5% of total wind power installed capacity in Germany was guaranteed throughout

the study period (3 years). In contrast, between 10% and 15% of installed capacity was wind capacity credit. Underpinning these results are the relatively homogeneous weather conditions and limited topographic features across the three studied countries. Other studies are more encouraging. For instance, Archer and Jacobson (2007) studied the decrease of wind power production fluctuation from interconnection of 19 wind farms in the Midwestern United States. They found a significant decline in fluctuation of total production compared to single wind farms, and a firm capacity about 15% of installed capacity. Cassola et al. (2008) proposed a method for optimal distribution of wind farms at ten locations in Corsica (France) for reducing temporal variability of total wind power production. They showed that around 16% of yearly average wind power could be used as reliable baseload. Finally, Kempton et al. (2010) analyzed the benefits of interconnecting offshore wind farms along the eastern coast of the United States. Based on analysis of data from 11 meteorological stations, they demonstrated that this interconnection would provide a reliable baseload (firm capacity). In the last three studies, the varied weather conditions and topographic features of the study areas explain the findings of significant amounts of firm capacity.

The benefits of solar energy aggregation have received less attention. In general, spatial variability of the solar resource at short time scales is significantly less than that of wind energy (Archer and Jacobson, 2003; Papadimas et al., 2010; Gueymard and Willcox, 2011; Widén, 2011). Nevertheless, clouds produce substantial spatial variability in solar energy production. Wiemken et al. (2001) analyzed spatial variability of PV production at short time scales in Germany, and the same topic was addressed by Mills and Wiser (2010) for the United States. The last two works reported that solar power has similar short-term variability as wind power. Although other phenomena, such as aerosols or solar cycles, may play a significant role, spatial variability of solar radiation at large spatial scales is mainly related to changes in cloud cover associated with variability of large-scale circulation patterns (Sánchez-Lorenzo et al., 2008, 2009; Chiacchio and Wild, 2010; Papadimas et al., 2010). In this regard, the North Atlantic Oscillation (NAO) is assumed as a major actor in the large scale circulation over the North Atlantic (Hurrel et al., 2003). A notable NAO impact on cloud cover variability and solar radiation at the surface over the entire North Atlantic area has been described (Trigo et al., 2002; Pozo-Vázquez et al., 2004; Lohmann et al., 2006; Sánchez-Lorenzo et al., 2008, 2009; Chiacchio and Wild, 2010; Papadimas et al., 2010).

Finally, one of the most promising ways to reduce power fluctuations from wind and solar energy is spatial aggregation of wind farms and solar plants. The idea is that prior knowledge of regional weather and climate patterns can reveal locations where wind and the solar resources are spatially anti-correlated. In that case, above-normal wind or solar resources can compensate below-normal resources elsewhere, resulting in spatial balancing. In such instance, by interconnecting advantageously-distributed wind farms and solar plants it may be possible to achieve a reduction in the combined power fluctuations and an increment in the time of power availability, eventually transforming solar and wind power into reliable (baseload) supply. Since solar and wind energy will contribute more to total electricity production in the future, it is worth analyzing the combined effect of the spatial distribution of these two sources. In this context, a balancing effect becomes effective when and where strong solar energy compensates weak wind energy, and vice versa. From a meteorological and climatological standpoint, the balancing effect between solar and wind resources is easily anticipated, given a sufficiently large region. Across Europe overall, wind resources tend to be higher in winter and lower in summer, and vice versa for solar resources. Although some projects intended for very high renewable penetration are founded on this idea of balancing (Trieb et al., 2005; Tröster et al., 2011), there has been little research in this emerging field. Heide et al. (2010, 2011) analyzed an optimal mix between solar (PV) and wind energy in Europe, within a scenario of very high penetration (100%) of these renewables. Their analyses were based on meteorological model estimates and carried out on seasonal time scales, with a constraint of reducing storage needs as much as possible. They gave an optimal seasonal mix of 55% wind and 45% solar. Widén (2011) analyzed balancing between solar and wind resources in Sweden, based on meteorological station data. He reported negative correlation between solar and wind resources (and thus balancing) on all time scales for the whole country, with monthly totals showing the highest negative correlations (seasonal variability). He also indicated greater hour-to-hour variability with increasing solar share. Finally, Nikolakakis and Fthenakis (2011) analyzed an optimum mix of wind and electricity sources for the state of New York. They found that considerably high penetration (up to 30%) of wind and solar can be attained, without adding storage.

1.1.3 Database for studying balancing

Databases represent one of the most important problems in the evaluation of renewable energy resource (solar and wind) potential within a region and, specifically, in the analysis of spatiotemporal balancing of those resources. Meteorological data (solar irradiation, wind speed and direction) can be obtained from weather measurement networks. However, these networks are usually insufficiently dense to adequately describe the rich spatial variations of solar irradiance and wind speed that are requisite to balancing studies. Moreover, installation and operation of meteorological masts and radiation stations is expensive.

There has been notable improvement in computational capabilities over recent decades, which allows increased use of Numerical Weather Prediction (NWP) models. These models give a comprehensive description of the atmospheric system, using initial and boundary conditions from atmospheric reanalysis. Based on downscaling techniques, current NWP models resolve local and regional circulation patterns and account for local topographic conditions. The models can provide accurate meteorological information, such as wind speed and direction and solar radiation over large regions, at high temporal (a few minutes) and spatial (a few km) resolution. The Weather Research and Forecasting (WRF) model is a state-of-the-art, next generation mesoscale NWP model, designed to serve both operational forecasting and atmospheric research. It is a non-hydrostatic model, with several available dynamic cores and numerous choices for physical parameterizations. It is suitable for a broad spectrum of applications, across scales ranging from meters to thousands of kilometers (Skamarock et al., 2008).

Despite the high resolution of current NWP models (km), there are still three main problems in estimation of surface meteorological variables, especially that of surface wind speed. These challenges are adequate representation of terrain surface properties, representation of topography and terrain morphology, and numerous physical processes at sub-grid scale.

The adequate representation of surface terrain properties is a key issue for obtaining accurate wind speed and direction estimates. NWP models, in particular the WRF, include land surface schemes that govern partitioning of available energy at the surface

between sensible and latent heat, and partitioning of available water between evaporation and runoff. Specifically, these land surface schemes account for land surface properties such as roughness length, albedo, thermal inertia, moisture and emissivity, according to land-use category and season of the year (Sertel et al., 2008). Continuing advances in remote sensing facilitate more accurate and higher resolution land-cover information, and take into account anthropogenic and natural changes in land use. These new maps may produce a more accurate description of the spatial variability of land use, and therefore terrain properties.

Topography and terrain morphology has a marked influence on surface meteorological variables, especially on surface wind speed and direction. Surface winds result from interaction between mesoscale circulation and other more local factors, many of which are related to topographic characteristics (elevation, aspect, slope) and terrain morphology (hills, valleys, and others). First, wind speed changes with elevation in the planetary boundary layer, as a result of reduced friction (Palomino and Martin, 1995). Second, terrain features can accelerate windflow. As it passes a summit, an approaching air mass is often squeezed into a thinner layer and therefore speeds up. Aside from elevation, aspect and slope can also modify windflow. Over a ridge, there is maximum acceleration when wind blows perpendicular to the ridge line. Terrain morphology is also important; windflow accelerates through passes along valleys aligned with the flow (channeling). If the region under study consists on flat and homogeneous land, WRF terrain representation may be accurate enough to provide reliable surface wind estimates. In complex topography areas, however, even when using spatial resolutions on the order of a few kilometers, unreliable surface wind estimates may be produced. Terrain representation in WRF is a key issue in spatial balancing studies. High spatial variability (and thus low spatial correlation) of regional wind speed is primarily caused by topographic features. Other factors, such as thermal contrast associated with water bodies, are also important.

Finally, the physical processes at sub-grid scale are accounted for in NWP by parameterizations. Most NWP has parameterization schemes for sub-grid processes, such as cloud Microphysics (MPH), Cumulus formation (CMS), Planetary Boundary Layer processes (PBL), Surface Layer Physics (SLP), Land Surface Layer (LSL) or Short- and Long-wave Radiation (SWR and LWR, respectively). Stensrud (2007)

presents a detailed description of these and other parameterizations. In the last decades, many different parameterization versions for each scheme have been proposed. However, their range of validity is highly dependent on the study region, season of the year, spatial and temporal scales, and variable of interest. In fact, given a spatial and temporal configuration, the skill of a model mainly depends on these physical parameterizations (Lynn et al., 2004; Fernández et al., 2007). As a consequence, a prior performance evaluation of different parameterization versions of the various schemes, for the given study area and application (i.e., meteorological variable), is recommended.

1.2 Objectives

The main objective of this thesis is to analyze spatiotemporal balancing of the wind energy resource alone and between the solar and wind energy resources in the Southern Iberian Peninsula, and its implication for a reduction in wind and solar power fluctuations. In particular, the aim is to investigate whether the existence of balancing patterns permits regional solar and wind energy to provide more stable (even baseload) power. The method consisted of two steps. In the first, a Principal Component Analysis (PCA) or Canonical Correlation Analysis (CCA) is done, and resulting spatiotemporal patterns are examined. The analysis type depends on whether the evaluation implies one resource (wind energy) or both (wind and solar energy). At this step, mesoscale atmospheric conditions associated with each PCA or CCA pattern are analyzed, to explain the observed balancing patterns from a physical standpoint. In the second step, based on the former analysis, we assess optimum locations for wind farms, combinations of PV plants and wind farms, and combinations of CSP plants and wind farms, for stable production. Using a reference wind farm and PV or CSP plant models, the hourly capacity factor (and its standard deviation) of these facilities, operating alone or interconnected, are evaluated at these locations. This permits analysis of the eventual contribution of these renewable technologies to stable power.

The study region is the southern half of the Iberian Peninsula, covering about 350,000 km^2. This region, though relatively small, has considerable spatial variability of main climate variables. This is related to varied topographic features, and the influence of the

adjacent Mediterranean Sea and Atlantic Ocean. These features suggest considerable spatial variability in wind speed and (to a lesser extent) solar radiation, and consequent existence of spatial balancing. Further, the region has considerable wind and solar energy resources, being one of the few regions in the world with significant wind, PV and CSP installed capacities (the three total about 25% of total Spanish power system installed capacity).

We used wind and solar energy estimates from the WRF. These constitute a reliable, and spatially and temporally coherent database, essential for balancing studies. Specifically, we used hourly wind speed and solar radiation data from one year, at 3 and 9 km spatial resolution. The analysis was conducted independently for each season and for the year. For wind energy, offshore areas were also included.

Given the topographic characteristics of the study region and their enormous importance for wind speed variability and, therefore, for the existence of spatial balancing associated with wind energy resources, we evaluated the reliability of regional wind estimates from WRF prior to the balancing analysis. In this preliminary evaluation, the first objective was to assess the relative roles of parameterization choice, terrain representation, and surface properties in WRF, as related to regional wind resource assessment. The second and more important objective was to achieve an optimal setup of WRF, for obtaining the wind and solar estimates used in the balancing analysis. This study was conducted at spatial resolutions from 1 to 9 km. No analogous work was done for solar radiation, mainly because this was already performed by other members of the research group (Ruiz-Arias et al., 2008, 2012b). Also, solar radiation has considerably less spatial variability than wind speed.

Finally, we evaluated the existence of wind and solar energy resource balancing associated with the NAO cycle in the Mediterranean area. The NAO is the main cause of interannual climate variability in the study region and has a different influence on wind and solar resources. Therefore, balancing between these resources at seasonal to interannual time scales can be anticipated. We used monthly means of daily integrated wind and solar energy data, which covered the entire North Atlantic and Mediterranean areas, including North Africa. The dataset was derived from satellite retrievals (solar energy) and meteorological reanalysis (wind energy and cloud cover), and extends over

a period of about 20 years.

1.3 Specific objectives and structure

This thesis is structured as a set of five papers and one book chapter, each dealing with a specific objective and a part of the aforementioned work. Specifically, the thesis has the following objectives, each associated with one book chapter or paper and a chapter of the Thesis.

Chapter 2

Paper: Sensitivity analisis of WRF wind estimates to land-cover representation and daily SST variability.

Specific objectives: Evaluation of the role of surface property representation and upgrading of SST in the reliability of WRF wind speed and direction estimates, with emphasis on regional wind resource assessment.

Chapter 3

Paper: Analysis of WRF wind estimate sensitivity to parameterization scheme choice and terrain representation in Andalusia (Southern Spain).

Specific objectives: Evaluation of the role of parameterization choice and terrain representation in the reliability of WRF wind speed and direction estimates, with emphasis on regional wind resource assessment.

Chapter 4

Paper: A method for evaluating spatial variability of wind energy resources: Application for assessing potential contribution of wind energy to baseload power.

Specific objectives: Evaluation of spatiotemporal variability of wind energy resources in the study area. Assessment of optimal wind farm locations to reduce power fluctuations.

Evaluation of potential contribution of regional wind energy to stable (baseload) power.

Chapter 5

Paper: Analysis of spatiotemporal balancing between wind and solar energy resources in the southern Iberian Peninsula.

Specific objectives: Evaluation of spatiotemporal balancing between wind and solar (derived from GHI) energy resources in the study region. Assessment of optimal locations of wind farms and PV plants to reduce power fluctuations. Evaluation of potential contribution of connected PV plants and wind farms to stable (baseload) power.

Chapter 6

Paper: Optimum allocation of wind farms and CSP plants for reducing power fluctuations.

Specific objectives: Evaluation of spatiotemporal balancing between wind and solar (derived from DNI) energy resources in the study region. Assessment of optimal locations of wind farms and Concentrating Solar Power (CSP) plants to reduce power fluctuations. Evaluation of potential contribution of connected CSP plants (without storage) and wind farms to stable (baseload) power.

Chapter 7

Book chapter: Impact of the NAO on solar and wind energy resources in the Mediterranean area.

Specific objectives: Evaluation of impact of the NAO on wind and solar resource interannual variabilities in the study region. Evaluation of the existence of balancing between wind and solar energy resources associated with the NAO cycle in the Mediterranean area.

Finally, **Chapter 8** presents the general conclusion of the thesis, as well as some

recommendations for future research.

1.4 Thesis Summary

To summarize the work, the abstract of each of the five papers, and the book chapter on which this thesis is structured, are reproduced below.

Chapter 2: A reliable description of terrain surface properties, especially the roughness length, is essential for obtaining accurate wind estimates based on Numerical Weather Prediction (NWP) models. Currently, land-surface schemes in these models employ land-cover categorical maps from which the terrain surface properties are derived. The continuous development in remote sensing provides new updated land-cover maps that accounts for both anthropogenic and natural changes in the land. The use of these new maps may allow NWP models to describe more precisely the surface properties. Moreover, the use of daily updates of the Sea Surface Temperature (SST) in the NWP integrations allows taking into account changes in stratification and temperature gradients in the sea/land interface, relevant for wind estimates. In this work an evaluation of the role of terrain surface properties representation in the WRF NWP model, as they relate to regional wind resource assessment, was conducted. In addition, the effect of the daily updating of the SSTs during the WRF integration in the wind estimates was also assessed. To this end, two different land-cover datasets were assessed: the GLCC (default dataset in the WRF) and a new one, here derived from the Coordination of Information on the Environment (CORINE) dataset. Four experiments were conducted by alternatively using the former land cover data bases and daily updated/prescribed SSTs. The work was conducted for the region of Andalusia (Southern Spain); 3 km spatial resolution hourly wind speed and direction estimates were tested against data collected along the year 2009 at four stations. Results showed, firstly, that the CORINE dataset describes more accurately the roughness length than the GLCC one and, therefore, wind estimates obtained with CORINE outperform in general those obtained with the GLCC. Differences in the performance of both land cover dataset were mainly found in the Mean Error and during the winter. Secondly, it was found that the use of daily updated SSTs improves the reliability of the wind estimates in summer

and autumn, especially at the coastal stations and mainly in terms of the ME values.

Chapter 3: This chapter reports on an evaluation of the relative roles of choice of parameterization scheme and terrain representation in the Weather Research and Forecasting (WRF) mesoscale model, in the context of a regional wind resource assessment. As a first step, 32 configurations using two different schemes for Microphysics (MPH), Cumulus (CMS), Planetary Boundary Layer (PBL), or Short- and Long-wave Radiation (SWR and LWR, respectively) were evaluated. In a second step, wind estimates that were obtained based on various experiments with different spatial resolution (1, 3 and 9 km) were assessed. The work focuses on Southern Spain. Estimates were tested against data from four stations providing hourly wind speed and direction data at 40 m above the ground level. Results from the first analysis showed that wind speed RMSE and ME values were mainly sensitive to the PBL parameterization selection, with RMSE differences between 3% and 8% and ME differences between -15% and 10%. The second analysis reported low RMSE values associated with higher spatial resolutions, with differences from 0.2 to 1 ms^{-1}. The sign of the bias was dependent on terrain morphology and spatial resolution, and absolute values tended to be considerably higher when using coarser spatial resolutions. Wind direction proved more sensitive to representation of terrain morphology around the station than to the model spatial resolution. Reduced RMSE of the wind speed estimates were observed in areas where wind direction was clearly constrained by terrain morphology, provided that this morphology was properly represented.

Chapter 4: In this chapter, we propose a method for analyzing the potential contribution of wind energy resources to stable (baseload) within a region. The method uses principal component analysis (PCA) for analyzing spatiotemporal balancing of wind energy resources and then assesses optimal wind farm location, to reduce power fluctuations. The ability of different wind turbines, alone or interconnected, to provide stable (baseload) power is ultimately evaluated at selected locations. The method was tested in the southern Iberian Peninsula, including offshore areas. We used hourly wind energy estimates for 2009 from the WRF mesoscale model at 3 km spatial resolution. First, the results show the existence of valuable spatial balancing patterns within the study region, but with a marked seasonality. The most important balancing patterns were discovered in the eastern area and near the Strait of Gibraltar. The various patterns were found to result

from the interaction of mesoscale zonal flow and the complex topography of the region. Second, the results indicate that optimal allocation and interconnection of wind farms across the region, by taking advantage of the aforementioned spatial balancing patterns, can substantially reduce wind power output fluctuations. This optimal allocation can, in some cases, generate stable power, thereby contributing to baseload power.

Chapter 5: Electricity from wind and, to a lesser extent, solar energy, is intermittent and not controllable. Unlike conventional power generation, therefore, this electricity is not suitable to supplybase load electric power. In the future, with greater penetration of these renewable sources,intermittency and control problems will become critical. We explore here the use Canonical Correlation Analysis (CCA) for analyzing spatiotemporal balancing between regional solarand wind energy resources. The CCA allows optimal distribution of wind farms and solarenergy plants across a territory, to minimize the variability of total energy input into the power supply system. The methodology was tested in the southern half of the IberianPeninsula, a region covering about 350.000 km^2. We used daily-integrated wind and solarenergy estimates in 2007 from the Weather Research and Forecasting (WRF) mesoscalemodel, at a spatial resolution of 9 km. Results showed valuable balancing patterns in thestudy region, but with a marked seasonality in strength, sign and spatial coverage. Theautumn season showed the most noteworthy results, with a balancing pattern extendingalmost over the entire study region. With location of reference wind farms and PV plants according to the balancing patterns, their combined power production shows substantially lower variability than production of the wind farms and PV plants separately, and combined production obtained with any other locations. Atmosphericcirculations associated with the balancing patterns were found to be significantly differentbetween seasons. In this regard, synoptic scale variability played an important role, but sodid topographic conditions, especially near the strait of Gibraltar.

Chapter 6: We propose a method for analyzing the potential contribution of Concentrating Solar Power (CSP) and wind energy to stable (baseload) power within a region. Firstly, Canonical Correlation Analysis (CCA) was used for analyzing the spatio-temporal balancing between solar (from Direct Normal Irradiance, DNI) and wind energy resources. Secondly, results of the CCA are used to assess the optimal locations of CSP plants and wind farms to reduce power fluctuations. The method

was tested in the southern Iberian Peninsula, including offshore areas. We used hourly solar and wind energy estimates for 2009 from the WRF mesoscale model at 3 km spatial resolution. Firstly, the CCA results showed the existence of valuable balancing patterns, resulting from the interaction of the mesoscale zonal flow and the complex topographic characteristics of the study region. Secondly, results showed that the optimal allocation and interconnection of the CSP plants and wind farms across the study region, taking advantage CCA results, substantially reduced the power output fluctuations (about 25%) and increased the time of power availability (up to more than 80%, i.e. close to availability provided fossil-fuel based power plants). This was found, ultimately, to be related with the existence of a 5-8 hours lag between the CSP plants and the wind farms peak power time.

Chapter 7: In this chapter, the influence of the NAO on the solar and wind energy resources in the Mediterranean area, in particular, and over the whole North Atlantic area, in general, has been explored based on the analysis of 20 years of reanalysis and satellite data. The analysis was carried out for the winter and annual periods and proved the existence of a marked influence of the NAO pattern on the spatial and temporal variability of the solar and wind energy resources in the study area. Particularly, the NAO signature on the solar/wind energy resources was found to be a north-south dipolar pattern, with the positive/negative centre over the Mediterranean area. Although the spatial patterns obtained are similar, the nature of the relationship obtained for wind energy was found to be less linear and more complex than that attained for solar energy. A composite analysis revealed that interannual variability of the solar and wind energy resources in the Mediterranean area can reach values above 20% in winter and 10% in the annual case associated with changes in the NAO phase. Finally, the analysis of the spatial patterns of the NAO influence on the solar and wind energy resources revealed the existence of spatial and local balancing between these two energy resources in the study area. Results are of interest regarding the estimation of the expected interannual variability of the wind farms and solar plants production in the study region.

CHAPTER 2

SENSITIVITY ANALISIS OF WRF WIND ESTIMATES TO LAND-COVER REPRESENTATION AND DAILY SST VARIABILITY

Santos-Alamillos F.J., D. Pozo-Vázquez, J.A. Ruiz-Arias and J. Tovar-Pescador. 2011. *Sensitivity analisis of WRF wind estimates to land-cover representation and daily SST variability*. Manuscript in preparation.

2.1 Introduction

Reliable and robust wind databases are fundamental for wind resources assessment. This assessment can be divided in two steps (Sempreviva et al., 2008): firstly, a regional wind assessment, which aims to evaluate the resources of a region in a first approach and, secondly, a detailed evaluation of specific locations, taking into account micro-scale effects as those related to the topography and terrain properties.

Currently, regional wind assessment is carried out using Numerical Weather Prediction (NWP) models (Lavagini et al., 2006; Zagar et al., 2006; Kanamitsu and Kanamaru, 2007; Byrkjedal et al., 2008; Hahmann et al., 2010; Shimada and Oshawa, 2011). These models allow obtaining a comprehensive description of the atmospheric system using

initial and boundary conditions from atmospheric reanalysis. Based on downscaling techniques, current NWP models resolve local and regional circulation patterns, taking into account local topographic surface features up to certain extend. As a consequence, these models can provide accurate meteorological information, such as wind speed and direction over large regions with a high temporal (few minutes) and spatial (few km) resolution. However, NWP models are not used directly for specific site wind resources assessment. To this end, micro-scale models, such as the Wind Atlas and Application Program (WasP, Mortensen et al. (1993, 1998)), the WindSim (Gravdahl and Harstveit, 2000) or the 3DWind (Undheim, 2005), are commonly used. In particular, the WAsP model uses horizontal and vertical extrapolation of measured wind data, based on the Wind Atlas methodology (Troen and Petersen, 1989), in order to obtain a wind climatology at the sites of interest. WAsP model is based on the physical principles of flows in the atmospheric boundary layer and accounts for the effects of different surface roughness conditions, sheltering effects due to the buildings and other obstacles, and the modification of the wind imposed by the specific terrain height variations around the site under study. To this end, WAsP model needs wind speed and direction observations provided by meteorological stations as input. Since these observations are scarce, some authors have proposed the use of NWP models estimates as input in these micro-scale models (Frank et al., 2001; Jiménez et al., 2008; Badger et al., 2010).

The accuracy of surface wind speed estimates based on NWP depends, mainly, on how the next three issues are addressed. First, a proper selection of the physical configuration of the model (mainly of the planetary boundary layer parameterization) is needed (Borge et al., 2008; Jiménez and Dudhia, 2012; Santos-Alamillos et al., 2012a). Second, an adequate representation of topography, which depends on the spatial resolution used in the model set up, is essential (Santos-Alamillos et al., 2012a). Both previous issues have been addressed in a previous work (Santos-Alamillos et al., 2012a) for the study region considered in this work. Finally, a satisfactory representation of the surface terrain properties is also a key issue. These properties are mainly characterized within the land surface schemes of the NWP models. These schemes govern the partitioning of available energy at the surface between sensible and latent heat, and control the segregation of the available water between evaporation and runoff. As a consequence the heat, moisture and momentum exchanges between the land surface and the overlying atmosphere are affected by these land surface properties (Sertel et al., 2008). Land surface schemes

contain specific values of land surface parameters such as the roughness length, albedo, thermal inertia, moisture or emissivity, which are derived from land-use category maps that usually vary on a seasonal basis. These land-use category maps are derived from remote sensing land-cover products (Pielke et al., 1999; Schweiger et al., 2005; Sertel et al., 2008; Kaya et al., 2008). The most important of such products are: the Global Land Cover Characteristics (GLCC, Loveland et al. (2000)), developed by the United States Geological Survey (USGS), the University of Maryland land cover classification (UDM, Hansen and Reed (2000)) and the Global Land Cover 2000 (Bartholome et al., 2002). In particular, the NWP model considered in this work, the Weather Research and Forecasting model (WRF, Skamarock et al. (2008)), includes the GLCC global-cover map for setting the values of the land surface parameters above mentioned. This map was derived from satellite estimates obtained along the period 1992-93 and has a 1 km spatial resolution (Chen, 2007; Ran et al., 2010).

Land surface properties exhibit a considerable spatial variability which affects mesoscale atmospheric circulations (Hartmann, 1994; Chen and Dudhia, 2001; Weaver and Avissar, 2001; Yang, 2004). In addition, these surface properties changes in time continuously as result of human and natural processes, such as urbanization, deforestation, desertification and natural disasters. The extent to which the land cover properties are accurately represented in NWP models have been analyzed in in several works along the last years. For instance, Ezber et al. (2007) concluded that the MM5 model have a poor (old) representation of the land properties in the Istanbul region. Pitman (2003) used vegetation data from the Atlas of Australian Resources (AUSLIG, 1990) in their studies to allow for a better representation of the land surface properties. Moreover, Sertel et al. (2008) developed a new land cover map, based on the GLCC, for regional climate modeling and compared it performance in the Marmara region (Turkey) against the default land-cover map in the WRF model. They found significant differences, especially in urban areas, and a high sensitivity of the temperature estimates to changes in the land-cover maps. Similarly, Pineda et al. (2004) concluded that surface properties in urban areas of the northern Iberian Peninsula were not properly represented in the MM5 model. As a consequence, these authors developed a new land-use map for this model based in the Coordination of Information on the Environment (CORINE) land-use map of the European Environment Agency NETLAND information package (EEAA, 2000) and compared surface wind speed and temperature estimates based on the default land

use properties and the new ones derived from the CORINE dataset. Results showed a slightly improvement in wind field estimates using the CORINE, especially in the wind direction. To sum up, to have an updated version of the land surface properties implemented in the NWP models is necessary if representative wind speed and direction estimates are aimed.

Aside from the model physical configuration, terrain and surface representation, it has been reported that the frequently updating of the Surface Sea Temperature (SST) values during the NWP models integrations leads to an improvement in the accuracy of the wind estimates (Muller at al., 2007). These authors concluded that the use of daily updated SSTs leads to a better consistency between the exchanges at the air/sea interface by taking into account changes in stratification and temperature gradients at this interface. This allows, ultimately, a better representation of the local circulations in the coastal line.

This work aims mainly to evaluate the role of surface properties representation in the WRF model as they relate to regional wind resource assessment. In addition, we aim to evaluate the effect of daily SST updating during the WRF integration in this regional assessment. To evaluate the sensitivity of WRF wind estimates to the terrain surface properties representation, wind estimates derived from two model integrations which used different land-cover maps were evaluated. The first land-cover map evaluated was the GLCC, that is, the default land-cover representation in the WRF model. In addition, a new land-cover map, derived from the CORINE dataset and reclassified according to the GLCC categories, was obtained and the corresponding wind estimates evaluated. In order to assess the role of the SST updating the two former model integrations were conducted both using daily varying and prescribed SSTs values. Therefore, four experiments were conducted and the resulting wind estimates evaluated. The work applies to the region of Andalusia (Southern Spain). Although relatively small, this region is characterized by varied topographic, geographic and weather conditions that make the evaluation especially challenging. Estimates are tested against data collected along the year 2009 from three stations that provided hourly wind speed and direction data at 10 m above ground level (m.a.g.l) and from one station that provided hourly wind speed and direction values at 30 and 60 m.a.g.l. Station locations are representative of different climatic, topographic and surface conditions, thus allowing a comprehensive evaluation of the WRF wind estimates.

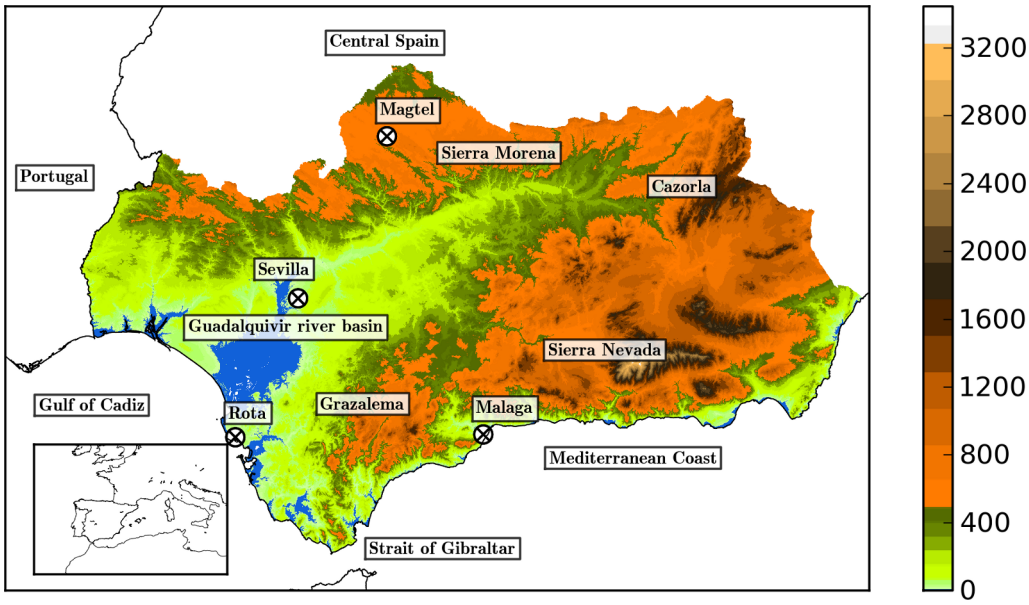


Figure 2.1. Study region and location of the 4 wind-measuring meteorological masts. Elevation is also graphed using a Digital Elevation Model of 90 m spatial resolution.

The work is organized as follows: Section 2.2 describes the study region, terrain characteristics and data. Section 2.3 details the methods and Section 2.4 the results. Finally, main conclusions are presented in Section 2.5.

2.2 Database and study area

The study region (Fig. 2.1) is Andalusia, in the southern Iberian Peninsula (IP). It extends over 87000 km^2. The region (latitude 35°30' to 38°30' N and longitude 7°30' to 1°30' W) is located in a transition zone between temperate and subtropical climates. From a topographic point of view, the region may be split into two different parts. The western part, covering around 40000 km^2, is a nearly homogeneous flat area, around 100 m above sea level (m.a.s.l.). The eastern part has very complex topography with several mountain areas, reaching 3482 m.a.s.l in the Sierra Nevada National Park (the highest elevation on the IP).

The atmospheric circulation over most of the IP is dominated by a semi-permanent, subtropical high-pressure center over the Azores Islands, particularly so in the south over the study region. The position and intensity of this center changes through the year. During winter, the high is at lower latitudes, allowing the region to be affected by zonal circulations from the west. During summer, the high migrates northward, blocking the westerly circulations over most of the IP and particularly over the study region (Pozo-Vázquez et al., 2001; Trigo et al., 2002; Castro-Díez et al., 2002). Although the entire region is under the influence of the Azores subtropical high, it has a wide range of climate conditions. This range is related to topographic features. The eastern part is less influenced by the Azores high, and more affected by the Mediterranean Sea (Esteban-Parra et al., 1998; Rodríguez-Puebla et al., 1998; Ramos-Calzado et al., 2008). The western part is actually the lower Guadalquivir River valley, and is exposed to mild and moist air coming from the Atlantic. Winds are channeled through this valley, generating relatively high wind speeds values in the upper part of the valley (Alsamamra et al., 2011). The eastern part is partially isolated from this Atlantic influence by the Sierra Nevada and Cazorla mountain ranges (Fig. 2.1). Annual precipitations over the region ranges from 300 $mmyear^{-1}$ in south-eastern area, to more than 2500 $mmyear^{-1}$ in the mountains near the Strait of Gibraltar (Ramos-Calzado et al., 2008). In addition, the study region is bounded on the south by the Atlantic (western part) and the Mediterranean (eastern part), representing about 900 km of coastline. Finally, one of the most important features is the strong semi-permanent winds at Strait of Gibraltar area.

WRF wind estimates validation was carried out based on data collected at four meteorological stations (Fig. 2.1). Three stations, corresponding to the Spanish National Weather Service (AEMET) network, include hourly values of wind speed and direction measured at 10 m.a.g.l collected along the year 2009. The fourth station, a meteorological mast owned by the private company Magtel, includes wind speed and direction measured at 30 and 60 m.a.g.l collected along the same period.

The areas corresponding to the four stations locations present different terrain complexity and geographic features. Since these factors have a marked influence on the surface wind (Santos-Alamillos et al., 2012a), a characterization of these features was here attempted. Many different parameters for characterizing terrain complexity have

Station	Measuring elevation (m)	Dist. to the coast (km)	Elevation (m)	(σ) (m)	rlf (m)
Málaga	10	2.3	11.0	8.98	48
Sevilla	10	75.0	29.4	4.45	30
Rota	10	1.5	20.2	7.98	31
Magtel	30 and 60	150.1	646.3	33.38	133

Table 2.1. Measuring elevations and main topographic characteristics of the station locations. The station location elevations and the distance to the coast are derived from 90-m spatial resolution Digital Elevation Map (DEM). The Standard deviation of elevation (denoted as σ) and the relief (denoted as rlf) parameters are also shown for each station. Both parameters were derived from the above mentioned DEM and computed over an area of 3×3 km centered at each station location. All values are in meters except distance to the coast which is in km.

been defined in the literature (Huaxing, 2008). In this work, we consider two type of terrain complexity parameters: the standard deviation of elevation (denoted as σ) and the relief (denoted as rlf), which is the difference between the highest and lowest altitude. Both parameters were derived from a 90-m spatial resolution Digital Elevation Model (DEM), computed on a 3×3 km grid box centered at each mast location. The values of the σ and rlf (terrain), along with the distance to the sea and the location station elevations, are displayed in Table 2.1. Two of the stations, Málaga and Rota, are located close to the sea and at low elevations. The Málaga station location area shows a higher topographic complexity than the Rota one, as derived from the rlf parameter. Sevilla station is located inland, at 75 km from the coast and at low elevation (about 30 m.a.s.l) and in an area of low topographic complexity. Finally, Magtel station is located at the north of the study region, at a relatively high elevation. In addition, this station location presents the highest topographic complexity among the four analyzed, as derived from the rlf and σ parameters.

Finally, a data quality control procedure based on Jiménez et al. (2010) was conducted. After this procedure, the 0.5% of AEMET and the 2.76% of the Magtel dataset were considered as suspicious records and, therefore, removed.

2.3 Methods

2.3.1 WRF set up

The WRF ARW v3.2 has been used in this work. The domain's setting is shown in Fig. 2.2. The outer domain has a spatial resolution of 27 km, covering the Iberian Peninsula and the northern part of Africa. The second domain has a spatial resolution of 9 km and it is extended over the southern part of the Iberian Peninsula. Finally, the third domain has a spatial resolution of 3 km and it is centered over the study region. Values corresponding to this third domain were finally evaluated. For the three domains, a two-way interaction was used, with a total of 36 vertical levels with 8 levels located in the first 1000 m.a.g.l. The first five lowest vertical levels, at approximately 4, 18, 43, 64 and 76 m.a.g.l, were used in a vertical interpolation to estimate the wind at the two measurement elevations (30 and 60 m.a.g.l) of the Magtel station. For the three AEMET stations, the standard 10 m.a.g.l wind speed provided by WRF output, was used. Initial and boundary conditions for the simulation were generated using the Climate Forecast System Reanalysis (CFSR, Saha et al. (2010)) with 0.5° spatial resolution and 6-hour time interval.

Physical configuration of the model was selected based on previous evaluations of the WRF performance in the study region (Fernández et al., 2007; Borge et al., 2008; Ruiz-Arias et al., 2008; Santos-Alamillos et al., 2012a). The RRTM scheme (Mlawer et al., 1997) was chosen for long-wave radiation, and the Dudhia Scheme (Dudhia, 1989) for short-wave radiation. The Kain-Fritsch scheme (Kain and Fritsch , 1993), was used for cumulus and the Yonsei University (Hong et al., 2006) planetary boundary layer scheme for the boundary layer. Finally, the Thompson graupel scheme (Thompson et al., 2006) was used for microphysics, and the unified Noah land-surface model for the land surface.

Newtonian relaxation or nudging was used in model integrations, using the parameter values proposed by Seaman (2000) and Otte (2008b). This technique relaxes the model toward the observed state by adding artificial forcing terms to the model predictive equations, based on the difference between the states weighted by nudge coefficients. Several works have demonstrated the advantages obtained when using nudging for simulating the wind field (Bao and Errico, 1997; Barna and Lamb, 2000).

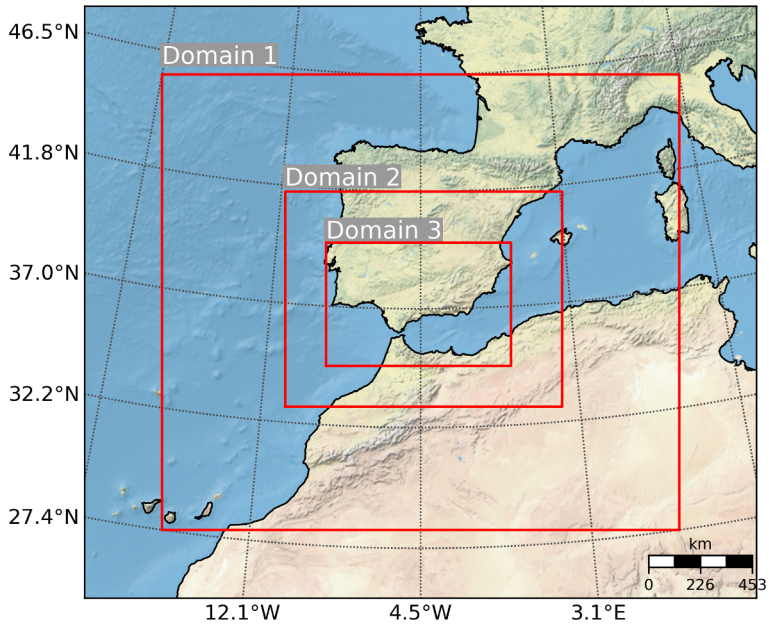


Figure 2.2. Spatial configuration of domains for the numerical simulation: three nested domains with 27, 9 and 3 km horizontal resolutions, respectively. Data from the inner domain (3 km) were analyzed.

Topography, land-use and land-water masks datasets were interpolated from the GLCC dataset for the two first domains, using a spatial resolution of 5' and 2' respectively. However, for the third domain, and in order to evaluate the sensitivity of WRF wind estimates to the terrain surface properties representation, two different land-cover data sets were assessed. In a first experiment, the GLCC land-cover dataset, the default in the WRF model and with a spatial resolution of 30" (about 1 km at the study region latitudes), was used. In a second experiment, a modified version of the CORINE 100 m spatial resolution land-cover map was assessed. Notably, since the CORINE and GLCC land uses categories differs, a reclassification of the CORINE to GLCC categories was conducted following Pineda et al. (2004). This reclassification uses an equivalence based on the Gower metric statistics (Gower, 1971), which compares the annual Normalized Vegetation Index (NDVI) cycle similarities between GLCC and CORINE categories. The method assumes that surface roughness is mainly due to vegetation cover and that there is a good relationship between soil moisture and vegetation presence. After the reclassification only 2% of the pixels of the CORINE land cover map have not associated a GLCC category. These pixels were classified using the nearest neighbor and based on

the reclassified CORINE categories.

Finally, the role of SST variability in the reliability of the wind estimates was assessed by alternatively maintaining prescribed or including daily variations in the SST. The SST values were interpolated to the ocean grid points on each model domain using the NCEP Version 2.0 global SST dataset (Reynolds et al., 2002), which is defined on a 1° × 1° grid and updated daily.

To sum up, four experiments were conducted and the corresponding wind estimates evaluated. The two first experiments used the GLCC land cover data set, using prescribed (hereinafter experiment E1) and daily varying SSTs (E3). The second two experiments used the reclassified CORINE land cover data set, using prescribed (E2) and daily varying SSTs (E4).

2.3.2 Evaluation statistics

The validation of different experiments was conducted based on various statistics for both wind speed and direction. First, we used the Root Mean Square Error (RMSE), which estimates the amount of scatter of the wind speed values:

$$RMSE = \sqrt{\frac{1}{N}\sum(m_i - o_i)^2}, \tag{2.1}$$

where N is the number of records, and m and o are modeled and observed wind speed values, respectively. Second, we used the Mean Error (ME), which quantifies overall bias of the wind speed values and detects model overestimation or underestimation:

$$ME = \frac{\sum(m_i - o_i)}{N}. \tag{2.2}$$

Traditionally, direction data have been evaluated using graphical methods. Simple methods, such as wind rose plots, have been used to understand directional characteristics.

However, these methods have limitations regarding meaningful statistical evaluation. Jammalamadaka and Sengupta (2001) defined the circular distance between any two points as the smaller of the two arc lengths between the points along the circumference. For angles α and β, the circular distance is defined as:

$$\Delta(\alpha, \beta) = min(\|\alpha - \beta\|, 360^\circ - (\|\alpha - \beta\|)). \tag{2.3}$$

Here we propose the use of an accuracy parameter (denoted as ACC) based on this circular distance for the evaluation of the WRF wind direction estimates. This parameter accounts for the percentage of times in which the circular distance between the observed and modeled wind direction is lower than a threshold, chosen as 30° here. Therefore, this parameter is defined as:

$$ACC(\alpha, \beta) = \frac{\sum_i 1) \text{ if } \Delta \leq 30^\circ)}{N}. \tag{2.4}$$

2.4 Results

2.4.1 Comparing GLCC and CORINE-derived land use maps

Fig. 2.3 shows land-cover categories maps over the study region corresponding to the 100-m spatial resolution CORINE dataset reclassified according to the GLCC categories, the former CORINE dataset but as used in the WRF 3 km spatial resolution integration, and the GLCC dataset used in the WRF integration (also with 3 km spatial resolution). A comparison between the last two land-cover maps, used in the WRF integrations, has been conducted using the confusion matrix (Sertel et al., 2008). This matrix consists on a simple cross-tabulation of the categorical map against observations or reference data, in a similar way than a contingency table. An accuracy statistic parameter, the Cohen's Kappa coefficient can be derived from this confusion matrix (Fitzgeral and Lees, 1994; Foody, 2002) in order to summarize the comparison. Cohen's Kappa statistic is a measure of overall accuracy of the image classification, computed as the mean of

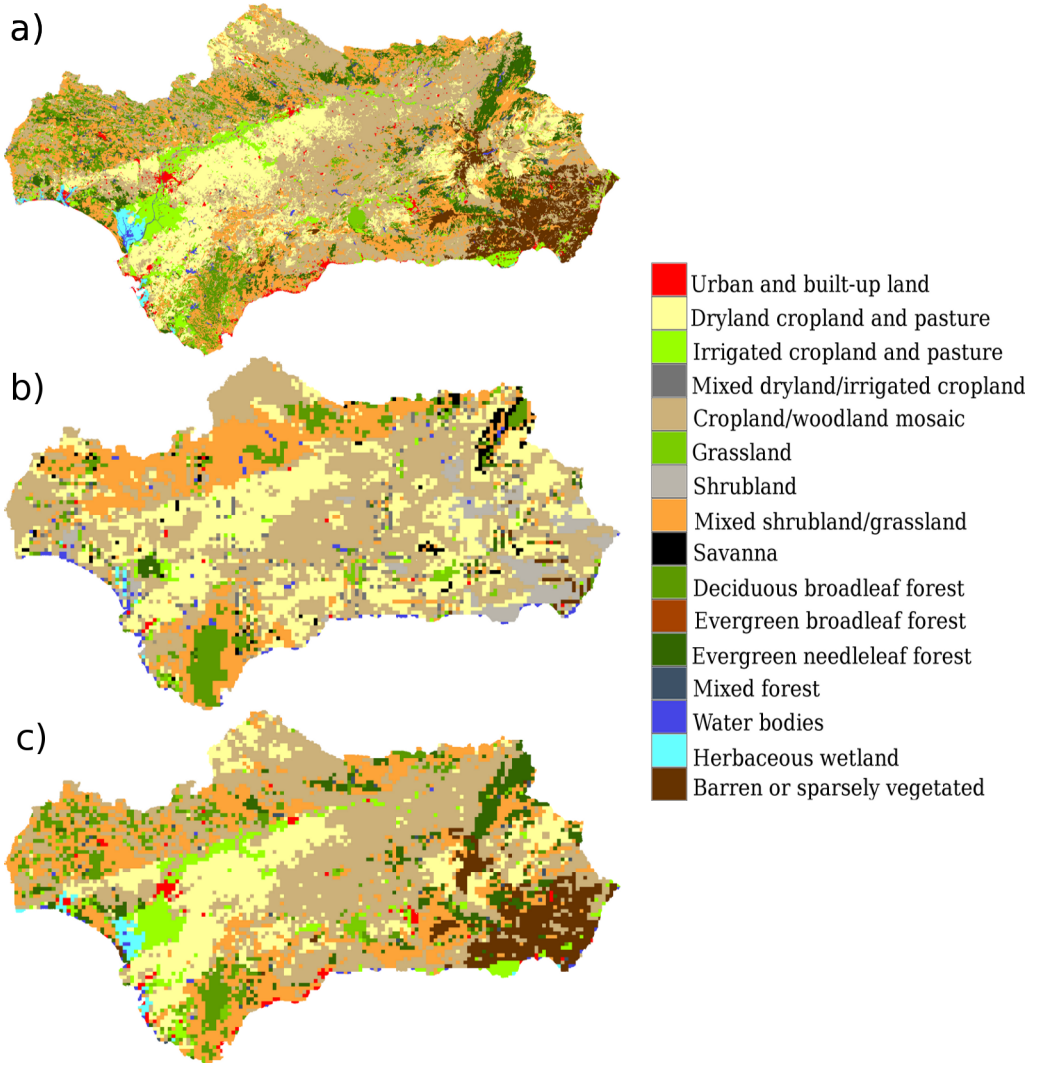


Figure 2.3. Land-cover maps categories. Fig. 2.3a represents the 100m spatial resolution CORINE Land-Cover reclassified to the GLCC Land-Cover map categories. Fig. 2.3b shows the 3km spatial resolution land-cover map of WRF using the GLCC map at 30" spatial resolution. Fig. 2.3c presents the 3km spatial resolution land-cover map of WRF using the implemented CORINE at 100m spatial resolution, reclassified to the GLCC categories.

Land-use Categories	CORINE 100-m (%)	GLCC 3 km (%)	CORINE 3 km (%)	Cohen's Kappa
Urban and built-up land	1.5	1.2	0.2	0.18
Dry-land cropland and pasture	17.7	17.1	26.4	0.45
Irrigated cropland and pasture	4.9	4.6	0.8	0.13
Mixed dry-land/irrigated cropland and pasture	—	—	1.8	—
Cropland/grassland mosaic	—	—	0.6	—
Cropland/Woodland mosaic	32.7	36.2	37.4	0.42
Grassland	2.5	1.3	1.3	0.40
Shrub-land	—	—	5.3	—
Mixed shrub-land/grassland	19.6	20.0	16.6	0.31
Savanna	—	—	1.6	—
Deciduous broad-leaf forest	6.9	5.5	5.0	0.36
Evergreen need-leaf forest	6.0	5.8	1.0	0.10
Mixed forest	0.8	0.5	0.1	0.14
Water bodies	0.7	0.5	1.3	0.88
Herbaceous wetland	0.8	0.9	0.1	0.16
Barren or sparsely vegetated	5.9	6.4	0.5	0.07

Table 2.2. Land-cover categories maps over the study region corresponding to: a) the 100-m spatial resolution CORINE dataset reclassified according to the GLCC categories; b) the GLCC dataset used in the WRF integrations (with 3 km spatial resolution); and c) the CORINE dataset but as used in the WRF 3 km spatial resolution integrations.

agreement between classified and reference data. This parameter ranges from 0 to 1, where 0 represents agreement due to chance only and 1 represents a perfect agreement between the two data sets. We computed the Kappa coefficient for each category and for all categories altogether. Following (Landis and Koch, 1987), the agreement between the two land cover maps is poor when Kappa < 0.4, good when 0.4 < Kappa < 0.7 and excellent when Kappa > 0.75.

Table 2.2 presents the land-use composition distribution for the three land-use maps, as well as the Kappa coefficients resulting from the comparison of the two 3 km spatial resolution land cover maps. The Cohen's Kappa coefficient value for all categories is 0.29, indicating therefore a general poor agreement between the two land-cover maps. In a more detailed analysis, dry-land cropland and pasture, cropland/woodland, grassland and water bodies categories show values above 0.4, and therefore present a good/excellent agreement. The rest of categories present a poor agreement, especially the urban and built-up land, irrigated cropland and pasture, evergreen need-leaf forest, mixed forest, herbaceous wetland and barren or sparsely vegetated categories, which show Kappa coefficient values below 0.2. Urbanized areas category (represented by red

color in Fig. 2.3) shows a poor agreement. Differences are especially remarkable in the Mediterranean coast and in high populated areas. Moreover, the irrigated cropland and pasture category presents also notable differences in both dataset. This category is observed in extensive areas in the CORINE 3 km land-cover map (Fig. 2.3c), especially in the Guadalquivir valley area and in some Mediterranean coastal areas. However this category is hardly observed in the GLCC map (Fig. 2.3b). Finally, the barren or sparsely vegetated category distribution areas also present notable differences between the two dataset (Kappa coefficient 0.07). This category is mainly observed in the south-eastern of the Iberian Peninsula (Fig. 2.3a, 2.3c) in the CORINE datasets. However, the GLCC dataset only included a 0.5% of this category, and many areas pertaining to this category in the CORINE dataset appears as shrub-land and dry-land, cropland and pasture categories in the GLCC dataset.

2.4.2 Evaluation of the terrain and surface length representation at the station locations

In this section, an evaluation of the model terrain elevation and roughness length representation around station locations is conducted. To this end, Table 2.3 shows, firstly, the stations location elevation as derived from a 90m-DEM (reference altitude) and those used in the 3 km spatial resolution WRF integration. Notable differences between the reference and modeled altitudes are observed for the Málaga and Magtel stations. For Málaga station, the model overestimates the reference elevation in about 55 m, while for Magtel station, a clear underestimation is observed (around 31 m). This misrepresentation of the station elevations is associated with the relative complex topography of the areas where these two stations are located (Section 2.2 and Table 2.1). The other two stations elevations are fairly reproduced in the model.

Secondly, roughness length values at station locations areas as derived from: the CORINE 100 m spatial resolution dataset, reclassified according to the GLCC categories and used as reference value, and as derived from the CORINE and GLCC datasets used in the 3 km spatial resolution WRF experiments were compared. Notably, mean roughness length values over an area of 9 × 9 km centered at the stations locations were computed based on each land cover dataset. In addition, since roughness length varies

Station	Elevation (m)		Mean Roughness length (m)					
	DEM	WRF	CORINE 100m		GLCC 3 km		CORINE 3 km	
			W	S	W	S	W	S
Málaga	11	66	0.41	0.41	0.20	0.20	0.40	0.50
Sevilla	29	25	0.20	0.23	0.16	0.21	0.20	0.29
Rota	20	19	0.32	0.35	0.10	0.15	0.27	0.33
Magtel	646	615	0.10	0.15	0.20	0.20	0.15	0.18

Table 2.3. Evaluation of elevations and roughness length (RL) values represented in WRF model. The first two columns shows the elevations of the station locations as derived from a 90 m spatial resolution Digital Elevation Model (DEM) and used in the WRF 3 km spatial resolution experiments. The following columns show the RL values, both for winter (W) and summer (S), computed over an area of 9 × 9 km centered at each station, using a) the CORINE 100 m spatial resolution land-cover maps and b) the GLCC and c) CORINE dataset used in the 3 km spatial resolution WRF experiments.

from winter to summer, values were obtained for both seasons. The roughness length values were obtained from the land use categories based on the reference values in WRF model.

Notable differences in the RL values are observed among the different datasets, particularly when comparing the two CORINE derived values and the GLCC one. In general, and as may be expected, the CORINE 3 km values are closer than the GLCC 3 km ones to reference values (CORINE 100-m). The greatest differences are observed at Málaga station, where the GLCC values are about half of the CORINE ones. At Sevilla station, the three land cover dataset offer similar RL values. Differences between the winter and summer RL values are higher in the CORINE 3 km dataset than in the other two datasets.

2.4.3 Evaluation of surface wind speed and direction estimates

Since Málaga, Rota and Sevilla stations present the same measuring elevation, 10 m.a.g.l and Magtel station presents specific measuring elevations (30 and 60 m.a.g.l) we have conducted the evaluation procedure independently for the first three stations and then

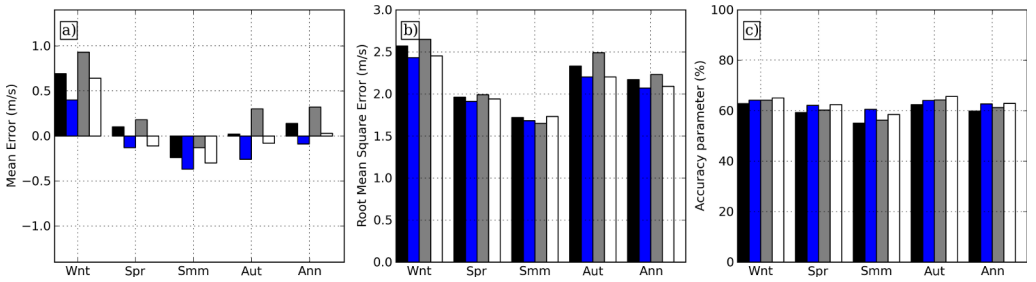


Figure 2.4. Evaluation results for Málaga station for all experiments and study periods. In particular Fig. 4a shows the ME values corresponding to the four experiments: E1 (black bar, GLCC dataset with prescribed SSTs), E2 (blue bar, CORINE dataset with prescribed SSTs), E3 (grey bar, GLCC dataset with daily updated SSTs) and E4 (white bar, CORINE dataset with daily updated SSTs). Fig. 2.4b and 2.4c are as in Fig. 2.4a but for RMSE and ACC parameter.

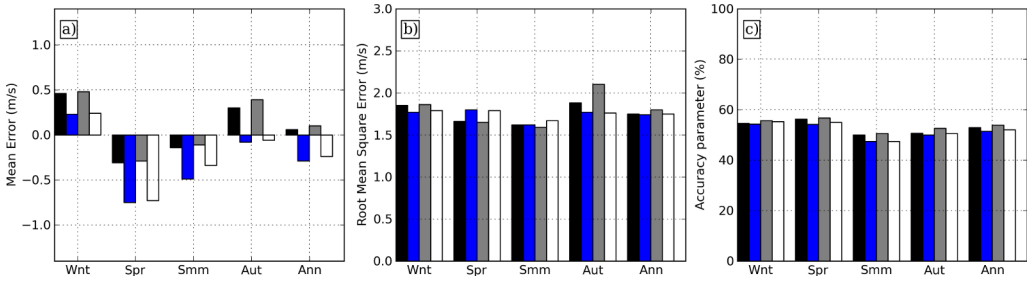


Figure 2.5. As in Fig. 2.4 but for Sevilla station.

for Magtel station. Figs. 2.4 to 2.6 show, respectively, the evaluation results for Málaga, Sevilla and Rota stations.

Relative low ME values are found: for most of the stations, study periods and experiments values are well below ± 0.5 ms^{-1}. Maximum values are found for Rota station (Fig. 2.6a), ranging from -1.0 (E4 in spring) to 1.1 ms^{-1} (E3 in autumn). In general, there is a clear tendency to overestimate wind speed values in winter and autumn, and to underestimate these values in spring and summer while annual values are close to zero. Málaga station presents the lowest negative values in spring and summer and the highest positive values during winter. This may be the results of the considerable overestimation of this station elevation by WRF model (Table 2.3), which leads to an

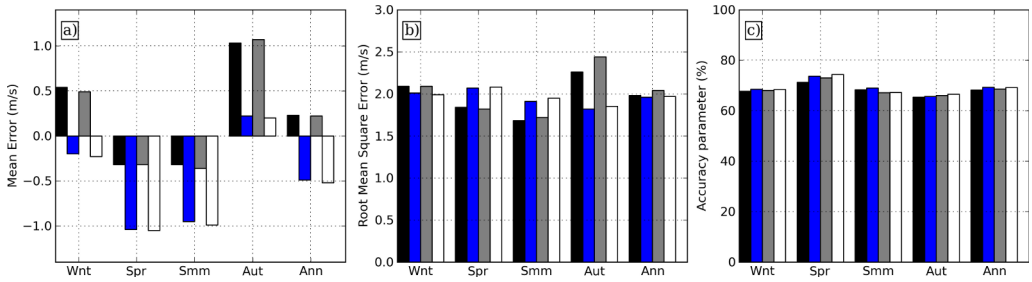


Figure 2.6. As in Fig. 2.4 but for Rota station.

overestimation of the wind speed (Jiménez and Dudhia, 2012; Santos-Alamillos et al., 2012a). At the other two locations, the role of the misrepresentation of elevation is less important, since elevation is fairly represented in WRF model (Table 2.3).

The role of land-cover representation in ME values is highly variable among stations and study periods. For instance, during winter, the CORINE land-cover (experiments E2 and E4) provides considerable lower (about the half) ME at the three stations. Maximum difference is observed at the Rota station: about 0.5 ms^{-1} against about -0.2 ms^{-1}. This result is consistent with the roughness length values presented in Table 2.3. As shown in this Table, winter roughness length values used in CORINE experiments are considerable closer to reference values than those used in the GLCC experiments. For instance, at Málaga station, the reference value is 0.41, CORINE uses 0.4 and GLCC 0.2. Therefore, the GLCC dataset considerably underestimates roughness length, given rise to higher ME values. Similar conclusions can be drawn for the Sevilla and Rota stations. For the rest of the seasons, results are more varied. Notably, during summer, the CORINE dataset tends to provide considerable higher negative ME values, particularly at Sevilla and Rota stations, where elevation is fairly represented in WRF model. At this season and for both stations, CORINE dataset provides considerable higher roughness length values than the GLCC (Table 2.3) and, at the same time, slightly higher values than reference ones. These overestimations reduce the wind speed values in the E2 and E4 experiments, leading to higher negative ME values associated with CORINE. On annual basis, the CORINE dataset provides better estimates, in terms of the ME, at Málaga but worse at Sevilla and Rota. At the Málaga stations, there seems to be a compensating effect between the overestimation of the wind speed due to the overestimation of elevation

and the underestimation of wind speed due to the overestimation of roughness length values (especially in summer). This gives rise to relatively low ME values associated with CORINE dataset, particularly at annual case.

The role of SSTs updating in ME values is significant but highly varying among seasons and stations. The most important effect is observed at Málaga station, where the SSTs updating clearly increases the ME values in winter and reduces these values during summer and autumn when is associated with CORINE land cover. This lead to an annual ME value close to zero for the experiment E4 (CORINE+SST updating). At Sevilla station, a slightly reduction in ME values is observed, for all the study periods excepting winter, when using the SSTs updating and the CORINE dataset. No significant effect is observed for Rota coastal station.

To sum up, CORINE land cover dataset tends to provide lower ME values during winter for all stations, while during summer, the GLCC shows a better performance. The annual ME values are lower when using the GLCC except for the Málaga station. In particular, at this station, a compensating effect between the overestimation of both the station elevation and the roughness length is observed, leading to very low ME values. The role of the SSTs is more limited, excepting for Málaga station, where the use of updated SSTs and CORINE dataset leads to the lowest ME values, excepting winter.

RMSE values (Figs. 2.4b, 2.5b and 2.6b) considerably differ between stations and experiments. Overall, the lowest values are found for Sevilla (Fig. 2.5b, below 2 ms^{-1}), intermediate values are observed at Rota (Fig. 2.6b, about $2ms^{-1}$) and maximum values are obtained at Málaga station (Fig. 2.4b, above $2ms^{-1}$). Note that the last-cited station presents the highest topographic complexity (Table 2.1) and a considerable elevation overestimation by WRF model (Table 2.3). Seasonal variations are quite remarkable, especially at the two coastal stations (Málaga and Rota), with maximum values in winter and autumn and minimum values in summer. The role of land-use datasets is similar to those assesed in the ME analysis, but with a lower magnitude differences. In general, as in the ME case, CORINE dataset provides slightly lower RMSE values at the three stations during winter and, remarkably, during autumn. Maximum differences are observed during this last season for Rota station (Fig. 2.6b, about 0.5 ms^{-1}). In contrast, and similarly to the ME case, during spring and summer the GLCC dataset

provides slightly lower RMSE values at Sevilla and Rota stations. The former seasonal results can be explained based on the more accurate representation of the roughness length by CORINE dataset during winter and by GLCC during summer. In addition, a compensating effect among seasons leads to very small differences between the RMSE values associated with the two land cover dataset in the annual analysis. Finally, the effect of the daily updating of the SSTs on the RMSE values seems to be very limited. The only remarkable result is the RMSE increment observed at the three stations during autumn when combining the use of updated SSTs and GLCC dataset.

To sum up, CORINE land-cover dataset tends to provide lower RMSE values during winter and autumn for all stations, while during the rest of seasons, GLCC shows a better performance. Results can be explained based on roughness length representation provided by both dataset. The annual analysis shows scarce differences in RMSE values, due to a compensating effect between seasons. The role of the SSTs is much more limited than in the case of ME analysis.

Finally, the ACC parameter tends to be higher at Rota station (Fig. 2.6c, above 60%) and lower at Sevilla station (Fig. 2.5c, well below 60%). The dependence of this parameter on the land-use dataset is low. The CORINE dataset tends to provide slightly higher ACC values at coastal stations (Málaga and Rota) and slightly lower values at Sevilla station. Finally the use of updates SSTs values tends to provide slightly higher ACC at the two coastal stations, for all experiments, but differences are low.

To conclude, the influence of land-surface representation and SSTs updating is more important on the ME than for the rest of evaluation statatistics. Influence on the RMSE is also important while being low on the ACC. Regarding the land-use dataset, the CORINE one provided lower ME and RMSE during winter and the GLCC during summer. These results can be explained based on the accuracy of roughness length representation provided by both datasets in summer and winter. At annual basis, a compensating effect among seasons gives rise to lower ME values associated with the CORINE dataset for Málaga station, and associated with the GLCC dataset for the other two stations. The annual analysis shows scarce differences in RMSE values, due to this compensating effect between seasons. Finally, a low sensitivity of wind direction to the land-use dataset is found. The CORINE dataset provides slightly higher ACC

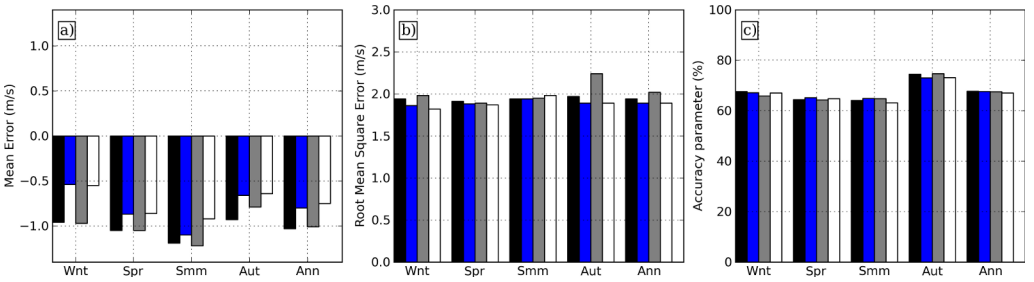


Figure 2.7. As in Fig. 2.4 but for Magtel station at 30 m.a.g.l.

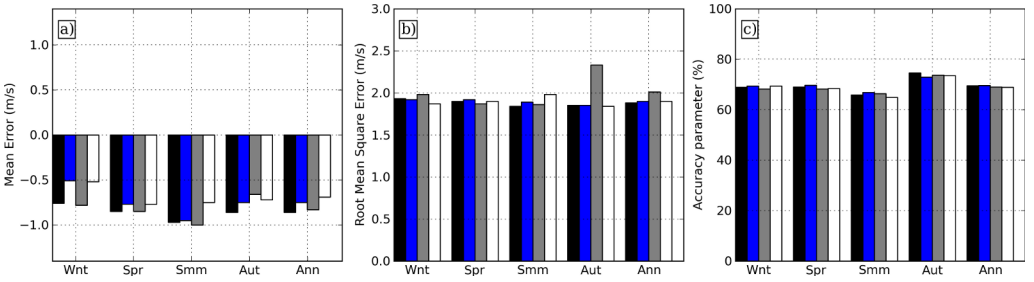


Figure 2.8. As in Fig. 2.4 but for Magtel station at 60 m.a.g.l.

values at the coastal stations (Málaga and Rota) and slightly lower values at Sevilla station. Regarding the SSTs updating, its influence is mainly observed in ME values and at coastal stations. Notably, at Málaga station, the use of updated SST in combination with CORINE land-cover tends to provide considerable lower ME values. Updated SSTs tends also to provide slightly better wind direction estimates at the two coastal stations, but differences are low.

2.4.4 Evaluation of wind speed and direction in Magtel station

In this section, an evaluation of modeled wind speed and direction estimates is conducted for Magtel station. As mentioned above, this station presents two specific measurement elevations, 30 and 60 m.a.g.l.

Figs. 2.7a and 2.8a show the ME values resulting from the four experiments conducted, for the different study periods. Overall, a marked underestimation of wind speed is observed for all cases and at both evaluation altitudes. This general negative bias can be explained based on, firstly, the notable underestimation of the station elevation in the WRF model and, secondly, the overestimation of the roughness length at the station location provide by both the CORINE and GLCC land cover datasets (Table 2.3). As may be expected, due to the reduced effect of the roughness length at higher elevations, the bias is about 25% lower at the highest evaluation altitude. At both measuring elevations, there is a clear seasonal dependence of ME values, being higher (in absolute value) during summer and lower during winter. A clear effect of the land-use dataset is observed. Notably, the CORINE dataset provides considerable lower ME values (in absolute value). Differences are remarkable during winter, when the bias associated with CORINE dataset is about the half of those associated with GLCC one. Differences decrease considerably at annual period. Note also that differences associated with the land-use dataset reduces with the measuring elevation. For instance, for the annual study, the use of the CORINE reduces about 20% the ME values at the 30 m.a.g.l measuring elevation (Fig. 2.7a), while at the 60 m.a.g.l one (Fig. 2.8a), the improvement is only about 10%. Finally, the use of updated SSTs shows a significant effect mainly during summer and when combined with the CORINE dataset; in such cases the bias diminishes about 20% at both measuring elevations. For the annual study, this reduction is weaker but relevant.

Similarly to the other three stations analyses, the role of land-use and SSTs showed to be considerable lower in the RMSE and the ACC parameter than in ME one. The CORINE dataset provides lower RMSE values at the lower measuring elevation (Fig. 2.7b), although differences are low. Maximum difference is observed in winter (about 0.1 ms^{-1}). Moreover, at the highest measuring elevation (Fig. 2.8b) performance of both land-cover datasets is similar. The updating of the SSTs seems to have a negligible effect on the RMSE values, except during autumn and in combination with the GLCC land cover, when particularly higher RMSE values are obtained.

Finally, the ACC values are considerable higher during autumn at both measuring elevation (Figs. 2.7c and 2.8c) compared to the rest of the seasons. Nevertheless, little sensitivity to both the land cover and SSTs is observed. Only slightly higher ACC values

are observed during autumn when using the GLCC dataset.

2.5 Summary and conclusions

The accuracy of wind speed and direction estimates based on Numerical Weather Prediction (NWP) models depends, mainly, on how three issues are addressed. Firstly, a proper selection of the physical configuration of the model, secondly, an adequate representation of topography, which depends on the spatial resolution used in the model set up, and thirdly, a satisfactory representation of the surface terrain properties.

These last properties are mainly characterized within the land surface schemes of the NWP models. These schemes use tabulated specific values of land surface properties such as roughness length, albedo, thermal inertia, moisture or emissivity, which are derived from land-use category maps that usually vary on a seasonal basis. Land surface properties exhibit a considerable spatial variability which affects mesoscale atmospheric circulations. In addition, these surface properties change in time continuously as result of human and natural processes, such as urbanization, deforestation, desertification and natural disasters. The continuous advances in remote sensing allow obtaining updated land-cover information, taking into account anthropogenic and natural changes in the land-use. Aside from the importance of the physical configuration and the terrain and surface representation, it has been reported that the daily updating of the Surface Sea Temperature (SST) during the NWP models integrations leads to an improvement in the accuracy of wind estimates.

In this work we have evaluated the role of surface properties representation in the WRF model as they relate to regional wind resource assessment. In addition, the importance of the daily updating of the SSTs in this regional assessment was also evaluated.

In order to evaluate the sensitivity of WRF wind estimates to the terrain surface properties representation, two different land-cover data sets were assessed. In a first experiment, the GLCC land-cover dataset, the default in the WRF model and with a spatial resolution of 30” (about 1 km at the study region latitudes), was used. In a

second experiment, a modified version of the recently released CORINE 100 m spatial resolution land-cover map, was assessed. In addition, in order to evaluate the role of the SSTs updating, the two former experiments were conducted both with daily varying and prescribed SST values. The study was conducted for the region of Andalusia (Southern Spain) at 3 km spatial resolution. Hourly wind speed and direction estimates were tested against data collected along the year 2009 at four stations, two coastal stations and two inland stations, with measuring elevations ranging from 10 to 60 m.a.g.l. The assessment was based on the Mean Error (ME), the Root Mean Square Error (RMSE) and a wind direction accuracy parameter (ACC). Seasonal and annual analyses were conducted independently.

Before the evaluation of the experiments, two analyses were carried out. In the first one, a comparison between the GLCC and the new CORINE land-cover maps used in the WRF integrations (3-km spatial resolution) was conducted. An overall poor agreement was observed between the two land use maps. A detailed analysis showed the main differences were associated with the urban and built-up land, irrigated cropland and pasture, evergreen need-leaf forest, mixed forest, herbaceous wetland and the barren or sparsely vegetated land surface categories. In the second analysis, an evaluation of the accuracy of the elevation and roughness length representation in the model at the four stations locations was conducted. Reference values for the elevation were taken from 90-m spatial resolution Digital Elevation Model, while for the roughness length, reference values were taken from the original 100-m spatial resolution CORINE land-cover map. Notable differences between the reference and modeled (at 3 km spatial resolution) elevation were observed for two stations: Málaga and Magtel, where elevation was overestimated and underestimated, respectively by the WRF model. Regarding the roughness length, it was found that the CORINE dataset provided, overall, a more accurate representation of roughness length that GLCC one.

The evaluation of the four experiments conducted for the different study periods and stations showed a remarkable influence of land surface dataset and the SSTs updating on ME values. Influence on the RMSE was also meaningful while was low on the ACC. Notably, the CORINE land-use dataset provided lower ME and RMSE values during winter and the GLCC during summer. These results were explained based on the accuracy of roughness length representation provided by both dataset during the

former seasons. At annual basis, a compensating effect among seasons conducted to lower ME values associated with the CORINE dataset for two of the station and with GLCC for the other two stations. The annual analysis showed scarce differences in RMSE values, due to the compensating effect between seasons. Finally, a low sensitivity of the wind direction to land-use was found. The CORINE dataset provided slightly higher ACC values at the coastal stations (Málaga and Rota) and slightly lower values at the Sevilla station. Regarding the SSTs updating, its influence was mainly observed in ME values and at coastal stations. Notably, at the Málaga station, the use of updated SST in combination with CORINE land-cover provided considerable lower ME values. Updated SSTs tends also to provide slightly better wind direction estimates at the two coastal stations, but differences were low.

The analysis of results for Magtel station, with two measuring elevations, provided some additional insights. Notably, it was found that the influence of land use dataset on wind estimates errors decreases with the elevation.

To conclude, it was observed that the CORINE dataset describes more accurately the roughness length than GLCC, and therefore, estimates obtained with CORINE outperform in general those obtained with GLCC. Differences were found mainly in the ME values. Finally, it was found that the use of daily updating SST, improved the ME values in summer and in autumn, especially at coastal stations.

CHAPTER 3

ANALYSIS OF WRF MODEL WIND ESTIMATE SENSITIVITY TO PARAMETERIZATION CHOICE AND TERRAIN REPRESENTATION IN ANDALUSIA (SOUTHERN SPAIN)

Santos-Alamillos F.J., D. Pozo-Vázquez, J.A. Ruiz-Arias, V. Lara-Fanego, and J. Tovar-Pescador J. 2011. *Analysis of WRF model wind estimate sensitivity to parameterization choice and terrain representation in Andalusia (Southern Spain)*. Manuscript submitted to Journal of Applied Meteorology and Climatology. In revision.

3.1 Introduction

Reliable wind resource assessment is a key issue in the evaluation of wind energy potential and in studies related to integration of wind energy electricity production (GE, 2010). Such wind resource assessment can be divided into two steps (Sempreviva et al., 2008) - a regional wind assessment, which evaluates resources of a region as a first approach, and a site-specific assessment, which is a detailed evaluation of specific areas that exhibit high potential in the regional assessment. Currently, regional wind assessment is mostly based on Numerical Weather Prediction (NWP) models (Frank et al., 2001; Landberg et al., 2003; Lavagini et al., 2006; Zagar et al., 2006; Kanamitsu

and Kanamaru, 2007; Jiménez et al., 2008; Hahmann et al., 2010; Shimada and Oshawa, 2011). NWP models facilitate a comprehensive description of the atmospheric system, using initial and boundary conditions from atmospheric reanalysis. Based on downscaling techniques, current NWP models resolve local and regional circulation patterns, taking into account local topographic surface features to a certain extent. Thus, these models can provide accurate meteorological information, such as wind speed and direction, over large regions at high temporal (a few minutes) and spatial (a few kilometers) resolution.

Despite the high resolution of current NWP models (km), there are still two main problems in estimation of surface meteorological variables, especially that of surface wind speed. These problems are representation of topography and terrain morphology in the modeled domains, and numerous physical processes at sub-grid scale.

Topography and terrain morphology have a marked influence on surface meteorological variables, especially on surface wind speed and direction. Surface winds result from interaction between mesoscale circulation and other more local factors, many of which are related to topographic characteristics (elevation, aspect, slope) and terrain morphology (hills, valleys, and others). First, wind speed changes with elevation in the Planetary Boundary Layer (PBL), as a result of reduced friction (Palomino and Martin, 1995). Secondly, terrain features can accelerate windflow. As it passes a summit, an approaching air mass is often squeezed into a thinner layer and therefore speeds up. Aside from elevation, aspect and slope can also modify windflow. Over a ridge, there is maximum acceleration when wind blows perpendicular to the ridge line. Terrain morphology is also important; wind flow accelerates through passes along valleys aligned with the flow (channeling). Similarly, topography may produce local areas of reduced wind speed, such as sheltered valleys and areas in the lee of a mountain ridge. It is also well known that in complex topography areas, spatial variability of solar radiation can be very high (Tovar-Pescador et al., 2006; Ruiz-Arias et al., 2009, 2012a). As a consequence, there may be strong local thermal gradients, causing mountain and valley wind regimes. If the study region is composed by flat and homogeneous land, WRF terrain representation may be accurate enough to provide reliable surface wind estimates. However, this representation may provide unreliable surface wind estimates in complex topography areas, even using high spatial resolutions. This issue is usually addressed

in specific site assessment, using microscale models such as the Wind Atlas Analysis and Application Program (WAsP; Mortensen et al. (1993)). This type of model provides site-specific wind estimates, based on terrain information and wind measurements from nearby stations, at very high spatial resolution (100 meters). Wind estimates based on WAsP are constrained by the existence of local measurements and by the complexity of the study area. In the last few years, several methods have been proposed for using NWP wind estimates as input to microscale models like WAsP (Frank et al., 2001; Berge et al., 2007).

NWP models represent physical sub-grid processes through use of parameterization schemes. In particular, most models include schemes to account for cloud Microphysics (MPH), Cumulus formation (CMS), Planetary Boundary Layer processes (PBL), Surface Layer Physics (SLP), Land Surface Layer (LSL) or Short- and Long-wave Radiation (SWR and LWR, respectively). Stensrud (2007) presented a detailed description of these and other parameterizations. In the last decades, many different parameterization versions have been proposed for each scheme. However, their validity is highly dependent on the study region, season of the year, and spatial and temporal scales of interest. In fact, given a spatial and temporal configuration, the skill of a model mainly depends on these physical parameterizations (Lynn et al., 2004; Fernández et al., 2007). As a consequence, a prior performance evaluation of different parameterization versions of the various schemes, for the given study area and application, is advisable.

The Weather Research and Forecasting (WRF) (Skamarock et al., 2008) is one of the most widely used NWP models, and is a reference in regional wind resource assessment. Over recent decades, many different parameterizations have been proposed for this model, especially for the PBL. PBL parameterizations are responsible for vertical sub-grid scale fluxes owing to eddy transports through the entire atmospheric column. Wind distribution is affected by factors such as PBL height, wind shear, and entrainment of free atmospheric air into the PBL, which determines momentum, heat and moisture exchanges at the top of the layer (Arya, 2001). These processes may vary considerably depending on, for instance, the study region or spatial and temporal scales. As a consequence, many authors have reported great sensitivity of WRF (and other NWP) surface wind estimates to PBL parameterization, in many areas of the world: central USA (Zhang and Zheng, 2004), South Korea (Kim et al., 2005; Kwun et al., 2009),

Spain (Pérez-Landa et al., 2007; Borge et al., 2008), Sweden (Miao et al., 2008), and southern California (Watson and Bauman, 2009).

Regarding other NWP parameterizations, the influence of selected schemes on surface wind speed estimates, though less important, could be significant. For instance, MPH schemes include explicitly resolved water vapor, cloud, and precipitation processes. According to Rajeevan et al. (2010), cloud microphysical processes are important because of their direct influence on cold pool strength (from rainfall evaporation) and latent heating (from condensation). Therefore, MPH processes can affect wind fields close to the surface. SWR parameterizations include visible and surrounding wavelengths that make up the solar spectrum, whereas LWR parameterizations include infrared or thermal radiation absorbed and emitted by gases and surfaces. Both these parameterizations may be important to surface wind, since solar radiation is the primary driver of PBL dynamics. Moreover, in complex topography, differences in surface radiation generate important thermal contrasts that in turn create local wind regimes. Finally, CMS schemes represent sub-grid scale effects of convective and/or shallow clouds. These schemes are mainly intended to account for vertical fluxes from unresolved updrafts and downdrafts, and compensating motions outside clouds. CMS parameterization schemes are largely evaluated for precipitation estimates (Kotroni and Lagouvardos, 2001), and literature focusing on wind estimates is scarce (Cohen, 2002). However, clouds have considerable effects on PBL processes, since they affect hydrologic processes through the heats of condensation and evaporation, and via redistributions of sensible and latent heats and momentum (Arakawa, 2004). Therefore, different CMS parameterization schemes may produce varying surface wind estimates.

Finally, some authors (Jiménez and Dudhia, 2012) have reported a positive bias in WRF wind speed estimates over plains and valleys (about 1 ms^{-1} at 10 m.a.g.l) and a negative bias over hills and mountains (about -3 ms^{-1} at 10 m.a.g.l). The main reason for the positive bias seems to be unresolved topographic features, such as hills or mountains in complex terrain. These can produce additional drag over that generated by vegetation (Beljaars et al., 2004; Jiménez and Dudhia, 2012), which is not parameterized in the WRF. The main reason for the negative bias is also these unresolved features. The magnitude of these biases is related to differences between station elevation and those in the model configuration.

This work evaluates the relative roles of terrain representation and choice of parameterization schemes in the WRF, as they relate to regional wind resource assessment. To evaluate the sensitivity of WRF wind estimates to the choice of parameterization schemes, we first evaluated 32 physical configurations resulting from combination of two different PBL, MPH, CMS, SWR and LWR parameterization schemes. For each scheme, we evaluated one widely used parameterization and a new one available in the recent WRF release (version 3.2). Therefore, a byproduct of this work is a comparative evaluation of the new schemes against the old ones. In a second step, to evaluate sensitivity of the wind estimates to the terrain representation and morphology in the WRF, we also evaluated wind speed and direction estimates obtained based on different experiments, at 1, 3 and 9 km spatial resolution. The work applies to the region of Andalusia (Southern Spain). Although relatively small, this region is characterized by varied topographic, geographic and weather conditions that make the evaluation especially challenging. Estimates are tested against data from four stations that provide hourly wind speed and direction data at 40 m.a.g.l. Station locations are representative of different topographic and climatic conditions, thus allowing a comprehensive evaluation of the WRF wind estimates. To sum up, the main objectives of this work are: First, to obtain a general model setup to be used for a long integration, toward evaluating wind resources in the study region; second, to evaluate the extent to which this single setup can provide accurate wind estimates, in a region characterized by strongly variable climate conditions; third, to assess the extent to which an increase in WRF spatial resolution gives better estimates, in a region characterized by the existence of areas with complex topography.

The chapter is organized as follows: Section 3.2 describes the study region, terrain characteristics and data. Section 3.3 details the methods and Section 3.4 the results. Finally, main conclusions are presented in Section 3.5.

3.2 Study region and data

The study region (Fig. 3.1) of Andalusia is in the southern Iberian Peninsula (IP). It extends over 87,000 km^2. The region (latitude 35°30' to 38°30' N and longitude 7°30'

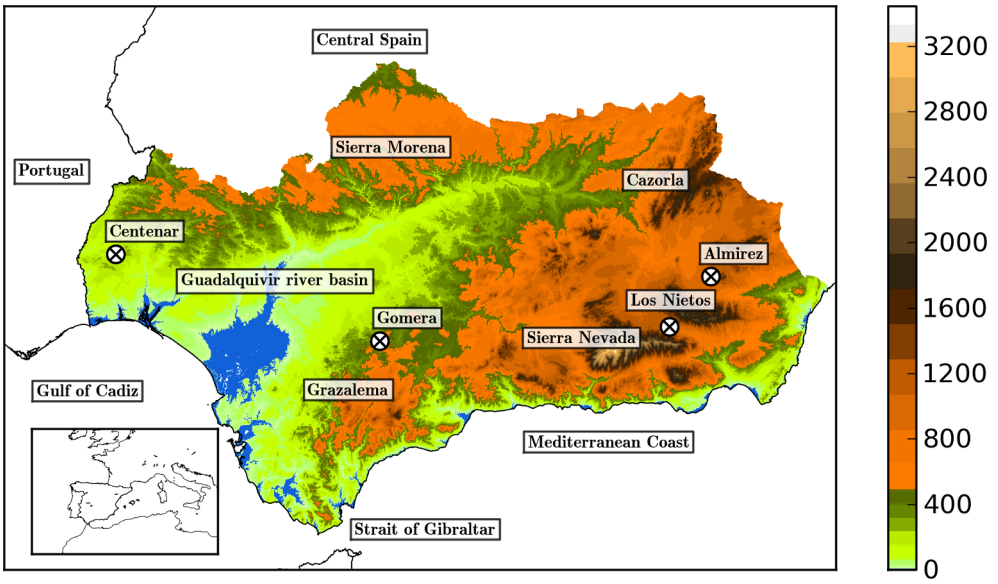


Figure 3.1. Location (small figure, bottom left) and principal topographic and geographic characteristics of study region. Locations of four validation stations are highlighted with crosses. Colors indicate elevation above sea level based on 90-m resolution Digital Elevation Model (DEM). Scale at right indicates elevation in meters above sea level.

to 1°30 W) is in a transition zone between temperate and subtropical climates. From a topographic point of view, the region may be split into two different parts. The western part, covering around 40,000 km^2, is a nearly homogeneous flat area, around 100 m above sea level (m.a.s.l.). The eastern part has very complex topography with several mountain areas, reaching 3482 m.a.s.l in Sierra Nevada National Park (the highest elevation on the IP).

The atmospheric circulation over most of the IP is dominated by a semi-permanent, subtropical high-pressure center over the Azores Islands, particularly so in the south over the study region. The position and intensity of this center changes through the year. During winter, the high is at lower latitudes, allowing the region to be affected by zonal circulations from the west. During summer, the high migrates northward, blocking the westerly circulations over most of the IP and particularly the study region (Pozo-Vázquez et al., 2001; Trigo et al., 2002; Castro-Díez et al., 2002). Although the entire region is under the influence of the Azores subtropical high, it has a wide

range of climate conditions. This range is related to topographic features. The eastern part is less influenced by the Azores high, and more affected by the Mediterranean Sea (Esteban-Parra et al., 1998; Rodríguez-Puebla et al., 1998; Ramos-Calzado et al., 2008). The western part is the lower Guadalquivir River basin. It is open to the Atlantic Ocean and to direct influence by atmospheric flow controlled by the Azores high. The Guadalquivir valley is exposed to mild and moist air from the Atlantic year round. Winds are channeled through this valley, generating strong mean surface wind speeds in the upper valley (Alsamamra et al., 2011). The eastern part is partially isolated from this Atlantic influence by the Sierra Nevada and Cazorla mountain ranges (Fig. 3.1). Consequently, annual precipitation over the region ranges from 300 $mmyear^{-1}$ in coastal, semi-desert southeast areas, to more than 2500 $mmyear^{-1}$ in mountains near the Strait of Gibraltar (Ramos-Calzado et al., 2008). In addition, the study region is bounded on the south by the Atlantic (western part) and the Mediterranean (eastern part), representing about 900 km of coastline. Finally, one of the most important wind features is strong, semi-permanent winds near the Strait of Gibraltar coast.

Validation of WRF estimates was carried out based on data from four meteorological masts (Fig. 3.1). These data were furnished by the wind division of Gamesa Corporation, and include hourly wind speed and direction data measured at 40 m.a.g.l for 16 days in the year 2005. The 16 days at each station were selected as representative of different periods in the year - data from 2-5 February were used to represent winter, 9-12 April spring, 28-31 August summer, and 7-10 October autumn. We also conducted a quality control procedure based on Jiménez et al. (2010), and no suspicious data were found. We used wind data collected at 40 m.a.g.l for the evaluation, rather than the much more common 10 m.a.g.l wind data at most meteorological stations. This gives the results greater representativeness for regional wind resource assessment. This is mainly because wind speeds measured at the lower elevation are frequently influenced by local features near the meteorological stations (buildings, vegetation, and others), which are definitely not captured in a NWP model.

The areas containing the four masts have very different terrain complexity and morphology. Since these factors have a marked influence on surface wind speed and direction, a characterization was attempted. This characterization is important to the discussion of the evaluation result in Section . Many different parameters for

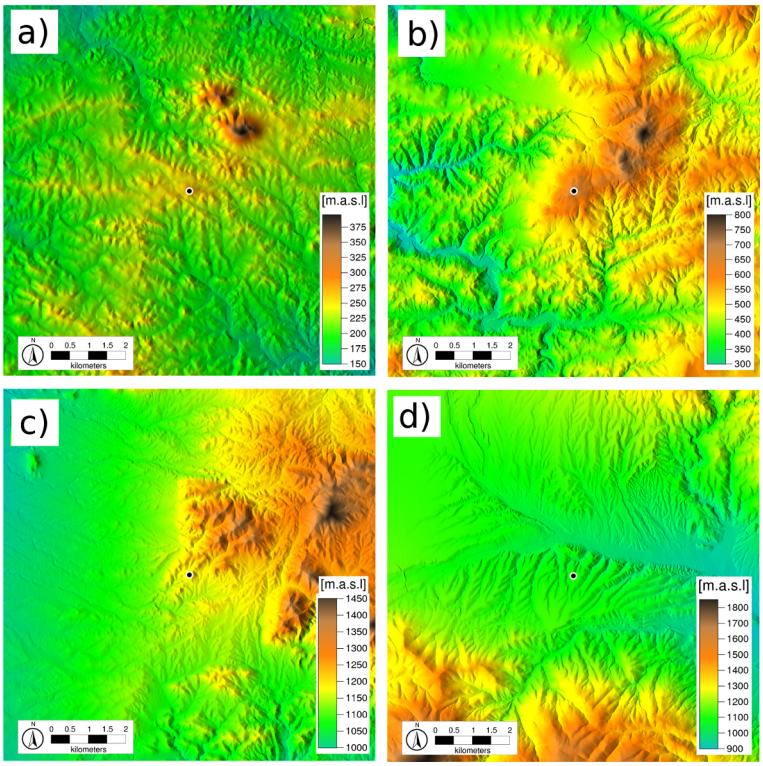


Figure 3.2. Topographic maps for Centenar (a), Gomera (b), Almirez (c) and Los Nietos (d) stations. Each map is 10 km × 10 km, centered at station location, and obtained based on a 10-m resolution DEM. Scale at right indicates elevation in meters above sea level.

characterizing terrain complexity have been defined in the literature (Huaxing, 2008), but most rely on Digital Elevation Models (DEM). In this work, we consider two type of parameters: the standard deviation of elevation (denoted as σ) and the relief (denoted as rlf), which is the difference between the highest and lowest altitude. We derived both parameters from a 90-meter spatial resolution DEM, computed on a 3 km × 3 km grid box centered at each mast location. Given the three WRF spatial resolutions considered (1, 3 and 9 km), σ and rlf represent sub-grid scale topographic complexity at the station locations. Table 3.1 shows these parameters for the four stations, along with station elevations derived from the DEM and WRF. The terrain topography and morphology surrounding the stations are represented in Figs. 3.2 and 3.3. Fig. 3.2 shows a detailed elevation map around the station locations, obtained from a 10-meter spatial resolution DEM. Fig. 3.3 also shows elevations maps around the stations, derived from a

Station	DEM (m)	WRF 9 km (m)	WRF 3 km (m)	WRF 1 km (m)	σ (m)	rlf (m)
Centenar	236	230	253	253	17	152
Gomera	540	486	498	530	67	310
Almirez	1195	1145	1187	1197	58	270
Los Nietos	1056	1117	1041	1048	38	158

Table 3.1. Main topographic characteristics at station locations. Displayed are elevations at station locations, from a 90-m spatial resolution Digital Elevation Map (DEM) and from WRF model using three different spatial resolutions (9, 3 and 1 km). Standard deviation of elevation (denoted as σ) and the relief (denoted as rlf) parameters are also shown for each station. Both parameters were derived from DEM and computed over an area of 3 km × 3 km centered at each station location. All values in meters.

90-meter DEM and WRF domains using the three spatial resolutions (1, 3 and 9 km). For better understanding of the terrain morphology, wind direction distributions observed at the four stations are also shown in Fig. 3.3.

Centenar station (Fig. 3.1) is in the western part of the study region, relatively close to the Atlantic Ocean. Thus, the climatology at this site is strongly influenced by mild and humid Atlantic winds throughout the year. The station is atop a hill (Fig. 3.2a), and the surrounding area has relatively low topographic complexity. In fact, this area has the smallest values of σ and rlf (17 and 152 m, respectively), and therefore the least topographic complexity among the analyzed stations (Table 3.1). Elevation in the WRF integrations ranges from 230 m (WRF 9 km) to 253 m.a.g.l (WRF 1 km), whereas the elevation in the DEM is 236 m.a.g.l. This WRF overestimation of station elevation appears associated with spatial averaging, since there are hills near the station (Figs. 3.2a and 3.3a). In this case, the coarser spatial resolution better represented the terrain elevation. Nevertheless, as observed in Fig. 3.3d, terrain morphology is more realistic at 1 km spatial resolution than at coarser resolutions (Figs. 3.3b and 3.3c). Wind direction variability at Centenar is substantially higher than the other stations (Fig. 3.3e).

Gomera station is in the middle of the study region, on the southern boundary of the Guadalquivir valley (Fig. 3.1). The station is also atop a hill (Fig. 3.2b), at an elevation of 540 m.a.g.l. The area around the station has the greatest topographic complexity among

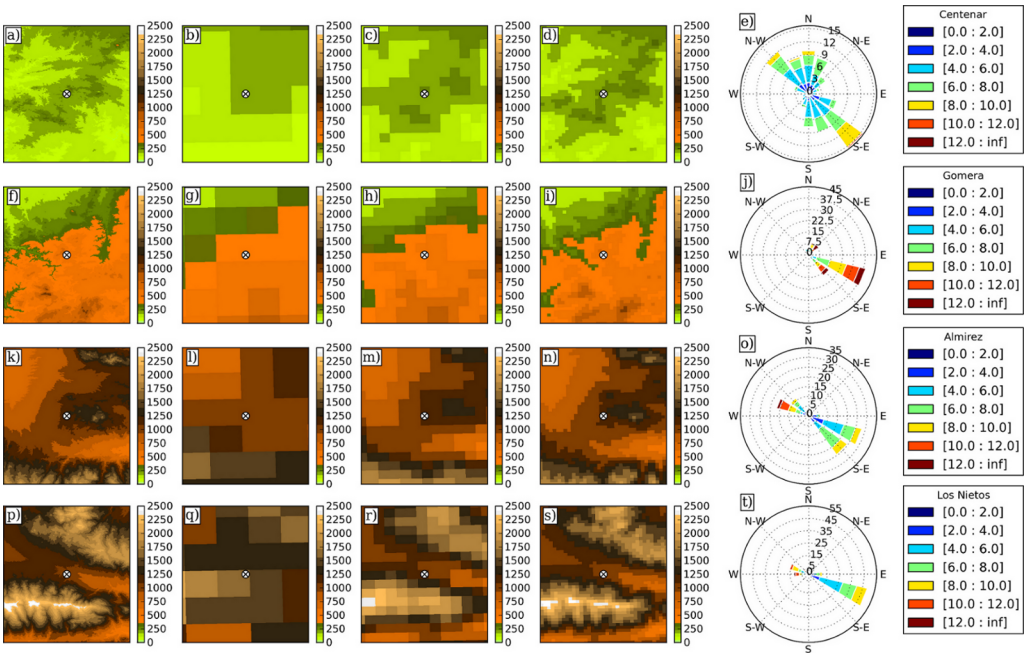


Figure 3.3. Terrain morphology and observed wind direction distribution for the four validation stations. a) Elevation map of a 50 x 50 km area centered on Centenar station, derived from 90-m DEM. b) - d) Elevation maps used, respectively, in the 9 km, 3 km and 1 km spatial resolution WRF setups for Centenar station. Areas of 50 × 50 km centered on the station are displayed, and scales at right indicate elevation in meters above sea level. e) Wind direction distribution observed at Centenar station at 40 m.a.g.l. Values in circles indicate percentage of observations; color scale at right indicates ranges of wind speed in ms^{-1}. f) - j) are as in a) - e), but for Gomera station. k) - o) are as in a)-e), but for Almirez station. p) - t) are as in a) - e), but for Los Nietos station.

the analyzed stations, as derived from values of σ m) and rlf (310 m) (Table 3.1). As a consequence and as expected, differences in the station elevation from the various WRF configurations are considerable - from 486 m (WRF 9 km) to 530 m.a.g.l (WRF 1 km). In this case, elevation and, notably, terrain morphology are much better represented by the 1 km WRF integration (Fig. 3.3i). The hilltop location and morphology of the surrounding terrain clearly determines the wind direction distribution (Fig. 3.3j), through enhancing the southeast direction.

Almirez station is in the far east of the region (Fig. 3.1), on the middle of a plateau of

considerable elevation (above 1000 m.a.g.l), facilitating continental climate conditions. Station elevation is 1195 m.a.g.l, in the foothills of a mountain range and near a valley (Fig. 3.2c). It has the second greatest topographic complexity after Gomera (Table 3.1). As the previous case, differences in station elevation from the different WRF configurations are considerable - from 1145 m (WRF 9 km) to 1197 m.a.g.l (WRF 1 km). Morphology of the surrounding topography clearly dominates the wind direction distribution (Fig. 3.2o), enhancing the southeast and northwest directions. Note that strongest winds are mainly from the northwest. Unlike the previous cases, station elevation (Table 3.1) and surrounding terrain morphology seem reasonably represented, in both the 3 km and 1 km WRF integrations (Figs. 3.3k, 3.3m and 3.3n). This will be confirmed when analyzing the results in Section .

Finally, Los Nietos station is also in the east, at high elevation (1056 m.a.g.l) (Fig. 3.1), with climate conditions very similar to Almirez. The main feature of this station is its location in the middle of a valley, with relatively low topographic complexity (Fig. 3.2d). As a consequence, this station has the lowest σ and rlf values, after Centenar (Table 3.1). Thus, as expected, terrain morphology (Figs. 3.3p, 3.3r and 3.3s) and station elevation (Table 3.1) are reasonably reproduced in both the 3 km and 1 km WRF configurations. Wind direction at this station is clearly controlled by the valley effect, and its distribution is the narrowest of the four analyzed (Fig. 3.3t).

To sum up, the four station locations have very different climate conditions, topographic complexity and terrain morphology. Los Nietos and Almirez stations are at elevations above 1000 m.a.g.l in the mountainous eastern part of the study region, and therefore have cold continental climates. In contrast, the Centenar station is at relatively low elevation in the eastern Guadalquivir River basin, an area characterized by a mild oceanic climate. For topography, the Gomera area has the highest topographic complexity, followed by Almirez. On the other hand, Los Nietos and, especially, Centenar are in areas of relatively low topographic complexity. Finally, the effect of terrain morphology near each station is important for wind direction distribution, particularly for Gomera, Almirez and Los Nietos.

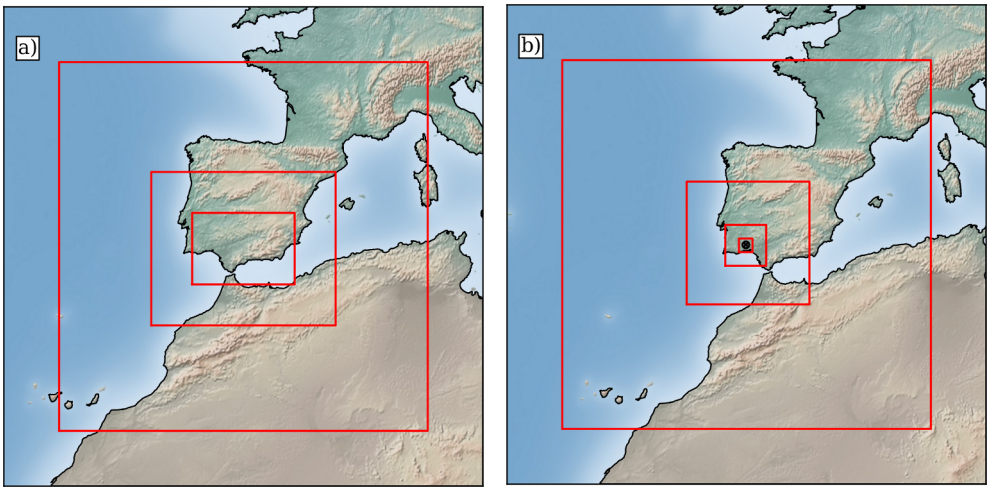


Figure 3.4. Spatial configuration of domains used for numerical simulations. a) Three nested domains at 27, 9 and 3 km spatial resolution for Andalusia (Southern Spain) used in first analysis. b) Four domains centered on Centenar station, at 27, 9, 3 and 1 km spatial resolutions used in second analysis. Similar spatial configurations, but centered on corresponding station locations, were used for remaining stations.

3.3 Methods

WRF model v3.2 was evaluated here. Simulations were conducted for the days mentioned in Section 3.2, at temporal resolution one hour. Two different spatial configurations were used, depending on the study.

The first study was on the influence of parameterization scheme choice on the wind speed and direction estimates. In this endeavor, the model configuration included three nested domains, with 27, 9 and 3 km spatial resolutions (Fig. 3.4a). Ultimately, data were analyzed for the third nested domain (3 km), centered on the study region. A two-way interaction was used in the three domains, with 36 vertical levels, 8 of which were within the first 1000 m above ground. The first five lowest vertical levels, at approximately 4, 18, 43, 64 and 76 m.a.g.l, were used in a vertical interpolation to estimate wind speed and direction at the measurement elevations. Topography, land use, and land-water mask datasets were interpolated from the USGS land cover dataset, with appropriate spatial resolution for each domain (5', 1' and 30", respectively). The second study was on

the effect of topography representation on the wind speed and direction estimates. In this effort, the model configuration included four nested domains, with 27, 9, 3 and 1 km spatial resolutions. An example of this spatial configuration is shown in Fig. 3.4b (Centenar station case). For the first three domains, a two-way interaction was used, but this option was turned off for the 1 km resolution domain. We used the same vertical configuration as in the previous study. Topography, land use, and land-water mask datasets were interpolated from the USGS land cover, with appropriate spatial resolution for each domain (5', 2', 30" and 30", respectively).

Parameterization	Routine Schemes	New schemes in WRF v3.2
PBL	YSU (P1) (Hong et al., 2006)	MYNN (P2) (Janjic, 2002)
MPH	Morrison-2M (M1) (Morrison and Gettelman, 2008)	Thompson (M2)
CMS	Kain-Fritsch (C1) (Kain and Fritsch , 1993)	Grell 3D (C2)
SWR	Goddard (S1) (Chou and Suarez., 1994)	RRTMG (S2)
LWR	RRTM (L1) (Mlawer et al., 1997)	RRTMG (l2)

Table 3.2. Schemes used to configure the 32 experiments, for Planetary Boundary Layer (PBL), Microphysics (MPH), Cumulus (CMS) or Long-wave and Short-wave Radiation (SWR and LWR, respectively) parameterizations. Column at left shows widely used schemes, implemented in older versions of WRF model; column at right shows newly implemented schemes in WRF version 3.2.

In the first study, a total of 32 physical configurations (Table 3.2) were evaluated. This evaluation was conducted with a 3 km spatial resolution. These configurations were composed as a combination of two different schemes for the PBL, MPH, CMS, MPH, SWR and LWR parameterizations - one widely-used and referenced scheme (first column in Table 3.2) and a new one, available in a recent WRF model release (version 3.2) (second column in Table 3.2). Selection of the old schemes for the various physical configurations was based on previous evaluations of WRF performance in the study region (Fernández et al., 2007; Borge et al., 2008; Ruiz-Arias et al., 2008). Table 3.3 shows the parameterization in each experiment. As explained in Section , results of the first study show that the wind estimates were sensitive mainly to the choice of PBL parameterization. As a consequence, for the sake of conciseness in the second study, only variations of PBL parameterization were considered, keeping the rest fixed. This considerably reduces the complexity of the analysis. Notably, in the second study, we evaluated the WRF wind estimates at three different spatial resolutions (1, 3 and 9 km), and used two alternative PBL parameterizations. Initial and boundary conditions for the simulation were generated using the ERA-Interim reanalysis (Uppala et al., 2008) with

0.7° spatial resolution and 6-hour time interval. Newtonian relaxation or nudging was used in model integration, using parameter values proposed by Seaman (2000) and Otte (2008b). This technique relaxes the model toward the observed state by adding artificial forcing terms to the model predictive equations, based on the difference between the states weighted by nudge coefficients. Several works demonstrate the improvements of nudging in simulating the wind field (Barna and Lamb, 2000). The simulations were conducted with a spin-up of 24 hours and outputs were saved every hour. Finally, modeled time series were extracted from the WRF grid, selecting the cell nearest the geographic coordinates of each station.

Nomenclature	Physical configuration	Nomenclature	Physical configuration
E1	P1-M1-C1-R1-L1	E17	P2-M1-C1-R1-L1
E2	P1-M1-C1-R1-L2	E18	P2-M1-C1-R1-L2
E3	P1-M1-C1-R2-L1	E19	P2-M1-C1-R2-L1
E4	P1-M1-C1-R2-L2	E20	P2-M1-C1-R2-L2
E5	P1-M1-C2-R1-L1	E21	P2-M1-C2-R1-L1
E6	P1-M1-C2-R1-L2	E22	P2-M1-C2-R1-L2
E7	P1-M1-C2-R2-L1	E23	P2-M1-C2-R2-L1
E8	P1-M1-C2-R2-L2	E24	P2-M1-C2-R2-L2
E9	P1-M2-C1-R1-L1	E25	P2-M2-C1-R1-L1
E10	P1-M2-C1-R1-L2	E26	P2-M2-C1-R1-L2
E11	P1-M2-C1-R2-L1	E27	P2-M2-C1-R2-L1
E12	P1-M2-C1-R2-L2	E28	P2-M2-C1-R2-L2
E13	P1-M2-C2-R1-L1	E29	P2-M2-C2-R1-L1
E14	P1-M2-C2-R1-L2	E30	P2-M2-C2-R1-L2
E15	**P1-M2-C2-R2-L1**	**E31**	**P2-M2-C2-R2-L1**
E16	P1-M2-C2-R2-L2	E32	P2-M2-C2-R2-L2

Table 3.3. Nomenclature of 32 physical configurations evaluated. Experiments E15 and E31, highlighted in bold, were used in analysis of terrain representation influence.

Validation of the different model configurations was done based on various statistics for both wind speed and direction. First, we used the Root Mean Square Error (RMSE), which estimates the amount of scatter of the wind speed values:

$$RMSE = \sqrt{\frac{1}{N}\sum(m_i - o_i)^2} \;\; or\ relative \;\; \frac{N\sum(m_i - o_i)^2}{\sum o_i} \cdot 100 \tag{3.1}$$

where N is the number of records, and m and o are modeled and observed wind speed values, respectively. Second, we used the Mean Error (ME), which quantifies overall bias of the wind speed values and detects model overestimation or underestimation:

$$ME = \frac{\sum(m_i - o_i)}{N} \quad or\ relative \quad \frac{\sum(m_i - o_i)}{\sum o_i} \cdot 100 \tag{3.2}$$

Traditionally, direction data have been evaluated using graphical methods. Simple methods, such as wind rose plots, have been used to understand directional characteristics. However, these methods have limitations regarding meaningful statistical evaluation. Jammalamadaka and Sengupta (2001) defined the circular distance between any two points as the smaller of the two arc lengths between the points along the circumference. For angles α and β, the circular distance is defined as:

$$\Delta(\alpha, \beta) = min(\|\alpha - \beta\|, 360^\circ - (\|\alpha - \beta\|)) \tag{3.3}$$

Here we propose the use of an accuracy parameter (denoted as ACC) based on this circular distance, for evaluation of the WRF wind direction estimates. This parameter accounts for the percentage of times in which the circular distance between the observed and modeled wind direction is lower than a threshold, chosen as 30° here. Therefore, this parameter is defined as:

$$ACC(\alpha, \beta) = \frac{\sum_i 1(\text{ if } \Delta \leq 30^\circ)}{N} \tag{3.4}$$

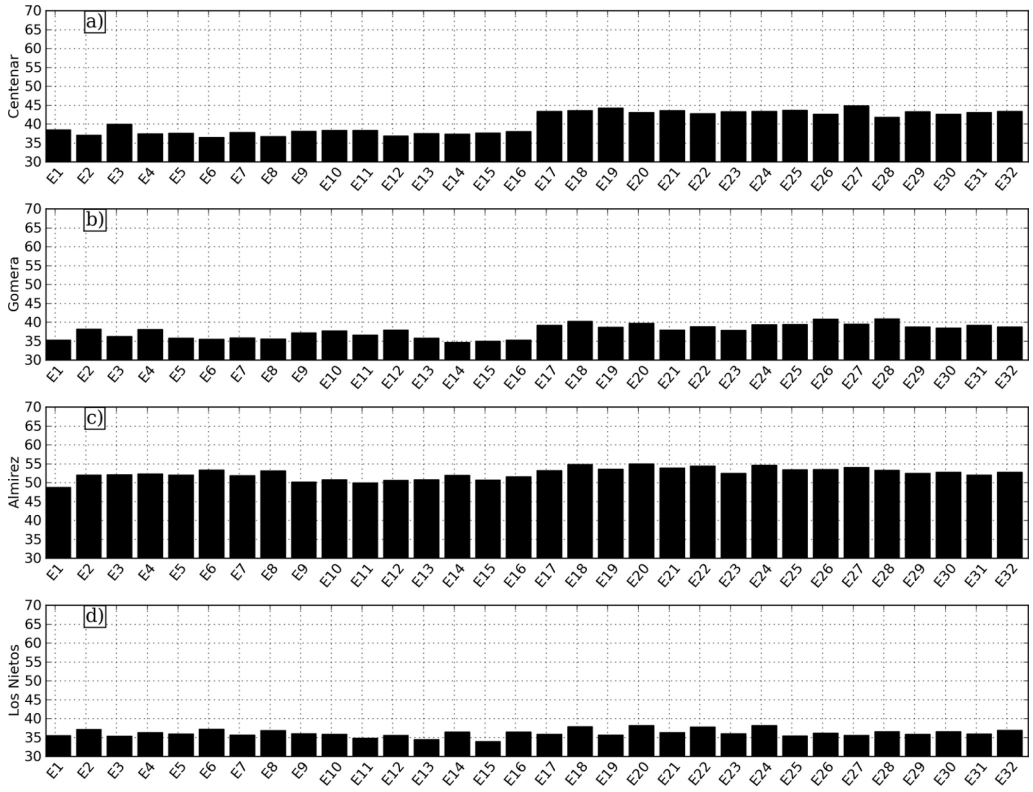


Figure 3.5. Relative Root Mean Square Error (RMSE) values for 32 different experiments at Centenar (a), Gomera (b), Almirez (c) and Los Nietos stations (d). Configuration of each experiment can be determined from Tables 3.2 and 3.3. Values are in %.

3.4 Results and discussion

3.4.1 Analysis of sensitivity to parameterization choice

Figs. 3.5 to 3.7 show, respectively, relative RMSE, relative ME and *ACC* values obtained for the 32 experiments at each station. Fig. 3.8 shows sensitivity of RMSE, ME and *ACC* values to the parameterization choice, for each station. To this end, the figure shows mean values of these parameters resulting from the 16 experiments in which each parameterization scheme is involved.

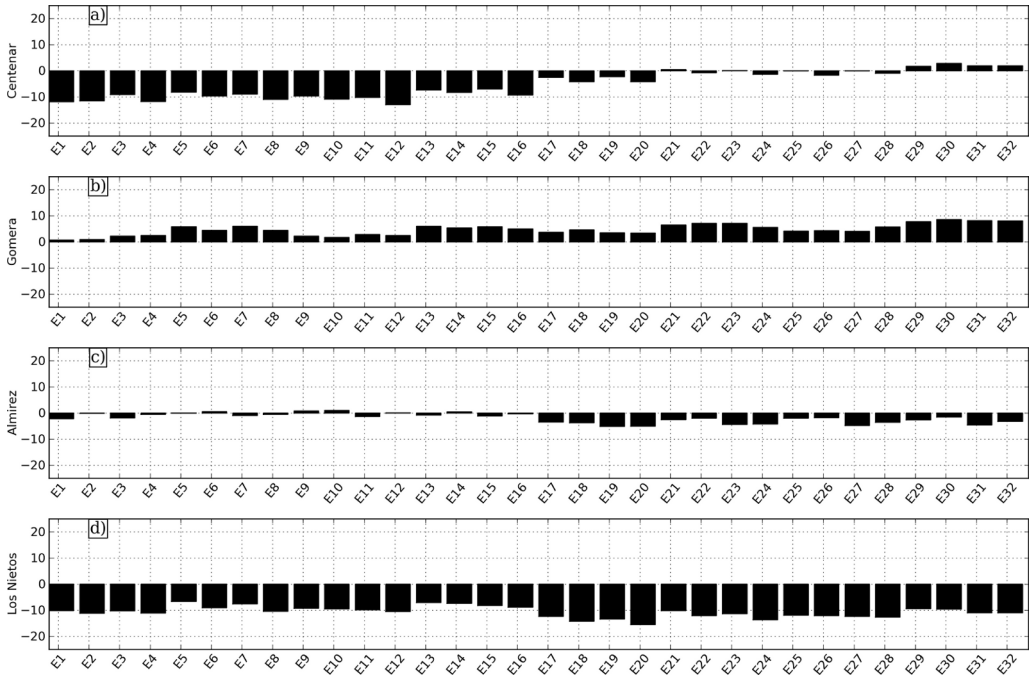


Figure 3.6. As in Fig. 3.5, but for Mean Error (ME).

The RMSE values (Fig. 3.5) show considerable differences among stations, being higher for Almirez and Centenar stations. Almirez has the highest values, between 45% and 55% for all experiments. In contrast, Los Nietos has the lowest values, between 35% and 40% for most experiments. Dependence of RMSE on physical configuration varies considerably among stations. Centenar is the most sensitive by a large amount, followed by Gomera. Recall that these are the lowest elevation stations, in the western part of the study area. A clear dependence of results on the PBL scheme is observed for these two stations. In particular, experiments E1 to E16, which used the P1 PBL scheme, produced considerably lower RMSE than experiments E17 to E32, which used the P2 PBL scheme. This is confirmed in Fig. 3.8. In particular, Fig. 3.8a shows that use of P1 PBL instead of P2 for Centenar reduces RMSE by 8% on average (38% versus 46%). The remaining stations show smaller differences associated with the PBL, less than 3% (Figs.3.8b to 3.8d). Sensitivity of RMSE to the other parameterizations is much less relevant for all stations. Therefore, aside from the PBL, there is no clear and systematic effect of parameterization selection on RMSE at any of the four stations. Nevertheless,

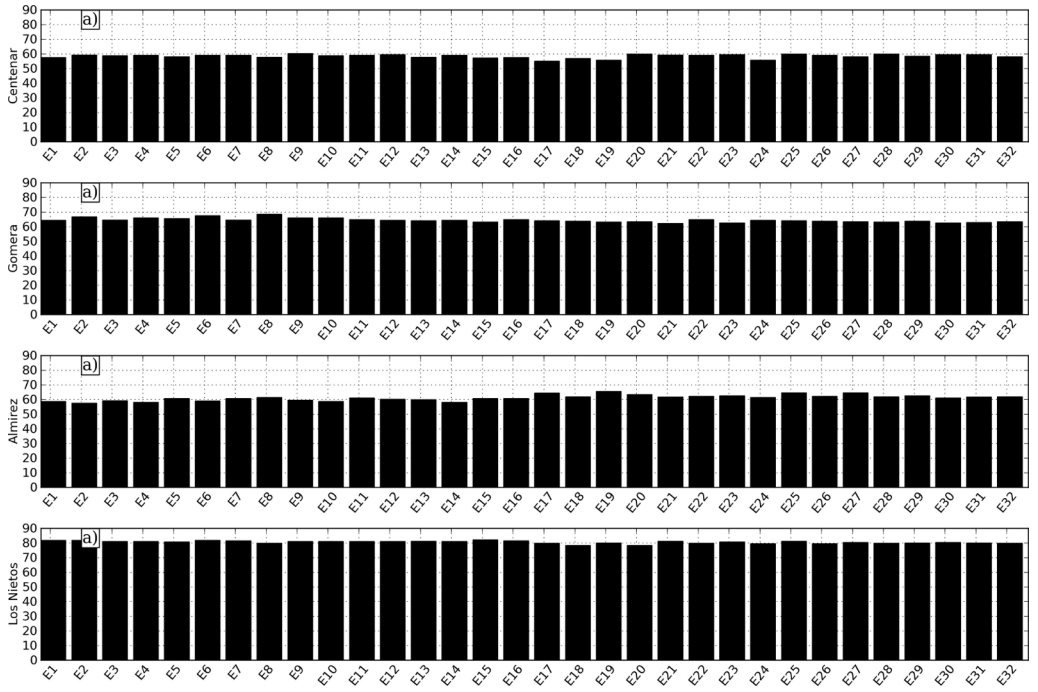


Figure 3.7. As in Fig. 3.4, but for wind direction *ACC* parameter.

there are certain combinations of schemes that perform better than others. Unfortunately, these combinations vary among stations. For instance, for Centenar, RMSE varies from about 37% (E6, best experiment) to 50% (E27, worst experiment). The best experiment for Gomera is E1 (36%), and the worst E27 (40%). The best experiments for Almirez and Los Nietos were E1 (48%) and E15 (33%), respectively.

Similar to RMSE, ME values (Fig. 3.6) show a notable dependence on the station and physical configuration, ranging from -15% to 10%. In addition, there are some pronounced features, shown in Fig. 3.6. On one hand, there is clear tendency to underestimate wind speed at Almirez and Los Nietos (Figs. 3.6c and 3.6d). The P1 parameterization performs considerably better than P2 at these stations. On the other hand, at Centenar and Gomera (Figs. 3.6a and 3.6b), ME values associated with the different experiments strongly vary. At Centenar, experiments E1 through E16 (using the P1 PBL scheme) show a negative bias, whereas experiments E17 through E32 (using the P2 scheme) produce slightly positive or near-zero MEs. Gomera has significantly

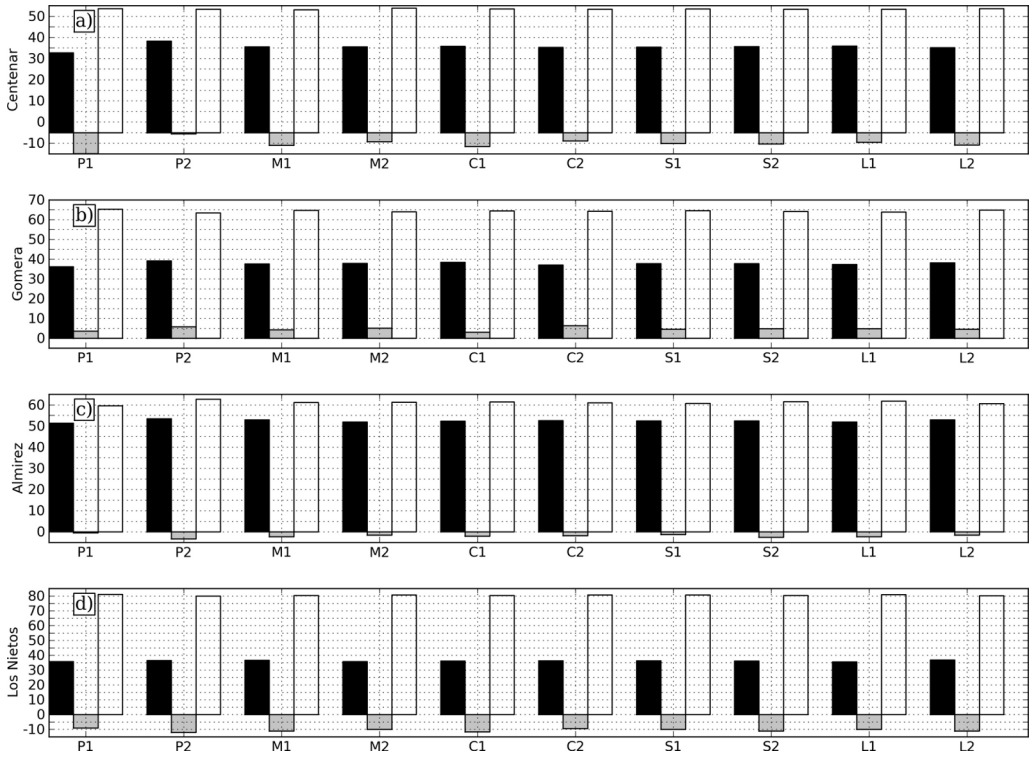


Figure 3.8. Results of sensitivity analysis of RMSE (first column), ME (second column) and wind direction *ACC* parameters (third column) to choice of parameterization. Mean values at four stations of these parameters, resulting from 16 experiments in which each parameterization scheme is involved, are displayed. Values are in %.

lower MEs associated with the P1 scheme. This high sensitivity of ME to the PBL parameterization is confirmed by Fig. 3.8. In particular, use of P1 for Centenar leads to a -10% ME on average, whereas P2 leads to a value near zero. In contrast, P1 performs better than P2 for the remaining stations, although differences are smaller than for Centenar. As with RMSE, the other schemes have little influence on ME. Again, no single experiments perform best for all stations, but experiment E14 performs reasonably at Almirez and Los Nietos (high elevations).

Regarding *ACC* (Fig. 3.7), Gomera (between 60% and 70%) and, especially, Los Nietos (above 80%) had the highest values. As highlighted earlier, these stations have wind directions strongly conditioned by nearby terrain morphology (Figs. 3.3b and 3.3d).

Therefore, it seems that terrain morphology at these stations is reasonably reproduced by WRF at 3 km spatial resolution; this will be confirmed in the next section. Centenar and Almirez had lower *ACC* values, close to 60%. The *ACC* parameter shows little sensitivity to the choice of parameterization. This is confirmed by Fig. 3.8. Only small differences (below 2%) associated with the PBL are observed. Therefore, wind direction estimation appears more sensitive to the terrain representation in WRF than to the choice of parameterization. This will be further analyzed in the next section.

3.4.2 Analysis of sensitivity to terrain representation

Results of the previous analysis show that the WRF wind estimates in the study region are mainly sensitive to the selection of PBL parameterization. As a consequence, in the analysis of this section, we only consider variations in this parameterization, keeping the rest fixed. This greatly reduces the complexity of this examination of terrain influence. As revealed in the previous section, none of the scheme combinations provided a clearly better representation of both wind speed and direction at the four stations. Nevertheless, among all experiments, E15 seemed to provide the best overall estimates. This experiment produced the lowest, or near the lowest, values of RMSE and ME for all stations (Figs. 3.5 and 3.6). The *ACC* score (Fig. 3.7) showed little variation among experiments. Therefore, we have selected E15 as a basis for the present analysis. Finally, we performed six experiments, involving the two physical configuration ($E15$ and $E31$) and the three spatial resolution (1, 3 and 9 km), to evaluate the effect of terrain representation on the WRF wind estimates. This implies maintaining the parameterization M2, C2, R2 and L1 in both experiments, changing only the PBL scheme. We refer to P1 as the experiment using the $E15$ physical configuration, and P2 as using the $E31$ configuration (Table 3.3).

Figs. 3.9, 3.10 and 3.11 show the RMSE, ME and *ACC* values, respectively, for the two physical configurations and three different spatial resolutions. The RMSEs (Fig. 3.9) show considerable dependence on the PBL, station and spatial resolution. At the four stations and for the three spatial resolutions, the P1 scheme generated lower RMSEs, with greater differences at Centenar (Fig. 3.9a). However, dependence on spatial resolution was much more complex. At Centenar and Gomera with the P1

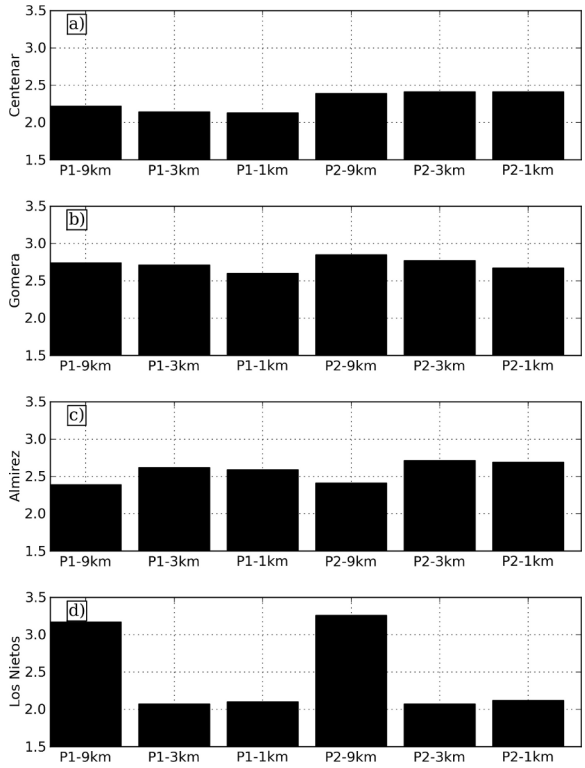


Figure 3.9. Results of sensitivity analysis of RMSE to spatial resolution of WRF setup. a) RMSE values of WRF wind speed estimates at Centenar station, using experiments 15 (P1) and 31 (P2) for three different spatial resolutions (9, 3 and 1 km). b) As in a), but for Gomera station. c) As in a), but for Almirez station. d) As in a), but for Los Nietos station. Values are in ms^{-1}.

scheme, slight improvement (about 0.2 ms^{-1}) of the RMSE was obtained by increasing spatial resolution. At Los Nietos, RMSE was considerably lower (about 2.1 ms^{-1}) at 1 km and 3 km than at 9 km (about 3.2 ms^{-1}) spatial resolution. Further, 3 km spatial resolution provided slightly lower values than 1 km for this station. Finally, Almirez had slightly lower values at 9 km than at the higher resolutions. Therefore, P1 schemes gave lower RSMEs and, in general, these decreased with increasing spatial resolution.

A general tendency to underestimate wind speed at Centenar and Gomera (Fig. 3.10a and 10b), regardless of PBL parameterization and resolution, can be discerned from Fig. 3.10. However, for the other stations, the bias depended mainly on spatial resolution. Unlike with RMSE, PBL parameterization had little influence on ME, with P1 the

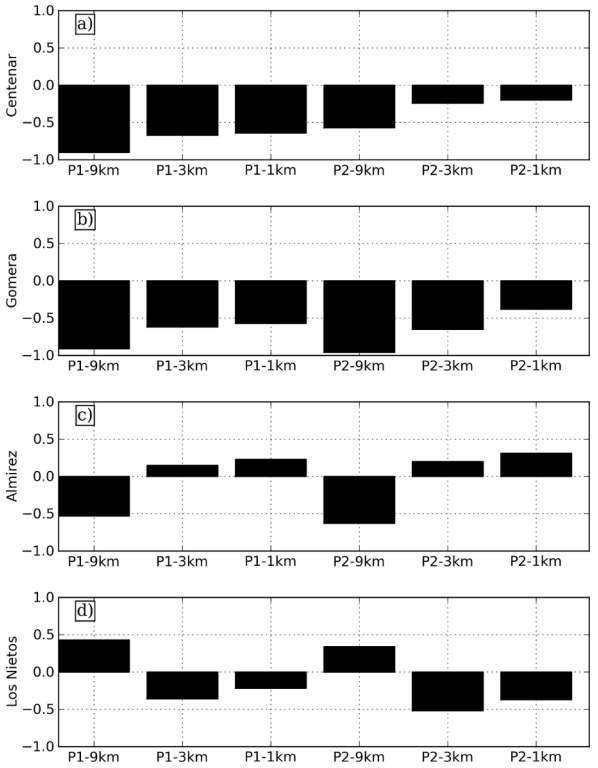


Figure 3.10. As in Fig. 3.9, but for Mean Error (ME). Values are in ms^{-1}.

experiment with superior performance. However, an exception was found for Centenar station, where there was slight improvement with P2 compared to P1. Detailed analysis of the results in Fig. 3.10 reveals an important and complex dependence of the bias on spatial resolution. On one hand, at Los Nietos the bias was positive at 9 km and negative at 3 and 1 km (Fig. 3.10d). As shown in Table 3.1, WRF overestimated station elevation at 9 km (1117 m.a.g.l), while underestimating it at 3 km (1041 m.a.g.l) and 1 km (1048 m.a.g.l) (the DEM shows 1056 m.a.g.l). The signs of the biases at Los Nietos may be caused by this overestimation/underestimation of station elevation. Since this station is in a flat area with low topographic complexity, according to (Jiménez and Dudhia, 2012), a positive bias (about 1 ms^{-1} at 10 m.a.g.l) is expected due to an unresolved drag effect of the terrain. Our results are compatible with existence of a small positive bias, substantially lower than 1 ms^{-1}. This is mainly because the measure elevation considered in the present evaluation is 40 m.a.g.l., at which the drag effect should be much lower than at 10 m.a.g.l.

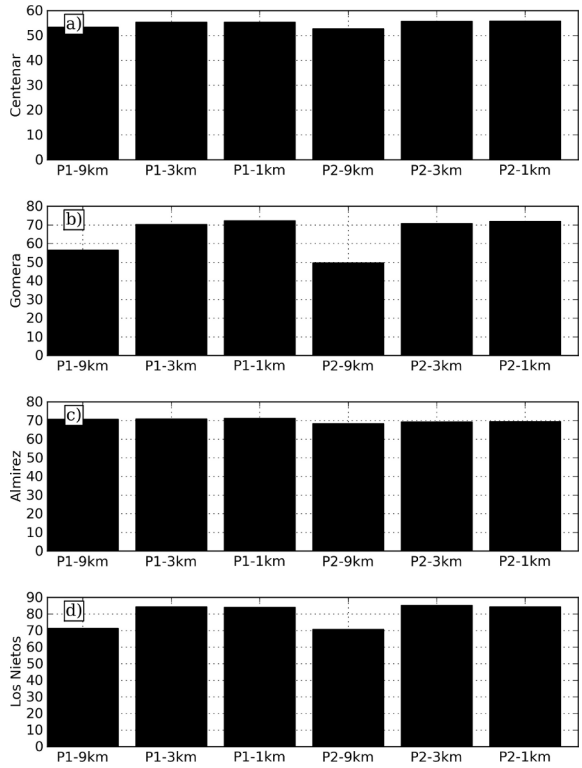


Figure 3.11. As in Fig. 3.9, but for wind direction *ACC* parameter. Values are in %.

Results for Gomera (Fig. 3.10b) clearly show the effect of elevation misrepresentation of mountains and hills on the wind estimates. This is a hilltop station, and WRF estimates of station elevation (Table 3.1) ranged from 486 m.a.g.l (9 km resolution) to 530 m.a.g.l (1 km resolution) (the DEM gave 540 m.a.g.l). As a consequence, the station had a negative bias in both P1 and P2 experiments, which decreased in magnitude with increasing spatial resolution. At Almirez (Fig. 3.10c) in the foothill area, the elevation misrepresentation effect was also evident. At 9 km resolution, station elevation from the WRF was 1145 m.a.g.l, significantly lower than that of the DEM (1195 m.a.g.l). This results in the negative bias in Fig. 3.10c (about 0.6 ms^{-1}). However, using the 3 km and 1 km spatial resolutions, the WRF station elevations are close to the DEM value, and only a slight positive bias (about 0.3 ms^{-1}) is observed. Finally, Centenar had a negative bias in all experiments (Fig. 3.10a), considerably greater at 9 km than at 3 and 1 km. The Centenar area has a low topographic complexity, with the station atop a smooth hill (Fig. 3.2a and 3.3a). Elevations from WRF varied, from 230 m at 9 km to 253 m.a.g.l

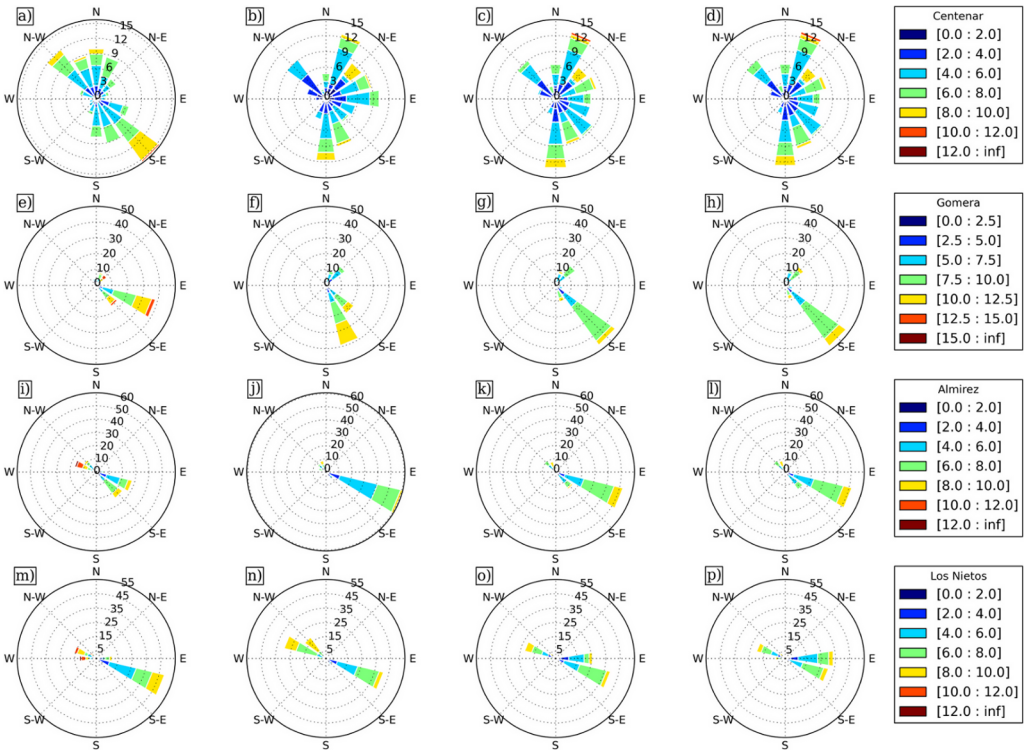


Figure 3.12. Modeled (based on best performing WRF configuration (E15) and using different spatial resolutions) and observed wind direction distributions, at 40 m.a.g.l measurement elevation of four stations. a) Observed, and b) - d) modeled (using 9, 3, and 1 km spatial resolutions, respectively) wind distributions for Centenar station. e) - h) are as a) - d), but for Gomera station. i) - l) are as a) - d), but for Almirez station. m) - p) are as a) - d), but for Los Nietos station. Values in circles indicate percentage of observations; color scale at right indicates ranges of wind speed in ms^{-1}.

at 1 and 3 km; the DEM indicated 236 m.a.g.l. Results in Fig. 3.10a indicate a tendency for WRF to underestimate wind speed at this station. This underestimation is clearly observed at 9 km, for which the station elevation from WRF was close to actual. At 1 km and 3 km, the negative bias was substantially less. This reduction is probably caused by a compensating effect in the wind speed estimates, associated with the overestimation of station elevation (about 20 m) at these spatial resolutions.

Several conclusions can be drawn from Fig. 3.11 regarding *ACC*. To aid interpretation of the results, Fig. 3.12 presents wind direction distributions from WRF, using P1

at the three spatial resolutions. The observed distribution is also shown. First, unlike with RMSE and ME, *ACC* estimates show little dependence on PBL parameterization. Meaningful differences were only observed at Gomera (Fig. 3.11b) for 9 km spatial resolution. In this case, the P2 scheme provided slightly lower *ACC* values. Second, there are notable differences among stations in the accuracy of wind direction estimates, as concluded in the previous section. Highest *ACC* values were observed for Los Nietos, and lowest for Centenar. Finally, the spatial resolution of the WRF setup had a significant influence on *ACC* for only two stations - Gomera (Fig. 3.11b) with very complex terrain, and Los Nietos (Fig 3.11d) with low topographic complexity. As highlighted in Section 3.2, these stations had the least wind direction variability, with this direction highly conditioned by nearby terrain morphology. Gomera is atop a hill (Fig. 3.2b). Terrain morphology surrounding the station seems reasonably reproduced at 3 km and 1 km (Figs. 3.3h and 3.3i), but not at 9 km (Fig. 3.3g). Therefore, the wind direction distribution is realistically reproduced at 3 km and 1 km (Figs. 3.12e, 3.12g and 3.12h). The location of Los Nietos station, in the middle of a valley (Fig. 3.2d, Figs. 3.3p and 3.3t) clearly modulates the wind direction distribution. The valley morphology at this station is reasonably represented at 3 km and 1 km, but not at 9 km resolution (Figs. 3.3p to 3.3s). As a result, wind direction distribution was reasonably reproduced at 3 km and 1 km (Figs. 3.12m, 3.12o and 3.12p). The Almirez area has complex topography (Fig. 3.2c and Table 3.1), and wind direction seems dominated by the terrain morphology (Figs. 3.3k and 3.3o). Unlike the previous cases, however, this terrain morphology appears reasonably reproduced not only by the 3 km and 1 km WRF, but also by the 9 km setup (Figs. 3.3k to 3.3n). Consequently, wind direction distribution was similarly reproduced at all spatial resolutions (Figs. 3.12i 3.12l), resulting in similar values of *ACC* (Fig. 3.11c). Finally, Centenar had the lowest *ACC* values (Fig. 3.11a), with little dependence on WRF spatial resolution. At this station with low topographic complexity, terrain morphology had little effect on the wind direction distribution (Figs. 3.3a and 3.3e). Therefore, differences in terrain representation at the three WRF resolutions (Figs. 3.3b to 3.3d) had scarce effect on the wind distribution estimates (Figs. 3.12b to 3.12d).

By comparing Figs. 3.9 and 3.11, a significant relationship between RMSE and *ACC* dependence on spatial resolution is observed. Notably, at Gomera and Los Nietos, both with their wind direction distributions strongly affected by terrain morphology, low RMSEs were associated with high ACCs and vice versa. For instance, at Los Nietos

(Figs. 3.9d and 3.11d), there was a notable difference between RMSEs and ACCs associated with the three spatial resolutions. As mentioned above, 3 and 1 km resolved the terrain morphology controlling wind direction, but not so the 9 km resolution. Thus, higher RMSEs and lower ACCs were produced with the latter coarse spatial distribution. A similar conclusion can be drawn for Gomera. Therefore, it is concluded that terrain morphology representation in WRF also affects wind speed estimates. Notably, reduced values of wind speed RMSE values are observed in areas where wind direction is clearly constrained by terrain morphology, providing this morphology is properly represented. Unlike the Los Nietos and Gomera cases, terrain morphology for Almirez station was reasonably reproduced at all three spatial resolutions, generating the similar *ACC* values in Fig. 3.11c.

Finally, based on Figs. 3.9 to 3.12, it is concluded that the WRF setup based on experiment E15 (P1) and 1 km spatial resolution provides the best wind speed and direction estimates overall at the four stations. Nevertheless, there are significant differences between stations in the reliability of these estimates. The RMSE ranged from about 2 ms^{-1} (Centenar and Los Nietos) to more than 2.5 ms^{-1} (Gomera and Almirez). The bias was from -0.5 ms^{-1} (Centenar and Gomera) to 0.3 ms^{-1} (Almirez), and *ACC* from about 55% at Centenar to more than 80% at Los Nietos. Wind direction distribution was fairly reproduced at Los Nietos (Figs. 3.12m-p). The predominant southeast wind direction was clearly reproduced by the model, although there is overestimation of values for the north through west directions. As highlighted earlier, this predominant wind direction can be explained by the channeling effect of surrounding topography (Figs. 3.2d, 3.3p and 3.3t). Furthermore, Los Nietos is affected by a strong thermal contrast between its area and the sea, which is just 40 km away through a long valley. The wind distribution was also reasonably reproduced at Gomera station (Figs. 3.12e and 3.12h), but with a bias about 25° toward the southeast. At Almirez (Fig. 3.12l), the principal wind directions were fairly well reproduced, with no bias; not so the distribution. The model indicated more cases than observed in the south through east directions, and less than observed in the north through west directions. Finally, the poorest estimation of the wind direction distribution is for Centenar (Figs. 3.12a and 3.12d). The model was able to estimate some of the predominant wind directions, but some of the model directions are not found in the observed data.

3.5 Summary and conclusions

In this work, we evaluated the relative roles of parameterization choice and terrain representation in the Weather Research and Forecasting (WRF) mesoscale model, as they pertain to regional wind resource assessment. In a first analysis, to evaluate sensitivity of WRF wind estimates to parameterization choice, 32 configurations (experiments) of the Microphysics (MPH), Cumulus (CMS), Planetary Boundary Layer (PBL) or Short- and Long-wave Radiation (SWR and LWR, respectively) parameterizations schemes were assessed. These experiments, with 3 km spatial resolution and one-hour output frequency, were conducted for the four seasons in the year 2005. In a second analysis, to evaluate sensitivity of the wind estimates to terrain representation in the WRF, experiments were conducted with three different spatial resolutions - 9 km, 3 km and 1 km. The study region was Andalusia (Southern Spain). Although relatively small, this region is characterized by varied topographic, geographic and weather conditions, which made the evaluation especially challenging. Estimates were evaluated with data collected at four stations, whose locations are representative of different climatic conditions and varied topographic complexity and morphology in the study region. The four stations provided hourly wind speed and direction data at 40 m.a.g.l. The WRF estimates were assessed using different statistics, which evaluated both wind speed and direction. Root Mean Square Error (RMSE) and Mean Error (ME) were used to evaluate wind speed. For evaluating wind direction, we used an accuracy parameter (ACC) that considers the percentage of times for which the circular distance between observed and modeled wind direction is less than a 30°.

Results of the first analysis show RMSE values of the wind speed estimates to be sensitive only to the PBL parameterization choice. Differences between 3% and 8% were observed, depending on the PBL parameterization and the station. Sensitivity of the wind speed RMSE values to other parameterizations was not significant. Nevertheless, some combinations of schemes (experiments) performed better than others. Unfortunately, these combinations differed among stations.

The ME values of wind speed showed significant dependence on the station and choice of PBL parameterization. Values ranged from -15% to 10%, depending on the station and experiment. ACC values showed little sensitivity to the choice of parameterization.

Only small differences (below 2%) associated with the PBL were observed. On the other hand, there were substantial differences between stations for *ACC* values, indicating that WRF wind direction estimates are highly sensitive to terrain characteristics.

Among all 32 experiments, experiment number 15, using the YSU (PBL), Morrison-2M (MPH), Grell-3D (CMS), RRTG (SWR) and RRTM (LWR) parameterizations schemes, performed the best. Since results of the first analysis showed that WRF wind estimates in the study region were mainly sensitive to the PBL parameterization selection, only variations of this parameterization were considered in the second analysis. Six experiments were conducted, with three spatial resolutions (1, 3 and 9 km) and two PBL parameterizations. The remaining parameterizations were chosen based on the best performing experiment from the first analysis.

In the second analysis, RMSEs showed considerable dependence on the PBL, station and spatial resolution. The P1 PBL parameterization (YSU scheme) generally provided lower RSME values. Overall, lower RMSEs were associated with higher spatial resolutions of WRF; differences were from 0.2 to 1 ms^{-1}, depending on the station.

Biases in the WRF wind speed estimates were very sensitive to model spatial resolution. This is mainly because higher resolution improves the representation of terrain elevation. The sign of the bias depended on terrain morphology and the spatial resolution, but absolute values tended to be much higher with coarser spatial resolution (9 km). A positive bias in WRF wind speed estimates near the ground in flat areas has been reported by other authors (Jiménez and Dudhia, 2012), associated with the terrain drag effect. This bias was found to be small at 40 m.a.g.l, the elevation considered in this work.

Physical configuration had little impact on wind direction distribution estimates. These estimates proved more sensitive to the representation of terrain morphology around the station than to the model spatial resolution. Depending on the terrain morphology, use of 3 km or even 9 km spatial resolution in the model may provide similar wind direction estimates as 1 km resolution. We observed a significant relationship between RMSE and *ACC* dependence on spatial resolution. Smaller RMSEs of the wind speed estimates and better representations of wind direction were observed in areas where wind direction is clearly constrained by terrain morphology, providing this morphology is properly

represented.

Finally, experiment number 15 at 1 km spatial resolution, provided the overall best estimates of wind speed and direction at the four stations. Nevertheless, there were significant differences between stations in the reliability of these estimates. The RMSE ranged from about 2 to more than 2.5 ms^{-1}. The bias was from -0.5 to 0.3 ms^{-1}, and the *ACC* from about 55% to more than 80%. Wind direction distribution was reliably reproduced with this WRF setup for most stations. Nevertheless, at some stations the model showed bias in the predominant directions, and at other stations it output wind directions not observed.

CHAPTER 4

A METHODOLOGY FOR EVALUATING THE POTENTIAL CONTRIBUTION OF WIND ENERGY TO BASELOAD POWER: A CASE STUDY IN ANDALUSIA (SOUTHERN SPAIN)

Santos-Alamillos F.J., D. Pozo-Vázquez, J.A. Ruiz-Arias, V. Lara-Fanego, and J. Tovar-Pescador. 2012. *A methodology for evaluating the potential contribution of wind energy to baseload power: A case study in Andalusia (Southern Spain)*. Manuscript in preparation.

4.1 Introduction

It is expected that worldwide primary energy demand will increase by 45%, and demand for electricity will increase by 80% between 2006 and 2030 (IEA, 2008). Consequently, without decisive action, energy-related greenhouse gas (GHG) emissions will more than double by 2050 (IPCC, 2007b). There are different paths toward stabilizing GHG concentrations, but a key issue in all of them is the replacement of fossil fuels by renewable energy sources. In this scenario, wind power is expected to play a key role (Mathiesen et al., 2011; Jacobson and Delucchi, 2011). Wind energy is the fastest growing renewable. In 2008, this energy provided nearly 20% of electricity consumption in Denmark, more than 11% in Portugal and Spain, over 4% in the entire European

Union (EU), and nearly 2% in the United States (IEA, 2009). In Spain, installed wind capacity reached 20.8 *GW* in 2010 (around 20% of the total system), the third largest figure among world countries. Wind electricity is estimated to contribute about 9% of global electricity production by 2030, growing to 12% by 2050 (IEA, 2009).

In the EU, regulations set a binding target of 20% of final energy consumption from renewable sources by 2020, along with a commitment to achieve at least a 20% reduction of GHG by 2020, as compared to 1990 (*European Directives 2009/28/EC and 2009/29/EC*). For Spain to achieve the 20% final consumption goal, a substantial increase in the contribution of wind electricity production is necessary, from the current 11% to about 30% (Gómez et al., 2010). Similar target increases in the share of wind energy are expected in other regions (Lund, 2007; Krajacic et al., 2011).

A major challenge will be the integration of these major wind (and solar) yields into the existing energy supply infrastructure (Lund, 2005, 2006). The challenge comes from the fluctuating nature of wind resources and their sensitivity to weather patterns, as compared to the relatively stable and predictable sources of conventionally generated electricity. These characteristics make the cost of renewables less competitive for power generation systems, because intermittent production creates negative externals that translate into grid integration costs. In particular, wind power intermittency has implications for both costs of wind integration into the electricity system (balancing costs), and costs associated with maintaining adequate system reliability (backup costs). Other technological solutions, such as energy storage, are is still immature for the large scale. Today, short term wind and solar power forecasting is the primary requirement for efficient integration of renewables into power systems, and for the reduction of grid integration costs (Saintcross et al., 2005; Kariniotakis, 2006; Lorenz et al., 2010; Lara-Fanego et al., 2011). Unfortunately, the skill of these forecasts is still limited, and unpredicted generation must be accommodated by system reserves. To sum up, as wind power contributes a higher proportion of all generation, it will become increasingly difficult for electrical system operators to effectively integrate such additional fluctuating power input. Thus, solutions that reduce power fluctuations are important if wind electricity is to significantly displace other electricity technologies.

One of the most promising ways to reduce the power fluctuation from wind energy is

to take advantage of the high spatial variability of this resource. The idea is that, since the spatial correlation of wind speed diminishes with distance, the combined output of numerous, widely-spaced wind farms should be smoother than the simple output of an individual power plant. This smoothing effect becomes significant provided that weather conditions across the interconnecting region are sufficiently variable and/or terrain complexity significant. If this is the case, above-normal wind speed at certain times and locations can compensate below-normal wind speed at other locations (negative spatial correlations), producing spatial balancing of the wind energy resource. In such cases, by interconnecting advantageously-distributed wind farms, it may be possible to achieve either secured minimum-wind output or secured peak-load, eventually transforming wind energy into a reliable supply.

There are numerous works in the literature that analyze the spatiotemporal variability of the wind energy resource and its consequence for wind power integration (Kahn, 1979; Landberg, 1997; Holttinen, 2005; Heide et al., 2010). In a recent work, Roques et al. (2010) analyzed wind power production across different European countries, to obtain the optimum combination of cross-country portfolios that minimize the variance of wind production. They concluded that wind power production across Europe varies considerably, and that an optimal combination of wind production at different locations can foster a much less variable total production.

There is no a clear consensus in the literature on evaluating the contribution of wind toward reducing the conventional capacity of power systems. In general, two types of parameters for describing the contributions can be distinguished: 'capacity credit' and 'firm capacity'.

Capacity credit provided by wind energy is often defined as the ability of this energy to contribute to the peak demands of a power system, while maintaining the same security of supply as conventional power plants (Boyle, 2008). In this sense, the capacity credit is the amount of thermal plant generation capacity that can be displaced from the power system, with the same reliability. It is usually expressed as the percentage of installed wind power capacity. Obtaining the capacity credit is no easy task, since a full modelling of the power system is necessary. Several studies have analyzed the wind energy capacity credit, in individual countries and for all Europe (Giebel, 2005, 2007; Gross et al., 2008).

The main conclusion was that wind power has capacity credit, but it is highly dependent on the supporting electric system, wind load factor and penetration level. On average, for a penetration of around 20%, the wind energy capacity credit could approach 20% of installed power (Gross et al., 2008).

In contrast, one can consider the firm capacity, that is, the fraction of installed wind capacity that is available with the same probability as that of a thermal plant (Giebel, 2005). With this definition, the firm capacity of wind energy can be regarded as baseload power. Although capacity credit and firm capacity are related, they are not the same. Firm capacity translates directly into potential fossil/nuclear baseload capacity reduction, whereas capacity credit may reduce the need for conventional maximum capacity while not affecting baseload capacity. In addition, capacity credit could be considerably greater than firm capacity, provided wind energy production is correlated with load demand. Unlike capacity credit, firm capacity can be assessed comparatively easily from pure wind data (Landberg, 1997).

In contrast to the capacity credit, the ability of wind energy to provide firm capacity (baseload) has been shown to be limited. For instance, Oswald et al. (2008) analyzed the ability of wind energy to provide reliable electricity in the United Kingdom (UK). The principal conclusion was that, although aggregation of output across the UK is smoother than the output of individual wind, this aggregation does not lead to a substantial firm capacity. Similar results were found in analogous aggregation studies for Denmark (Ostergaard, 2008) and Germany (Weigt, 2009). In the latter study, it was concluded that only 0.5% of the total wind power installed capacity in Germany was guaranteed throughout the study period (3 years). In contrast, between 10% and 15% of the installed capacity was wind capacity credit. Underpinning these results are the relatively homogeneous weather conditions and limited topographic features across the three studied countries. Other studies are more encouraging. For instance, Archer and Jacobson (2007) studied the decrease of wind power production fluctuation through interconnection of 19 wind farms in the Midwestern United States. They found a significant decline in the fluctuation of total production compared to single wind farms, and a firm capacity of about 15%. Cassola et al. (2008), proposed a method for the optimal distribution of wind farms at ten locations in Corsica (France), to reduce temporal variability of total wind power production. They showed that around 16% of

yearly average wind power could be used as reliable baseload. Finally, Kempton et al. (2010) analyzed the benefits of interconnecting offshore wind farms along the east coast of the United States. Based on analysis of data from 11 meteorological stations, they demonstrated that this interconnection would provide a reliable baseload (firm capacity). In the last three studies, the varied weather conditions and topographic features of the study areas explain the findings of significant amounts of firm capacity.

This work examines the ability of wind energy in Andalusia (Southern Spain) to provide reliable baseload power. To this end, an initial estimate of wind energy resources in the study region, including offshore areas, is obtained based on a numerical weather prediction (NWP) model simulation. Second, principal component analysis (PCA) is used for analyzing the spatial variability of the regional wind energy resource and, in particular, to highlight the existence of spatial balancing. Then, results of the PCA are used to assess the optimal location of wind farms (both onshore and offshore) in the study region, to provide firm capacity. Finally, the firm capacity provided by different combinations of offshore and onshore wind farms in the aforementioned locations, is estimated. There is no analysis of the ability to provide capacity credit. Although relatively small, the region is characterized by varied topographic, geographic and weather conditions. This fact anticipates the existence of considerable wind speed spatial variability and, ultimately, spatial balancing of wind energy resources.

This paper is organized as follows: Section 4.2 deals with the study area, data and method. Section 4.3 describes the results. Finally, in Section 4.4, a summary and conclusions are presented.

4.2 Methods and study area

4.2.1 Study region

The study region (Fig. 4.1) is Andalusia, in the southern Iberian Peninsula (IP). It extends over 87000 square km^2. The region (latitude 35°30' to 38°30' N and longitude 7°30' to 1°30' W) is in a transition zone between temperate and subtropical climates.

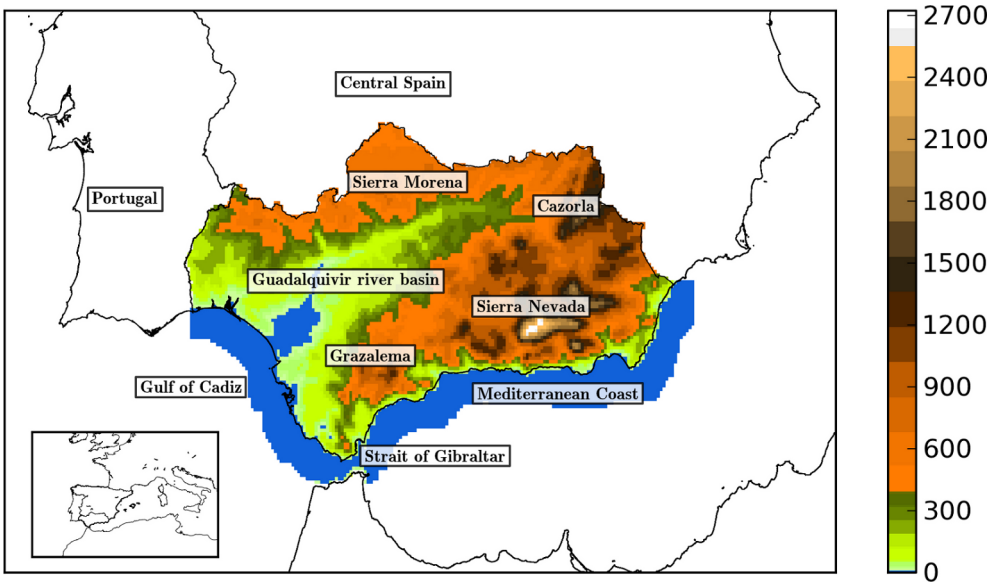


Figure 4.1. Location (small figure, bottom right) and principal topographic and geographic characteristics of study region. Color map indicates elevation based on the same 3 *k*m spatial resolution Digital Elevation Map (DEM) used in the model simulation, to derive study data. Scale at right indicates elevation in meters above sea level.

From a topographic point of view, the region may be split into two different parts. The western part, covering around 40000 km^2, is a nearly homogeneous flat area, around 100 meters above sea level (m.a.s.l.). The eastern part has very complex topography, with several mountain areas, reaching 3482 m.a.s.l in the Sierra Nevada National Park (the highest elevation on the IP). Surface wind speed spatial variability is related to mesoscale circulation and other, more localized factors, such as topographic characteristics (elevation, aspect, slope, and others) or thermal contrast near water bodies (Hutchinson et al., 1984; Weber and Furger, 2001; McVicar et al., 2007, 2008). The atmospheric circulation over most of the IP is dominated by a semi-permanent subtropical high-pressure centre over the Azores islands, particularly so in the south where the study region is located. The position and intensity of this centre changes through the year. During winter, the high is at lower latitudes, allowing the region to be affected by zonal circulations from the west. During summer, the high migrates northward, blocking the westerly circulations over most of the IP and particularly the study region (Pozo-Vázquez et al., 2001; Trigo et al., 2002; Castro-Díez et al., 2002).

Although the entire region is under the influence of the Azores subtropical high, the region has a wide range of climate conditions. The eastern part is less influenced by that high, and more affected by the Mediterranean Sea (Esteban-Parra et al., 1998; Ramos-Calzado et al., 2008; Rodríguez-Puebla et al., 1998). These differences are related to topographic features. The western part is actually the lower part of the Guadalquivir River basin. It is open to the Atlantic Ocean and to direct influence by the atmospheric flow controlled by the Azores high. The Guadalquivir River valley is exposed to mild and moist air from the Atlantic year-round. Winds are channelled through this valley, generating strong mean surface wind speeds in the upper valley (Alsamamra et al., 2011). The eastern part is partially isolated from this Atlantic influence by the Sierra Nevada and Cazorla mountain ranges (Fig. 4.1). Consequently, annual precipitation values over the region range from 300 $mmyear^{-1}$ in the coastal, semi-desert southeast areas, to more than 2500 $mmyear^{-1}$ in the mountains near the Strait of Gibraltar (Ramos-Calzado et al., 2008). In addition, the study region is bounded on the south by the Atlantic (western part) and the Mediterranean (eastern part), representing about 900 km of coastline. Finally, one of the most important features regarding wind energy are strong, semi-permanent winds near the coast of the Strait of Gibraltar. Here, low-speed winds are channeled and accelerated through this 11 km-wide topographic feature. In summary, despite the relatively small size of the region, the interaction of mesoscale circulation, topographic and geographic features causes notable surface wind speed spatial variability across it (Alsamamra et al., 2009, 2011; AEA, 2009).

Installed wind power capacity in the region totalled about 3 GW at the end of 2011, and plans are to reach 5 GW by 2013 (PASENER, 2007). In addition, the region contains areas of great significance for offshore wind energy, especially near the Strait of Gibraltar (Sempreviva et al., 2008; Todt et al., 2010). Although development of offshore wind farms in these areas is in its early stages, the offshore wind energy resource is addressed herein.

4.2.2 Data

Region-wide wind energy resources at 80 meters above ground level (m.a.g.l.) were obtained from an integration with the WRF (Weather Research and Forecasting) NWP

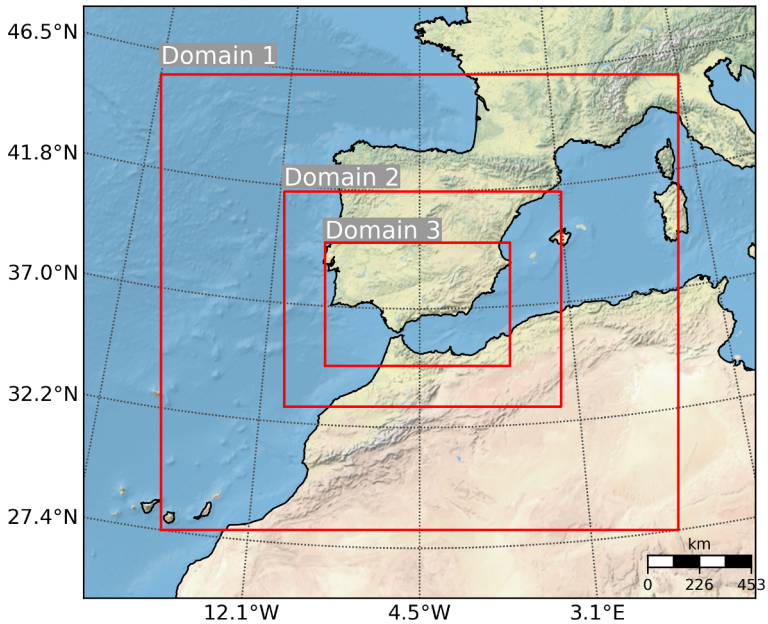


Figure 4.2. Spatial configuration of domains for numerical simulation: three nested domains with 27, 9 and 3 km horizontal resolutions, respectively. Data from the inner domain (3 km) were analyzed.

model (Skamarock et al., 2008). Simulations were conducted for the year 2009, at a temporal resolution of one hour. The model configuration included three nested domains, with 27, 9 and 3 km spatial resolutions (Fig. 4.2). We used 36 vertical levels, 8 levels within the lowest 1000 m.a.g.l.. The five lowest vertical levels, which are important for wind energy applications, were approximately located at 4, 18, 43, 64 and 80 m.a.g.l. This last level was used to obtain modelled wind speed and wind energy values. Ultimately, data were analyzed for the third nested domain, with 3 km spatial resolution and centred on the study region. This analysis included offshore areas up to 20 km from the coast, a distance considered feasible for offshore wind energy projects (Fichaux et al. , 2009).

The physical configuration of the model was selected based on previous evaluations of WRF performance in the study region (Fernández et al., 2007; Borge et al., 2008; Ruiz-Arias et al., 2008). The RRTM scheme (Mlawer et al., 1997) was chosen for longwaveradiation, and the Dudhia Scheme (Dudhia, 1989) for short wave radiation. The Kain-Fritsch scheme (Kain and Fritsch , 1993), was used for cumulus and the Yonsei

University planetary boundary layer scheme for the boundary layer (Hong et al., 2006). The Thompson graupel scheme (Thompson et al., 2006) was used for microphysics, and the unified Noah land-surface model for the land surface.

Newtonian relaxation or nudging was used in model integration, using the parameter values proposed by Seaman (2000) and Otte (2008b). This technique relaxes the model toward the observed state by adding artificial forcing terms to the model predictive equations, based on the difference between the states weighted by nudge coefficients. Several works demonstrate the improvements of nudging in simulating the wind field (Barna and Lamb, 2000).

We used initial and boundary conditions from the Climate Forecast System Reanalysis (Saha et al., 2010) with spatial resolution 0.5° and updates every 6 hours. It has been reported that the Surface Sea Temperature (SST) update during WRF model integration improves the accuracy of wind speed, especially for offshore winds (Muller at al., 2007). In this work, SSTs were interpolated to ocean grid points in each model domain, using the NCEP version 2.0 global SST dataset (Reynolds et al., 2002). This dataset is updated daily, on a 1° × 1° grid.

4.2.3 Wind speed spatial variability analysis

A widely-used method to analyze the spatiotemporal variability of an environmental variable is Principal Component Analysis (PCA) (Preisendorfer, 1998). This method allows reduction of the initial dataset dimension into a few representative variables. The new variables, called principal components (PCs) and often referred to as modes of variability, are obtained as linear combinations of the initial variables. These combinations are obtained such that the new variables account for the maximum fraction of the variance contained in the original dataset. The coefficients of the linear transformation, known as loading factors, range from -1 to 1 and represent correlations between the original field variables and corresponding PC, at each point. A map of the loading factors of a particular PC can be used to analyze spatial balancing of the variable studied. Areas of positive and negative loads (dipolar patters) in the map are indicative of balancing, being the significance of this balancing related to the magnitude of the loads.

A PCA analysis was done based on wind speed estimates provided by the WRF model. To this end, hourly wind speed values at 80 m.a.g.l. were used to obtain daily-integrated wind power values based on:

$$E_{daily\ wind} = \sum_{i=1}^{24} \left(\frac{1}{2} \rho v^3 \right) \times 1h \tag{4.1}$$

where ρ is air density at sea level and u_i and v_i are the hourly meridional and zonal wind components respectively at 80 m.a.g.l. Then, the PCA was conducted based on these daily values. Although we also did an analysis based on hourly values, the daily PCA analysis was chosen to reduce the complexity of resulting patterns. The analysis was conducted independently for each season and for the annual period. The first five modes were analyzed for each period, accounting for 78% (summer) to 94% (winter) of the variance of the field (Table 4.1).

Finally, to understand the nature of the wind power modes resulting from the PCA, a brief description of associated mesoscale atmospheric circulations is given. We produced composite maps of daily mean sea level pressure (SLP) and horizontal surface wind speed (10 m.a.g.l.) anomalies, associated with the fifteen (thirty in the annual case) maximum and minimum values of the corresponding PC series. The composites were derived from the ERA-Interim reanalysis (Uppala et al., 2008) dataset, covering a 4000 × 4000 km^2 region centred on the Iberian Peninsula. For a more detailed view, composite maps of daily mean horizontal wind component anomalies at 80 m.a.g.l., derived from WRF 3-km integration, were created. Again, these composites were computed with the fifteen maximum and minimum values of the respective PC series (thirty for the annual case). The aforementioned anomalies were computed based on the corresponding analysed period (seasonal or annual).

4.2.4 Wind power balancing analysis

From the PCA analysis, several modes of variability were further examined for potential interest to balancing. To this end, four locations (grid points) were selected for each

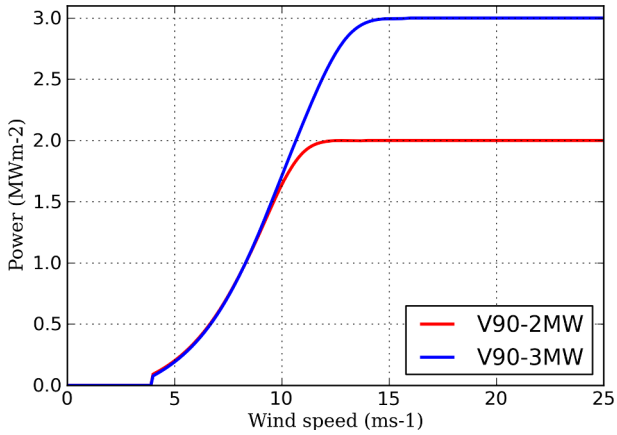


Figure 4.3. Power curves of the *V90-2MW* (red line) and *V90-3MW* (blue line) wind turbines. First turbine was used to assess onshore locations and the second for offshore locations.

mode of variability. Among these selections, there were two onshore grid points with the highest positive and negative loading factors (On+ and On- hereafter), and two offshore grid points with analogous loadings (Off+ and Off- hereafter). At these four locations, we considered corresponding hourly wind speed time series at 80 m.a.g.l., derived from the WRF 3-km integration. Based on these time series, hourly wind power time series produced by a reference wind turbine were computed. For onshore locations, the selected wind turbine was a *Vestas V90-2.0 MW*, with a rated nominal power of 2 MW and hub height 80 m.a.g.l. For offshore locations, the selected wind turbine was a *Vestas V90-3.0 MW*, of nominal power 3 MW and the same hub height. Fig. 4.3 shows the power curves for both turbines. Finally, the wind power time series were normalized, dividing by the respective nominal power, obtaining the corresponding hourly capacity factor time series.

These four capacity factor time series represent the spatial variability of the wind energy resources accounted for by the corresponding mode of variability. In a further step, we analyzed the gain in wind power reliability attained by different combinations (connections) between the selected onshore and offshore sites. Three types of connections were evaluated: Onshore connection (denoted as On, from the connection of On+ and On- locations); Offshore connection (denoted as Off, from the connection of Off+ and Off-); and the connection of all sites (denoted as All). To characterize power

output fluctuations for both standalone and connected wind turbines, we used the mean and standard deviation of the hourly capacity factor throughout the study period. Also computed was the firm capacity, that is, the fraction of installed wind capacity that is online with the same probability as a conventional thermal power plant. This probability can be highly variable, depending on the technology (nuclear, coal, gas). In this work, we use the reference value 87.5%, as in (Archer and Jacobson, 2007). This is the average availability factor reported for thermal power plants in Spain (Gómez et al., 2010; REE, 2010)) Again, this firm capacity was computed for both individual and connected wind turbines, and expressed as a percentage of the installed nominal power.

4.3 Results

This section presents analysis results of the spatial balancing of wind energy resources in Andalusia. The analysis was done independently for each season and for the entire year. Table 4.1 summarizes the PCA results of the daily integrated wind power data, for the various analysis periods. In general, the first mode accounted for a substantial amount of the total variance, ranging from 28% in summer to 71% in autumn. This first mode accounts for a spatially coherent variability across the study region, that is, loading factors are positive elsewhere in the region (not shown). Although interesting, this is not relevant to the balancing study. This first mode can be considered as background coherent temporal mode of variability in the entire region, to which the temporal variability represented by the other modes should be added. In contrast, the second and third modes do show areas of positive and negative and loading and, consequently, evidence for balancing. The fourth and fifth modes, which also show balancing areas in some cases, account for only a small fraction of the total variance. Therefore, in the following section, we consider only the second and third modes for each analysis period.

4.3.1 Winter

The second mode of the winter data PCA accounts for 13% of total variance, and corresponding loading factors are displayed in Fig. 4.4a. A dipolar mode is clearly

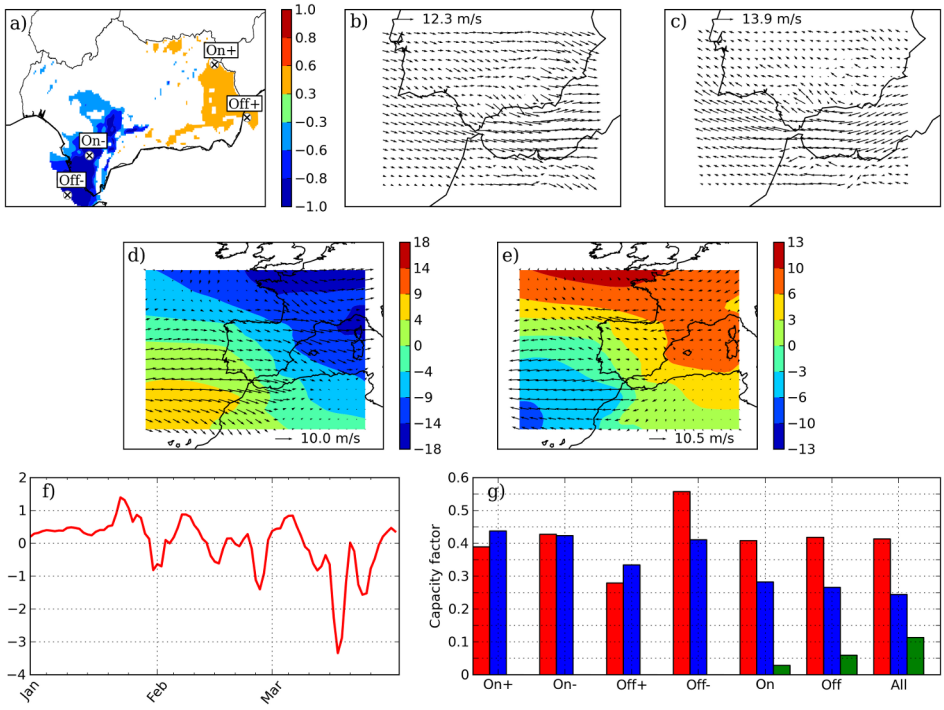


Figure 4.4. Second mode of winter principal component analysis (PCA). a) Loading factors map. Only statistically significant values (above 0.3 or below -0.3) are displayed. b) Composite of daily-mean horizontal wind components at 80 m.a.g.l., corresponding to 15 highest positive anomalies of the PC series of this second winter mode. Data are taken from inner domain of the simulation (see Fig. 4.2). c) As in b), but for 15 lowest negative anomalies. d) Composite of daily mean sea level pressure and horizontal wind components at 10 m.a.g.l., corresponding to 15 highest positive anomalies of the PC series of this second winter mode. Data are obtained from ERA-INTERIM reanalysis dataset. In all Figs., wind speeds are scaled according to the reference at top or bottom, which indicates maximum wind speed in ms^{-1}. f) Principal component time series. Values are standardized anomalies. g) Mean (first column) and standard deviation (second column) of hourly capacity factor and firm capacity (third column), for the four selected sites in Fig. 4.4a (On+, On-, Off+ and Off-), various connections between them (Onshore connection (On), Offshore connection (Off)) and connection between all sites (All)).

Study period	Mode 1 (%)	Mode 2 (%)	Mode 3 (%)	Mode 4 (%)	Mode 5 (%)	Total (%)
Winter	66.27	12.51	6.25	3.63	1.83	90.62
Spring	51.38	15.34	6.53	5.44	4.08	83.00
Summer	27.88	21.34	15.59	6.13	4.55	75.50
Autumn	70.86	8.22	7.30	2.95	2.00	91.44
Annual	64.08	9.08	7.91	5.17	1.76	88.00

Table 4.1. Summary of results of principal component analysis (PCA) of wind energy resources in the study region. The table shows, for seasonal and annual analysis, the explained variance associated which the five most significant modes. Last column shows the variance accounted for by all five modes togegher. Only modes 2 and 3 were considered for a detailled study.

evident. Positive loads from 0.3 to 0.6 are observed in the east, including an offshore area. Negative loads from -0.6 to -0.8 are found in the southwest, including the Strait of Gibraltar, Grazalema and adjacent offshore areas. The PC series (Fig. 4.4f) shows considerable variability at synoptic time scales (as expected), particularly from February onwards. This dipolar pattern indicates the existence of spatial balancing between the areas of high positive and high negative loads, which merits further analysis. Figs. 4.4b to 4.4e indicate that this balancing is associated with a meridional gradient of SLP anomalies. Particularly, high positive anomalies in the PC are associated with positive SLP anomalies in the southwestern IP (Fig. 4.4d). These anomalies generate strong westerly wind anomalies across the entire region, most intense in the east (Fig. 4.4b). This enhancement seems to be associated with topographic features in this area. Firstly, westerly winds are channelled through the Guadalquivir River basin, which is open to the Atlantic Ocean, creating strong surface wind speeds in the upper valley. Secondly, in the upper valley, wind speeds are enhanced by the Cazorla mountain range, which has steep slopes with a perpendicular aspect to these westerly winds. There are also valleys in this range, through which these westerly winds are channelled and accelerated. This produces the positive loading factors seen in the east. Wind speed is also strong in the strait of Gibraltar area, but anomalies are negative, causing the negative loads seen in Fig. 4.4a. Negative anomalies in the PC are associated with negative SLP anomalies centred over the southwest IP (Fig. 4.4e). These anomalies generate region-wide easterly winds, which are significantly intensified by the channelling effect of the strait (Fig. 4.4c) and

by hill/channeling effects of nearby mountain ranges (Grazalema). At the same time, relatively weak easterly winds are observed in the eastern part of the region.

To sum up, the spatial balancing between wind energy resources in the eastern area and Strait of Gibraltar area, as highlighted by this PCA mode, appears to result from the interaction of mesoscale zonal flow and topography. On one hand, westerly winds are channelled by the Guadalquivir River basin, giving rise to strong anomalies in the upper valley. On the other hand, easterly winds are greatly intensified in the strait of Gibraltar area, the only open flat area this flow encounters along its trajectory. The next step is to evaluate the potential impact of this spatial balancing on the stability of wind power production in the region. Fig. 4.4g presents the mean and standard deviation of the hourly capacity factor, along with the firm capacity, corresponding to a wind turbine sited at each of the four selected locations in Fig. 4.4a, and to various combinations (interconnections) of these turbines. These four locations summarize the spatial balancing accounted for by the second PCA mode of the winter analysis. The mean and the standard deviation of the capacity factor are close to 0.4 for the onshore locations. This value is substantially lower for the Off+ locations (eastern part of the region), and considerably higher in the Off- area (Strait of Gibraltar). At the latter location, the capacity factor approaches 0.55. A clear reduction in the standard deviation is obtained for the set of connections between the various locations. For instance, for the connection of onshore sites, the standard deviation declines from more than 0.4 to less than 0.3. When all sites are connected, the standard deviation drops to 0.24. Therefore, power fluctuates more slowly for interconnected wind farms, as noted by other authors (Archer and Jacobson, 2007; Kempton et al., 2010). Finally, connection of the various sites produces firm capacity. This firm capacity is relatively modest for connection of the onshore locations only (0.03, 3%), noticeable for the offshore connection (5%), and large when both onshore and offshore sites are connected (11%).

Fig. 4.5 shows results for the third mode of the winter PCA, which explains about 7% of the variance (Table 1). As with the previous mode, a dipolar pattern is evident (Fig. 4.5a), with positive loads (between 0.3 and 0.6) south of the study area (Strait of Gibraltar, Grazalema and areas offshore of the Mediterranean coast). There are negative loads (between -0.3 and -0.6) in the western area. As in the previous case, the PC series shows marked synoptic variability. Fig. 4.5d indicates that positive anomalies in the PC

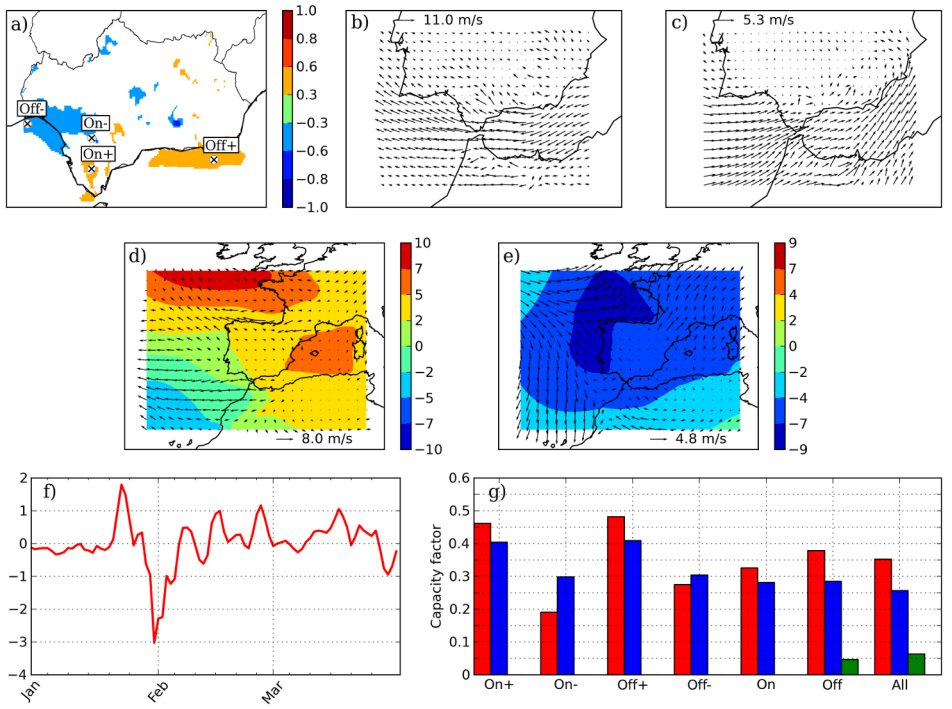


Figure 4.5. As in Fig. 4.4, but for third mode of winter analysis.

are associated with anomalous SLP patterns similar to those in Fig. 4.4e. Specifically, negative SLP anomalies in the southwestern IP are associated with strong easterlies winds along the Mediterranean coast and over the Grazalema mountains, areas with positive loading factors in Fig. 4.5a. On other hand, Fig. 4.5e indicates that negative anomalies in the PC series are linked with a meridional circulation over the region, caused by a centre of negative SLP anomalies in the northwestern IP. This SLP pattern brings relatively strong southwesterly winds over the western area, which has negative loading factors as seen in Fig. 4.5a.

Fig. 4.5g shows a high capacity factor (0.45) for the On+ location, higher than that obtained in the previous case (Fig. 4.4g). The On- location shows a relatively modest capacity factor (0.19) and large standard deviation. For the offshore locations, Off+ has a capacity close to 0.5 and Off- has a smaller value (0.28). As in the previous case, connecting the wind farms significantly diminishes the standard deviation, from values in excess of 0.4 in some locations to about 0.25 when all wind farms are interconnected.

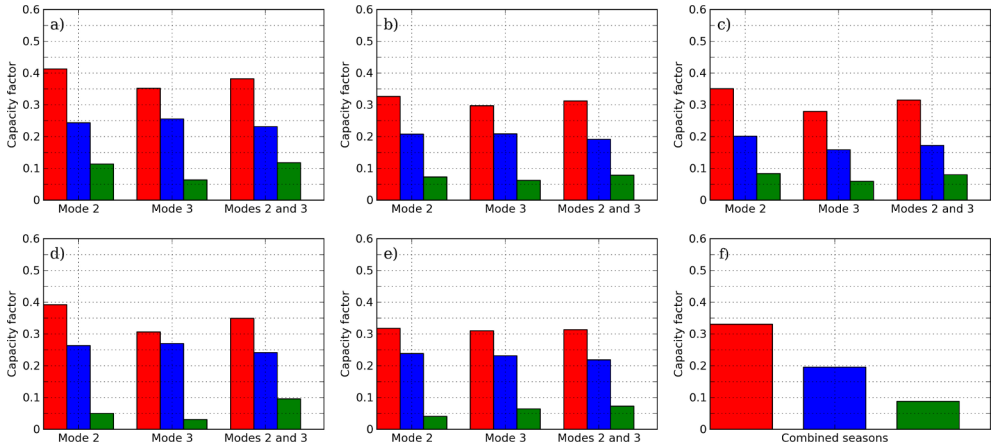


Figure 4.6. a) Mean (first column) and standard deviation (second column) of hourly capacity factor and firm capacity (third column) of second and third modes of winter PCA analysis (represented in Figs. 4.4 and 4.5), along with values obtained from the combination of these modes (modes 2 and 3). b) As in a), but for spring analysis. c) As in a), but for summer. d) As in a), but for autumn. e) As in a), but for annual analysis. f) As a) but connecting all selected locations resulting from the four seasonal analysis; values were computed year around.

For firm capacity, this second winter PCA mode only generates significant values for the offshore connection (4%) and interconnection of all sites (7%).

Finally, the advantages derived from interconnecting all selected locations in the two prior PCA modes are explored further. Fig. 4.6a shows the capacity factor, standard deviation and firm capacity resulting from interconnecting all locations in Figs. 4.4a and 4.5a. This achieves a relatively modest improvement in standard deviation and firm capacity. The standard deviation declines from 0.24 and 0.25 (second and third mode, respectively) to 0.23 when both modes are interconnected. Interconnection increases the firm capacity as much as 12% (11% for the second mode and 7% for the third mode).

4.3.2 Spring

The second mode spring PCA accounted for 16% of the variance (Table 1). Corresponding loading factors are shown in Fig. 4.7a. The spatial pattern of the loading

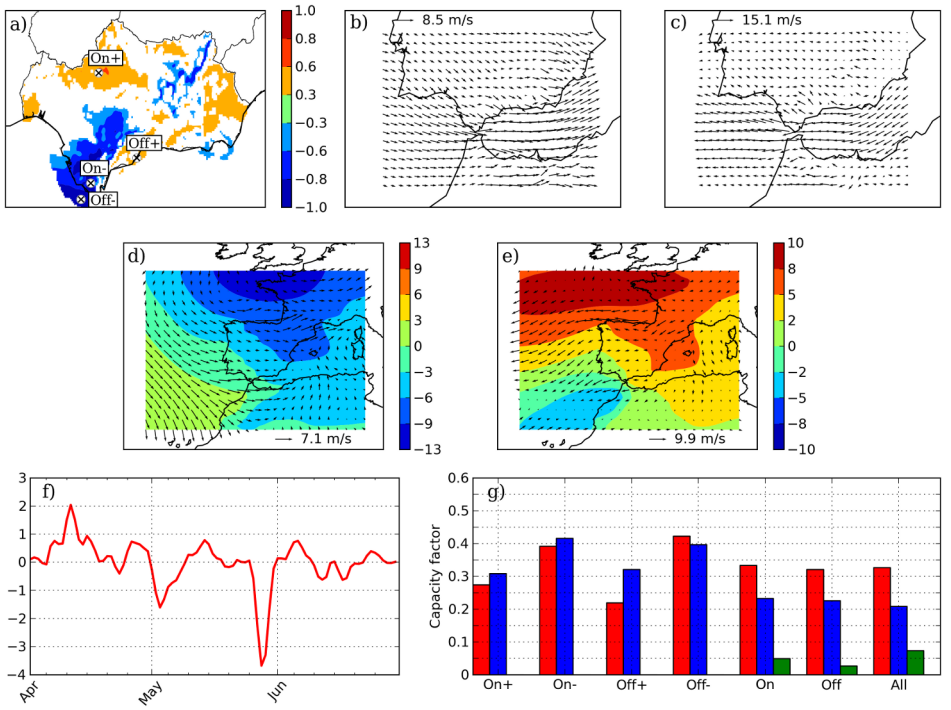


Figure 4.7. As in Fig. 4.4, but for spring analysis

resembles that from the second winter mode (Fig. 4.4a). A dipolar mode is again clear, with positive loads (from 0.3 to 0.6) in central (Sierra Morena mountains) and eastern areas (Cazorla mountains), and in an area offshore of the Mediterranean coast. Negative loads (from -0.3 to -0.8) are found in the northeast and, more prominently, in the southwest (Strait of Gibraltar and Grazalema areas, including offshore locations). The PC series (Fig. 4.7f) shows considerable variability at synoptic time scales.

Mesoscale atmospheric circulations associated with this balancing pattern (Figs. 4.7b to 4.7e) are similar to those from the second winter mode (Fig. 4.4), but the circulation over the region is less zonal. High positive anomalies in the PC are associated with northwesterly wind anomalies across the region (Figs. 4.7b and 4.7d). These winds are enhanced by topographic features of the Sierra Morena mountains in the centre and Cazorla mountains in the east, leading to the positive loadings in Fig. 4.7a. Wind speed is also strong near the Strait of Gibraltar, but anomalies are negative, causing the negative loads observed in Fig. 4.7a. Negative anomalies in the PC are connected with

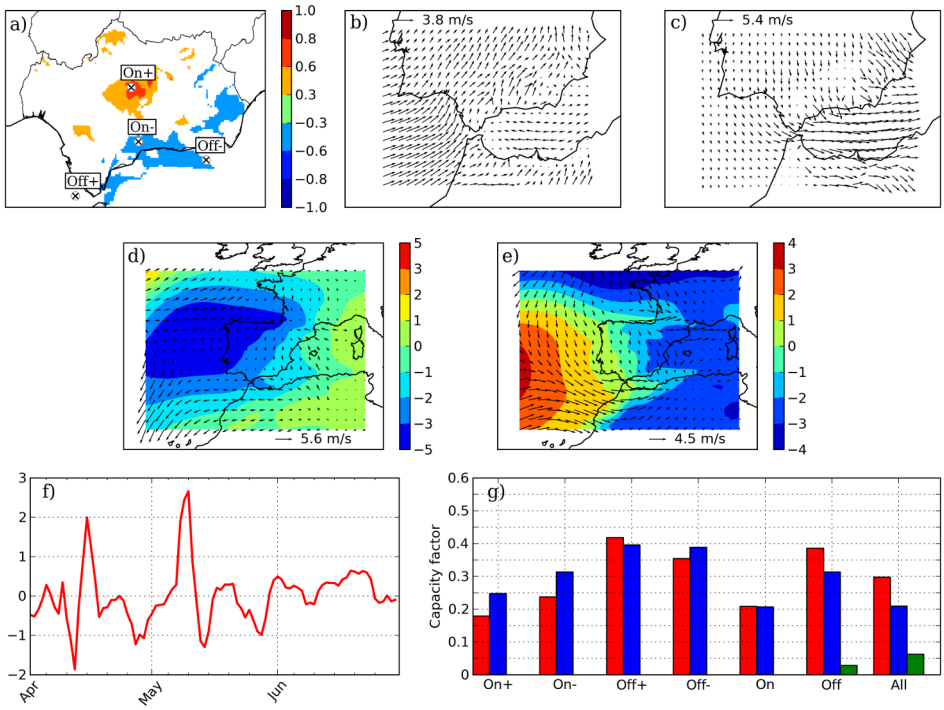


Figure 4.8. As in Fig. 4.5, but for spring analysis

northeasterly winds region-wide (Figs. 4.7c and 4.7e). These winds are significantly enhanced by the channelling effect of the Strait of Gibraltar and by hill effects in nearby mountain ranges (Grazalema). In summary, the spatial balancing observed in the second PCA mode for spring is similar to that of this mode for winter, and they have similar atmospheric circulations.

Fig. 4.7g shows high capacity factors for the On- (0.39) and Off- (0.42) locations. In contrast, the Off+ site shows a relatively modest capacity factor (0.22) and high standard deviation. In any case, the capacity factors are significantly lower than those seen in Fig. 4.4g. As in the winter analysis, wind farm connection reduces the standard deviation, from more than 0.4 at certain locations to almost 0.2 when interconnected. This reduction is greater than that of the winter analysis (Figs. 4.4g and 4.5g). Firm capacity is 5% for connection of the onshore locations, and 2% for the offshore ones. Finally, connecting all locations provides a 7% firm capacity value.

The third mode of the spring PCA explains 7% of the variance (Table 1); loadings are illustrated in Fig. 4.8a. The dipolar pattern is again present, but its spatial distribution differs substantially from the previous patterns. Strong positive loadings are observed inland, at the centre of the study region, with values up to 0.8. Weak positive loads are in an offshore area, west of the Strait of Gibraltar. Negative loads (between -0.3 and -0.6) are seen east of the strait, along the Mediterranean coast (both onshore and offshore), and in the east. The PC series (Fig. 4.8f) shows pronounced synoptic scale variability and a clear upward trend at its end. Figs. 4.8b to 4.8e show that the dipolar pattern in Fig. 4.8a is related to meridional circulation anomalies. In particular, high positive anomalies in the PC are associated with a low SLP centre in the northwest IP (Fig. 4.8d), which produces south wind anomalies region-wide. These winds are channelled through the Guadalquivir River basin and strengthen when they encounter topographic features in the central region (Fig. 4.8b). This gives rise to the positive loads in this area (Fig. 4.8a). At the same time, this SLP centre causes low wind speeds on the Mediterranean coast. High negative anomalies in the PC series are linked to a zonal gradient of SLP anomalies, with positive values over the Azores and negative ones over the Mediterranean (Fig. 4.8e). This SLP pattern brings north wind anomalies to the region. The interaction of these northerly wind anomalies with the topography explains the load patterns in Fig. 4.8a. Comparing Fig. 4.8c to Fig. 4.1, it seems that the negative loads in the offshore area east of the Strait of Gibraltar are produced by the channelling effect caused by mountains near the strait (including the Grazalema mountains). The negative load along the Mediterranean coast (onshore and onshore) appears to result from the channelling effect between the Grazalema and Sierra Nevada mountains, and negative loads in the east are caused by channelling between the Sierra Nevada and Cazorla mountains.

Fig. 4.8g shows that, for this mode, mean and standard deviation values of the offshore capacity factor are substantially higher than onshore ones. Capacity factors ranged from 0.18 (On+) to 0.42 (Off+), while standard deviations were from 0.25 (On+) to 0.4 (Off+). As in the previous cases, the connection of wind farms reduces the standard deviation, from 0.4 in some cases to 0.21 when all locations are connected. For firm capacity, the connection of only the offshore wind farms gives a 3% value, while the connection of all locations produces 6%, with a 0.3 capacity factor.

Finally, Fig. 4.6b shows the capacity factor, standard deviation and firm capacity

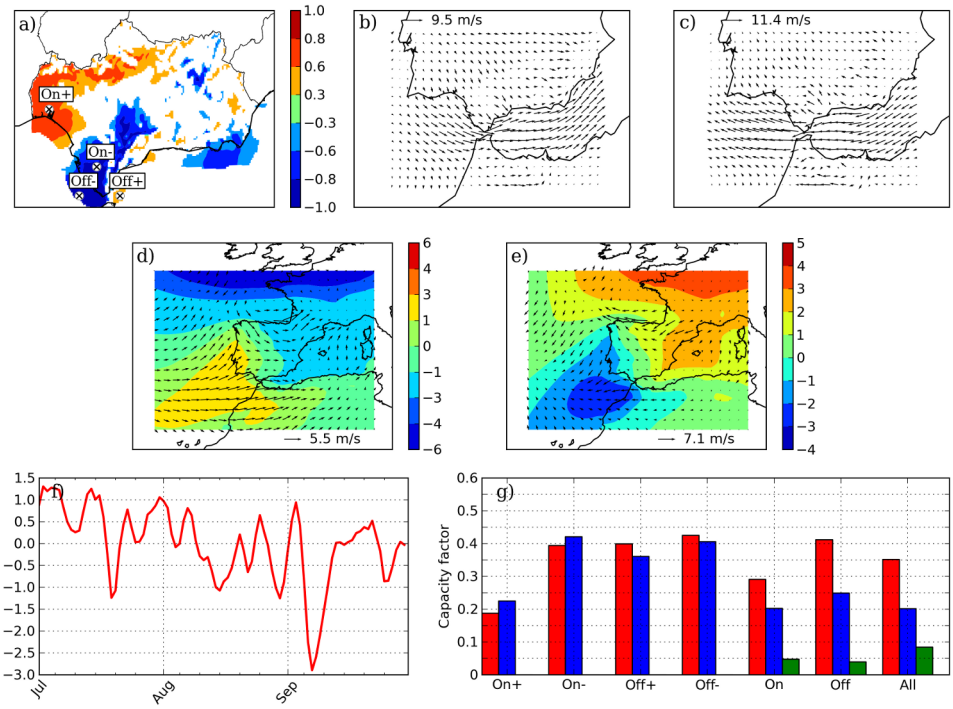


Figure 4.9. As in Fig. 4.4, but for summer analysis

resulting from interconnecting all locations in Fig. 4.7a and 4.8a. A relatively modest improvement in standard deviation and firm capacity was obtained. In particular, the standard deviation drops from 0.21 in the second and third modes to 0.19 when both modes are interconnected; firm capacity increases to 8

4.3.3 Summer

The second mode of the summer PCA analysis accounted for 22% of total variance. The loading factors map (Fig. 4.9a) shows a clear dipolar pattern. Strong positive loads (0.6 to 0.8) are observed in western and northwestern areas, including offshore areas in the Gulf of Cádiz. Strong negative anomalies (-0.6 to -0.8) are seen in the Strait of Gibraltar area, Grazalema mountains and in an offshore area in the Mediterranean, in the eastern part of the region. The PC series (Fig. 4.9f) shows pronounced synoptic-scale temporal

variability. Figs. 4.9b to 4.9e show that the dipolar loading factor map is associated with changes in zonal circulation. High positive anomalies in the PC series are associated with the interaction of strong northwest wind anomalies (Fig. 4.9b) with topography in the eastern area (Sierra Morena mountains), leading to the positive loads found in Fig. 4.9a. At the same time, this northwest flow is tied to relatively low wind speeds near the strait (areas of negative loads in Fig. 4.9a). High negative anomalies in the PC are associated with easterly wind anomalies, caused by a low SLP centre in the southwest (Fig. 4.9e). This easterly flow is enhanced in the strait area and eastern Mediterranean (Fig. 4.9c), as evidenced by areas of high negative loads in Fig. 4.9a.

First of all, Fig. 4.9g shows high capacity factor values, except for the On+ case. Second, as in the previous cases, interconnection reduces the standard deviation. For instance, the offshore connections generate a capacity factor of 0.41 and standard deviation of 0.25; compare to the initial values of this standard deviation, 0.37 and 0.4. Both onshore and offshore connection provides firm capacity -5% and 4%, respectively. Finally, interconnecting all onshore and offshore locations furnishes a 0.35 capacity factor, a 0.2 standard deviation, and an 8% firm capacity value.

The third mode of the summer PCA analysis accounted for 16% of the variance. Corresponding loading factors are displayed in Fig. 4.10a. A dipolar pattern is evident, with positive loads (between 0.3 and 0.6) in the northern and eastern parts of the region (Sierra Morena, Sierra Nevada and Cazorla) and weak positive offshore loads west of the strait. Negative loads (-0.3 to -0.8) are observed on the Mediterranean coast and in the western part of the study region, including offshore areas. The corresponding PC series (Fig. 4.10f) shows synoptic variability, with marked anomalies at the beginning of the series. Figs. 4.10b and 4.10d indicate that the high positive anomalies in the PC series results from interaction of northeasterly wind anomalies with topography in the east and north of the study area (Sierra Morena, Cazorla and Sierra Nevada mountains). This causes the positive loads observed in Fig. 4.10a. In contrast, Figs. 4.10c and 4.10e indicate that high negative values in the PC are caused by westerly wind anomalies in the region. These anomalies are intensified on the Mediterranean coast and in the west (areas of negative loads in Fig. 4.10a).

Similar to the third mode results of the spring PCA, Fig. 4.10g shows that for this third

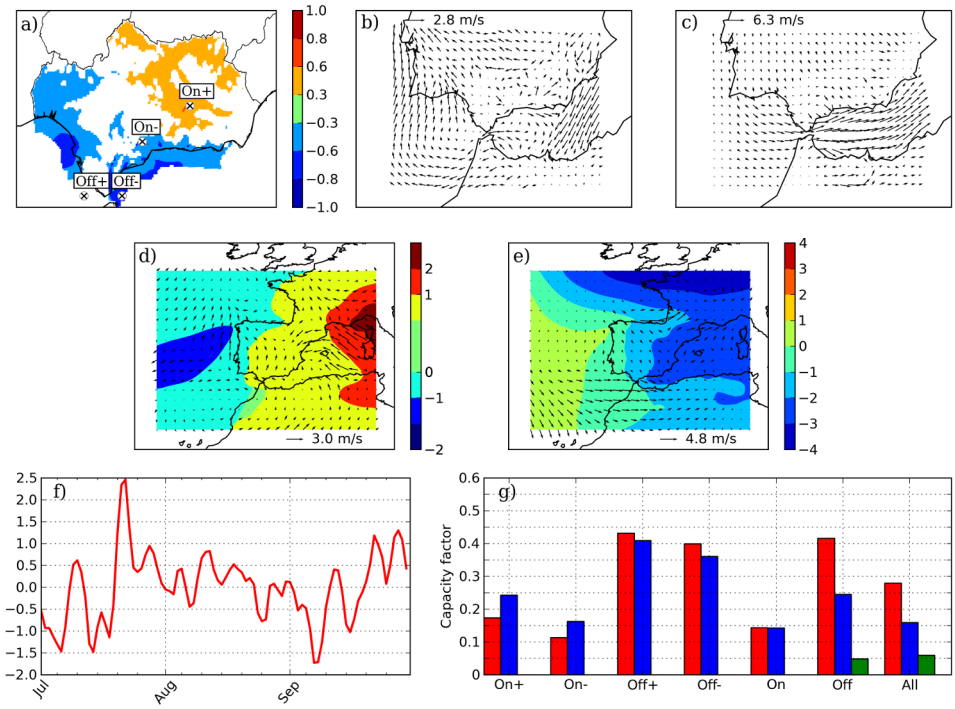


Figure 4.10. As in Fig. 4.5, but for summer analysis

mode of the summer PCA, mean and standard deviation values of the offshore capacity factor are substantially higher than the onshore ones. Capacity factors were from 0.12 (On-) to 0.43 (Off+), and the standard deviation was from 0.17 (On-) to 0.41 (Off+). This mode shows one of the most significant standard deviation reductions for interconnected locations, to a value of 0.16. For firm capacity, connection of only offshore wind farms provides 4%, while connection of all locations gives 5% with a 0.28 capacity factor.

Finally, Fig. 4.6c shows the capacity factor, standard deviation and firm capacity stemming from interconnection of all locations in Figs. 4.9a and 4.10a (second and third spring modes). A relatively modest improvement in standard deviation was attained, but no improvement in firm capacity (the final value was 8%, the same as the second mode).

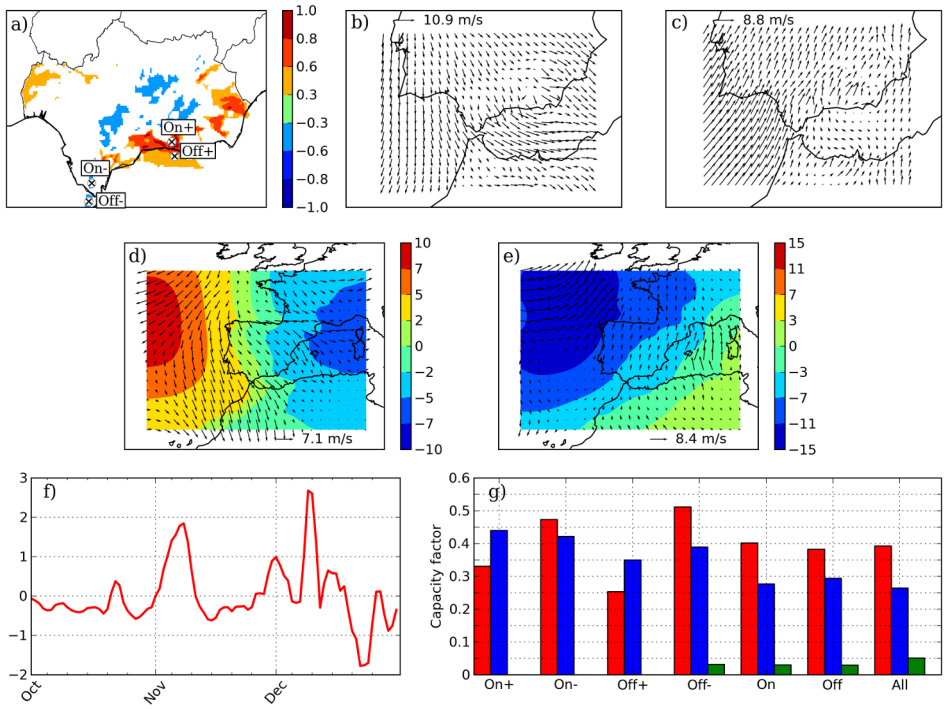


Figure 4.11. As in Fig. 4.4, but for autumn analysis

4.3.4 Autumn

The second mode of the Autumn PCA accounted for 9% of the variance. The corresponding loading factor pattern is represented in Fig. 4.11a. The pattern closely resembles that of the third mode of the spring PCA (Fig. 4.8a), but the loadings have opposite sign. A clear balancing is observed between the region centre and the offshore area west of the Strait of Gibraltar (areas of negative loading), and the Mediterranean coast (onshore and offshore) and eastern part of the region (areas of positive loadings). The corresponding PC series (Fig. 4.11f), as in previous cases, shows synoptic variability, with some strong anomalies in the middle of the series. Figs. 4.11a to 4.11e closely resemble the Figs. corresponding to the third spring mode (Figs. 4.8b to 4.8e). Therefore, the balancing pattern associated with this second mode of the autumn PCA seems to be caused by the same atmospheric circulations associated with the balancing pattern of the third mode of the spring PCA.

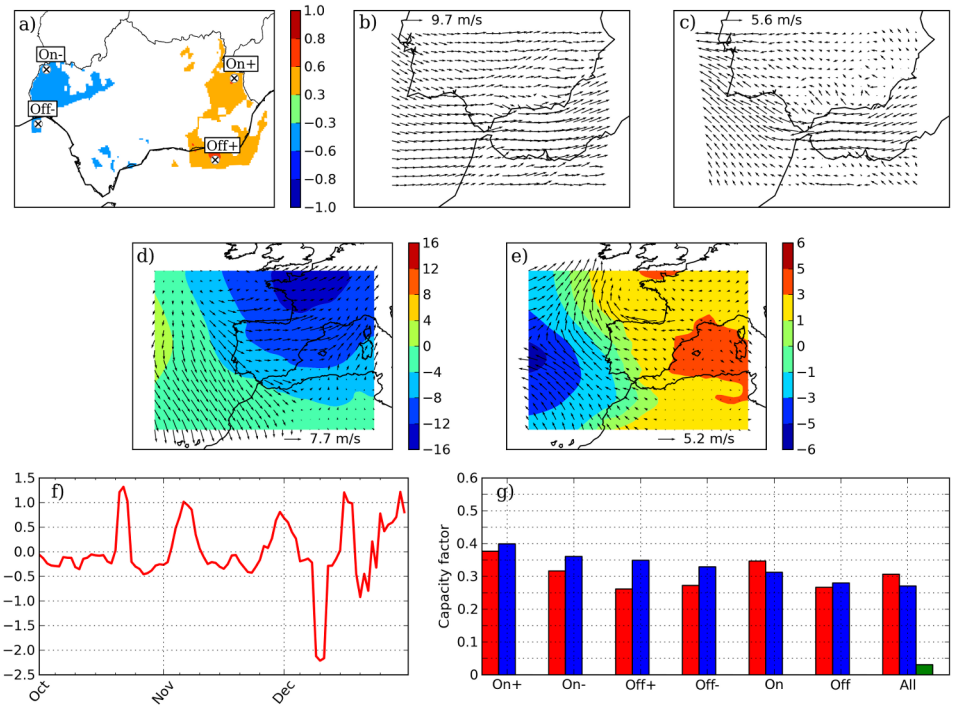


Figure 4.12. As in Fig. 4.5, but for autumn analysis

Fig. 4.11g shows a high capacity factor for the On- (0.47) and Off- (0.51) locations. The Off+ value is modest by comparison (0.27). Note the relatively low standard deviation of the Off- location. As in the previous cases, interconnection greatly reduces the standard deviation, to 0.27 when all locations are connected, with a 0.4 capacity factor. Unlike all previous cases, however, the Off- location alone, without any connection to other locations, does provide firm capacity (3%). Connection of only onshore wind farms provides 3%, whereas connection of offshore locations gives 4%. Finally, by connecting all selected sites, firm capacity reaches 5%.

The third mode of the autumn PCA accounted for 8% of the variance. The corresponding loading factor map (Fig. 4.12a) shows a weak dipolar pattern. Positive loadings are observed in the far east, including offshore areas in the Mediterranean, while negative loads are evident in the far west (including offshore areas). High positive values in the PC appear to be caused by the interaction of strong regional northwesterly wind anomalies, caused by a low SLP centre northeast of the IP, with topography in the

eastern area (Cazorla mountains) (Figs. 4.12b and 4.12d). Note that the northwest flow becomes southwesterly east of the Mediterranean coast (where offshore positive loads are situated). Wind speed is also high in the west, but anomalies are negative, leading to the negative loads seen in Fig. 4.12a. High negative anomalies in the PC seem to be associated with southeast flow in the region (Fig. 4.12e), generated by a low SLP centre over the Azores. These southeasterlies are enhanced over the Grazalema mountains and west of the Sierra Morena mountains (where negative loads are seen in Fig. 4.12a). At the same time, relatively weak easterlies are observed in the eastern area (where positive loads are seen in Fig. 4.12a).

Fig. 4.12g shows a relatively low capacity factor and relatively high standard deviation with this third autumn mode. Capacity factors ranged from 0.26 (Off+) to 0.38 (On+), and standard deviations from 0.32 (Off-) to 0.4 (On+). Similar to prior cases, connection of the various locations lowers standard deviation substantially. Firm capacity is only obtained for connection of all locations (3%).

Finally, Fig. 4.6d shows the capacity factor, standard deviation and firm capacity upon interconnection of all locations mapped in Figs. 4.11a and 4.12a. Remarkable improvement is achieved, especially for firm capacity (the maximum improvement of all cases). Firm capacity increases from 5% (second mode) and 3% (third mode) to 10%. For this case, capacity credit is 0.36 and standard deviation drops to 0.24.

4.3.5 Annual period

The loading factor map of the second mode of the annual PCA (accounting for 10% of total variance) is presented in Fig. 4.13a. This map clearly resembles the balancing pattern of the second mode of the winter analysis (Fig. 4.4a), that is, a dipolar mode with positive loads (0.3 to 0.8) in the east (including an offshore area), and negative loads (-0.6 to -0.8) in the southwest (Strait of Gibraltar and Grazalema areas, including offshore). This map also shares some major characteristics of the second spring mode (Fig. 4.7a), and autumn second and third modes (Figs. 4.11a 4.12a). The PC series (Fig. 4.13f) shows large variability from November through March. As expected, Figs. 4.13b to 4.13e closely resemble their counterparts in Fig. 4.4. Therefore, the same conclusion

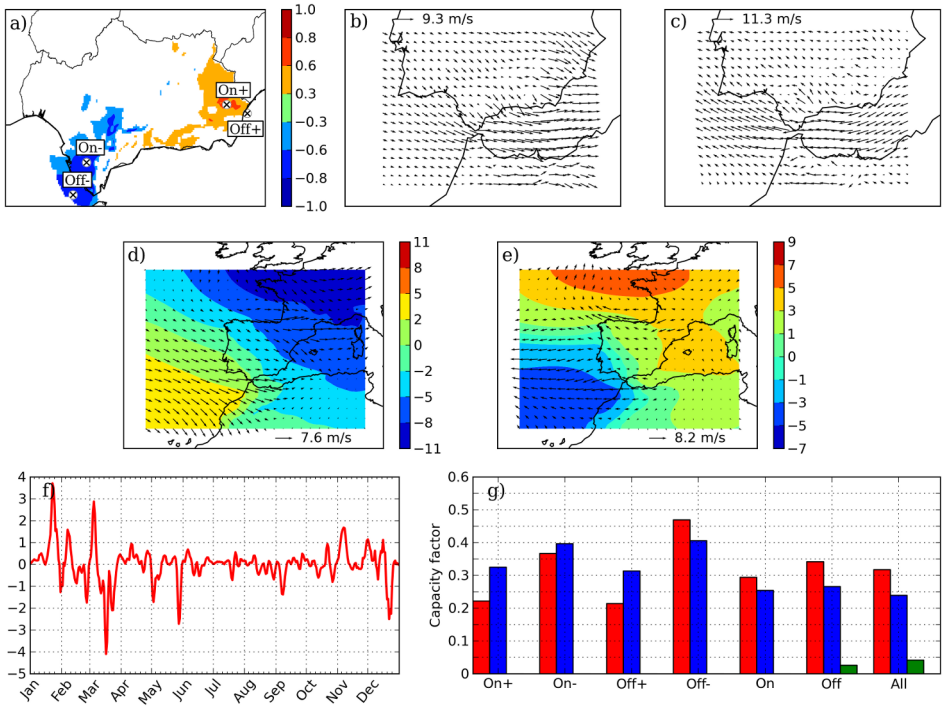


Figure 4.13. As in Fig. 4.4, but for annual analysis. In this case, composite maps were obtained based on 30 highest positive anomalies of corresponding PC series.

for the second mode of the winter analysis is reached for this second mode of the annual analysis. That is, there is annual spatial balancing between the wind energy resource in the eastern and Strait of Gibraltar areas, caused by the interaction of mesoscale zonal flow and regional topography. There is a high capacity factor for the Off- (0.47) and On- (0.38) locations (Fig. 4.13g). Connection of the offshore locations produces a capacity factor of 0.34, with a notable reduction of standard deviation (0.26) and a relatively low firm capacity (2%). Connection of onshore locations does not provide firm capacity. Finally, by connecting all locations, a 0.31 capacity factor is obtained, with a further reduction of standard deviation (0.23). Firm capacity increases to 3%.

The third mode for the annual PCA accounted for 8% of total variance. The loading factor map (Fig. 4.14a) clearly resembles the balancing pattern of the third mode of the winter analysis (Fig. 4.5a). Therefore, and given the results of the second mode, the annual analysis is clearly conditioned by the winter results. This is expected from the

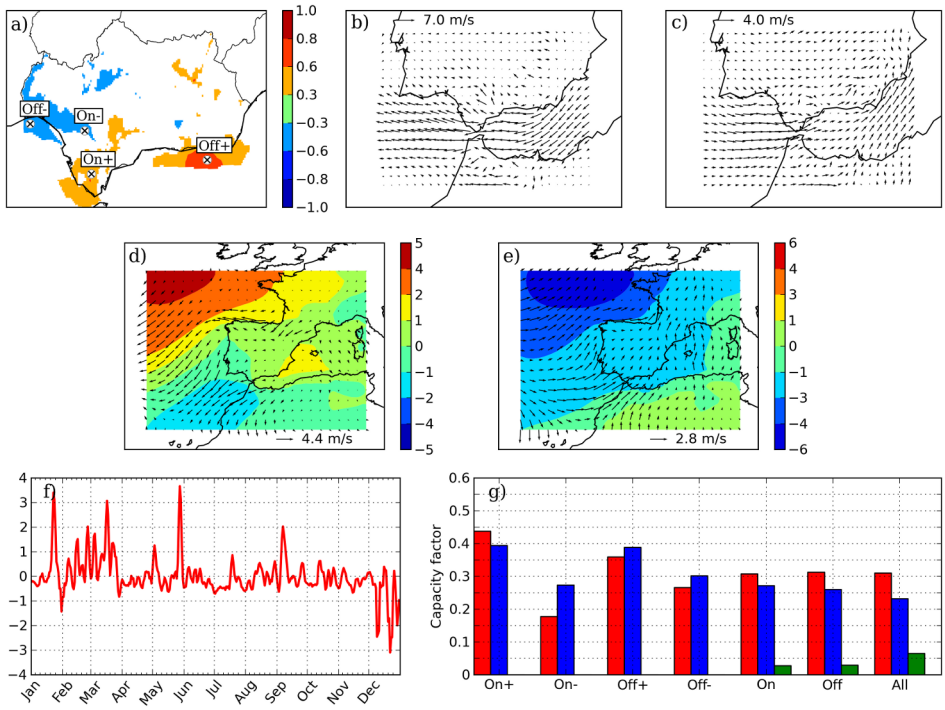


Figure 4.14. As in Fig. 4.5, but for annual analysis. In this case, composite maps were obtained based on 30 highest positive anomalies of corresponding PC series.

stronger atmospheric circulation over the region during winter. Positive loads (0.3 and 0.8) are found in the south (Strait of Gibraltar, Grazalema and Mediterranean offshore areas) and negative loads (between -0.3 and -0.6) in the west, including offshore. The map of Fig. 4.14a shares some key characteristics with the maps for the third spring mode (Fig. 4.8a), and second summer (Fig. 4.9a) and autumn modes (Fig. 4.11a). The PC series (Fig. 4.14f) shows higher variability from April to September compared to that shown in Fig. 4.13f.

Figs. 4.14b to 4.14e closely resemble their counterparts in Fig. 4.5. Therefore, the same conclusion for the third winter mode, regarding the atmospheric circulation involved in the balancing seen in Fig. 4.5a, applies for the balancing revealed here (in Fig. 4.14a). Fig. 4.14g shows a relatively high capacity factor for the On+ (0.43) and Off+ (0.39) locations. Connection of onshore locations results in a capacity factor of 0.3, standard deviation of 0.27, and firm capacity 2%. Very similar values are obtained by

interconnecting offshore locations. When all locations are connected, a capacity factor of 0.30 is achieved, along with a standard deviation of 0.23. Firm capacity increases significantly, to 6

Fig. 4.6e shows the capacity factor, standard deviation and firm capacity resulting from interconnecting all locations in Fig. 4.13a and Fig. 4.14a. Slight improvement is accomplished for standard deviation (down to 0.22) and firm capacity (up to 7%).

Finally, Fig. 4.6f shows the capacity factor, standard deviation and firm capacity values resulting from interconnecting all the locations resulting from the four seasonal analysis. That is, all the locations highlighted in Figs. 4.4, 4.5, 4.7, 4.8, 4.9, 4.10, 4.11 and 4.12. Values were computed year around. Compared to the annual analysis (Fig. 4.6e), a slight improvement is obtained for the standard deviation (down 0.20) and capacity credit (up to 0.33) and firm capacity (up 9%). However, note that results showed in Fig. 4.6e were obtained based on the interconnection of 8 locations (4 for each annual mode), while results in Fig. 4.6f correspond to the interconnection of 32 locations.

4.4 Summary and conclusions

In this work, we have proposed and evaluated a method for analyzing the potential contribution of wind energy resources to stable (baseload) power over a region. The method consists of two steps. In the first, spatial variability of the wind energy resource is analyzed based on principal component analysis (PCA). This method facilitates recognition of spatial balancing of this energy resource, that is, of areas within the region where wind power varies out of phase (negative spatial correlation). In the second step, PCA results are used to assess optimal locations (onshore and offshore) of wind farms in the region, for provision of stable (baseload) power, i.e., firm capacity. We did not attempt an analysis of the ability to furnish capacity credit.

The methodology was tested in the region of Andalusia (Spain), in the southern Iberian Peninsula. Although relatively small (87000 km^2), this region is characterized by varied topographic, geographic and weather/climate conditions. These conditions led us to

expect considerable spatial variability in wind speed and, consequently, spatial balancing of the wind energy resource. Our first step was obtain wind speed estimates from the Weather Research and Forecasting (WRF) mesoscale model. The speeds at 80 meters above ground level, at 3 km spatial resolution and one-hour temporal resolution, were estimated throughout the year 2009 over the entire region, which includes offshore areas up to 20 km from the coast. Then, the PCA was carried out independently for each season and the annual period. From the PCA, various balancing patterns were identified and described in terms of associated mesoscale atmospheric circulations. For each balancing pattern, four locations (two onshore and two offshore) were selected for potentially less variable combined wind power output (balanced). At each location, the potential power generation of a wind turbine was estimated. We evaluated a Vestas-V90 (2 MW nominal power) for the onshore locations, and a Vestas-V90 (3 MW nominal power) for the offshore sites. Finally, the ability of these wind turbines to provide stable power was assessed. To this end, means and standard deviations of the hourly capacity factor over the study period were computed, for both standalone and connected wind turbines. In addition, we computed the firm capacity, which is the fraction of installed wind capacity that is online with the same probability as that of a conventional thermal power plant (assumed to be 87.5%). Analogously, this firm capacity was computed for both individual and connected wind turbines, and expressed as a percentage of the installed nominal power.

First of all, the results showed the existence of valuable spatial balancing of wind energy resources over the study region, but with marked seasonality. The most important spatial balancing pattern was found between resources in the east and near the Strait of Gibraltar. This pattern was most pronounced in the annual and winter analyses, but was also evident in the other seasons. The second most important spatial balancing pattern was between the resource in the south, mainly on Mediterranean coast, and in the western area. This pattern was second in importance within the annual and winter analyses, but was also apparent in the other seasons. Both spatial balancing patterns were discovered to result from the interaction of mesoscale zonal flow with topographic features in the region.

Second, the results show that siting of wind farms across the region can be optimized by taking advantage of the aforementioned spatial balancing patterns. Such siting can substantially reduce wind power output fluctuations and, in some cases, produce firm

capacity, thereby contributing to baseload power. Most importantly, it was observed that the standard deviation decreased substantially when the number of connected sites was increased. These results are in accord with other works (Archer and Jacobson, 2007) confirming that site aggregation smoothes fluctuations. The reduction was highly dependent on season and which sites were interconnected, but an overall standard deviation decrease of about one third resulted with interconnection of both offshore and onshore sites. This reduction has important consequences for wind energy grid integration. First, other generators within the power system can take advantage of this smoother fluctuation to compensate deviations, allowing time to ramp up or down. Second, since standard deviation is a measure of the reserves necessary for wind energy grid integration, interconnection appears to significantly diminish these necessities. Finally, it was found in all analyzed periods that the interconnection of wind farms creates firm capacity. Again, values were highly dependent on the season and interconnected sites. Higher values were found for winter (11%) and lowest for summer (8%). During autumn, one of the selected offshore locations alone, without connection, provided a 3% firm capacity value.

The evaluated procedure can be easily applied to areas of arbitrary size, for optimizing grid power output. The method facilitates planning of the location of future wind farms within a region, so that total electricity production will fluctuate less. This may result in greater use of wind energy as reliable, baseload electric power. Currently, renewable projects are developed in locations with either maximum wind or sun. In our view, locating future projects should also consider the power supply fluctuation of each renewable. To inform this endeavour, we will augment the present analysis of meteorological balancing with an investigation of load demand. We plan to extend this work by increasing the analysis period, to test the stability of its results against the interannual climate variability in the study region.

CHAPTER 5

ANALYSIS OF SPATIO-TEMPORAL BALANCING BETWEEN WIND AND SOLAR ENERGY RESOURCES IN THE SOUTHERN IBERIAN PENINSULA

Santos-Alamillos F.J., D. Pozo-Vázquez, J.A. Ruiz-Arias, V. Lara-Fanego, and J. Tovar-Pescador. 2011. *Analysis of the spatio-temporal balancing between wind and solar energy resources in the southern Iberian Peninsula.* Journal of applied meteorology and climatology. In press.

5.1 Introduction

It is expected that worldwide primary energy demand will increase by 45%, and demand for electricity will increase by 80% between 2006 and 2030 (IEA, 2008). Consequently, without decisive action, energy-related greenhouse gas (GHG) emissions will more than double by 2050, and increased oil demand will intensify concerns over the security of supply. There are different paths toward stabilizing GHG concentrations, but a key issue in all of them is the replacement of fossil fuels by renewable energy sources. In this scenario, solar and wind electricity will play a key role. There are two main solar electricity technologies: the direct conversion of sunlight into electricity (photovoltaic, PV) and concentrating solar power (CSP). PV systems enable direct

conversion of sunlight into electricity through semiconductor devices, through their receipt of global horizontal irradiance (GHI). Today, PV provides 0.2% of total global electricity generation. Germany is the highest producing country in the world, with 17.3 *GW* installed capacity, followed by Spain with above 4 *GW* (about 4% of the installed capacity) (IEA, 2010b). While its use is small today, PV power has a particularly promising future, as it is projected to provide around 5% of global electricity consumption by 2030, increasing to 11% by 2050 (IEA, 2010b). CSP plants concentrate direct normal irradiance (DNI) to produce electricity based on the thermodynamic cycle. In addition, this technology has the advantage of being able to store the solar energy. Current penetration of this technology is low, about 1 *GW* capacity (mostly in Spain), but it is expected to contribute about 5% of annual global electricity production by 2050 (IEA, 2010a). Wind energy is the fastest growing renewable. In 2008, wind energy provided nearly 20% of electricity consumption in Denmark, more than 11% in Portugal and Spain, over 4% in the entire European Union (EU) and nearly 2% in the United States (IEA, 2009). By 2030, wind electricity is estimated to contribute about 9% of global electricity production, growing to 12% by 2050 (IEA, 2009). In the EU, regulations set a binding target of 20% of final energy consumption from renewable sources by 2020, along with a commitment to achieve at least a 20% reduction of greenhouse gases by 2020, compared to 1990 *(European Directives 2009/28/EC and 2009/29/EC)*. For Spain, to achieve this 20% final consumption goal, a substantial increase in the contributions of wind and solar energy to electricity production is necessary, from the current 15% to more than 45% (Gómez et al., 2010). Most of this increment will be located in the southern Iberian Peninsula (the study region here). Similar target increases in the share of these renewables are expected in other regions (Jacobson and Delucchi, 2011).

A major challenge will be the integration of these large-scale wind and solar yields into existing energy supply infrastructure. The challenge comes from the fluctuating nature of the solar and wind resources and their sensitivity to indeterminate weather patterns, as compared to the relatively stable and predictable sources of conventionally generated electricity. These characteristics make the cost of these renewables less competitive for power generation systems, because intermittent production creates negative externals that translate into grid integration costs. Short term wind and solar power forecasting is the primary requirement for efficient integration of renewables into power systems,

and for the reduction of grid integration costs (Saintcross et al., 2005; Kariniotakis, 2006; Lorenz et al., 2010; Lara-Fanego et al., 2011). Unexpected generation must be accommodated by system reserves. Therefore, as wind and solar power contributes a higher proportion of all generation, it will become more difficult for electrical system operators to effectively integrate such additional fluctuating power input. Thus, solutions that reduce power fluctuations are important if wind and solar electricity is to significantly displace other electricity technologies and will contribute reliable power similar to base load of conventional plants.

One of the most promising ways to reduce the power fluctuation from renewables is to take advantage of the spatial variability of these resources. Since the spatial correlation of wind and (to a lesser extent) solar energy resources diminishes with distance, interconnection of wind and solar power in a region will reduce fluctuations in total production. That is, a balancing effect can be achieved because of variable weather and climate conditions across a region. When this balancing is reached, the combined output of numerous, widely spaced renewable energy plants, based on the same or different resources (but mainly wind and solar), would be smoother than the output of individual power plants. In addition, such disperse generation is expected to reduce forecast error, thereby reducing grid integration cost.

Kahn (1979) and Landberg (1997) conducted the earliest analyses on smoothing or spatial balancing of wind energy resources. More recently, Archer and Jacobson (2007) studied a reduction of wind power production fluctuation through the interconnection of 19 wind farms in the Midwestern United States. They found a significant decline in the fluctuation of total production, compared to single wind farms. Consequently, they demonstrated that interconnected wind farms could supply reliable base load power. Cassola et al. (2008) proposed a method for optimal distribution of wind farms at ten locations in Corsica (France), to reduce temporal variability of total wind power production. They concluded that, based on this distribution, around 16% of yearly average wind power could be used as reliable base load. Kempton et al. (2010) analyzed the benefits of interconnecting offshore wind farms along the east coast of the United States, concluding that aggregation of production considerably reduces wind power fluctuation.

The benefits of solar energy aggregation have received less attention. In general, the spatial variability of the solar resource is significantly less than that of wind energy (Archer and Jacobson, 2003; Papadimas et al., 2010; Gueymard and Willcox, 2011; Widén, 2011). Nevertheless, clouds produce substantial spatial variability in solar energy production. Wiemken et al. (2001) analyzed spatial variability of PV production in Germany. Similarly, this spatial variability across the United States was addressed by Mills and Wiser (2010). They reported variability similar to that of wind energy.

Since solar and wind energy will contribute more to total electricity production in the future, it is worth analyzing the combined effect of the spatial distribution of these two sources. In our context, a balancing effect becomes effective when and where strong solar energy compensates weak wind energy, and vice versa. From a meteorological and climatological point of view, the balancing effect between solar and wind resources can be easily anticipated, given a large enough region. Over Europe, wind resources tend to be higher in winter and lower in summer, the opposite for solar resources. Balancing seems very dependent on the temporal and spatial scales considered (Pozo-Vázquez et al., 2011). Although some projects intended for very high renewable penetration are founded on the idea of balancing (Trieb et al., 2005; Tröster et al., 2011), there has been little research in this new field. Heide et al. (2010, 2011) analyzed the optimal mix between solar (PV) and wind energy in Europe within a scenario of very high penetration (100%) of these renewables. Their analyses were based on meteorological model estimates and were carried out on seasonal time scales, with a constraint of reducing storage needs as much as possible. They gave an optimal seasonal mix of 55% wind and 45% solar. Widén (2011) analyzed balancing between solar and wind resources in Sweden, based on meteorological station data. He reported a negative correlation between solar and wind resources (and thus balancing) on all time scales at a national scale; monthly totals provided the highest negative correlations (seasonal variability). He also showed a greater hour-to-hour variability when the solar share increases.

We explore here the use of Canonical Correlation Analysis (CCA) for assessing the spatiotemporal balancing between the solar and wind energy resources over a region. The CCA decomposes two sets of space-time dependent variables into pairs of spatial patterns (canonical modes), such that they are maximally correlated. Therefore, the CCA will eventually highlight the existence of balancing between solar and wind energy

resources, depending on the nature (sign and strength) of the canonical patterns. In this sense, the CCA finds the optimal distribution of wind farms and solar energy plants over a territory, to minimize the variability of total energy input into the power supply system. The methodology was tested in the southern half of the Iberian Peninsula, a region covering about 350000 km^2. The varied topographic and geographic conditions of the region lead to an anticipation of the existence of balancing effects between solar and wind energy resources. In addition, this region produces a substantial part of the wind energy (more than 40%) and solar energy (90%) in Spain (UNESA, 2010). We used daily-integrated wind and solar energy estimates from 2007, based on the Weather Research and Forecasting (WRF) mesoscale model (Skamarock et al., 2008), at a spatial resolution of 9 km. These studies were done seasonally and for the complete period. Atmospheric conditions associated with the balancing pattern were also examined.

This paper is organized as follows. Section 5.2 presents the study area and methodology, including the dynamical downscaling setup. Results are presented in section 5.3. Finally, a summary and some conclusions are presented in section 5.4.

5.2 Methods and study area

5.2.1 Study area

The study region (Fig. 5.1) corresponds roughly to the southern half of the Iberian Peninsula, covering about 350000 km^2. Henceforth, the word 'region' or 'regional' will refer to the entire study region, whereas 'parts,' 'areas' and geographic directions will refer to sub-regions within that larger region. The region is located in a transition zone from temperate to subtropical climates, bounded on the south by the Atlantic Ocean and Mediterranean Sea. Several areas within the region can be characterized by their dominant topographic features. The southwest, corresponding to western Andalusia and the south of Portugal, is an almost homogeneous area, open to the Atlantic Ocean. The central and northern parts have an intermediate topographic complexity. In particular, central Spain is a plateau with a mean elevation of about 700 m. Transition from this area to central Portugal is relatively smooth. Finally, complex topography dominates the

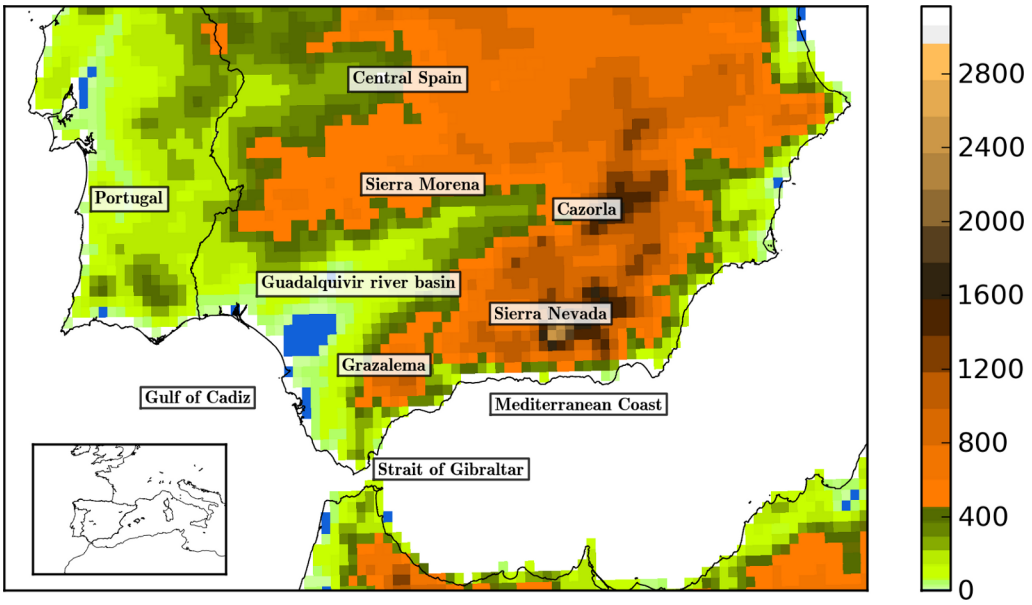


Figure 5.1. Location, topographic and geographic characteristics of the study region. Shaded areas indicate elevation based on a 9 km spatial resolution Digital Elevation Map, the same spatial resolution of the analyzed data. Scale at right indicates elevation in meters above sea level.

east and southeast parts of the region. This area contains several mountain ranges and includes the Sierra Nevada national park, with a maximum elevation of 3482 m (highest on the Iberian Peninsula). Since the region borders both the Mediterranean Sea (at the south) and the Atlantic (at the west), there are extensive coastal areas where local thermal contrasts strongly influence the wind energy resource.

The large-scale circulation over the region is mainly driven by a semi-permanent subtropical high pressure center over the Azores islands, which varies in location and intensity during the year. During winter, this high is situated at lower latitudes, allowing the Iberian Peninsula to be affected by zonal circulations from the west, while in summer it migrates northward, blocking the westerlies over most of the peninsula (Trigo et al., 2002, 2004). The Azores subtropical high is the southern part of the NAO (North Atlantic Oscillation) dipolar atmospheric variability pattern (Hurrel et al., 2003), which is linked to large-scale atmospheric dynamics and the modulation of the strength of the westerlies over the European region (Pozo-Vázquez et al., 2000; Castro-Díez et al., 2002; Gámiz-

Fortis et al., 2008).

Although the entire region is under the influence of the Azores subtropical high, the region experiences a wide range of climate conditions. This range is related to orography (Fig. 5.1) and numerous synoptic disturbances of Atlantic origin, which cause enormous spatial variability in precipitation and other climate variables (Trigo and DaCammara, 2000; Trigo et al., 2004). For example, the eastern part is less influenced by the Azores high, and more affected by the Mediterranean Sea. In fact, annual precipitation values across the region range from 300 mmyear-1 in the coastal semi-desert southeast to more than 2500 $mmyear^{-1}$ in the mountains near the strait of Gibraltar (Romero et al., 1998; Ramos-Calzado et al., 2008). Since mesoscale spatial variability of solar radiation is mainly related to cloudiness, this variability is relatively high in the region (Pozo-Vázquez et al., 2004; Alsamamra et al., 2009; Pozo-Vázquez et al., 2011).

Surface wind speed variability is associated not only with mesoscale circulations but also with other more localized factors. Many of these are related to topographic characteristics (elevation, aspect, slope, surface roughness, etc.), and others with thermal contrast near water bodies (Hutchinson et al., 1984; Weber and Furger, 2001; McVicar et al., 2008). The complex topography and the influence of the Atlantic Ocean and the Mediterranean Sea combine to produce marked spatial variability in regional wind speeds (Alsamamra et al., 2011). In particular, when winds associated with strong thermal contrast between the Mediterranean Sea and Atlantic Ocean are channeled and accelerated through the strait of Gibraltar, strong easterlies (known as Levante) are produced. In summary, the interaction of mesoscale circulations, topographic and geographic features generates substantial spatial variability in wind speed and solar radiation in the region, in spite of its relatively small size.

5.2.2 Mesoscale model configuration

The Weather Research and Forecasting (WRF) model v3.0 has been used in this work. The domain configuration is shown in Fig. 5.2. The outer domain has a spatial resolution of 27 km, covering the Iberian Peninsula and parts of northern Africa. The inner domain has a spatial resolution of 9 km and covers the southern Iberian Peninsula. Topography,

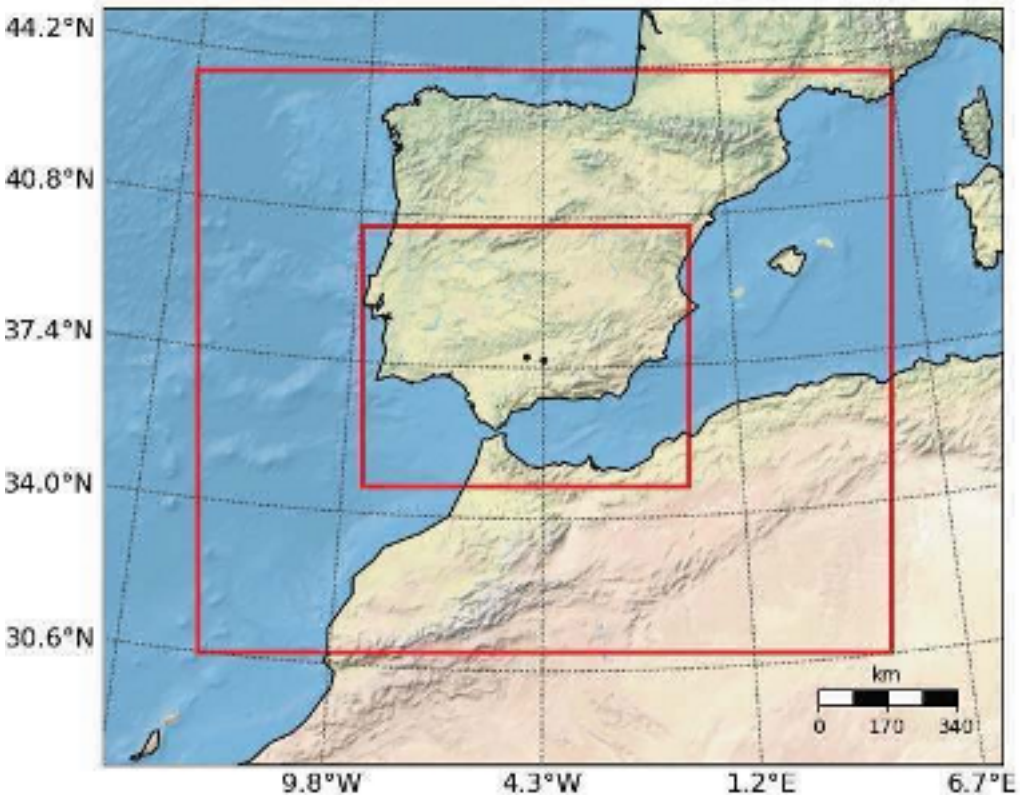


Figure 5.2. Spatial configuration of domains for the numerical simulation-two domains, two-way nested with 27 and 9 km horizontal resolutions. Data for the inner domain were analyzed. The dots are the centers of the two domains.

land use and land-water mask datasets were interpolated from USGS land-cover, with appropriate spatial resolution for each domain (5' and 2', respectively). A two-way interaction was used for both domains, with 27 vertical levels, seven of which are within the first 1000 m above the ground. The second level was used to obtain wind speed estimates and corresponding wind energy values. Since the height of this second level fluctuates with pressure, we have computed the mean and standard deviation over the study period and entire inner domain. The mean value was 28.96 m above ground level ($m.a.g.l$) with standard deviation 0.4 m. Therefore, this second level provides estimates of wind energy around 30 $m.a.g.l$.

Parameterization schemes for the WRF were selected based on several parameterization evaluation studies in the region (Fernández et al., 2007; Borge et al., 2008; Ruiz-Arias et al., 2008, 2012a; Argüeso et al., 2011). For the long-wave radiation, we selected the Rapid Radiation Transfer Model (RRTM) scheme (Mlawer et al., 1997). For the short-wave solar radiation, we used the Dudhia scheme (Dudhia, 1989). The Kain-Fritsch scheme (Kain and Fritsch , 1993) was used for cumulus, the Yonsei University Planetary Boundary Layer (YSU PBL) scheme (Hong et al., 2006) for the boundary layer and Thompson Graupel (Thompson et al., 2006) for the microphysics. Finally, the Noah land surface model (Chen and Dudhia 2001) was used. Finally, (Argüeso et al., 2011), using a set up similar to the one here, proved that the WRF model was able to correctly reproduce the climate of the study region.

Initial and boundary conditions were generated from Global Forecast System (GFS) model output, with spatial resolution 0.5°. In particular, the analysis provided by this system every 6 hours were used to upgrade the boundary conditions. Simulations were conducted for the year 2007. Following Hahmann et al. (2010), integration periods of eight days, with a spin-up of 24 hours, were used, and outputs were saved every hour. The balancing analysis computed daily-integrated wind and solar energy values based on WRF modeled solar radiation and wind speed, within the inner domain (9 km spatial resolution). Wind speed estimates at 30 $m.a.g.l.$ (second vertical level) at one hour intervals were used to estimate daily-integrated wind energy values based on:

$$E_{daily\ wind} = \sum_{i=1}^{24} \left(\frac{1}{2} \rho v^3 \right) \times 1h \tag{5.1}$$

Where v is the wind speed every hour and ρ is air density at sea level. Similarly, daily-integrated solar energy estimates were obtained based on hourly estimates of shortwave downward solar radiation (Global Horizontal Irradiation, GHI) at the surface:

$$E_{daily\ solar} = \sum_{i=1}^{24} GHI_i \times 1h \tag{5.2}$$

Raw daily solar and wind energy time series were normalized for each season, taking

January through March to be winter, April through June spring, July through September summer, and October to December autumn. This standardization ensures that all elements possess temporal stationarity and are weighted equally.

5.2.3 Balancing analysis methodology

Spatio-temporal balancing between solar and wind energy resources in the region was analyzed based on the CCA (Barnett and Preisendorfer, 1987; Bretherton et al., 1992; Von Storch and Zwiers, 2001). CCA is a multivariate statistical model that facilitates study of interrelationships among sets of multiple dependent variables and multiple independent variables. Whereas multiple regressions predict a single dependent variable from a set of multiple independent variables, CCA simultaneously predicts multiple dependent variables from multiple independent variables. Here, the dependent and independent sets of variables are the solar energy and wind energy fields in the study region. To this end, CCA explores the association between different composites of variables in the two sets. Particularly, CCA derives a set of weights for each set variables, so the resulting composite variables (pairs of canonical variables) are maximally correlated (canonical correlation). This results in the first canonical mode. The procedure can be repeated, attaining successive canonical modes derived from residual or leftover variance from earlier modes. That is, the second pair of canonical variables is derived so that they exhibit the maximum correlation, but are derived based on variance not accounted for by the first canonical mode. Since successive pairs of canonical variables are based on residual variance, each of the pairs of variables is orthogonal and independent of all other variables derived from the same set of data. The maximum number of canonical variables (and therefore canonical modes) that can be extracted from the sets of variables equals the number of variables in the smallest data set. The strength of relationship between each pairs of canonical variables is reflected by the canonical correlation. When squared, the canonical correlation represents the amount of variance in one canonical variable accounted for by the other canonical variable. This also may be called the amount of shared variance between the two canonical variables.

There are no generally accepted guidelines regarding suitable sizes for canonical correlations, and thusfor the number of canonical modes to analyze (Anderson et al.,

2011). Rather, the decision is usually based on the contribution of the findings to better understanding of the research problem under study. In this work, and as a first approach, the statistical significance of canonical correlations was analyzed based on the F statistic (Bartlett, 1941). Only canonical modes with canonical correlation statistically significant at the 0.05 level were retained for subsequent interpretation. In a second approach, only canonical modes with canonical correlations values above 0.4 were considered. This arbitrary selected and stringent value allows retention of only the most important balancing modes for further analysis. The rest of the canonical modes, with considerable lower canonical correlation, do not provide valuable information regarding the coupling of wind and solar resources in the region.

Homogeneous canonical loadings have been used as a basis for interpretation of the canonical modes. In particular, homogeneous canonical loadings are the simple linear correlation between the original observed variables in the field and their corresponding canonical variables. By mapping these correlations, the spatial pattern associated with the corresponding canonical mode can be analyzed. The canonical loading reflects the variance that the observed variable shares with the canonical variable, and can be interpreted as a factor loading in assessing the relative contribution of each variable to each canonical mode. The larger the coefficient, the more important it is in deriving the canonical mode.

The CCA eventually highlights the existence of balancing between solar and wind energy resources, depending on the nature (sign and strength) of canonical correlation and canonical loading patterns. For the purposes here, we look for canonical modes whose associated canonical patterns indicate areas in which solar and wind energy are meaningfully anti-correlated. The CCA was applied to the daily-integrated, seasonally standardized wind and solar energy fields. Data analysis was done for each season of the year and for the entire year. First, to avoid computational problems with the sample size, the daily data were pre-filtered using a Principal Component Analysis (PCA) (Barnett and Preisendorfer, 1987). This is a widely-used method to analyze spatiotemporal variability of an environmental variable. In particular, this method allows reduction of the initial dataset dimension into a few representative variables (modes). The new variables, called principal components (PCs) and often referred to as modes of variability, are obtained as linear combinations of the initial variables.

These combinations are obtained such that the new variables account for the maximum fraction of the variance contained in the original dataset. The number of modes retained in the PCA analysis is a compromise, between the need to retain as much as possible of the signal and the requirement of noise reduction. The number of retained modes was determined such that an increase by one would minimally change the canonical correlation results (Von Storch and Zwiers, 2001). In all analyzed cases (seasonal and annual data), five modes proved to be a good compromise. These five modes explained between 75% and 93% of solar energy variance, and between 70% and 80% of wind energy variance. Second, the CCA analysis was performed based on the retained modes. Next, the canonical modes were projected again into the original dataset based on the PCA, to represent their associated spatial patterns.

Finally, mesoscale atmospheric conditions associated with each canonical pattern were analyzed. To this end, we computed composite maps of daily-mean horizontal wind components at 30 $m.a.g.l$ and daily-mean solar radiation anomalies at the surface, associated with the 15 (30 for the annual analysis) maximum and minimum values of wind energy canonical time series. Data for these composites were taken from the WRF integration outer domain (Fig. 5.2), which covers the entire Iberian Peninsula and northwest Africa at a spatial resolution of 27 km.

5.3 Results

In this section, the results of the CCA analyses are presented. These analyses were done for each season of the year and for the entire year, independently. Only the canonical modes that produced a canonical correlation higher than 0.4, were analyzed. To understand the nature and strength of the coupled wind-solar energy modes, a brief description of the associated mesoscale atmospheric conditions is presented for each mode. Table 5.1 summarizes the principal results of the CCA analyses. The canonical correlation and the associated explained variances are presented, for the selected modes and for each period.

Study Period	Mode	Var. Solar Energy (%)	Var. Wind Energy (%)	Can. Correlation
Winter	Mode 1	38.1	31.0	0.55
Winter	Mode 2	26.3	7.4	0.51
Spring	Mode 1	6.0	7.0	0.61
Spring	Mode 2	9.3	16.0	0.52
Summer	Mode 1	26.5	17.0	0.73
Summer	Mode 2	12.8	8.6	0.64
Summer	Mode 3	12.2	10.3	0.52
Autumn	Mode 1	23.2	25.7	0.51
Autumn	Mode 2	6.6	23.2	0.45
Annual	Mode 1	42.2	6.5	0.46
Annual	Mode 2	8.3	13.3	0.40

Table 5.1. Summary of results of the Canonical Correlation Analysis (CCA). In particular, the table shows, for the seasonal and annual analysis, the solar and wind energy field explained variance associated which each canonical mode. The last column shows canonical correlation values. Only canonical modes with a canonical correlation higher than 0.4 were analyzed.

5.3.1 Winter

Only two modes with a canonical correlation higher than 0.4 were found for winter (Table 5.1). The time series of the leading mode (Fig. 5.3) have a canonical correlation of 0.55. Both the solar and wind energy canonical time series exhibit a positive trend, ending in high positive anomalies during March (Fig. 5.3c). Also remarkable is that solar energy exhibits higher variability than wind energy. The leading mode accounts for around 38% of the variance of the solar energy and 31% of the wind energy fields. Their respective spatial patterns (Fig. 5.3a and 5.3b) show a coupling between the solar energy in the west (especially in Portugal, where correlation reaches 0.8) and the wind energy in the Gulf of Cádiz and western strait of Gibraltar area (where correlations values approach 0.7). This coupling is associated with a marked meridional circulation over the western Iberian Peninsula. Positive wind and solar energy anomalies (Fig. 5.3d) are found in central and southern Portugal, which are associated with northerly winds (usually cold and dry during winter). The unique topographic features in the

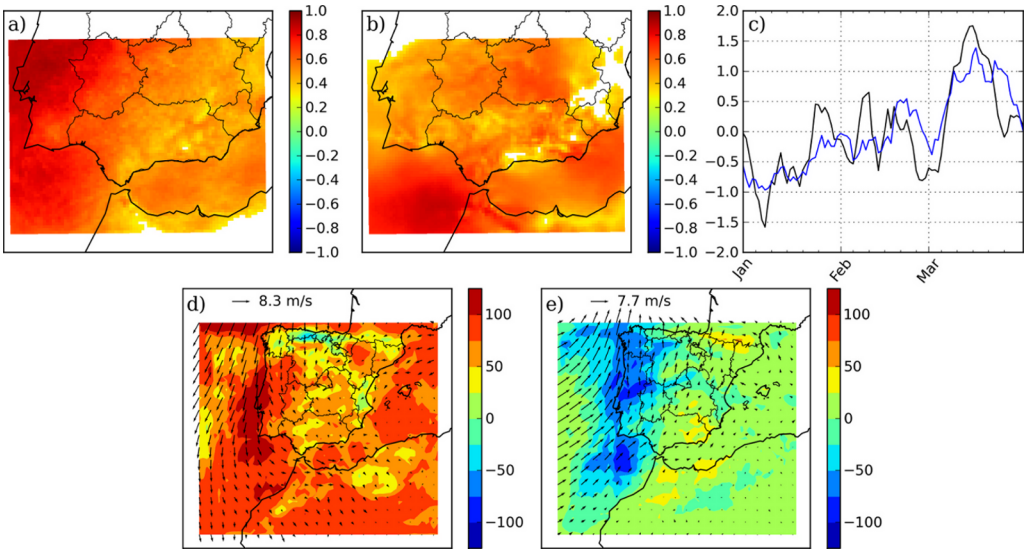


Figure 5.3. First mode of the CCA resulting from the winter analysis. a) Homogeneous correlation (canonical loadings) map for the solar energy and b) for the wind energy. c) Canonical time series, filtered with a 3-day moving average filter. Solid black and dotted grey lines are canonical series for solar and wind energy, respectively. d) Composite of daily-mean horizontal wind components at 30 m AGL, and solar radiation anomaly values at the surface corresponding to the 15 highest positive anomalies of the wind energy canonical time series. e) As in d), but for the lowest 15 negative values. Solar radiation data units are Wm^{-2} and scale represent the range of the anomalies. Wind speeds are scaled according to the reference at top of d) and e), which indicates maximum wind speed in ms^{-1}. Composites were obtained based on the WRF model estimates in the outer domain (9 km), which has a spatial resolution of 27 km.

strait of Gibraltar area turn this north flow into strong westerly winds (called Poniente), generating positive wind energy anomalies in this area. In contrast, negative wind and solar energy anomalies (Fig. 5.3e) are associated with southwesterly flows. This circulation usually brings relatively warm and humid air into the west, fostering more cloudiness and resultant negative solar energy anomalies. In addition, winds over the strait of Gibraltar area are weaker than normal (respect to the normalization period, here 3 months), causing negative wind energy anomalies. Note that this leading mode of winter CCA analysis does not show areas where balancing between solar and wind energy resources occurs.

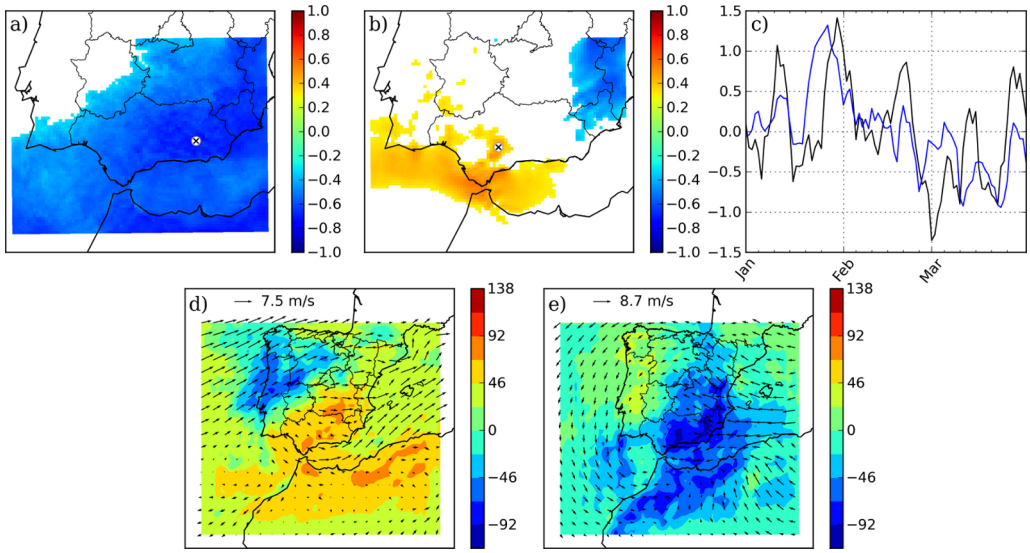


Figure 5.4. As in fig. 5.3, but for the second mode of the CCA resulting from the winter analysis. The two crosses indicate the grids selected for the balancing time series analysis.

The time series of the second mode (Fig. 5.4) have a canonical correlation of 0.51. Both the wind and solar time series exhibit considerable variability. A spectral analysis reveals that this variability is mainly associated with a 3-6 day range, and therefore related to synoptic activity. This was further confirmed by analysis of the synoptic maps associated with this mode. This second mode accounts for around 26% of the solar energy field variability and around 8% of the wind energy field variability. Their spatial patterns (Fig. 5.4a and 5.4b) are much more interesting from the balancing point of view. On the one hand, this second mode presents negative loads on the solar energy field in almost the entire region, particularly over Andalusia, were values reach -0.6. On the other hand, positive loads are found in the wind energy field near the strait of Gibraltar, with values up to 0.5. Therefore, this second mode accounts for a balancing effect between the wind energy in the latter area and solar energy in most of the region. The mesoscale atmospheric circulations associated with this balancing are presented in Fig. 5.4d and 5.4e. Notably, positive solar and negative wind energy anomalies are associated with relatively high pressure over the Gulf of Cádiz, which brings stable conditions to the study area (positive solar energy anomalies) and weaker westerly winds over the strait

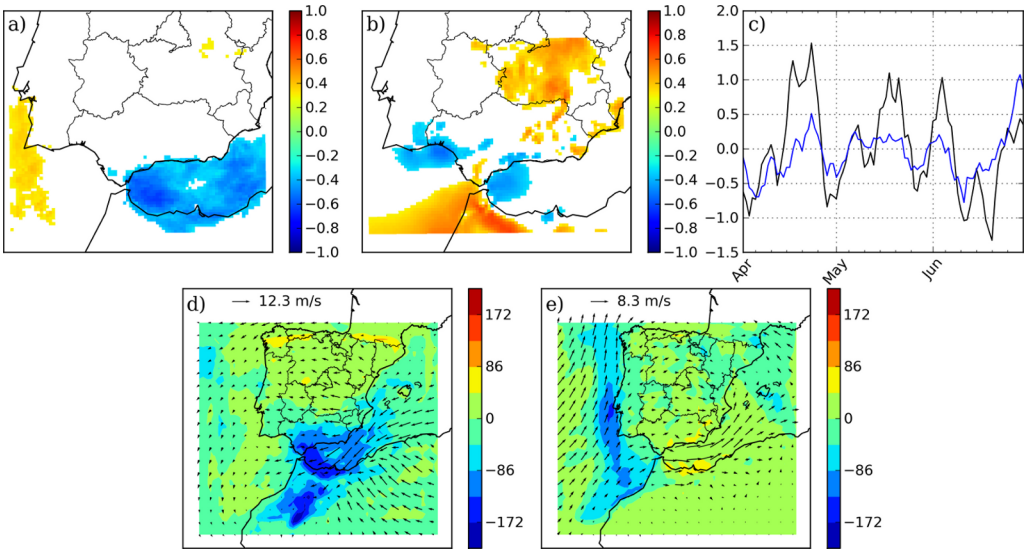


Figure 5.5. As in Fig. 5.3, but for the first mode of the CCA resulting from the spring analysis.

of Gibraltar area (negative wind energy anomalies). Alternatively, negative solar and positive wind energy anomalies are associated with low pressure to the west of this area. In the latter scenario, frontal activity brings cloudiness to most of the region, and in the former scenario, strong easterly winds (Levante) to the strait of Gibraltar area.

5.3.2 Spring

During spring, two canonical modes were selected (Table 5.1) for further analysis. The time series of the leading mode (Fig. 5.5c) have a canonical correlation of 0.61. Both series exhibit clear variations with monthly and synoptic time scale variability. This leading mode of the spring CCA analysis accounts for only about 6-7% of the variability of the solar and wind energy fields. Nevertheless, this mode is remarkable because it locally explains more than 35% of the variance (correlations higher than 0.6), and because the spatial pattern indicates a balancing effect. For the solar energy field (Fig. 5.5a), negative correlations (-0.6) are observed in the eastern strait of Gibraltar area. For wind energy (Fig. 5.5b), relatively high positive correlations are observed in the central

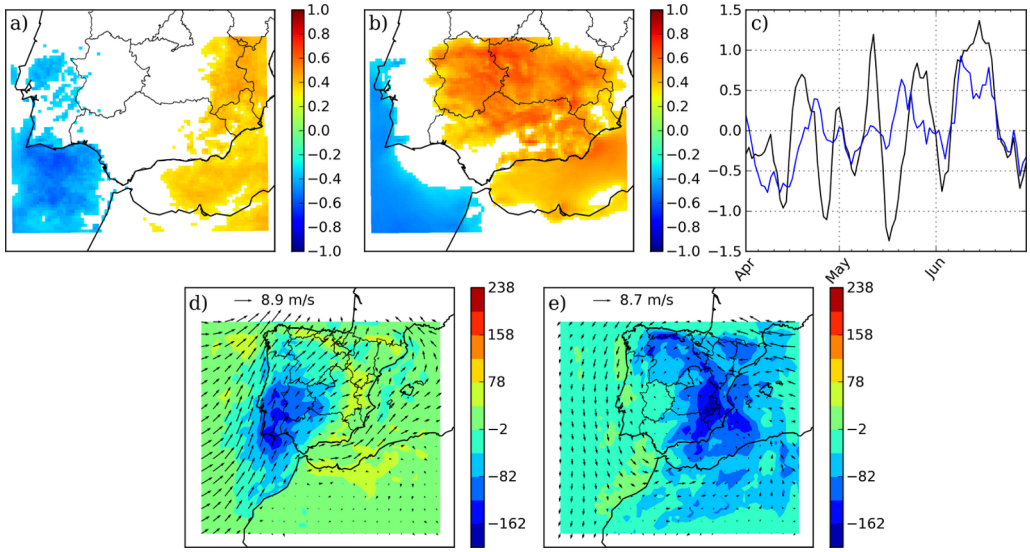


Figure 5.6. As in Fig. 5.3, but for the first mode of the CCA resulting from the spring analysis.

strait area and regional mountain ranges (correlations above 0.5). Therefore, the leading mode of the spring analysis accounts for a weak (but statistically significant) balancing effect between solar and wind energy in the region. Positive solar energy anomalies over southern Portugal (and negative anomalies in eastern strait of Gibraltar, an area of interest here) and positive wind energy anomalies over the central strait area are associated with an easterly flow over the entire southern Iberian Peninsula, intensified near the strait (Fig. 5.5d). This easterly flow brings cloudy conditions to the coastal areas of the southern part of the region, reducing solar energy availability. Alternatively, negative solar energy anomalies over southern Portugal (and positive anomalies at the eastern strait of Gibraltar), along with negative wind energy anomalies over the central strait area, are associated with westerly winds over the strait area (Fig. 5.5e). These winds have weaker than average speeds over this area, decreasing wind energy.

The time series of the second mode (Fig 5.6) have a canonical correlation of 0.52, and exhibit high variability at synoptic time scales (Fig. 5.6c). This second mode of the spring CCA analysis accounts for around 9% of the variability of solar energy and 16% of wind energy. The corresponding spatial patterns (Fig. 5.6a and 5.6b) indicate

a weak (but statistically significant) balancing between solar energy in the western part of the region and wind energy in its central and eastern parts. This balancing is relatively weak, because correlation between the canonical mode and the solar field (homogeneous correlation) is relatively low. Fig. 5.6d and 5.6e present the mesoscale atmospheric conditions associated with this balancing. Positive solar energy anomalies over the eastern part of the region (and therefore negative ones over the western part, an area of interest here) and positive wind energy anomalies over the central and eastern parts (Fig. 5.6d) are associated with a southerly flow over the southeastern peninsula. This circulation usually advects warm and humid air and therefore generates more cloudiness, resulting in negative solar energy anomalies across this area. Wind speeds are intensified (mainly by topographic features) in some parts of the central and eastern region, producing positive wind energy anomalies. In contrast, negative solar energy anomalies in the east (and therefore positive ones in the west), along with negative wind energy anomalies (Fig. 5.6e), are caused by a low pressure center covering almost the entire peninsula. This low pressure center brings north winds (usually cold and dry) to the eastern part of the region, producing positive solar energy anomalies there. This low causes weak winds (negative wind energy anomalies) in the central and eastern parts of the region, however.

5.3.3 Summer

For summer, three canonical modes were selected (Fig. 5.1). The time series of the leading mode (Fig. 5.7c) have a canonical correlation of 0.73, and exhibit a decrease from July to the beginning of September. In addition, considerable variability is observed at synoptic time scales. This leading mode of the summer CCA analysis accounts for around 26% of the solar field variability, and 17% of the wind energy field. The corresponding spatial patterns (Fig. 5.7a and 5.7b) show a positive coupling between the solar energy in the entire region and the wind energy in its eastern part. No balancing is observed. This mode resembles the leading mode of the winter analysis (Fig. 5.3). Mesoscale atmospheric conditions (Fig. 5.7d and 5.7e) are similar to those of Fig. 5.3. The coupling seems to be associated with meridional circulations in the eastern Iberian Peninsula. Positive (negative) wind and solar energy anomalies are associated with northerly (southerly) winds over the east and south of the peninsula.

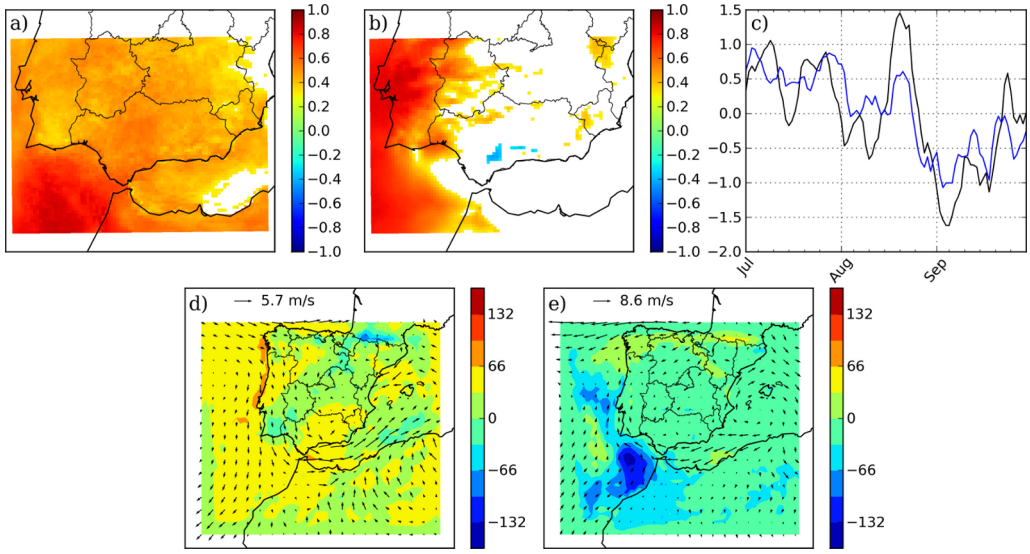


Figure 5.7. As in Fig. 5.3, but for the first mode of the CCA resulting from the summer analysis.

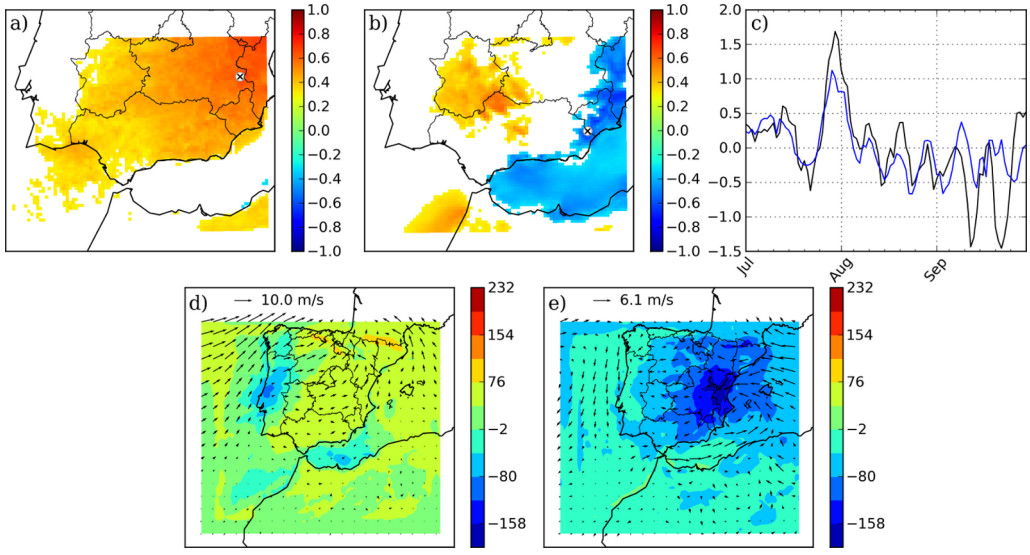


Figure 5.8. As in Fig. 5.3, but for the second mode of the CCA resulting from the summer analysis. The two crosses indicate the grids selected for the balancing time series analysis.

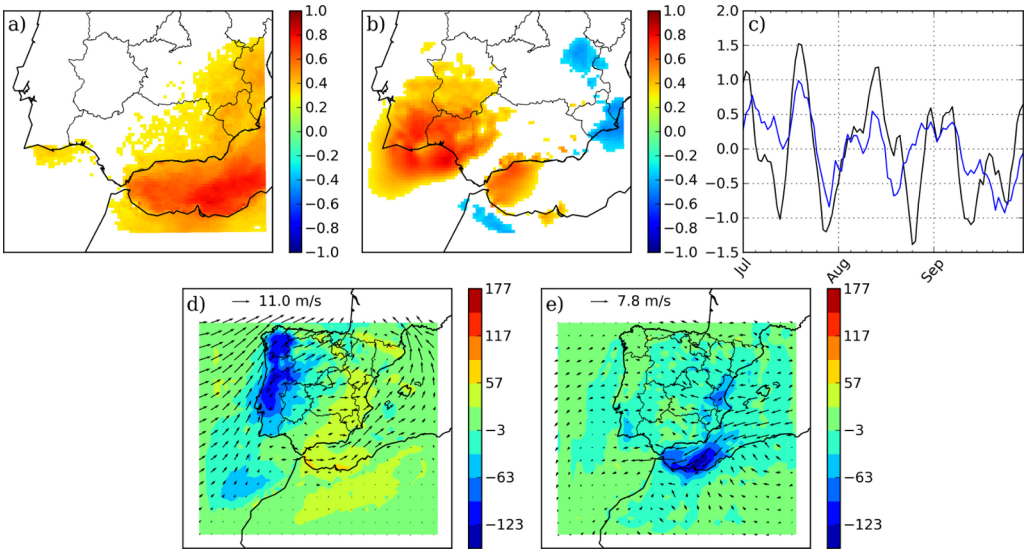


Figure 5.9. As in Fig. 5.3, but for the third mode of the CCA resulting from the summer analysis.

The times series of the second summer mode (Fig. 5.8c) have a canonical correlation of 0.64, and have considerable temporal variability at synoptic time scales. This second mode accounts for around 13% of the solar field variability, and 9% for wind energy. The corresponding spatial patterns (Fig. 5.8a and 5.8b) indicate balancing between the solar energy over nearly the entire region and the wind energy in the south and east. Relatively high and positive correlations are observed for solar energy over nearly the entire study region, within highest values (around 0.7) in the east. Negative correlations (around -0.7) are observed in the wind energy field along coastal areas to the south and east. On one hand, positive solar radiation anomalies in the entire region and negative wind energy anomalies in the east and south are associated with westerly winds over the central peninsula, and weak southwesterly winds over the south and east (Fig. 5.8d). On the other hand, negative solar radiation anomalies and positive wind anomalies in the east and south are associated with a low pressure center in the eastern peninsula (Fig. 5.8e). This center strengthens the wind over the eastern and southern peninsula, giving rise to those positive wind anomalies, but its associated frontal activity brings cloudiness to central and eastern areas, reducing solar energy availability.

The third mode (Fig 5.9) gives a canonical correlation of 0.52. Both wind and solar energy time series (Fig. 5.9c) show considerable variability at both monthly and synoptic time scales. This mode accounts for around 12% of the variability of solar energy, and about 10% of wind energy. The corresponding spatial patterns resemble those of the springtime leading mode (Fig 5.5). In particular, positive correlations are observed in the solar energy pattern of coastal areas of the southern and eastern region, although values are relatively weak (about 0.4). For the wind energy pattern, positive correlations are found in southwestern areas and to the east of the strait of Gibraltar. Negative loads are observed in northeastern areas. Mesoscale atmospheric conditions are similar to those observed for the spring leading mode (Fig. 5.4). On one hand, positive solar radiation and wind anomalies in the southeast are associated with southwesterly and westerly winds (Fig. 5.9d). On the other hand, negative solar radiation and wind anomalies are associated with easterly flow over the entire southern peninsula, intensified near the strait of Gibraltar (Fig. 5.9e). This easterly flow brings cloudy skies to the eastern part of the region, reducing solar energy availability.

5.3.4 Autumn

The autumn analysis showed probably the most interesting results for the balancing between solar and wind energy resources, region-wide. The first two canonical modes had canonical correlation values over 0.4 (Table 5.1), and were analyzed in more depth. The time series of the leading mode (Fig. 5.10c) had a canonical correlation of 0.51. A spectral analysis of these time series revealed that this variability is mainly associated with synoptic scale activity. Moreover, there is a noticeable decrease during October and November. This leading mode accounts for around 2% of the solar energy field variability and for about 25% of the wind energy field variability. The spatial patterns show a balancing effect between the solar and wind energy resources almost region-wide. Relatively high positive correlations are observed for the solar energy field across the entire region (Fig. 5.10a), reaching 0.8 in the west, near the Gulf of Cádiz. Large negative correlations are observed for the wind energy field across the entire region, except the very southeast. Minimum values (-0.8) are again observed in the western area, near the Gulf of Cádiz. Therefore, the leading mode of the autumn CCA analysis indicates a general balancing between solar and wind energy, nearly extending over the

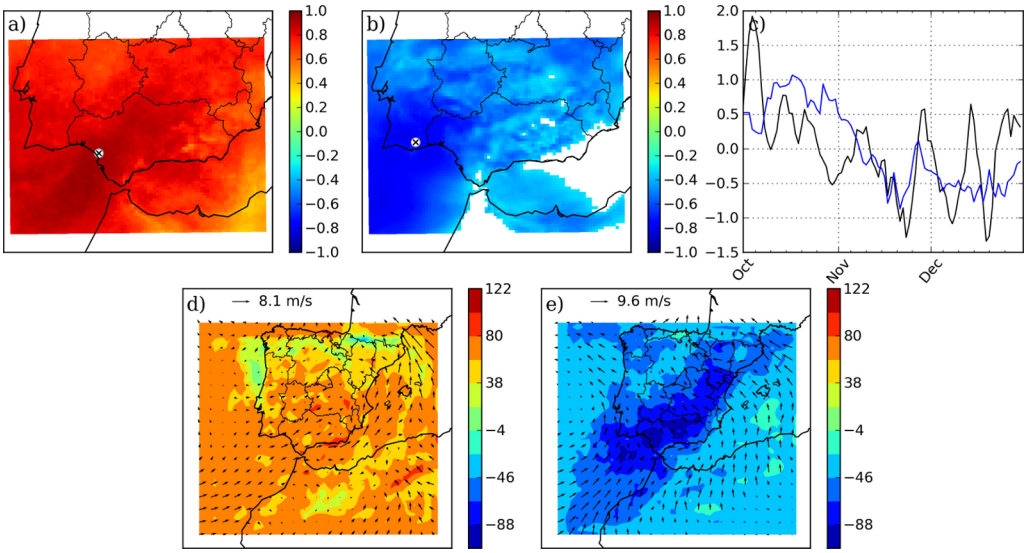


Figure 5.10. As in Fig. 5.3, but for the first mode of the CCA resulting from the autumn analysis. The two crosses indicate the grids selected for the balancing time series analysis.

entire region. Positive solar and negative wind energy anomalies are associated with westerly winds in the region (Fig. 5.10d), while negative solar and positive wind energy anomalies are associated with a low pressure center west of Portugal (Fig. 5.10e). This low pressure center brings southerly winds over most of the region, and associated frontal activity brings cloudiness (negative solar energy anomalies) and relatively high wind speeds (positive wind energy anomalies).

The time series of the second mode (Fig. 5.11c) have a canonical correlation of 0.45. Both wind and solar time series vary considerably, at both synoptic and monthly time scales. This second mode accounts for considerably lower solar energy variability than the leading mode (about 6%), but a similar value for wind energy (23%). The spatial patterns (Fig. 5.11a and 5.11b) show strong positive correlations in the solar field (greater than 0.6) over the eastern part of the region. Negative correlations in the wind energy field are found over nearly the entire region, although minimum values (0.8) are observed over eastern, central and northern areas. This second mode again indicates a balancing effect between the wind energy in the aforementioned areas and solar radiation

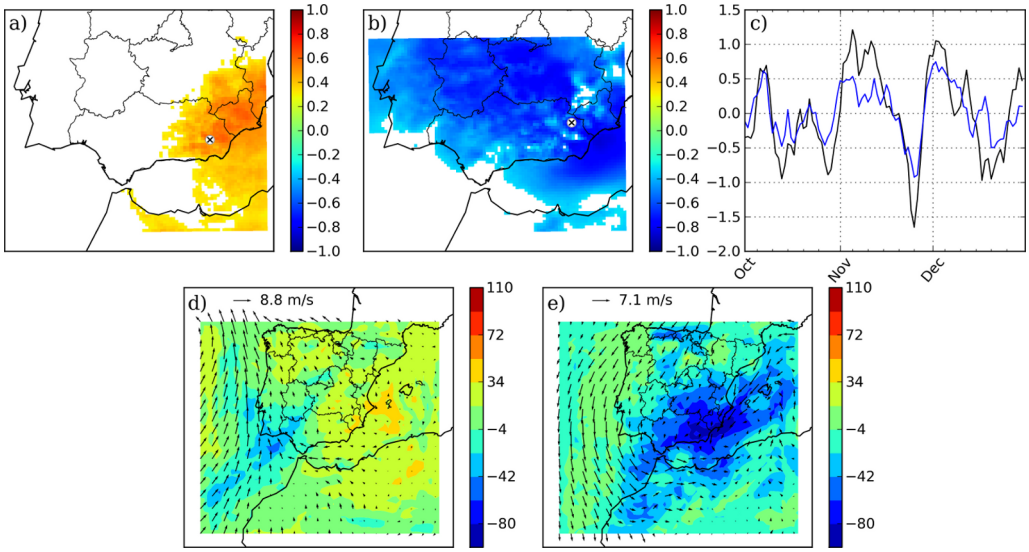


Figure 5.11. As in Fig. 5.3, but for the second mode of the CCA resulting from the autumn analysis. The two crosses indicate the grids selected for the balancing time series analysis.

in the very east of the region. On one hand (Fig. 5.11d), positive solar and negative wind energy anomalies are associated with a meridional circulation over the eastern Iberian Peninsula. Weak southerlies are observed over central and southeastern areas, generating positive solar and negative wind anomalies in those areas. On the other hand, negative solar and positive wind anomalies are associated with a low pressure center in the southeast of the region, over the Mediterranean Sea (Fig. 5.11e). This center brings northeasterly winds over the eastern part of the region, leading to positive wind energy anomalies, while the frontal activity of this low brings cloudiness to very eastern areas, reducing solar radiation.

5.3.5 Annual period

Previous results differ according to the season studied, further emphasizing the seasonal dependence of coupling between the wind and solar energy resources in the region. Therefore, the annual analysis, which averages all seasonal characteristics, produced

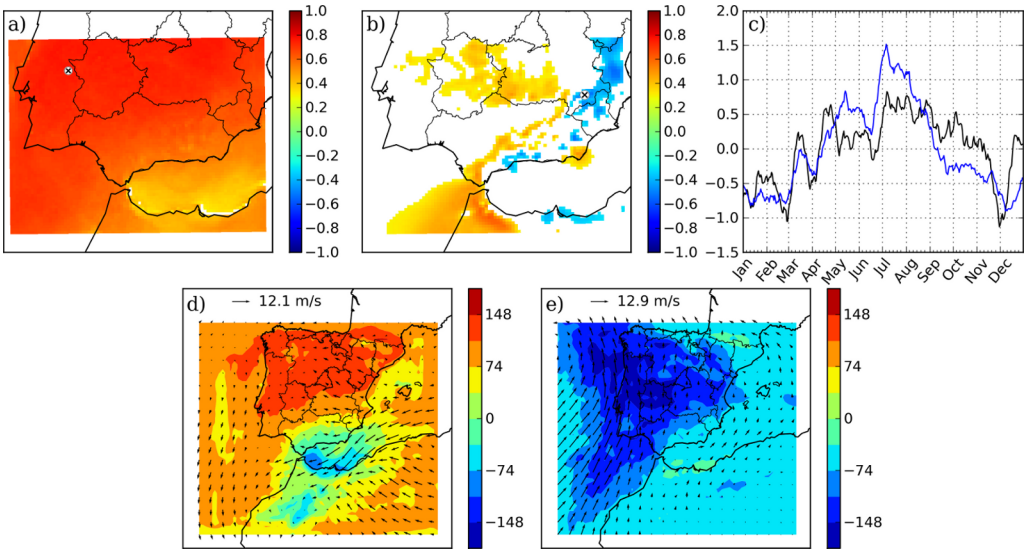


Figure 5.12. As in Fig. 5.3, but for the first mode of the CCA resulting from the annual analysis. Composites in d) and e) were obtained based on the 30 highest positive and lowest negative anomalies of the wind energy canonical time series. The two crosses indicate the grids selected for the balancing time series analysis.

only two pairs of statistically significant canonical patterns (Table 5.1). The leading mode time series (Fig. 5.12c) have a canonical correlation of 0.46, and a clear annual cycle is apparent, with higher values during summer. Monthly and synoptic scale variability is also evident. This mode accounts for 42% of the solar energy variability, but only about 7% of the wind energy. The spatial patterns show positive correlations in the solar field almost region-wide, with higher values to the west and north (Fig. 5.12a). For wind energy, positive correlations (about 0.5) are found near the strait of Gibraltar and mountainous zones of the central part of the region. There is negative correlation (about -0.5) over some southern areas, along the Mediterranean coast near the strait, and in the east. Therefore, the leading annual mode indicates weak but statistically significant annual balancing between solar and wind energy in the aforementioned areas. This mode resembles the leading mode of the spring analysis (Fig. 5.5), and the third mode of the summer analysis (Fig. 5.9). The associated atmospheric circulations also resemble the corresponding modes from spring and summer. On one hand, positive solar radiation anomalies in the entire study region and positive wind anomalies at the strait of Gibraltar (and therefore, negative wind anomalies along the coastal Mediterranean near Gibraltar)

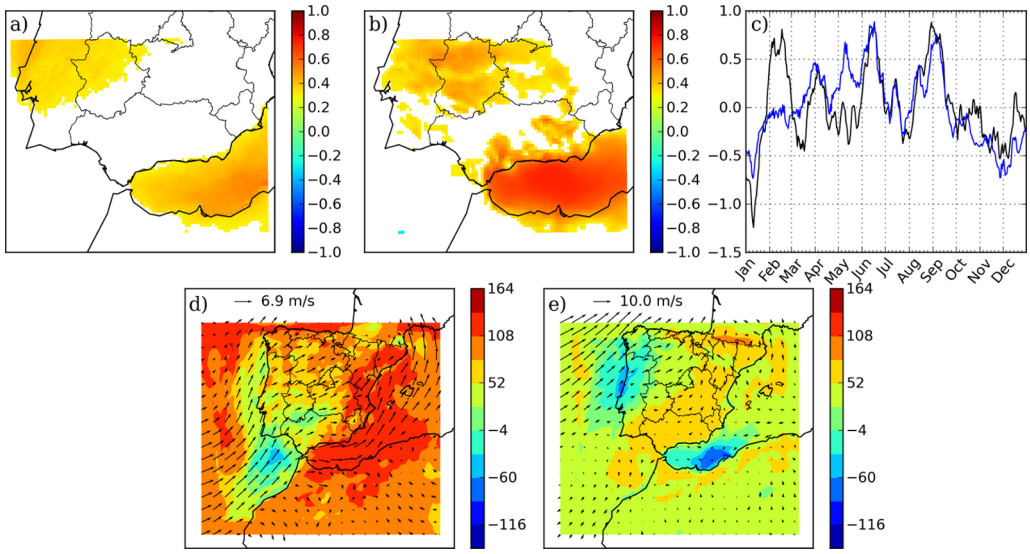


Figure 5.13. As in Fig. 5.12, but for the second mode of the CCA resulting from the annual analysis.

are associated with easterly flow over the entire southern peninsula, intensified in the strait area (Fig. 5.12d). This easterly flow brings cloudiness to the entire study region, reducing the solar radiation availability. On the other hand, negative solar radiation anomalies in the whole study area and negative wind anomalies at the strait of Gibraltar (and therefore, positive wind anomalies at the coastal areas of the Mediterranean near Gibraltar) are associated with southerly flow at the western part of the Iberian Peninsula (Fig. 5.12e).

The time series of the second mode have a canonical correlation of 0.4 (Fig. 5.13c), and demonstrate considerable monthly variability. This second mode accounts for 8% of the variance of the solar field and 13.5% of the wind field. Spatial patterns show weak positive correlations in solar energy over Portugal and the Mediterranean coast (Fig. 5.13a). Positive wind energy correlations are also observed (Fig. 5.13b) in these areas, but values are higher. Therefore, no balancing effect is observed. Atmospheric conditions show that positive solar and wind energy anomalies are associated with southwesterly flow over the western part of the region, which turns into westerly flow in the eastern part. On the other hand, negative wind anomalies are associated with high pressure over

the gulf of Cádiz, which weak winds over the region.

5.3.6 Balancing times series analysis

Based on the results of the previous section, we further analyzed the balancing between solar and wind energy resources in the study region. In particular, solar and wind energy time series at various locations were compared in cases of noteworthy resource balancing (Fig. 5.14). The locations were selected based on their correlation (loading factor) values on the wind and solar map, i.e., the highest ones (one negative and other positive). The time series were extracted directly from the raw, daily-integrated and normalized wind and solar energy database, and detrended based on linear regression. Fig. 5.14a shows wind and solar energy time series for locations highlighted with a cross in Fig. 5.14, which are therefore representative of balancing observed during the second canonical mode of winter. Correlation between the time series was -0.53, and the percentage of days during winter with opposite sign anomalies was 63%. Similarly, Fig. 5.14b shows wind and solar energy time series for locations highlighted in Fig. 5.8 (second summer mode). Similar results emerged in this case, with a correlation around -0.34, and a percentage of cases with opposite sign anomalies of 62%. Figs. 5.14c and 5.14d represent locations highlighted in Fig. 5.10 (first autumn canonical mode) and Fig. 5.11 (second autumn canonical mode), respectively. The autumn season showed the greatest balancing between solar and wind resources in the region. This is further confirmed by this particular analysis, i.e., the time series in Fig. 5.14c has a correlation of -0.46 and a percentage of days with opposite sign anomalies of 63%. The time series in Fig. 5.14d have a correlation of -0.56, and a percentage of days with opposite sign anomalies of 71%. Fig. 5.14e shows wind and solar energy time series for locations highlighted in Fig. 5.12 (first annual mode). For this annual case, correlation of these time series is -0.32 and the percentage of days with opposite sign anomalies was 58%.

Finally, an additional and quantitative study of the balancing was done. At grid points highlighted in Fig. 5.12 (first annual mode) by crosses, and that correspond to grids with maximum balancing (negative correlation), the energy production of a reference photovoltaic (PV) plant (grid point with in Fig. 5.12a) and reference wind mill (grid point with a cross Fig. 5.12b) were evaluated. The wind speed and solar radiation

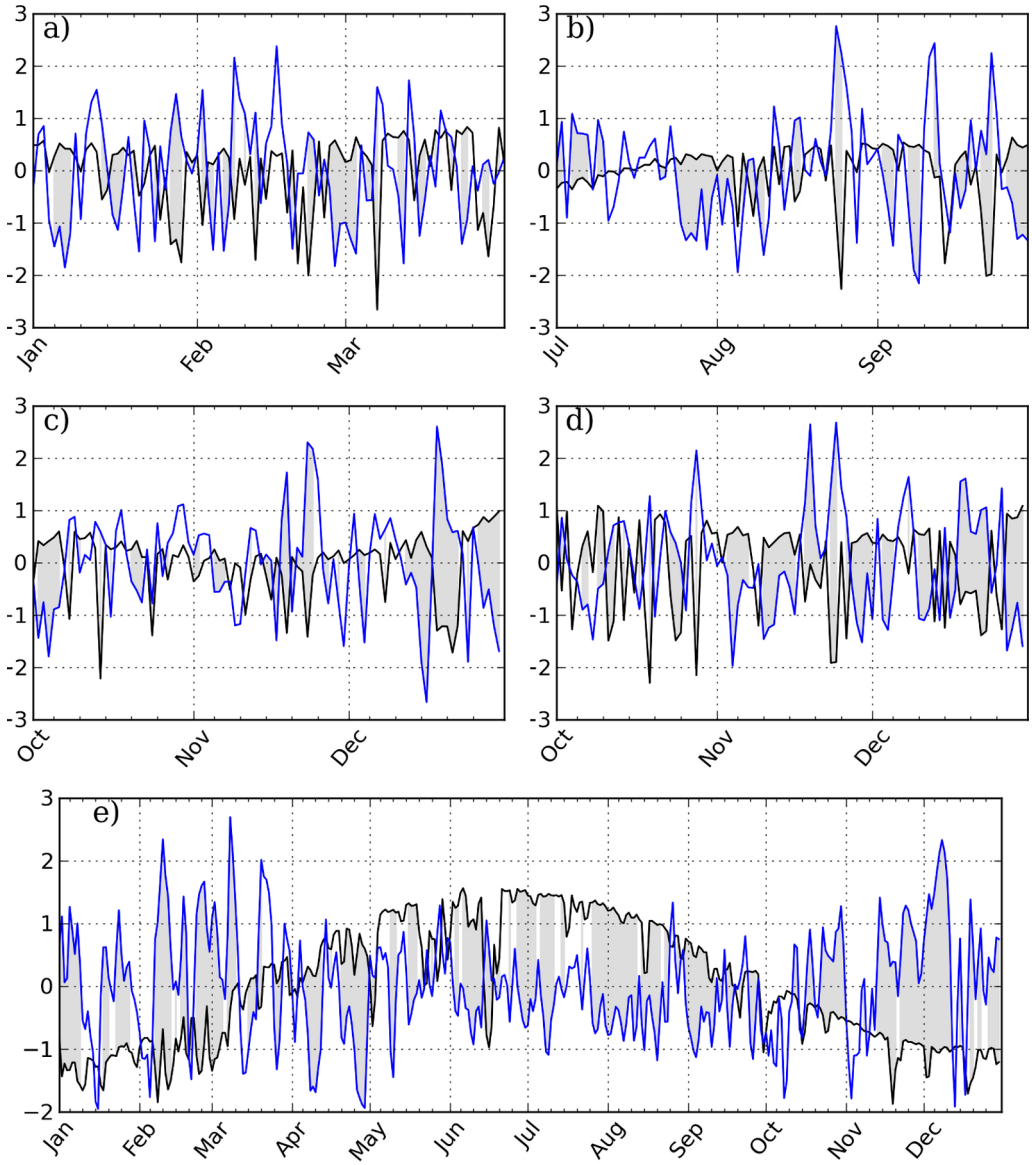


Figure 5.14. Representative time series of the main balancing patterns obtained in this study. a) Time series representative of the balancing pattern of the second winter canonical mode (Fig. 5.4). In particular, the anomaly time series of the solar energy (grey dashed) and wind energy (black continuous) corresponding to the points highlighted in Fig. 5.4a and 5.4b are represented. Shaded areas highlight days with solar and wind energy anomalies of opposite sign. b) As in a), but for the second summer mode (Fig. 5.8). c) As in a), but for the first autumn mode (Fig. 5.10). d) As in a), but for the second autumn mode (Fig. 5.11). e) as in a) but for the first annual mode (Fig. 5.12).

time series were extracted directly from the raw data at these locations, and were used for estimating the hourly energy production over the study period (2007). For wind energy, we computed the energy produced by a *Vestas V90-2.0 MW* wind mill, with a rated nominal power of 2 MW. Since the hub of this wind mill is at 80 $m.a.g.l$, wind speed derived from the model was accommodated to this altitude by vertical interpolation using splines. The resulting wind power energy hourly series were normalized, dividing by the respective nominal power, obtaining corresponding wind energy hourly capacity factor time series. Similarly, the hourly production of a reference PV plant was computed following Ruiz-Arias et al. (2012b). Specifically, the PV potential for electricity production was calculated based on a traditional fixed PV system with panels inclined 30° over the horizontal and permanently oriented southward. Production was normalized by the nominal power to obtain an hourly capacity factor. Finally, the wind and PV hourly capacity factors were combined in a single series, representative of the combined power. Normalization was also used for this combined time series, for proper evaluation. Then, the standard deviations of the hourly wind and PV capacity factor time series were compared with those of the combined wind and solar capacity factor time series. The standard deviation is a measure of intermittency in production, and therefore may be used to evaluate the balancing between solar and wind energy. Fig. 5.14 shows wind, PV and combined capacity factor time series for selected periods of the year. Balancing is clearly observed in these representative time series, notably those of winter and autumn (Figs. 5.14a and 5.14d). In general, it is clear that combination of wind and solar power smoothes the variability of power output. Notably for the entire year, the standard deviations of wind energy and PV capacity factor time series were 0.33 and 0.31, respectively. On the other hand, for the combined capacity factor time series, standard deviation declined to 0.21. To have a reference for the benefit of balancing, we computed the average of standard deviation of combined capacity over the entire study region, assuming the wind mill and solar PV plants are located at the same site. The value obtained is 0.24. Finally, we calculated standard deviation of combined capacity factor for the grid points with highest correlation(and least balancing) (highlighted by triangles in Figs. 5.12a and 5.12b), obtaining a value of 0.27. The former analysis was also conducted for the second winter mode (Fig. 5.4), one of the most significant balancing patterns obtained in the CCA. For this winter case, standard deviation of combined capacity factor is 0.18 at the points of greatest balancing (grid with crosses in Figs. 5.4a and 5.4b). The average value for the entire study region,

assuming collocated wind mill and solar PV plants, is 0.22, while the value for the grid points with least balancing (highest positive correlation, highlighted by triangles in Figs. 5.4a and 5.4b) is 0.26.

In both cases, annual and winter, a substantial reduction in standard deviation of combined capacity factor is obtained when locating wind farm and PV plants based on the CCA results. As may be expected, the reduction is greater for the winter case (which shows a noteworthy balancing pattern) than for the annual case (which shows a weaker pattern).

5.4 Summary and conclusions

In the present work, we have proposed and evaluated a method for analyzing the spatiotemporal balancing between the solar and wind energy resources in a region. The method attempts to find the optimal distribution of wind farms and solar energy plants over a territory, to minimize the variability of energy input into the power supply system. The methodology applies a canonical correlation analysis (CCA) to solar and wind energy fields in the region, and then analyzes the corresponding coupled spatio-temporal canonical patterns. The method was tested in the southern half of the Iberian Peninsula, covering about 350000 km^2. The study region, though relatively small, possesses considerable spatial variability in the main climate variables, owing to varied topographic features and the influence of the adjacent Mediterranean Sea and Atlantic Ocean. We used wind and solar energy estimates from the Weather Research and Forecasting (WRF) mesoscale model. Daily-integrated solar and wind (at 30 $m.a.g.l$) energy fields from 2007 were analyzed, at a spatial resolution of 9 km. Independent seasonal and annual analyses were done, and the atmospheric circulations associated with each coupled canonical mode were investigated.

Results show the existence of valuable balancing between the solar and wind energy resources in the region, but with a marked seasonality. In particular, during winter, a noteworthy balancing was observed between the solar energy resources over almost the entire study region and the wind energy resources near the strait of Gibraltar.

During spring, weak balancing was observed between solar energy near the eastern strait of Gibraltar and wind energy in the central strait area and mountainous interior of the region, and between solar energy in the southwestern Iberian Peninsula and wind energy in the central and eastern peninsula. Important balancing was evident in summer between the solar energy over almost the entire region and wind energy in the south and east. Finally, the autumn season turned out to have the most important balancing effect. During this season, balancing between the solar and wind energy resources extended over the entire region, although it was more important in the southwestern and southeastern areas. Atmospheric circulations associated with these coupled patterns showed a marked seasonal dependence. Synoptic scale variability greatly influenced the balancing, but so did topography, especially near the strait of Gibraltar.

The annual analysis, which represents an averaging of the seasonal results, showed only a weak balancing between region-wide solar energy and coastal wind energy near the strait of Gibraltar and in the eastern part of the region. These relatively poor results from the annual analysis compared to the seasonal ones can be attributed to averaging. That is, coupling between wind and solar energy resources varied considerably in strength, sign and spatial coverage through the year, resulting in a null effect from seasonal averaging. Based on the CCA analysis, we further analyzed time series of the wind and solar energy resources at locations of the greatest balancing. The most important results were found for the second mode during autumn. Wind and solar energy time series representative of this mode showed a correlation of -0.56, and 71% of the time, the sign of the anomalies was opposite. Finally, when locating reference wind farms and PV plants according to the balancing patterns, their combined power production showed substantially lower variability than production of wind farms and PV plants separately, and combined production achieved by any other locations

Our procedure can be easily applied to areas of arbitrary size, to optimize the grid power output. The method facilitates planning of the location of future wind and solar energy plants across a region, so that total electricity production (solar plus wind) will have smaller fluctuations. This may result in greater use of renewables as reliable, base load electric power. Currently, renewable projects are developed in locations with either maximum wind or sun. In the future, project locations should also take into account the fluctuation of power supply from each renewable. To inform this endeavor in the future,

we will augment the present analysis of meteorological balancing with an investigation of load demand.

It should be emphasized that we only attempted a seasonal analysis, to highlight the existence of balancing patternsover the year. This seasonal analysis should be extended to the reference climatic period (i.e., 1981-2010). This would permitevaluation of the stability of the presented seasonal balancing patterns over this reference period, and would make our results more useful for deciding power plant placement. In addition, our results were constrained by the use of model estimates instead of measurements.

CHAPTER 6

OPTIMUM LOCATION OF WIND FARMS AND CSP PLANTS FOR REDUCING POWER FLUCTUATIONS

Santos-Alamillos F.J., D. Pozo-Vázquez, J.A. Ruiz-Arias, V. Lara-Fanego, and J. Tovar-Pescador J. 2012. *Optimum location of wind farms and CSP plants for reducing power fluctuations*. Manuscript in preparation.

6.1 Introduction

It is expected that worldwide primary energy demand will increase by 45%, and demand for electricity will increase by 80% between 2006 and 2030 (IEA, 2008). However, the sustainability of the current power generation systems, mainly based on fossil fuels, are questioned because the energy-related greenhouse gas (GHG) emissions will more than double by 2050 (IPCC, 2007c). In particular, 85% of current primary energy driving global economies comes from the combustion of fossil fuels and accounts for 56.6% of all anthropogenic GHG emissions (IPCC, 2011). There are different paths toward stabilizing GHG concentrations, but a key issue in all of them is the replacement of fossil fuels by renewable energy sources. In the EU, regulations set a binding target of 20% of final energy consumption from renewable sources by 2020, along with a commitment to achieve at least a 20% reduction of GHG by 2020, as compared to 1990 (European Directives 2009/28/EC and 2009/29/EC). In this scenario, solar and wind

energy technologies are expect to play a key role (Mathiesen et al., 2011; Jacobson and Delucchi, 2011).

Wind energy is the fastest growing renewable. In 2008, this energy provided nearly 20% of electricity consumption in Denmark, more than 11% in Portugal and Spain, over 4% in the entire European Union (EU), and nearly 2% in the United States (IEA, 2009). In Spain, installed wind capacity reached 20.8 GW in 2010 (around 20% of the total system), the third largest figure among world countries. Wind electricity is estimated to contribute about 9% of global electricity production by 2030, growing to 12% by 2050 (IEA, 2009). For Spain to achieve the 20% final consumption goal, a substantial increase in the contribution of wind electricity production is necessary, from the current 11% to about 30% (Gómez et al., 2010). Similar target increases in the share of wind energy are expected in other regions (Lund, 2007; Krajacic et al., 2011).

Concentrating Solar Power (CSP) is a technology that has been developed for more than 25 years, mainly supported in countries as USA and Spain. Different technologies (parabolic troughs, solar tower, Fresnel reflectors and parabolic dishes) are now competing but the most extended is the parabolic trough, which accounts for most of the existing commercial plants (IEA, 2010a). Although the global stock of the CSP plants neared 1 GW capacity as early 2010, the current projects in development or under constructions in more than a dozen countries (including China, India, Morocco, Spain and the United States) are expected to total 15 GW (IEA, 2010a). In particular, the installed power in Spain by the end of 2011 was 750 MW, of which the 93% is of parabolic troughs. Moreover, an additional advantage of CSP plants is the thermal storage capability, typically of 7.5 hours, that allows the production can be scheduled in some way and the plants may be regarded as dispatchable (Usaola, 2011).

A major challenge will be the integration of these major wind and solar yields into the existing energy supply infrastructure (Lund, 2005, 2006). This challenge comes from the intermittent nature of wind and solar resources and their sensitivity to the weather patterns, as compared to the relatively stable and predictable sources conventionally generated electricity. This disadvantage makes the cost of renewable technologies less competitive than conventional productions systems, because intermittent production creates negative externals that translate into grid integration costs. Thus, solutions

that reduce power fluctuations are important if wind and solar electricity is to significantly displace other electricity technologies. Today, short-term wind and solar power forecasting is the primary requirement for efficient integration of renewables into power systems, and for the reduction of grid integration costs (Saintcross et al., 2005; Kariniotakis, 2006; Lorenz et al., 2010; Lara-Fanego et al., 2011). Unfortunately, the skill of these forecasts is still limited and other technological solutions, such as energy storage, are is still immature for the large scale.

One of the most promising ways to reduce the power fluctuations from wind and solar energy is the spatial aggregation of wind farms and solar plants. The idea is that a previous knowledge of the weather and climate patterns over a region can evidence locations where the wind, the solar or both wind and solar resources are spatially anticorrelated. If this is the case, above-normal wind or solar resources can compensate below-normal wind or solar resources at other locations, resulting thus in a spatial balancing. In this case, by interconnecting advantageously-distributed wind farms and solar plants it may be possible to achieve a substantial reduction in the combined power fluctuations and an increment in the time of power availability, eventually transforming solar and wind energy into reliable (even baseload) supply.

There are, mainly, two parameters for evaluating the contribution of renewable technologies toward reducing the share of conventional thermal fossil-fuelled power plants in a power systems: capacity credit and firm capacity. On the one hand, the capacity credit is related with the ability of the renewables to contribute to the peak demands of a power system, while maintaining the same security of supply as conventional power plants (Milborrow, 2008). On the other hand, the firm capacity is defined as the fraction of installed renewable capacity that is available with the same probability as that of a thermal plant (Giebel, 2005). Therefore, firm capacity can be used to assess the contribution of the renewables to baseload power.

There are numerous works in the literature that analyze the spatiotemporal variability of the wind energy resource and its consequence for wind power integration (Kahn, 1979; Landberg, 1997; Holttinen, 2005). In a recent work, Roques et al. (2010) showed an optimal combination of wind production in different European countries would foster a much less variable total production. Nevertheless, some studies showed that the ability

of wind energy to provide firm capacity (baseload) is limited. For instance, Oswald et al. (2008) concluded that although the aggregated production of wind farms across the United Kingdom reduces the wind power variability, this aggregation does not lead to a substantial amount firm capacity. Similar results were found in analogous aggregation studies for Denmark (Ostergaard, 2008) and Germany (Weigt, 2009). In the latter study, it was concluded that only 0.5% of the total wind power installed capacity in Germany was guaranteed throughout the study period (3 years). In contrast, between 10% and 15% of the installed capacity was wind capacity credit. The main reason for obtaining the former results is the existence of relative homogeneous weather conditions and limited topographic features in these three countries. Other analysis are more encouraging, for instance Archer and Jacobson (2007) studied the decrease of wind power production fluctuation through interconnection of 19 wind farms in the Midwestern United States. They found a significant decline in the fluctuation of total production compared to single wind farms, and that about 15% if the installed power can be used as based load (firm capacity). Similar results were found by Cassola et al. (2008) in an analysis of the optimal distribution of wind farms in Corsica (France). Kempton et al. (2010) analyzed the benefits of interconnecting offshore wind farms along the east coast of the United States. Based on analysis of data from 11 meteorological stations, they demonstrated that this interconnection would provide a reliable baseload power. Finally, Santos-Alamillos et al. (2011) demonstrated that a substantial increases in the stability of the power, even baseload power, can be obtained by interconnecting wind farms optimally located in southern Spain. In these last studies, the varied weather conditions and topographic features of the study areas explains the significant amounts of firm capacity. Finally, in a recent work (Mason and Archer, 2012) proposed several ancillary methods for transforming, throughout storage, wind electricity into firm capacity. The benefits of solar energy aggregation have received less attention. Mainly, because the spatial variability of the solar resources is significantly less than that of wind energy (Archer and Jacobson, 2003; Papadimas et al., 2010; Gueymard and Willcox, 2011; Widén, 2011; Wiemken et al., 2001; Mills and Wiser, 2010).

Since solar and wind energy will contribute more to total electricity production in the future, it is worth analyzing the influence of the spatial distribution of these two sources in the stability of their combined power production. In othis context, a balancing effect becomes effective when and where strong solar energy compensates weak wind energy,

and vice-versa. From a meteorological and climatological point of view, balancing between solar and wind resources can be easily anticipated, given a large enough region. Over Europe, wind resources tend to be higher in winter and lower in summer, the opposite for solar resources. Balancing seems very dependent on the temporal and spatial scales considered (Pozo-Vázquez et al., 2011). Although some projects intended for very high renewable penetration are founded on the idea of balancing (Trieb et al., 2005; Tröster et al., 2011), little research effort in this field has been made so far. Among this effort and important contribution was done by Heide et al. (2010, 2011), who analyzed the optimal mix between solar (PV) and wind energy in Europe within a scenario of very high penetration (100%) of these renewables. Their analyses were based on meteorological model estimates and were carried out on seasonal time scales, with a constraint of reducing storage needs as much as possible. They gave an optimal seasonal mix of 55% wind and 45% solar. Widén (2011) analyzed balancing between solar and wind resources in Sweden, based on meteorological station data. He reported a negative correlation between solar and wind resources (and thus balancing) on all time scales. He also showed a greater hour-to-hour variability when the solar share was increased. Nikolakakis and Fthenakis 2011 analyzed the optimum mix of wind and solar electricity for the state of New York. They found that considerable high penetration (up to 30%) of wind and solar can be achieved without adding storage capabilities. In a recent work (Santos-Alamillos et al., 2011), we analyzed the spatial balancing between the solar energy (from global solar irradiance GHI) and the wind energy resources in Southern Spain by means of Canonical Correlation Analysis (CCA). The CCA decomposes two sets of space-time dependent variables (solar and wind energy fields) into pairs of spatial patterns (canonical modes), such that they are maximally correlated. The CCA can eventually highlight the existence of balancing between solar and wind energy resources, depending on the nature (sign and strength) of the canonical patterns. In this sense, the CCA finds the optimal distribution of wind farms and solar energy plants over a territory in order to minimize the variability of total energy input into the power supply system. We obtained valuable balancing patterns in the study region. When locating reference wind farms and PV plants according to these balancing patterns, their combined power production showed to have a substantially lower variability than the production of the wind farms and PV plants separately and that the combined production obtained by any other locations.

In this work, we examine the ability of wind farms and CSP plants in the southern Iberian Peninsula to provide reliable (baseload) power. To this end, estimates of the wind and solar (from Direct Normal Irradiance, DNI) energy resources in the study region, including offshore areas, are obtained based on a numerical weather prediction (NWP) model simulation. Secondly, the CCA was used to assess the optimal location of wind farms and CSP plants in the study region in order to provide stable power. Notably, the power variability and availability provide by different combinations of wind farms and CSP plants, optimally allocated based on the CCA results, are evaluated. These analyses were done seasonally and for the complete period. Atmospheric conditions associated with the balancing pattern were also examined.

The work is organized as follows: Section 6.2 deals with the study area, data and method. Section 6.3 describes the results. Finally, in Section 6.4, a summary and some conclusions are presented.

6.2 Methods, data and study area

6.2.1 Study area

The study region (Fig. 6.1) corresponds roughly to the southern half of the Iberian Peninsula, covering about 350.000 km^2. The region is located in a transition zone from temperate to subtropical climates, bounded on the south by the Atlantic Ocean and Mediterranean Sea. Several areas within the region can be characterized by their dominant topographic features. The southwest, corresponding to western Andalusia and the south of Portugal, is an almost homogeneous at area, open to the Atlantic Ocean. The central and northern parts have an intermediate topographic complexity. In particular, central Spain is a plateau with a mean elevation of about 700 m. Transition from this area to central Portugal is relatively smooth. Finally, complex topography dominates the east and southeast parts of the region. This area contains several mountain ranges and includes the Sierra Nevada national park, with a maximum elevation of 3482 m (highest on the Iberian Peninsula). Since the region borders both the Mediterranean Sea (at the south) and the Atlantic (at the west), there are extensive coastal areas where local thermal

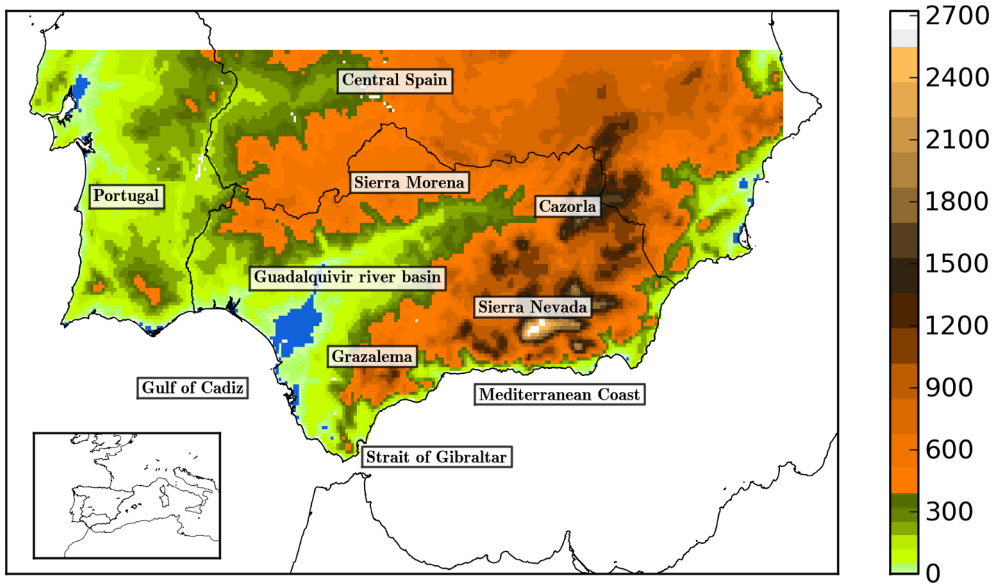


Figure 6.1. Location (small figure, bottom right) and main topographic and geographic characteristics of study region. Gray scale colors indicate elevation based on the same 3-km spatial resolution Digital Elevation Map used in the model simulation, to derive study data. Scale at right indicates elevation in meters above sea level.

contrasts strongly influence the wind energy resource.

The large-scale circulation over the region is mainly driven by a semi-permanent subtropical high pressure center over the Azores islands, which varies in location and intensity during the year. During winter, this high is situated at lower latitudes, allowing the Iberian Peninsula to be affected by zonal circulations from the west, while in summer it migrates northward, blocking the westerlies over most of the peninsula (Trigo et al., 2002, 2004). The Azores subtropical high is the southern part of the North Atlantic Oscillation (NAO) dipolar atmospheric variability pattern (Hurrel et al., 2003), which is linked to large-scale atmospheric dynamics and the modulation of the strength of the westerlies over the European region (Pozo-Vázquez et al., 2001; Gámiz-Fortis et al., 2008; Trigo and DaCammara, 2000).

Although the entire region is under the influence of the Azores subtropical high, the region experiences a wide range of climate conditions. This range is related to orography (Fig. 6.1) and numerous synoptic disturbances of Atlantic origin, which cause enormous

spatial variability in precipitation and other climate variables (Trigo and DaCammara, 2000; Trigo et al., 2004). For example, the eastern part is less influenced by the Azores high, and more affected by the Mediterranean Sea. In fact, annual precipitation values across the region range from 300 $mmyear^{-1}$ in the coastal semi-desert southeast to more than 2500 $mmyear^{-1}$ in the mountains near the strait of Gibraltar (Romero et al., 1998; Ramos-Calzado et al., 2008). Solar radiation, highly conditioned by the cloudiness variability, suffer a considerable spatial and temporal variability, especially during winter (Hutchinson et al., 1984; Alsamamra et al., 2009; Pozo-Vázquez et al., 2011).

Surface wind speed variability is associated not only with mesoscale circulations but also with other more localized factors. Many of these are related to topographic characteristics (elevation, aspect, slope, surface roughness, etc.), and others as the thermal contrast near water bodies (Hutchinson et al., 1984; Weber and Furger, 2001; McVicar et al., 2008). As a consequence, the complex topography of the region and the influence of the Atlantic Ocean and the Mediterranean Sea combine to produce a marked spatial variability in regional wind speeds. In summary, and in spite of its relatively small size, the interaction of mesoscale circulations with the varied topographic and geographic features of the study region generates a marked spatial variability in the solar radiation and, particularly, in the wind speed.

6.2.2 Data

Direct solar and wind energy at 80 meters above the ground level (m.a.g.l.) energy resources were obtained from integrations with the Weather Research and Forecasting (WRF) Numerical Weather Prediction (NWP) model (Skamarock et al., 2008). Simulations were conducted for the year 2009 at a temporal resolution of one hour. The model configuration included three nested domains, with 27, 9 and 3 km spatial resolution (Fig. 6.2). We used 36 vertical levels, with the first 8 within the lowest 1000 m.a.g.l. In particular, the five lowest levels, which are important for regional wind energy applications, were approximately located at 4, 18, 43, 64 and 80 m.a.g.l. This last level and the third domain, with 3 km spatial resolution, were used to calculate the wind and direct solar energy.

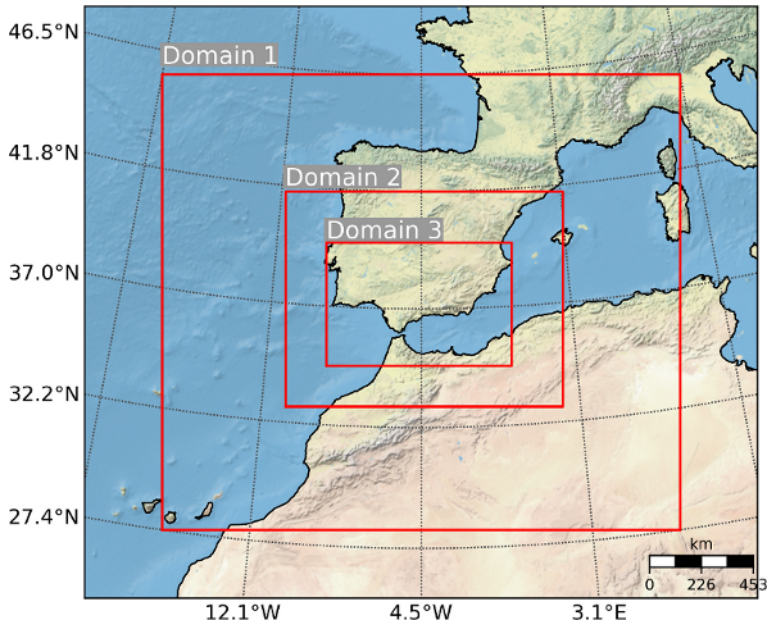


Figure 6.2. Spatial configuration of domains for numerical simulation: three nested domains with 27, 9, and 3 km horizontal resolutions, respectively. Data from the inner domain (3 km) were analyzed.

The physical configuration of the model was selected based on previous evaluations of WRF performance in the study region (Fernández et al., 2007; Borge et al., 2008; Ruiz-Arias et al., 2008). The RRTM scheme (Mlawer et al., 1997) was chosen for longwave radiation, and the Dudhia Scheme (Dudhia, 1989) for short wave radiation. The Kain-Fritsch scheme (Kain and Fritsch , 1993) was used for cumulus and the Yonsei University planetary boundary layer scheme for the boundary layer (Hong et al., 2006). The Thompson graupel scheme (Thompson et al., 2006) was used for microphysics, and the unified Noah land-surface model for the land surface. Newtonian relaxation or nudging was used in model integration, using the parameter values proposed by (Seaman, 2000; Otte, 2008b). This technique relaxes the model toward the observed state by adding artificial forcing terms to the model predictive equations, based on the difference between the states weighted by nudge coefficients. Several works have demonstrated an improvements in the reliability of the wind estimates when using this nudging procedure (Barna and Lamb, 2000).

We used initial and boundary conditions from the Climate Forecast System Reanalysis

(Saha et al., 2010) with spatial resolution 0.5 deg and updates every 6 hours. It has been reported that the Surface Sea Temperature (SST) update during WRF model integration improves the accuracy of wind speed, especially for offshore winds (Muller at al., 2007). In this work, SSTs were interpolated to ocean grid points in each model domain, using the NCEP version 2.0 global SST dataset (Reynolds et al., 2002). This dataset is updated daily, on a 1° × 1° grid. Wind speed estimates at 80 m.a.g.l. (fifth vertical level) were used to estimate the daily-integrated wind energy values based on:

$$E_{daily\ wind} = \sum_{i=1}^{24} \left(\frac{1}{2} \rho v^3 \right) \times 1h \tag{6.1}$$

where u and v are the horizontal wind components very hour, ρ is the air density at the sea level. The wind power dataset included onshore and offshore areas up to 20 km from the coast, a distance considered feasible for offshore wind energy projects (Fichaux et al. , 2009). Although the DNI is not a meteorological variable provided directly by WRF model, this variable can be derived based on GHI. To this end, we have used the model proposed by (Ruiz-Arias et al., 2010):

$$DNI_i = (1 - k_d)\, GHI_i \cdot cos^{-1}(\theta_i) \tag{6.2}$$

$$k_d = 0.952 - 1.041 \cdot exp\left(-exp\left(2.300 - 4.702 k_t\right)\right) \tag{6.3}$$

where k_t is the clearness index. Similarly to the wind energy case, daily integrated solar energy values (based on the DNI) were computed as:

$$E_{daily\ solar} = \sum_{i=1}^{24} DNI_i \times 1h \tag{6.4}$$

6.2.3 Balancing method

Spatio-temporal balancing between solar and wind energy resources in the region was analyzed based on the Canonical Correlation Analysis (CCA) (Barnett and Preisendorfer, 1987; Bretherton et al., 1992; Von Storch and Zwiers, 2001). The procedure is fully explained in (Santos-Alamillos et al., 2011). The CCA is a multivariate statistical technique that allows us to study the relationships of two sets of variables, in this case, the daily solar and wind energy. This technique aims to find a set of weights for each set of variables (canonical loadings) so the resulting composite variables (pairs of canonical series) are maximally correlated (canonical correlation). This will result in the first canonical mode. This procedure can be repeated, deriving successive canonical modes derived from residual or leftover variance from earlier modes with an additional constraint: each set of weights for each initial dataset has to be orthogonal. The strength of the relationship between each pairs of canonical variables is reflected by the canonical correlation. In this work, only canonical modes with canonical correlations values above 0.4 were considered. This arbitrary selected and stringent value allows retaining only the most important balancing modes. Homogeneous canonical loadings have been used as a basis for interpretation of the canonical modes. In particular, homogeneous canonical loadings are the simple linear correlation between the original observed variables in on field and it corresponding canonical variable. By mapping these correlations, the spatial pattern associated with the corresponding canonical mode can be analyzed. The canonical loading reflects the variance that the observed variable shares with the canonical variable and can be interpreted like a factor loading in assessing the relative contribution of each variable to each canonical mode. The larger the coefficient, the more important it is in deriving the canonical mode.

The CCA will eventually highlight the existence of balancing between the solar and wind energy resources, depending on the nature (sign and strength) of the canonical correlation and the canonical loading patterns. For the purposes of this work, we look for canonical modes whose associated canonical patterns indicate areas in which solar and wind energy are meaningfully anticorrelated. The CCA was applied to the daily-integrated, seasonally standardized wind and solar energy fields. The data analysis was done for each season of the year and for the entire year. To avoid computational problems with the sample size, the daily data were pre-filtered using a Principal Component

Analysis (PCA) (Barnett and Preisendorfer, 1987) prior the CCA was conducted.

Finally, to understand the nature of the solar and wind power canonical model resulting from the CCA, a brief description of the associated mesoscale atmospheric circulations is given. We produced composite maps of daily mean horizontal wind components at 10 m.a.g.l and daily mean anomalies of the cloud fraction, associated with the fifteen (thirty for the annual analysis) maximum and minimum values of solar energy canonical time series. The composites were derived from the ERA-Interim reanalysis (Uppala et al., 2008) dataset, covering a 4000 × 4000 km region centred on the Iberian Peninsula. Moreover, for a more detailed view, composite maps of daily mean horizontal wind components anomalies at 80 m.a.g.l derived from the WRF 3-km integrations, were also produced. Again, these composites were computed with the fifteen maximum and minimum values of the respective solar energy canonical time series. The aforementioned anomalies were computed based on the corresponding analyses periods (seasonal or annual).

6.2.4 Solar and wind power times series balancing analysis

Finally, an additional and quantitative study of the balancing was carried out. Firstly, for each mode, two locations (grid points), one in the solar map and one in the wind map, were selected. These locations were selected as those presenting the highest maximum positive and negative loading, i.e. the maximum balancing between the solar and wind energy resources associated with the corresponding CCA mode. Secondly, at the selected grid points, the energy production of a reference wind turbine and CSP plant were evaluated.

In order to compute the wind power capacity factor time series, we used hourly wind speed time serie at 80 m.a.g.l derived from the WRF 3-km integration. Based on this time series, the hourly wind power produced by a reference wind turbine was computed. For onshore locations, the selected wind turbine was a VESTAS V90-2.0 MW, with a rated nominal power of 2 MW and hub height 80 m.a.g.l. For offshore locations, the selected wind turbine was a VESTAS V90-3.0 MW, of nominal power 3 MW and the same hub height. Fig. 6.3 shows the power curves for both turbines. Finally, the wind

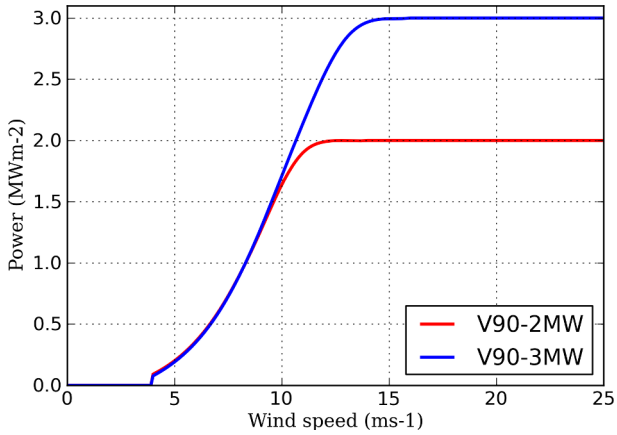


Figure 6.3. Power curves of the V90-2MW (dashed line) and V90-3MW wind turbines. The first turbine was used to assess onshore locations and the second for offshore locations.

power time series were normalized, dividing by the respective nominal power, obtaining the corresponding hourly capacity factor time series.

Different types of CSP technologies have been developed, with significant variations in the design, efficiency, costs and power production (Zhang et al., 2010). The parabolic trough is currently the most mature and commercially available CSP technology (EERE, 1997; Sargent and Lundy, 2003). For these reason, we have selected this technology for evaluating the solar power production. CSP and, particularly, parabolic trough plants can be designed with storage system, and its inclusion is an investment decision (IEA, 2010a). The storage allows power production not depend on the instantaneous resource, but the power production cost is also higher, about 9% for a plant with 7 hours of nominal power storage time (IEA, 2009). In this work, we have considered a parabolic trough CSP plant without thermal storage. For the operation of this type of plants, a minimum value of the DNI is needed; here this value has been taken as 300 Wm^{-2} (Kearny and Price, 2004). The solar power has been estimated based on the plant model proposed in (Zhang and Smith, 2008). This model considers a CSP reference plant of 100 MW of nominal power and without storage. The model assumes constant optical efficiency (ϵ_{OPT}), heat collector element thermal losses ($Loss_{HCE}$ (Wm^{-2}), solar field piping heat losses ($Loss_{SFP}$), turbine gross efficiency (ϵ_t), and electric parasitic loss ($Loss_p$)(Wm^{-2}), which means that these parameters do not vary with the irradiance

level. These parameters are use to formulate the relationships among solar output, solar field size, and direct irradiance level, as expressed in:

$$PW_{CSP} = \epsilon_t A_{sf} \left(DNI \cdot \epsilon_{OPT} - Loss_{HCE} - Loss_{SFP}\right) \cdot \left(1 - Loss_p\right) \tag{6.5}$$

where PW_{CSP} is the CSP plant power output, A_{sf} is the collecting area of the solar field and DNI is the value of the DNI. Lastly, PW_{CSP} time series were normalized, dividing by the nominal power, obtaining the hourly capacity factor time series.

Finally, to characterize the power output fluctuations, we computed the percentage of time at which the different values of the hourly capacity factor of the CSP plant alone, the wind turbine alone and the connected wind farm and CSP plant are available. In addition, the standard deviation of the hourly capacity factor for the plants alone and interconnected were also analyzed. The former analyses were conducted for each period of analysis independently.

6.3 Results and discussion

In this section, the results of the CCA analyses are presented. These analyses were conducted for each season of the year and for the entire year independently. Only the canonical modes that produced a canonical correlation higher than 0.4 are analyzed, excepting the second mode of the annual study, which was analyzed presenting only 0.3 canonical correlation value. Table 6.1 summarizes the principal results of the CCA analysis. Notably, the canonical correlations and the associated explained variances are presented for each mode and for each study period.

6.3.1 Winter

Only two modes with a canonical correlation higher than 0.4 were found for winter (Table 6.1). The time series of the leading mode (Fig. 6.4c) have a canonical correlation

Study period	Mode	Solar Energy Variance (%)	Wind Energy Variance (%)	Canonical Correlation Correlation
Winter	1	49	39	0.65
Winter	2	25	9	0.43
Spring	1	34	27	0.66
Spring	2	16	7	0.43
Summer	1	65	17	0.62
Summer	2	7	12	0.44
Autumn	1	34	50	0.68
Autumn	2	20	20	0.49
Annual	1	62	44	0.54
Annual	2	4	19	0.30

Table 6.1. Summary of results of the canonical correlation analysis (CCA). In particular, the table shows, for the seasonal and annual analysis, the solar and wind energy field explained variance associated which each canonical mode. The last column shows the canonical correlation values.

of 0.65. Both the solar and wind energy canonical time series exhibit a considerable variability at both monthly and synoptic time scales. This leading mode of the winter analysis accounts for around 49% of the variance of the solar energy and 39% of the wind energy fields. Their respective spatial patterns (Figs. 6.4a and 6.4b) show a notably balancing pattern. On the one hand, this first mode presents positive loads on the solar energy field in almost the entire region, particularly over the central area, where values reach 0.8. On the other hand, the wind energy shows negative loads in the whole region (especially in the central part, where loadings reaches -0.8), except in the western part of the strait of Gibraltar area (where loading values approach 0.8). Therefore, this first mode accounts for a balancing effect between the solar energy and the wind energy in the whole region except the western part of the Gibraltar strait area.

The mesoscale atmospheric circulations associated with this balancing pattern are presented in Figs. 6.4d, 6.4e, 6.4g and 6.4h. Notably, positive solar and negative wind energy anomalies are associated with north-easterly flow over the study region. This circulation brings, usually, cold dry atmospheric conditions over the study region, causing the positive solar energy anomalies. The relatively weak north-easterly winds are channeled and intensified in the Grazalema mountain area and the Gibraltar strait

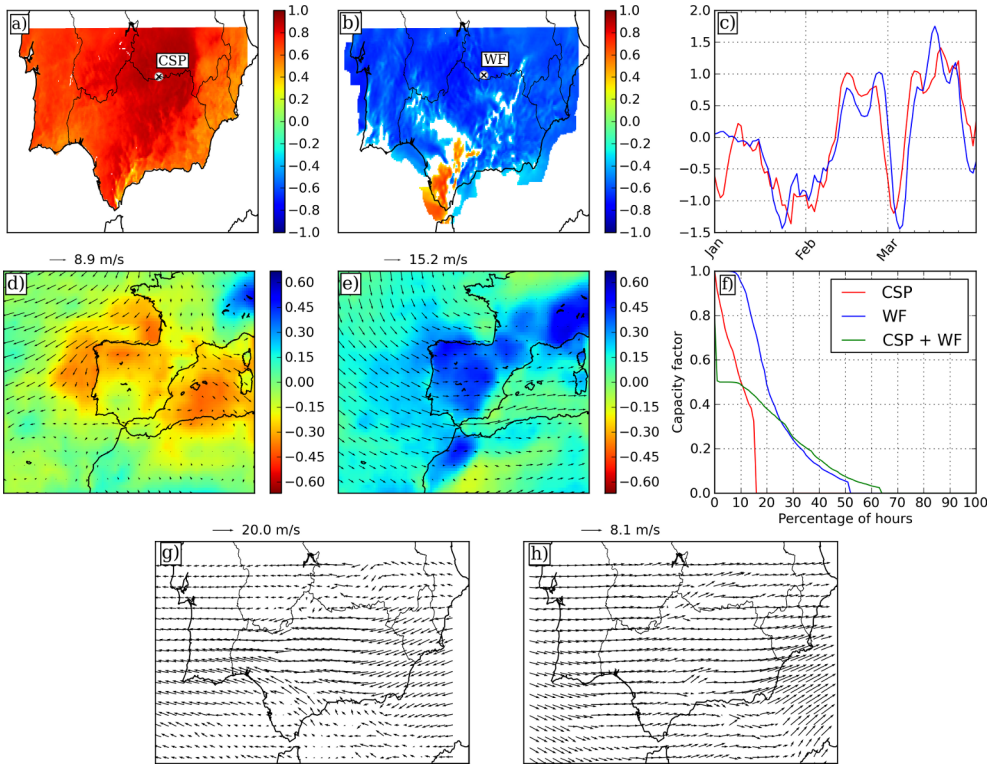


Figure 6.4. First mode of the CCA resulting from the winter analysis. a) Homogeneous correlation (canonical loadings) map for the solar energy and b) for the wind energy. In both figures, only values above 0.3 or below -0.3 (statistically significant) are displayed. The two crosses indicate the grids selected for the analysis presented in section 6.3. c) Canonical time series, filtered with a 5-day moving average filter. Solid black and dotted grey lines are the canonical series for solar and wind energy, respectively. d) Composite of daily-mean horizontal wind components at 10 m.a.g.l and cloud fraction anomalies corresponding to the 15 highest positive anomalies of solar canonical time series. e) As in d), but for the lowest 15 negative values. Wind speed are scaled according to the reference at top of Figs. d) and e), which indicates maximum wind speed in ms-1. Composites were obtained based on the ERA-INTERIM reanalysis with a spatial resolution of 25 km. f) Percentage of time at which each value of the hourly capacity factor of a reference CSP plant (CSP, dashed grey), a reference wind turbine (WF, dashed black), located at the grid points indicated in a) and b) respectively, and their interconnection (CSP+WF black continuous) are available. Capacity factor values and percentages are computed over the study period (here winter, 3 months). g) Composite of daily-mean horizontal wind components at 80 m.a.g.l, derived from the WRF 3-km spatial resolution integrations, corresponding to the 15 highest positive anomalies of solar canonical time series. h) As in g), but for the lowest 15 negative values. Wind speeds are scaled according to the reference at top of Figs. g) and h), which indicates maximum wind speed in ms-1.

area (easterly winds), given rise to the positive wind energy anomalies in this area. Alternatively, negative solar and positive wind energy anomalies are associated with low pressure over France. In the latter scenario, frontal activity brings cloudiness to most of the region, therefore, reducing the solar energy availability. In contrast, this frontal activity brings positive wind energy anomalies, except for the western Gibraltar strait area. Note that the interpretation of the wind speed anomalies in Figs. 6.4d, 6.4e, 6.4g and 6.4h requires the information from Figs. 6.4a, 6.4b and 6.4c and to take into account the normalization period, here 3 months.

The former results indicate the existence of a notable balancing between the wind and solar energy resources in the study area. Fig. 6.4f shows the percentage of time at which the hourly capacity factor values of a CSP plant and wind farm located at the grid points indicated in Figs. 6.4a and 6.4b, respectively, are available. These locations present the highest positive (solar) and negative (wind) loading and, therefore, represent the grids points with the highest balancing. The percentage of time at which the capacity factor values of the CSP plant and wind farm connected (combined CSP+WF hereinafter) is also displayed.

A non-zero CSP capacity factor is available about 20% of the time, with values close to 1 around 10% of the time. Regarding the wind energy, a non-zero value is obtained above 45% of the time, with values close to 1 around 10% of the time. Finally, the combined CSP+WF shows a considerable improvement in the capacity factor: a non-zero value is obtained around 65% of the time, with values above 0.5 around 20% of the time (note that a 0.5 capacity factor value for the combined CSP+WF is equivalent, in terms of generated power, to a 1 capacity factor for the CSP plant of wind farm). Finally, Table 6.2 shows the standard deviation of the hourly capacity factor for the CSP plant, the wind farm and the combined CSP+WF. For reference, the mean values of the former standard deviations along the study area (only inland) obtained when locating at the same grid point the CSP plant and wind farm are also displayed. Note that, the combination of the CSP plant and wind farm reduces substantially the standard deviation: from 0.19 and 0.20 for the CSP plant and wind farm individually to only 0.13 for the combined CSP+WF. Reference values are considerable higher: 0.21 for the combined CSP+WF compared to the 0.13 value obtained when locating the CSP plant and wind farm plants according to the CCA balancing patterns.

Study period	CSP	WF	WF+CSP
Winter (Reference)	0.20	0.34	0.21
Winter 1	0.19	0.20	0.13
Winter 2	0.16	0.21	0.13
Spring (Reference)	0.20	0.31	0.20
Spring 1	0.21	0.31	0.17
Spring 2	0.11	0.35	0.20
Summer (Reference)	0.19	0.25	0.17
Summer 1	0.19	0.24	0.15
Summer 2	0.20	0.13	0.11
Autumn (Reference)	0.19	0.31	0.19
Autumn 1	0.20	0.20	0.14
Autumn 2	0.21	0.25	0.17
Annual (Reference)	0.25	0.17	0.19
Annual 1	0.20	0.31	0.20
Annual 2	0.19	0.36	0.19

Table 6.2. Standard deviation of the hourly capacity factor of a CSP plant, wind farm (WF) and the combined CSP+WF. Values were computed at the locations selected for each mode (Figs. from 6.4 to 6.13) and for the corresponding time period. For each season and for the annual case, the mean values of the standard deviations along the study area (only inland) obtained when locating at the same grid point the CSP plant and wind farm are also displayed (reference value).

The time series of the second mode (Fig. 6.5c) have a canonical correlation of 0.43. Both the wind and solar time series exhibit an upward trend. This second mode accounts for around 25% of the solar energy field variability and only 9% of the wind energy field variability. Their spatial patterns (Figs. 6.5a and 6.5b) are less interesting from the balancing point of view than those corresponding the first mode. Particularly, a coupling (not balancing) between the solar energy in the east of the study region (where correlation reaches 0.8) and the wind energy in the south, near the Mediterranean coast (where correlations values approach 0.8) are observed. Only modest negative correlations are observed in the mountain areas of the southeast of the study area (Sierra Nevada), but values are below -0.2. Therefore, this second canonical mode accounts for a small balancing between wind energy at these last areas and the solar energy in the eastern part of the study region.

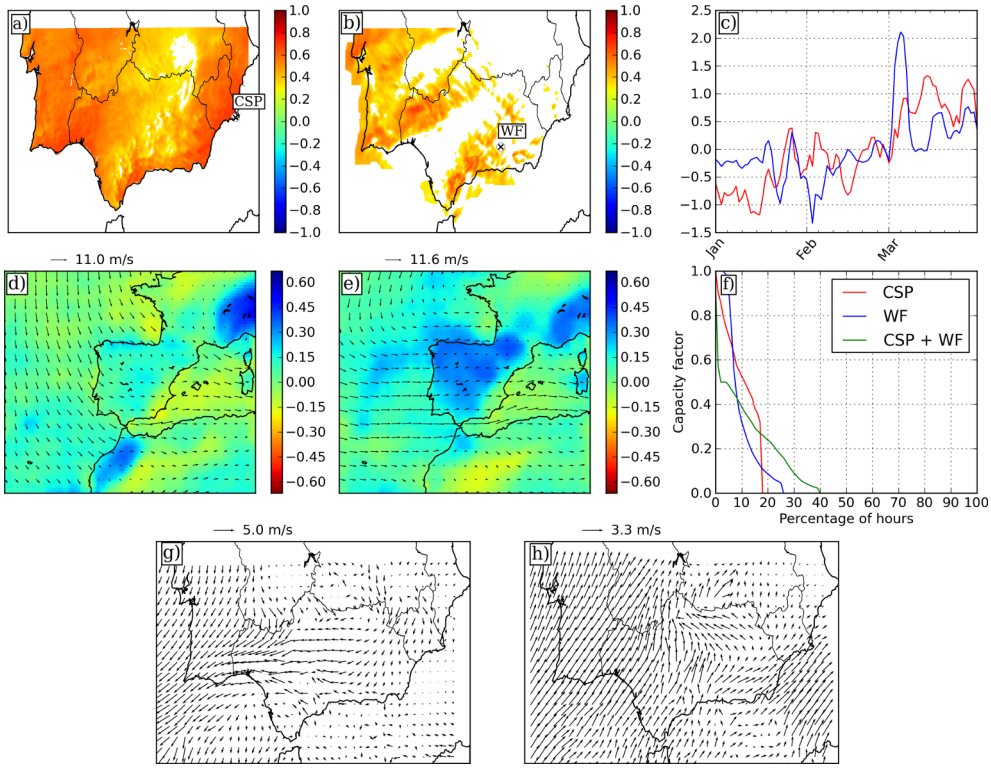


Figure 6.5. As in Fig. 6.4, but for second mode of winter analysis. The two crosses indicate the cells selected for the analysis.

The above mentioned coupling is associated with a marked zonal circulation over the study area. Positive solar energy anomalies in the eastern part of the study area are associated with the presence of north-westerly winds (Figs. 6.5d and 6.5g), that provide clear-sky conditions to this area once they crosses the whole Iberian Peninsula (high positive loads in Fig. 6.5a). The interaction of these westerly winds with topography brings positive wind energy anomalies at the south of the study area, near to the Mediterranean coastal areas, and to some part in the southwest of the study region. In contrast, negative solar energy anomalies are observed associated with a low pressure center over the north of the Iberian Peninsula. This center gives rise to south-westerly winds (Figs. 6.5e and 6.5h), usually bringing warm and humid air into the west of the study area, fostering more cloudiness and resultant negative solar energy anomalies. Positive wind energy anomalies are the results of the interaction of this flow with the topographic features of the southeastern part of the study region. Results in Fig. 6.5f

reflect the relatively low balancing pattern derived from this second winter mode. For instance, when locating the CSP plant and wind farm as showed in Figs. 6.5a and 6.5b, the combined CSP+WF capacity factor only shows a non-zero value 45% of the time. In addition, note the modest capacity factor of the wind farm when located as indicated in Fig. 6.5b. Regarding the standard deviation (Table 6.2), the combined CSP+WF shows a value of 0.13, compared to the 0.16 for the CSP plant and 0.21 of the wind farm. Compare to the first winter mode, the standard deviation of the CSP+WF is similar, but the capacity factor is substantially lower.

6.3.2 Spring

Two modes with a canonical correlation higher than 0.4 were found for winter (Table 6.1). The time series of the leading mode (Fig. 6.6c) have a canonical correlation of 0.66. Both the solar and wind energy canonical time series exhibit a considerable variability, mainly at synoptic time scale (3 to 6 days). This leading mode of the spring analysis accounts for around 34% of the variance of the solar energy and 27% of the wind energy fields. Their respective spatial patterns (Figs. 6.6a and 6.6b) closely resemble those of the winter leading mode (Figs. 6.6a and 6.6b), but loading values are slightly lower. Positive loads on the solar energy field are observed in almost the entire region (except the extreme southeast), with the highest values (0.7) at the north of the study region. Wind energy shows negative loads in almost the entire region (especially in the northeastern part, where loadings reach -0.7), except in the western part of the strait of Gibraltar area (where loading values approach 0.6). Therefore, as in the first winter mode, this first spring mode accounts for a balancing effect between the solar energy and the wind energy in the whole region except the western part of the strait of Gibraltar area and the southeast part of the study region.

Mesoscale atmospheric conditions are similar to those observed for the winter leading mode (Fig. 6.4). On one hand, positive solar and negative wind energy anomalies are associated with north-easterly flow over the study region (Figs. 6.6d and 6.6g). This circulation brings, usually, cold dry atmospheric conditions over the study region, causing positive solar energy anomalies. The relatively weak north-easterly winds are channeled and intensified in the Grazalema mountains and the strait of Gibraltar area

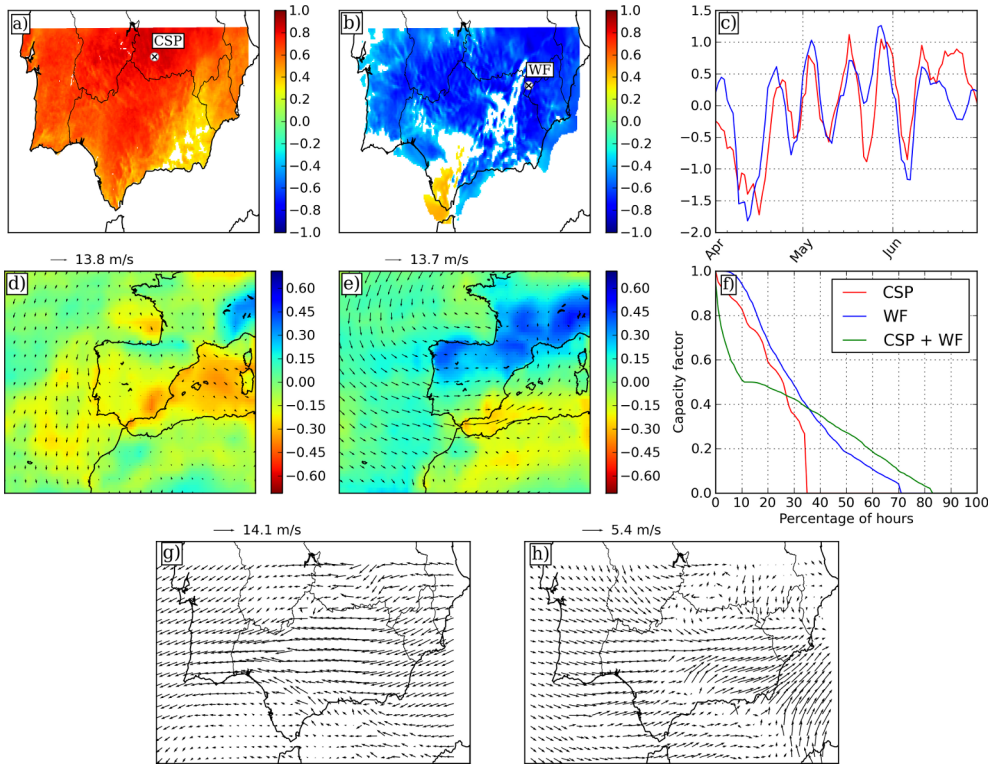


Figure 6.6. As in Fig. 6.4, but for first mode of spring analysis. The two crosses indicate the grids selected for the analysis.

(easterly winds), given rise to the weak but positive wind energy anomalies in this area. On the other hand, negative solar and positive wind energy anomalies are associated with low pressure over France (Figs. 6.6e and 6.6h). In the last cited scenario, frontal activity brings cloudiness to most of the region, therefore, reducing the solar energy availability. Moreover, this frontal activity brings positive wind energy anomalies, except for the western strait of Gibraltar area. Maximum wind energy anomalies are observed over the Cazorla area, where the westerly winds associated with the low are enhanced by to the topographic features.

As for the first winter mode, the former results indicates the existence of a notable balancing between the wind and solar energy resources in the study area. Fig. 6.6f shows the hourly capacity factor of a CSP plant and the wind farm located at the grid points indicated in Figs. 6.6a and 6.6b, respectively, locations with the highest positive (solar)

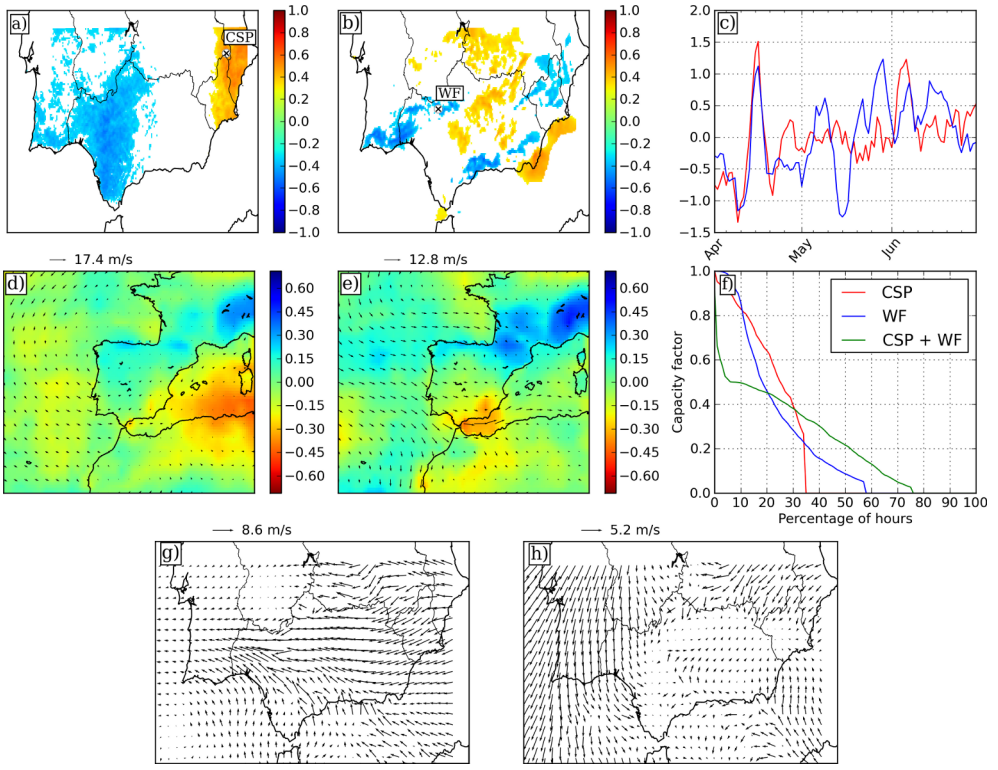


Figure 6.7. As in Fig. 6.4, but for second mode of spring analysis. The two crosses indicate the grids selected for the analysis.

and negative (wind) loading and, therefore, the highest balancing. All capacity factors are considerable higher than those obtained in the winter analysis. A non-zero CSP capacity factor is available more than 40% of the time, with values close to 1 around 20% of the time. Regarding the wind energy, a non-zero value is obtained above 70% of the time, with values close to 1 around 10% of the time. Finally, the combined CSP+WF shows a considerable improvement in the capacity factor: a non-zero value is obtained around 85% of the time, with values above 0.5 around 40% of the time. Moreover, a considerable reduction in the standard deviation is obtained when combining the CSP plant and wind farm (Table 6.2): from 0.21 and 0.31 for the CSP plant and wind farm individually to 0.17 for the combined CSP+WF (reference value is 0.20).

The time series of the second mode (Fig. 6.7c) have a canonical correlation of 0.43. This second mode accounts for around 16% of the solar energy field variability and only 7%

of the wind energy field variability. Their spatial patterns (Figs. 6.7a and 6.7b) shows a balancing between the solar energy resources in the western of the study region and the wind energy resources in the central and very eastern part of the study area. Maximum solar energy loads (0.7) are found in center of the Guadalquivir valley, while maximum negative wind energy loads (-0.7) are observed over the southeastern coastal area of the study region. These positive solar energy and negative wind energy anomalies are associated with north flows over the study region (Figs. 6.7d and 6.7g). This circulation brings clear-sky conditions over the western half of the study area and, then, positive solar energy anomalies. In contrast, the interaction of the mesoscale northerly flow with topography gives rise to weak southerly winds over the southwest of the study region, causing negative wind energy anomalies in this region. Figs. 6.7e and 6.7h shows that negative solar energy anomalies in the western half of the study region are associated with southeasterly winds over the study region, which brings cloudy conditions. In contrast, this mesoscale circulation gives rise to strong north-easterly winds and, then positive wind energy anomalies over the southeast of the study region. The topographic enhancement of this flow gives also rise to positive wind energy anomalies in the Cazorla mountain areas.

Fig. 6.7f shows the hourly capacity factor of a CSP plant and the wind farm located at the grid points indicated in Figs. 6.7a and 6.7b, representing the grids with the highest balancing. Capacity factors are notably: a non-zero CSP capacity factor is available more than 40% of the time, with values close to 1 around 20% of the time. Regarding the wind energy, a non-zero value is obtained near 70% of the time, with values close to 1 around 10% of the time. Finally, the combined CSP+WF show a considerable improvement in the capacity factor (although less than in the first spring mode): a non-zero value is obtained around 75% of the time, with values above 0.5 around 30% of the time. To conclude, Table 6.2 shows a considerable reduction in the standard deviation when combining the CSP plant and wind farm: from 0.22 and 0.35 for the CSP plant and wind farm individually to 0.20 for the combined CSP+WF.

6.3.3 Summer

Two modes with a canonical correlation higher than 0.4 were found for summer (Table 6.1). The time series of the leading mode (Fig. 6.8c) have a canonical correlation of 0.62. Both the solar and wind energy canonical time series exhibit a negative trend. This leading mode of the summer analysis accounts for around 65% of the variance of the solar energy and 17% of the wind energy fields. Their respective spatial patterns (Figs. 6.8a and 6.8b) resemble those of the second spring mode (Figs. 6.7a and 6.7b), but loading values are substantially higher. Positive loads on the solar energy field are observed in the entire region, with the highest values (0.8) at the central area. Wind energy shows a dipolar behavior, with positive loads in the western part of the study region and negative loads in the southeastern part, where maximum negative values (-0.7) are observed. Therefore, this first summer mode accounts for a balancing effect between the solar energy in the whole study region and the wind energy the southeastern part of this study area.

The associated mesoscale atmospheric conditions are similar to those observed for the second spring mode (Fig. 6.7). The positive solar and negative wind energy anomalies are associated with northerly flow over the study region (Figs. 6.8d and 6.8g). This circulation brings clear-sky conditions over the whole study region and, then, positive solar energy anomalies. In contrast, the interaction of the mesoscale northerly flow with topography give rise to weak southerly winds over the southwest of the study region, given rise to negative wind energy anomalies in this region. Figs. 6.8e and 6.8g shows that negative solar energy anomalies in the region are associated with southwesterly winds. Moreover, this mesoscale circulation gives rise to strong north-easterly winds and, then positive wind energy anomalies, over the southeast of the study region and the Cazorla mountains (this last due to topographic enhancement of the wind flow).

The notably coupling observed in this first summer mode is further confirmed in the analysis of the capacity factors. Fig. 6.8f shows the capacity factor of a CSP plant and the wind farm located at the grid points indicated in Figs. 6.8a and 6.8b, representing the grids with the highest balancing. As expected, the CSP capacity factor shows high values: a non-zero value is available about 45% of the time, with values close to 1 more than 20% of the time. Regarding the wind energy, values are lower than for the spring

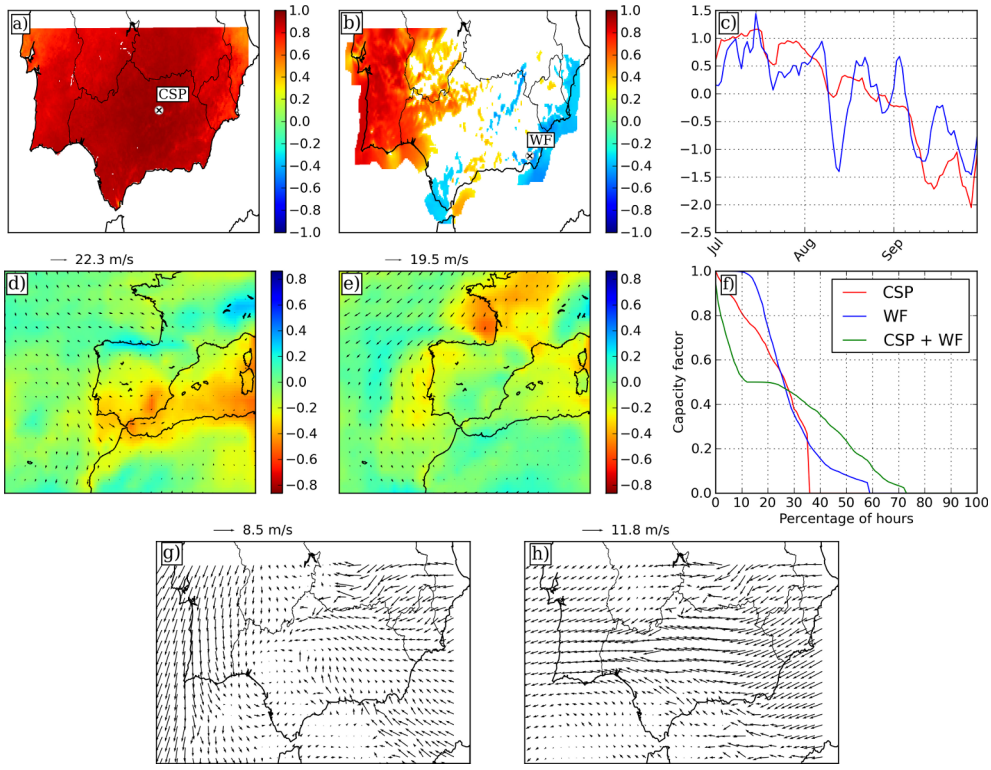


Figure 6.8. As in Fig. 6.4, but for first mode of summer analysis. The two crosses indicate the grids selected for the analysis.

analyses: a non-zero value is obtained near 50% of the time, with values close to 1 around 5% of the time. Finally, the combined CSP+WF shows a very important improvement (higher than those obtained during winter and spring) in the capacity factor: a non-zero value is obtained around 75% of the time, with values above 0.5 around 30% of the time. To conclude, a considerable reduction in the standard deviation is obtained when combining the CSP plant and wind farm (Table 6.2): from 0.19 and 0.24 for the CSP plant and wind farm individually to 0.15 for the combined CSP+WF.

The time series of the second mode (Fig. 6.9c) have a canonical correlation of 0.44. Both the wind and solar time series exhibit a considerable variability at synoptic time scales. This second mode accounts for around 7% of the solar energy and 12% of the wind energy field variability. Their respective spatial patterns (Figs. 6.9a and 6.9b) resemble those of the first winter (Fig. 6.4) and spring modes (Fig. 6.6). In particular, these patterns

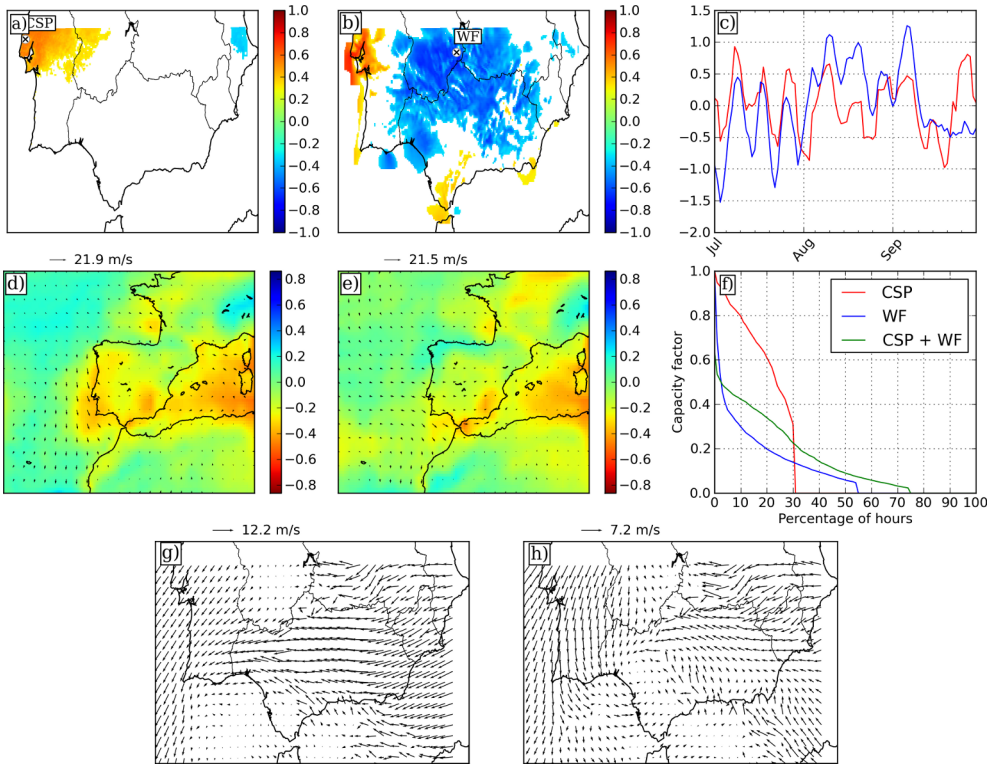


Figure 6.9. As in Fig. 6.4, but for second mode of summer analysis. The two crosses indicate the grids selected for the analysis.

show a weak, but significant, balancing between the solar energy resources at the north west, where maximum positive correlation (0.6) are observed, and the wind energy resources at the central area of the study region, where maximum negative correlation (-0.6) are identified. This balancing is associated with a marked meridional circulation over the study area. Positive solar energy anomalies in the northwestern and negative wind energy in central part of the study area are associated with northeasterly winds (Figs. 6.9d and 6.9g). The interaction of these westerly winds with topography brings positive wind energy anomalies at the northwest and some areas in the south of the study region. In constrast, negative solar energy and positive wind energy anomalies are associated with north winds over the western and easterly winds over the rest of the study region (Figs. 6.9e and 6.9h).

Results in Fig. 6.9f reflect the notably balancing derived from this second summer mode.

CSP capacity factor shows a high value (but lower than in the first summer mode): a non-zero value is available about 38% of the time, with values close to 1 about 15% of the time. Regarding the wind energy, a non-zero value is obtained near 55% of the time, but values close to 1 are hardly observed. Finally, the combined CSP+WF shows a very important improvement the capacity factor: a non-zero value is obtained around 80% of the time, with values above 0.5 around 20% of the time. Moreover, a notable reduction of the standard of capacity factor deviation is observed in the combined CSP+WF: from 0.20 and 0.13 for the CSP plant and wind farm individually to 0.11 for the combined CSP+WF (reference value is 0.17).

6.3.4 Autumn

The leading mode of the autumn analysis shows the most interesting balancing pattern. The time series of this leading mode (Fig. 6.10c) has a canonical correlation of 0.68 (the highest correlation in all the study). A clear negative trend is observed in both the solar and wind time series, along with a considerable variability at synoptic time scale. This leading mode accounts for around 34% of the solar energy field variability and for about 50% of the wind energy field variability. The respective spatial patterns clearly resemble those of the first winter (Fig. 6.4) and spring (Fig. 6.6): a balancing effect between the solar and wind energy resources almost region-wide. Relative high positive loading factors are observed for the solar energy at the center of the study region (Fig. 6.10a), reaching 0.8. However, in the western and eastern areas, loadings are weaker. In contrast, large negative loadings are observed for the wind energy field across the entire region, except in the very west and in some areas in the south and east. Therefore, the leading mode of the autumn CCA analysis indicates a general balancing between solar and wind energy, nearly extending over the entire region. Positive solar and negative wind energy anomalies are associated with easterly winds over the study region in the region (Figs. 6.10d and 6.10g). Negative solar and positive wind energy anomalies are associated with a low pressure center located over France (Fig. 6.10e). This low pressure center brings southwesterly winds over the study area (Fig. 6.10h), and their associated frontal activity brings cloudiness and relatively high wind speeds, causing negative solar and positive wind energy anomalies.

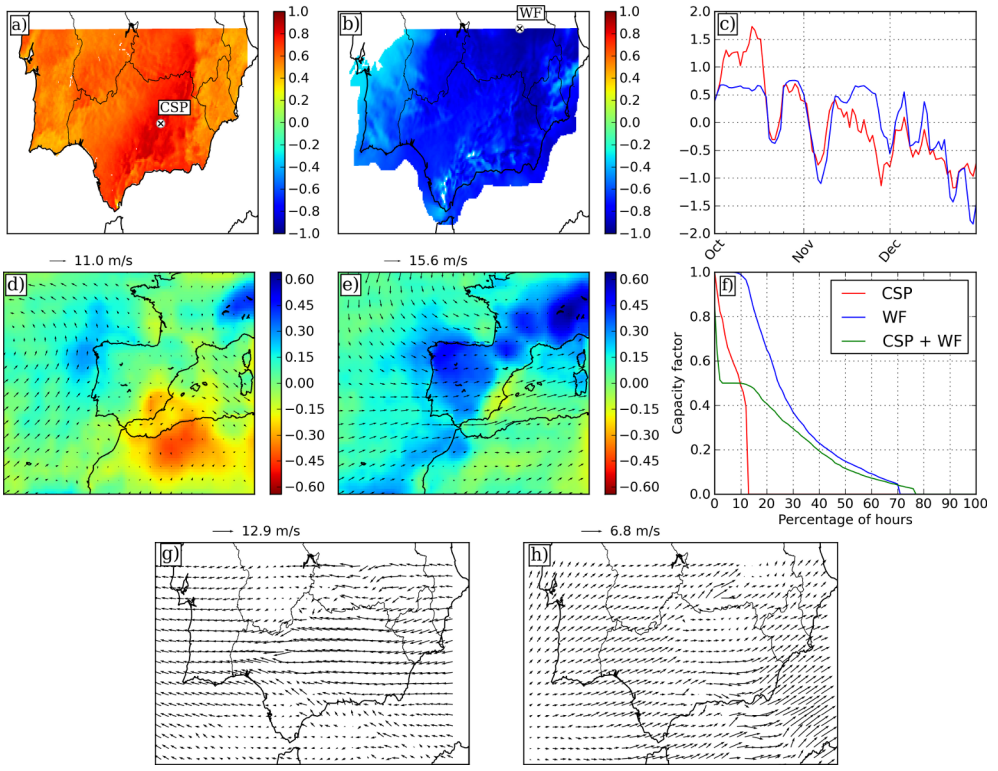


Figure 6.10. As in Fig. 6.4, but for first mode of autumn analysis. The two crosses indicate the grids selected for the analysis.

Results in Fig. 6.10f reflect the notably balancing pattern derived from this first autumn mode. As may be expected, CSP capacity factor shows relatively low values: a non-zero value is only available about 20% of the time, with values close to 1 about 5% of the time. Regarding the wind energy, a non-zero value is obtained near 70% of the time, with values close to 1 about 10% of the time. Finally, the combined CSP+WF shows an important improvement of the capacity factor: a non-zero value is obtained around 80% of the time, with values above 0.5 around 20% of the time. Finally the standard of capacity factor of the combined CSP+WF is considerable low 0.14, compared to the 0.20 value of both the CSP and Wind farm individually (Table 6.2).

The time series of the second mode (Fig. 6.11c) have a canonical correlation of 0.49. Both the wind and solar time series exhibit a considerable variability at synoptic time scales. This second mode accounts for around 20% of both the solar and wind

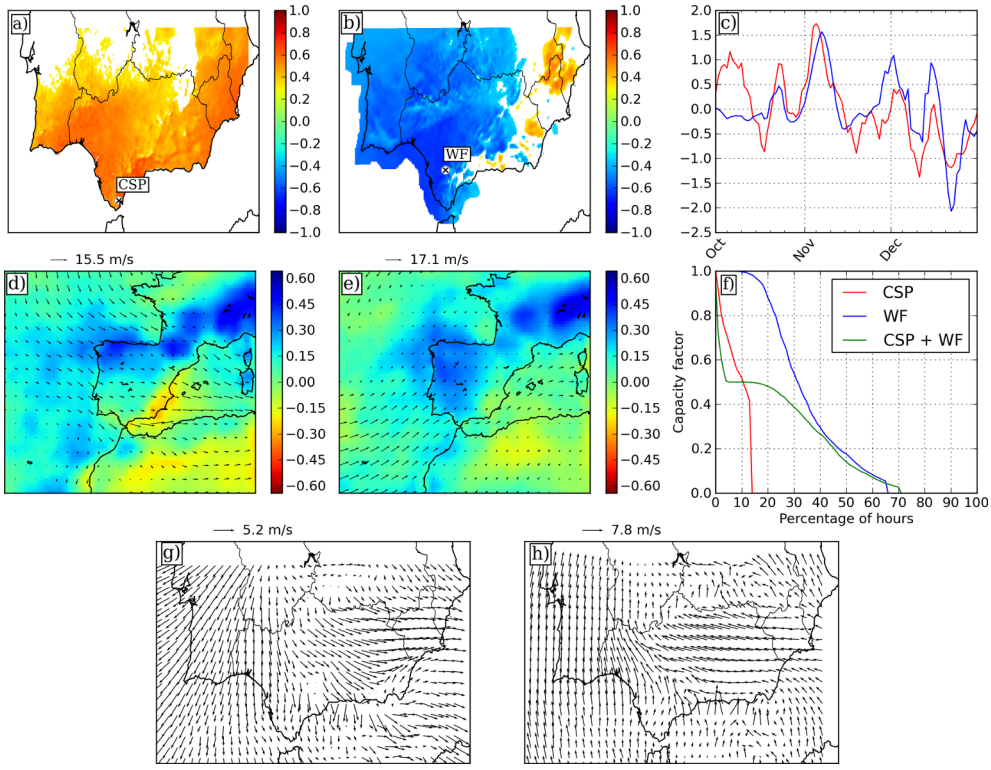


Figure 6.11. As in Fig. 6.4, but for second mode of autumn analysis. The two crosses indicate the grids selected for the analysis.

energy fields variability. Their respective spatial patterns (Figs. 6.11a and 6.11b) show a balancing between the solar energy resources at half south and the wind energy at half west of the study region. Maximum positive correlations in the solar field (0.6) are observed near the Mediterranean coast in the south and at the northeast of the study region. Maximum negative loadings (-0.6) in the wind field are identified at the southwest of the study area. Areas of positive loading factors in the wind energy field are observed and the northeast and some mountainous zones at the southeastern of study region.

This balancing is associated with a marked meridional circulation over the study area. Positive solar energy anomalies in the half south and negative wind energy ones at the half west of the study area, are associated with northwesterly winds (Figs. 6.11d and 6.11g). These winds brings cloud-free conditions, and then positive solar energy

anomalies, to the south of the study region (air masses loss their humidity when travelling across the Iberian Peninsula). In contrast, winds are weaker than normal over the half east of the study area (negative wind energy anomalies). Positive wind energy loads observed in Fig. 6.11b are caused by the interaction of these northwesterly winds with topography. In constrast, negative solar energy and positive wind energy anomalies are associated with southeasterly flows over the study area (Figs. 6.11e and 6.11h). This flow brings cloudy conditions, reducing the solar energy availability, but giving rise to positive wind speed, and then, positive wind energy anomalies over the half west part of the study area.

As in the first mode, CSP capacity factor values are relatively low (Fig. 6.11f): a non-zero value is observed about 20% of the time, with values close to 1 about 5% of the time, for the location highlighted in Fig. 6.11a. Regarding the wind energy, a non-zero value is obtained near 65% of the time and values close to 1 are observed about 10% of the time at the grid point highlighted in Fig. 6.11b. Finally, the combined CSP+WF shows a notable improvement the capacity factor: a non-zero value is obtained around 75% of the time, with values above 0.5 around 20% of the time. As in the previous case, the standard deviation (Table 6.2) is notably reduced: from 0.21 for the CSP plant and 0.25 for the wind farm to 0.17 for the combined CSP+WF.

6.3.5 Annual period

Results of the previous sections show considerable seasonal differences in both the spatial patterns and the strength of the balancing patterns. Results of the annual analysis reflect the most important seasonal pattern characteristics. In particular, two modes were analyzed as results of the annual study. The time series of the leading mode (Fig. 6.12c) have a canonical correlation of 0.54 (Table 6.1). The time series show a better agreement in winter and spring than in the rest of the year. A clear annual cycle is presented, with higher values during summer. Monthly and synoptic scales of variability are also evident. This leading mode accounts for a substantial part of the variance of the solar energy (62%) wind energy (44%) fields. Their respective spatial patterns (Figs. 6.12a and 6.12b) clearly resembles those of the first winter (Fig. 6.4), spring (Fig. 6.6) and autumn (Fig 10) modes and the second summer mode (Fig. 6.9). Positive loadings on the solar energy

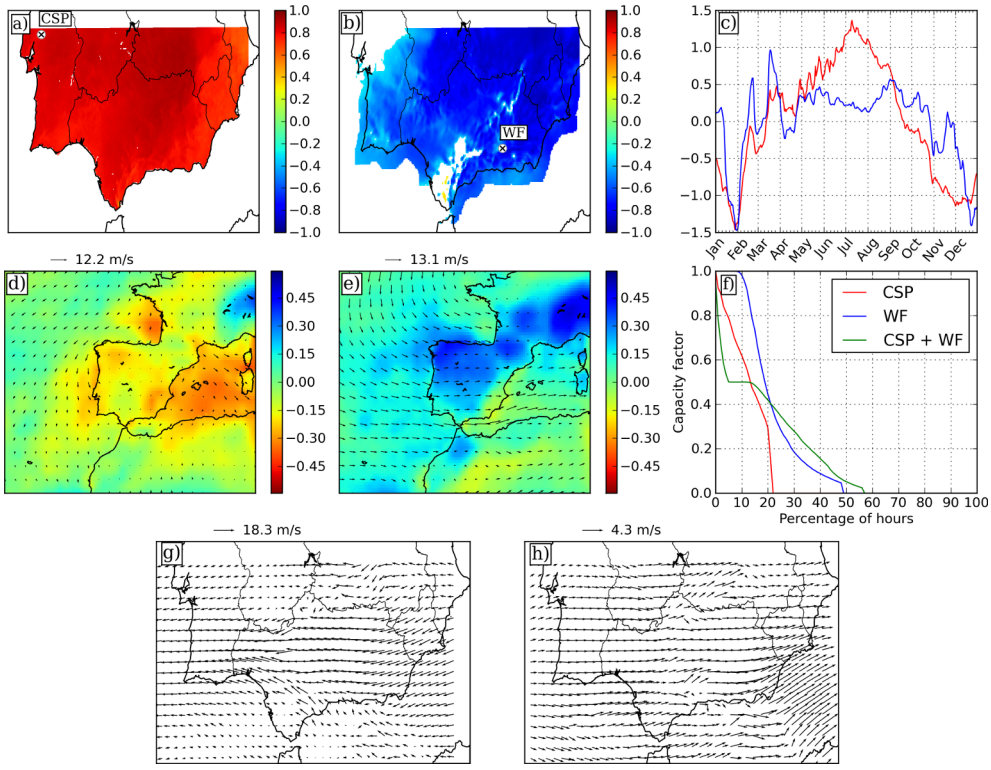


Figure 6.12. As in Fig. 6.4, but for first mode of the annual analysis. Composites in d), e), g) and h) were obtained based on the 30 highest positive and lowest negative anomalies of the solar energy canonical time series. Canonical time series have been filtered with a 20-day moving average filter. The two crosses indicate the grids selected for the analysis.

field are observed in the entire region (Fig. 6.12a), with maximum values (0.8) over the central area. In the wind energy field (Fig. 6.12b), negative loads are observed the whole region (highest negative loads at the northeastern, -0.8) except the western part of the strait of Gibraltar area. Therefore, this first mode annual mode accounts for a balancing effect between the solar energy and the wind energy in the whole region except in the western part of the strait of Gibraltar area.

The mesoscale atmospheric circulation conditions associated with this first annual mode (Figs. 6.12d, 6.12e, 6.12g and 6.12h) are similar to that found associated with the first winter mode (Fig. 6.4).

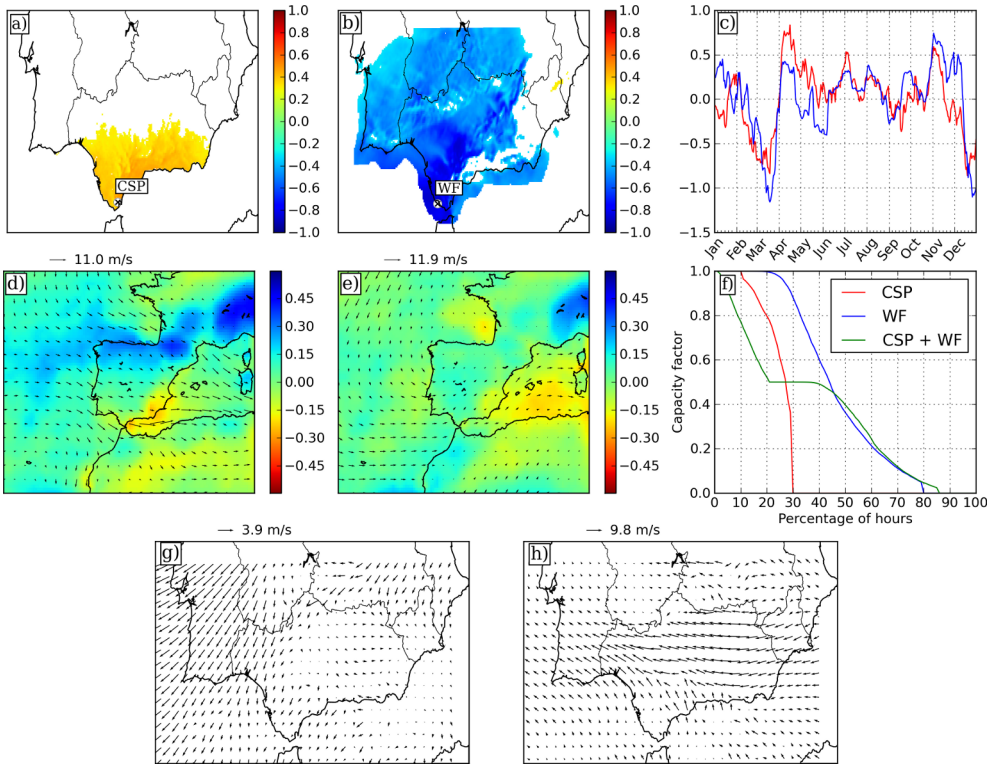


Figure 6.13. As in Fig. 6.12, but for second mode of the annual analysis. The two crosses indicate the grids selected for the analysis.

The former balancing patterns are clearly reflected in the capacity factor analysis (Fig. 6.12f). When located at the grid point highlighted in Fig. 6.12a, the CSP plant shows a non-zero value around 30% of the year, with values close to 1 around 15% of the time. The wind farm located at the grid point selected in Fig. 6.12b report non-zero capacity factor about 65% of the time, with values close to 1 around 10% of the time. Note the relatively small spatial separation between the two plants (about 100 km). Finally, the combined CSP+WF shows a considerable improvement in the capacity factor: a non-zero value is obtained near 80% of the time, with values above 0.5 near 30% of the time. Lastly, a remarkable reduction in the standard deviation of the capacity factor connecting the CSP and WF is observed: from 0.2 for the CSP plant and 0.25 for the wind farm to 0.15 for the combined CSP+WF (Table 6.2). Note that the reference value for the combined CSP+WF is 0.2.

The time series of the second mode (Fig. 6.13c) have a canonical correlation of 0.3. This second mode accounts for around 4% of the solar energy field variability and only 19% of the wind energy field variability. The time series show, mainly, variability at synoptic times scales. Their spatial patterns (Figs. 6.13a and 6.13b), resemble those of the second spring (Fig. 6.7) and autumn (Fig. 6.11) modes, and show a weak but significant balancing between the solar energy at the south and the wind energy in the half west of the study region. Maximum solar energy loads (0.5) are found at eastern part of Gibraltar strait area while maximum negative (-0.7) wind energy loads are observed western of this area (maximum values are located at offshore grid points). The mesoscale atmospheric circulation conditions associated with this second annual mode (Figs. 6.13d, 6.13e, 6.13g, and 6.13h) are similar to that found associated with the second spring mode (Fig. 6.7).

The analysis of the capacity factor of a CSP plant and a wind farm located as indicated in Figs. 6.13a and 6.13b, respectively, shows valuable results. As in the previous case, there is a relatively small spatial separation between the two plants (about 100 km). Capacity factors of the CSP are non-zero about 30% of the time, with values close to 1 around 10% of the time (Fig. 6.13f). Values are lower than in the previous annual mode. For the wind farm, a non-zero value is obtained 80% of the time and values close to 1 around 20% of the time. These values are substantially higher than those obtained in the first annual mode. Finally, the combined CSP+WF shows a slightly improvement in the capacity factor: a non-zero value is obtained around 85% of the time, with values above 0.5 around 40% of the time. Note that, although the improvement obtained with the combination of the CSP plant and the wind farm is lower than those obtained with the first annual mode (Fig. 6.12f) the percent of time with capacity factor above 0.5 is substantially higher. This is mainly due to the good wind energy resources of the location highlighted in Fig. 6.13b. Finally, a notable reduction in the standard deviation is obtained by combining the CSP and wind farm: from 0.19 and 0.36 for the CSP plant and wind farm individually to 0.19 for the combined CSP+WF.

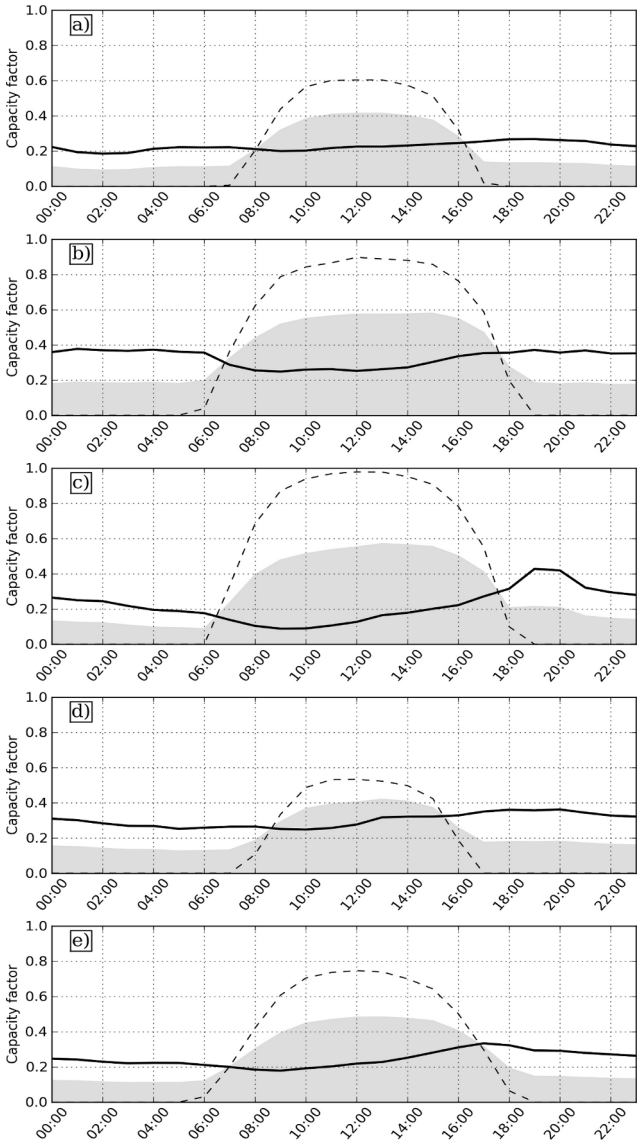


Figure 6.14. a) Daily mean cycle of the hourly wind (continuous line), CSP (dashed line) and combined CSP+WF (shaded areas) capacity factor values for the location highlighted in Fig. 6.4 (first winter mode). b) As in a) but for the locations highlighted in Fig. 6.6 (first spring mode). c) As in b) but for the locations highlighted in Fig. 6.8 (first summer mode). d) As in a) but for the locations highlighted in Fig. 6.10 (first autumn mode). e) As in a) but for the locations highlighted in Fig. 6.12 (first annual mode). The daily mean cycle was computed based on the corresponding analysis period.

6.3.6 Balancing time series analysis

Fig. 6.14 shows the daily mean cycle of the hourly capacity factors of CSP, WF and CSP+WF for the first mode of the five studied periods. Aside from the obvious balancing associated to the day and night periods, and caused by the cero CSP energy production during the nights, Fig. 6.14 shows also other interesting features. Firstly, the wind capacity factors tend to be higher when the CSP capacity factors are lower or event zero and vice-versa. For instance, in spring and summer (Figs. 6.14b and 6.14c), the minimum wind capacity factors are observed during the central part of the day, when the CSP capacity factors shows the maximum values. During spring (Fig. 6.14b) the capacity factor values during the central part of the day are about half of those observed the rest of the day (about 0.25 versus 0.4). This difference is even higher during summer (Fig. 6.14c): from about 0.15 at 10:00h to more than 0.4 about 20:00 h. This late case shows the most evident lag between the CSP plant peak production time, at midday, and corresponding time for the wind farm, about 20:00 h, i.e, a time lag of about 8 hours. For winter (Fig. 6.14a) and autumn (Fig. 6.14 d), a similar time lag between the CSP plant and wind farm peak production is observed. Nevertheless, for these last cases, wind capacity factor shows lower differences along the day than in spring and summer. Overall, the best balancing between the solar and wind energy production is observed during spring. For this season, wind energy production is higher not only during the afternoon (as in summer and autumn) but also during the night (period 00:00 h to 6:00).

Finally, the annual case (Fig. 6.14e) shows similar features as those observed in the seasonal analysis. In particular, wind energy production is lower when the solar energy production is higher. The main difference is that the time lag between peak productions is lower (about 5 hours), since the peak of the wind energy is observed about 17:00 h. Wind energy capacity factor along the day varies from 0.2 near midday to more than 0.3 near the peak at 17:00 hours. Lastly, note that, in all the analyzed cases, the differences along the day of the CSP capacity factor are substantially higher than in the case of the wind farm. Based on these differences, and in order to provide a stable energy production along the day taking advantage of the balancing between the solar and wind energy production, the wind energy installed capacity should be substantially higher than those of the solar energy. On a first approach, and based on results in Fig. 6.14, it seems that wind energy installed capacity should be two or three times those of the solar energy.

Nevertheless, this issue merit a further analysis not attempted here.

6.4 Summary and conclusions

In this work, we have proposed and evaluated a method for analyzing the potential contribution of wind power and concentrating solar power (CSP) technologies to stable (baseload) power over a region. The method attempts to find the optimal distribution of wind farms and CSP plants over a territory in order to minimize the variability of energy input into the power supply system. The methodology, first, applies a canonical correlation analysis (CCA) to solar (obtained based on direct normal irradiation, DNI) and wind energy fields in the region, and then analyzes the corresponding coupled spatio-temporal canonical patterns. Secondly, and based on the former analysis, the best location of CSP plants and wind farms, regarding a stable production, are localized. At these locations, the capacity factor of a reference CSP plant and wind turbine and that obtained when connecting both (combined CSP+WF) were computed and evaluated. In addition, standard deviations of the hourly capacity factors, for both standalone wind turbine and referenced CSP plant and the CSP+WF, factor were analyzed. This allowed for a quantitate evaluation of the balancing between the CSP plant and wind farm and, then, for the eventual contribution of these renewable technologies to stable power.

The method was tested in the southern half of the Iberian Peninsula, covering about 350.000 km2. The study region, though relatively small, possesses considerable spatial variability in the main climate variables, owing to varied topographic features and the influence of the adjacent Mediterranean Sea and Atlantic Ocean. In addition, this areas possess considerable wind energy resources and, particularly, solar energy resources. Principally, this region is has highest CSP installed capacity (about 1 GW) in the world. We used wind and solar energy estimates from the Weather Research and Forecasting (WRF) mesoscale model. Daily-integrated solar and wind (at 80 m AGL) energy fields from 2009 were analyzed, at a spatial resolution of 3 km over the region, including offshore areas up to 20 km from the coast. Independent seasonal and annual analyses were done, and the atmospheric circulations associated with each coupled canonical mode were investigated.

First of all, the results showed the existence of valuable balancing between the solar (obtained based on direct normal irradiation) and wind energy resources over the study region for the all the analyzed periods. Although the balancing pattern differed among seasons, there were some common features across seasons that are reflected in the annual analysis. The most important spatial balancing pattern was found to be between the solar energy resources in the whole region and the wind energy resources in all the study area except the western part of the Strait of Gibraltar zone. This balancing pattern was the leading one, and therefore the stronger one, for the winter, spring and the annual analysis. During autumn this balancing between the solar and wind energy resources even extended over the whole study region, including the strait of Gibraltar area. The explained variance associated with this leading mode ranged from 34% (autumn and spring) to 62% (annual) in the solar field and from 27% (spring) to 50% (autumn) in the wind energy field. The former balancing pattern was explained based on zonal circulation and their interaction with the topography over the study area. The leading summer mode showed to be different, accounting for a balancing between the solar energy in the whole study region and the wind energy in the southeastern part of the study area. The second most important balancing mode was found to be between the solar energy resources at the south and the wind energy resources in the half west of the study region. This pattern was the second mode for the spring, autumn and annual analysis and was explained based on meriodional circulation and their interaction with the topography over the study area. The explained variance associated with this second mod ranged from 4% (annual) to 20% (autumn) in the solar field and from 7% (spring) to 20% (autumn) in the wind field.

The analysis of the power generation of CSP plant and wind turbines located taking advantage of the aforementioned spatial balancing patterns showed some interesting results. Firstly, the capacity factor availability of the aggregated CSP plant and wind farm showed a significant increment compared to those of the individual CSP plant and wind farm. As may be expected, this increment was more important when allocating the wind farms and solar plant based on the results of the leading canonical modes. For the winter leading mode, a non-zero value for the capacity factor was found around 65% of the time (10% for the CSP and 45% for the wind farm individually), with values above 0.5 (i.e., equivalent to capacity factor 1 for the CSP plant or the wind farm) close to 25% of the time. The leading spring mode showed, probably, the most interesting results:

a non-zero value for the CSP capacity factor 85% of the time (40% for the CSP and 70% for the wind farm individually), with values above 0.5 around 40% of the time. The leading summer mode showed also notable results: a non-zero value for the CSP capacity factor around 75% of the time (45% for the CSP and 50% for the wind farm individually), with values above 0.5 around 30% of the time. Also the leading autumn mode provided notable results: a non-zero value for the CSP capacity factor was found around 75% of the time (45% for the CSP and 50% for the wind farm individually), with values above 0.5 around 30% of the time. Finally, the leading annual mode showed similar results: a non-zero value for the CSP capacity factor was found near 80% of the time (30% for the CSP and 65% for the wind farm individually), with values above 0.5 around 30% of the time.

Finally, the analysis of the mean daily cycle of the hourly wind, CSP and combined CSP+WF capacity factor time series for the leading CCA modes showed some interesting features. Notably, the minimum wind power capacity factors are observed along the central part of the day, when the CSP capacity factors shows the maximum values. In addition, for the all the seasonal analysis, a lag of about 8 hours was observed between the CSP plant (about midday) and the wind farm (about 20:00 h) maximum power production time. For the annual analysis, this lag reduced to 5 hours. Finally, it was observed that the differences along the day of the CSP plants capacity factor were substantially higher than in the case of the wind farms. Based on these differences, and in order to provide a stable energy production along the day taking advantage of the balancing patterns, it was concluded that the wind energy installed capacity should be two or three times higher than those of the solar energy. Nevertheless, the analyses of the best mix of solar and wind energy resources in the study region merit a separate analysis not attempted here.

The former results shows that availability of the power provided by the combination of CSP plant and the wind farm, when taking advantage of the CCA balancing pattern, can be close to availability provided fossil-fuel based power plants and, therefore, close to be considered baseload power. In addition, the use of the energy storage capabilities of the CSP plants, not considered here, by taking into account the results of the hourly mean capacity factor analysis, may results in a considerable increment in the power availability. This analysis will be attempted in a future work.

The analysis presented in this work can be easily applied to areas of arbitrary size, facilitating the planning of the location of future wind farms and CSP plants within a region, so that total electricity production will fluctuate less. Particularly, the methodology presented in this work, can be useful in renewable energy integration studies. In these integration studies, the modeled power production of existing and future renewable energy-based power plants (solar plant, wind farms, hydropower plants, etc) located on a particular region, are analyzed in order to obtain the optimal mix regarding a stable, and correlated to the demand, renewable power generation (GE, 2010; Gómez et al., 2010; Heide et al., 2010; Krajacic et al., 2011; Jacobson and Delucchi, 2011; Ruiz-Arias et al., 2012a).

CHAPTER 7

THE IMPACT OF THE NAO ON SOLAR AND WIND ENERGY RESOURCES IN THE MEDITERRANEAN AREA

Pozo-Vázquez D., **F.J. Santos-Alamillos**, V. Lara-Fanego, J.A. Ruiz-Arias, J. and Tovar-Pescador. 2012. *The impact of the NAO on solar and wind energy resources in the Mediterranean Area* in Hydrological, Socioeconomic and Ecological Impacts of the North Atlantic Oscillation in the Mediterranean Region. Springer. 213-231.

7.1 Introduction

According to the latest estimates, it is expected that the worldwide primary energy demand will increase by 45% and the demand for electricity will increase by 80% between 2006 and 2030 (IEA, 2008). As a consequence, and without a decisive action, energy-related greenhouse gases (GHG) emissions will more than double by 2050 and the increased oil demand will intensify the concerns over the security of supplies. There are different pathways to stabilize GHG concentrations, but a key issue in all of them is the replacement of fossil fuels by renewable energy sources. European Union (EU) regulations, for example, set a binding target for 20% of the EU's total energy supply to come from renewable by 2020 (corresponding to a sharp increase from the modest 6.5% observed in 2007). Furthermore, they set a firm target of cutting 20% of the EU's

greenhouse gases emissions by 2020 relative to 1990. In this scenario, solar and wind energies (the renewables with the most mature technology aside from the hydropower) will necessarily play a key role.

There are three main solar technologies: the direct conversion of sunlight into electricity (Photovoltaic, PV), the concentrating solar power (CSP) and the solar thermal collectors for heating and cooling (SHC). PV and CSP technologies are meant to produce electricity, while SHC can only be used for heating and cooling purposes. PV systems enable direct conversion of sunlight into electricity through semi-conductor devices, through the global horizontal irradiance (GHI) they receive. Today, PV provides 0.2% of total global electricity generation, being Germany the leading country in the world, with 5 GW installed capacity, followed by Spain with above 4 GW (about 4% of the installed capacity). While its use is small today, PV power has a promising future. Actually, global PV capacity has been increased at an average annual growth rate of more than 40% since 2000 and it has significant potential for long-term growth over the next decades. In particular, PV is projected to provide around 5% of global electricity consumption by 2030, rising to 11% by 2050 (IEA, 2010a). In this context, the Mediterranean area (France, Italy, Greece) are expected to play a major role (IEA, 2010a). The basic concept of CSP is relatively simple: CSP devices concentrate energy from the sun's rays to heat a receiver to high temperatures. This heat is then transformed first into mechanical energy (by turbines or other engines) and then into electricity. The solar energy that CSP plants use is measured as direct normal irradiance (DNI), which is the energy received on a surface tracked perpendicular to the sun's rays. CSP developers typically set a bottom threshold for DNI of about 2000 $kWhm^{-1}year^{-1}$. Below that, other solar electric technologies that take advantage of both direct and diffuse irradiance, such as PV, are assumed to have a competitive advantage. Good DNI is usually found in arid and semi-arid areas with reliably clear skies, which typically lies at latitudes from 15 to 40° North or South. As a consequence, one of the most favorable areas for the CSP technology is the Mediterranean basin. As of early 2010, the global stock of CSP plants neared 1 GW capacity, mainly in Spain (about 0.5 GW). Projects now in development or under construction in more than a dozen countries (including China, India, Morocco, Spain and the United States) are expected to totalize 15 GW, and CSP is expected to contribute about 5% (1500 GW) of the annual global electricity production in 2050 (IEA, 2010b). In particular, potential in the Middle East and North Africa would cover about 100

times the current consumption of the Middle East, North Africa and the European Union combined (IEA, 2010b). Finally, wind energy is probably the most cost-effective of the renewable energy technologies. It must be stressed that wind energy was the renewable source with the fastest growing rate: since 2000, cumulative installed capacity has grown at an average rate around 30% per year (GWEC, 2007). In 2008, wind energy provided nearly 20% of electricity consumption in Denmark, more than 11% in Portugal and Spain, over 4% of all EU electricity and nearly 2% in the United States (IEA, 2009). By 2030, wind electricity is estimated to be produced annually from over 1000 *GW* of wind installed capacity, corresponding to 9% of global electricity production with an expected rising to 12% in 2050 ((IEA, 2009).

The Mediterranean area presents some special features regarding the transition from a fossil era to a greener one. In fact, the region presents considerable wind and outstanding solar energy resources that would make this transition easier. According to different studies (DLR, 2007; Desertec, 2010; Coopers, 2010), Europe and North Africa together could produce by 2050 about 80% of their electricity needs from renewables, if their respective grids were sufficiently interconnected.

The expected huge development of the renewable energies in the coming decades will demand a corresponding development of the so-called energy meteorology science. Energy meteorology includes all the aspects of the meteorology and climatology relevant for the renewable energies. In fact, the meteorological and climate information is a key issue at the various stages of a renewable energy project, as outlined in Fig. 7.1. In particular, in the first stages (project development), the climate information is required in terms of the resource evaluation. This evaluation includes data obtained based on direct measurement, satellites and models estimations. Once operating, weather forecasts are needed for the yield integration in the power grid. This requires information from both satellite (nowcasting) and forecasts from Numerical Weather Prediction models (forecasting) (Lara-Fanego et al., 2011). Accurate information on expected solar irradiance or wind speed is used for the management of the electricity grids, the scheduling of conventional power plants and also for decision making on the energy market. Monthly and seasonal forecasts are also of interest for maintaining operation and strategic planning, as they can potentially allow the electricity system operators to estimate the energy production availability and the electric network operator to

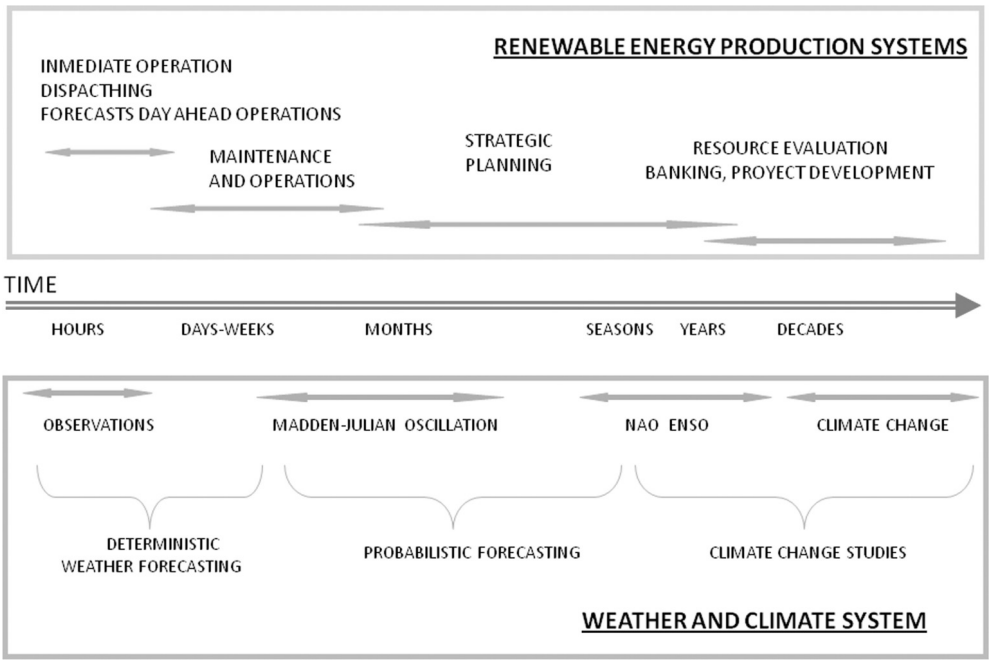


Figure 7.1. The relationship between the weather and climate and different activities related to the renewable energy.

conveniently adapt demand and resources (Weisser and Foxon, 2003). Accurate resource evaluation is a key issue in the first stages of a renewable energy project. In particular, as the life span of wind farms or solar plants (both PV and STPP) is about 20 years, the economic feasibility study of the project should consider an adequate estimation of the interannual variability of the resources. Usually, the resource evaluation is mainly based on field measurements collected at meteorological stations. Since these measures are expensive and time consuming, typically only a few years of data are available for the investment decision making (Barbour and Walker, 2008). However, a few years of measurements do not generally account for the natural climate variability of the resources. Consequently, the projected production could significantly vary from 1 year to another and through decades. Therefore, some complementary studies, usually based on satellite estimates or model simulations, are necessary for a reliable renewable energy resources evaluation. Aside from these very important economic aspects, the evaluation of interannual variability is crucial regarding the reliability of a power system with a high penetration of renewable energy.

An important area of research regarding the resources evaluation is the analysis of the balancing between different renewables. There are two different types of balancing: spatial and local balancing. Spatial balancing takes place if the combined output of many variable renewable energy plants, based on same or different resources (mainly wind and solar), at different locations over a wide area, is smoother than the output of individual power plants (Von Bremen, 2008). Note that the spatial balancing is a consequence of the different weather and climate conditions over large regions. Moreover, local balancing takes place when, within the same location, the combined output of two different renewable energy plants, based on different resources (wind and solar), is smoother along time than the output of each individual plant. Several studies show that the existence of spatial or local balancing allows increasing the reliability of solar and wind plants yields, provided the grid are sufficiently interconnected (Von Bremen, 2008; Cassola et al., 2008; Kempton et al., 2010).

Although other phenomena, as aerosols or solar cycles, may play a significant role, interannual variability of the solar radiation is mainly related to changes in the cloud cover associated with changes in the large scale circulation patterns (Sánchez-Lorenzo et al., 2008, 2009; Chiacchio and Wild, 2010; Papadimas et al., 2010). Concerning the wind resources, surface winds are also mainly driven by large scale circulation. Nevertheless, local features such as surface roughness, local thermal contrast and orography can modify their spatial and temporal features, especially in areas of complex topography as the Mediterranean region (Burlando, 2009; Li et al., 2010). Furthermore, the North Atlantic Oscillation (NAO) is recognised as a major actor regarding the interannual variability of the large scale circula- tion in the Mediterranean area, especially during winter (Hurrel et al., 2003). In particular, the impact of the NAO on the cloud cover variability and in solar radiation at the surface at the whole North Atlantic area has been previously described (Trigo et al., 2002; Pozo-Vázquez et al., 2004; Lohmann et al., 2006; Sánchez-Lorenzo et al., 2008, 2009; Chiacchio and Wild, 2010; Papadimas et al., 2010).

However, the NAO impact on the wind and, therefore, wind energy resources is almost unexplored. Therefore, the NAO can plausibly have significant effects on the wind and solar energy resources in the Mediterranean basin which are worth to be analyzed. In this work we present an analysis of the impact of the NAO on the solar and wind

energy resources in the Mediterranean area. In particular, the study aims to evaluate the role of the NAO in the interannual variability of the wind and solar energy. Monthly means of daily integrated wind and solar energy data, covering the whole North Atlantic and the Mediterranean area, including the north of Africa, are analyzed. The dataset were derived from satellite retrievals (solar energy) and meteorological reanalysis (wind energy and cloud cover) and extends over a period of about 20 years. We first carried out a correlation analysis to explore the linear relationship between the NAO and the solar and wind energy. An analysis of the cloud cover-NAO correlation is also undertaken. In a second part, a composite analysis is used to study the linear and non-linear component of the solar and wind energy anomalies response to the NAO phases. Finally, the eventual existence of balancing between the wind and solar energy resources associated with the NAO cycle is explored.

The work is organized as follows: Section 2 describes the dataset and the processes used to derive the wind and solar energy data. Section 3 deals with the results. Finally, in Section 4 some concluding remarks are outlined.

7.2 Data description

Two dataset have been used in this work. Firstly, the ERA-Interim reanalysis dataset was used to derive cloud cover data and the wind energy resources. The ERA-interim global reanalysis are the third generation of reanalysis of the European Center for Medium Range Weather Forecasts (ECMWF). Original data have a spatial resolution of about 0.7° and a temporal step of 3 h (Simmons et al., 2007). In this work we have analyzed the period 1989-2008. Wind speed at 10 m above the surface at 3 h interval were used to estimate daily integrated values of the wind energy based on:

$$E_{daily\ wind} = \sum_{i=1}^{8} \left(\frac{1}{2} \rho v^3 \right) \times 3h \tag{7.1}$$

where v is the wind speed every 3 h and ρ is the density of the air at sea level. Note the energy units are (Wh). Based on these daily integrated wind energy estimates,

monthly means values were computed. Finally, winter season and annual mean values were computed based on the monthly values. December through February were used for the winter, while annual values were computed from December of the preceding year to November of the considered year. Regarding the cloud cover, daily mean values were computed based on the 3 h interval values. Then, monthly mean values and winter and annual mean values were computed based on the same procedure that for the wind data. Solar energy was derived from the Irradiance at the Surface derived from ISCCP cloud (ISIS) dataset (Lohmann et al., 2006). It consists of 3-hourly values of direct normal and global irradiances at the surface that have been derived by means of one-dimensional radiative transfer computations. The ISIS dataset covers the time period 1984-2004, with a spatial resolution of 280 × 280 km^2. Note that 3-h temporal resolution of ISIS enables the study of daily cycles. The daily integrated solar energy estimates were obtained along the period 1985-2004 based on the global irradiance data:

$$E_{daily\ solar} = \sum_{i=1}^{8} GHI_i \times 3h \tag{7.2}$$

where GHI is the global irradiance every 3 h. As for the wind energy, and based on these daily integrated solar energy estimates, monthly means values were computed and, then, winter season and annual mean values were obtained. Both the ERA-interim and the ISIS dataset have a global coverage. In this work, although the analysis has been focused in the Mediterranean region, the study area has been extended to the whole North Atlantic region, including the north of Africa, from latitude 20° northward. Finally, the winter and annual NAO index as defined by (Hurrel et al., 2003) was used to monitor the NAO.

7.3 Results

7.3.1 NAO-Solar Energy Correlation Analysis

Figs. 7.2a and 7.2b show the sample correlation coefficients between the NAO index and the solar energy for the winter and annual cases, respectively. During the winter, a

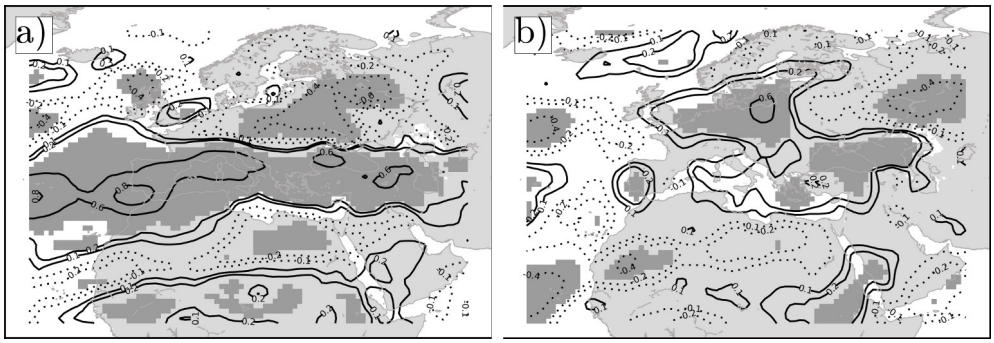


Figure 7.2. a) Correlation between the NAO index and the solar energy for the winter season. The period of analysis covers 2005-2004. Dots indicate negative correlation while continuous line indicates positive correlation. Shading indicates local statistical significance of the difference at 90% confidence level based on a t-test. b) as in a) but for the annual data.

dipolar pattern can be observed: while almost the whole Mediterranean region presents positive correlations, most part of central and northern Europe presents negative values. The highest positive correlation values (0.8) are located over the southwest of the Iberian Peninsula. Also over most part of the central and eastern Mediterranean area high positive values (0.6) are observed. On the other hand, the highest negative correlations are located over the north west of Russia (-0.6) and British Islands (-0.4). Note also the relatively weak, but significant, negative correlation obtained over Egypt. Results are in agreement with those recently presented by Papadimas et al. (2010), which showed the existence of a Mediterranean solar radiation spatial variability mode associated with the NAO during the winter. Regarding the annual correlation map, it resembles the winter case but displaced north-eastward and with weaker values. In particular, the highest positive correlations (0.6) are found over Poland and the Baltic area. Regarding the Mediterranean area, weak but statistically significant positive correlations (0.2) are found over the southwest of the Iberian Peninsula and the eastern Mediterranean area and weak negative correlations over the north of Egypt. Since interannual variability of the solar radiation is mainly associated with cloud cover, the former NAO-solar energy correlation patterns should resemble the NAO-cloud cover spatial correlation over the study area.

Figs. 7.3a and 7.3b show the correlation between the NAO index and the total cloud cover for the winter and annual cases, respectively. As expected, both the winter and annual patterns are in agreement with those observed in Fig. 7.2. In particular, it should be noted

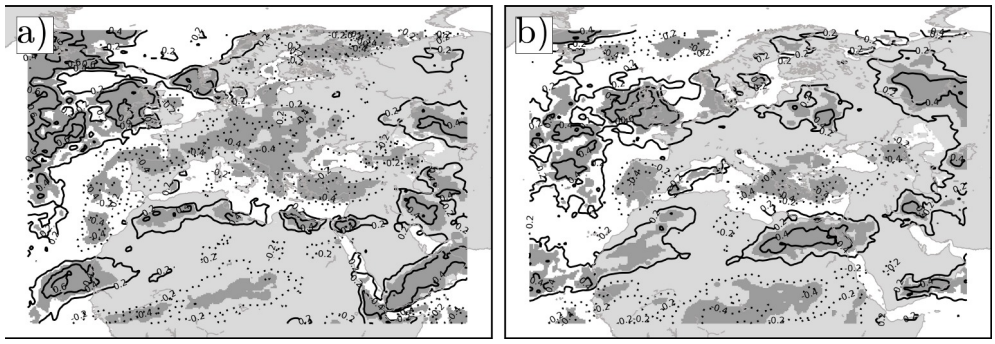


Figure 7.3. a) Correlation between the NAO index and the cloud cover for the winter season. The period of analysis covers 1989-2008. Dots indicates negative correlation while continuous line indicates positive correlation. Shading indicates local statistical significance of the difference at 90% confidence level based on a t-test. b) as in a) but for the annual data.

the negative correlation pattern covering the majority of the Mediterranean area during winter (Fig. 7.3a), with the maximum negative values (-0.3) located over the central and eastern sectors. In contrast, positive correlation values (0.6) are found over Ireland. These results are in agreement with the analysis of the cloud-cover NAO relationship of Trigo et al. (2002). Concerning the annual case (Fig. 7.3b), negative correlation values (about -0.3) are observed over the west of the Iberian Peninsula and the eastern Mediterranean area, in agreement with the patterns observed in Fig. 7.2b. In any case, correlations are, both for the winter and annual case, weaker than those obtained for the solar energy.

7.3.2 NAO-Wind Energy Correlation Analysis

Figs. 7.4a and 7.4b show the correlation between the NAO index and the wind energy for the winter and annual cases, respectively. In both cases, a dipolar pattern can be observed, with negative correlation values over the whole Mediterranean region and positive correlations concentrated over central and northern Europe. Noteworthy, the correlations are weaker than those obtained for the solar energy, indicating a weaker linear relationship between the NAO and the wind energy. Note that annual dipolar pattern seems to be shifted south-eastward compared to the winter case. In particular, for the winter, the maximum positive correlations (0.6) are found over the north of the

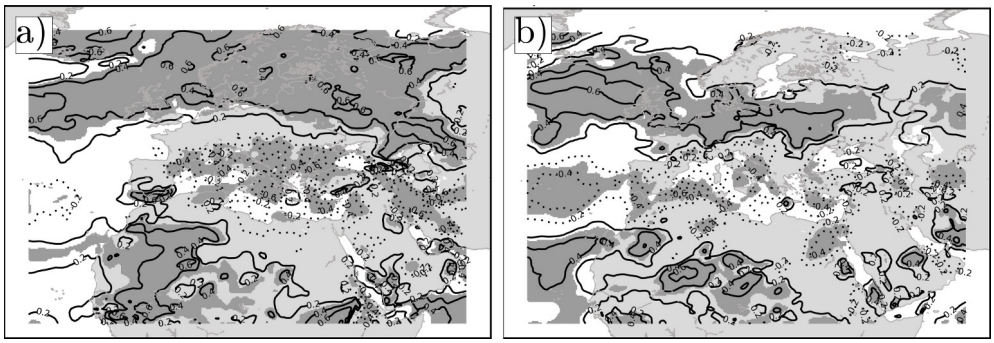


Figure 7.4. a) Correlation between the NAO index and the wind energy for the winter season. The period of analysis covers 1989-2008. Dots indicate negative correlation while continuous line indicates positive correlation. Shading indicates local statistical significance of the difference at 90% confidence level based on a t-test. b) as in a) but for the annual data.

British Islands and the Scandinavian Peninsula. For the annual case, these high positive values are also observed in central Europe. Furthermore, the maximum negative values are found over Greece in winter and over the north of Algeria in the annual case. Note the striking feature over the Gibraltar Strait area during winter. Over this area, high positive correlation values (0.6) are found while negative values are found in the rest of the Mediterranean area. This feature, which deserves more research in the future, is probably related to the special topographic characteristic of this area.

7.3.3 Solar Energy Composite Analysis

In this section, composite patterns of winter solar energy anomalies are obtained as a function of the state of the NAO. Data are represented as anomalies (in percentage) from the mean of complete study period (1985-2004). Fig. 7.5a shows the composite of solar energy anomalies for winters in which the value of NAO index was positive (NAO > 1) and Fig. 7.5b for winters in which the NAO index was negative (NAO<-1). The differences between positive NAO and normal NAO (i.e., -1 < NAO < 1) winters (Fig. 7.5c) and negative NAO and normal NAO winters (Fig. 7.5d) are also shown. Finally, the differences between the anomalies during positive and negative NAO winters (i.e., the differences between Figs. 7.5c and 7.5d) are represented in Fig. 7.2e. Note

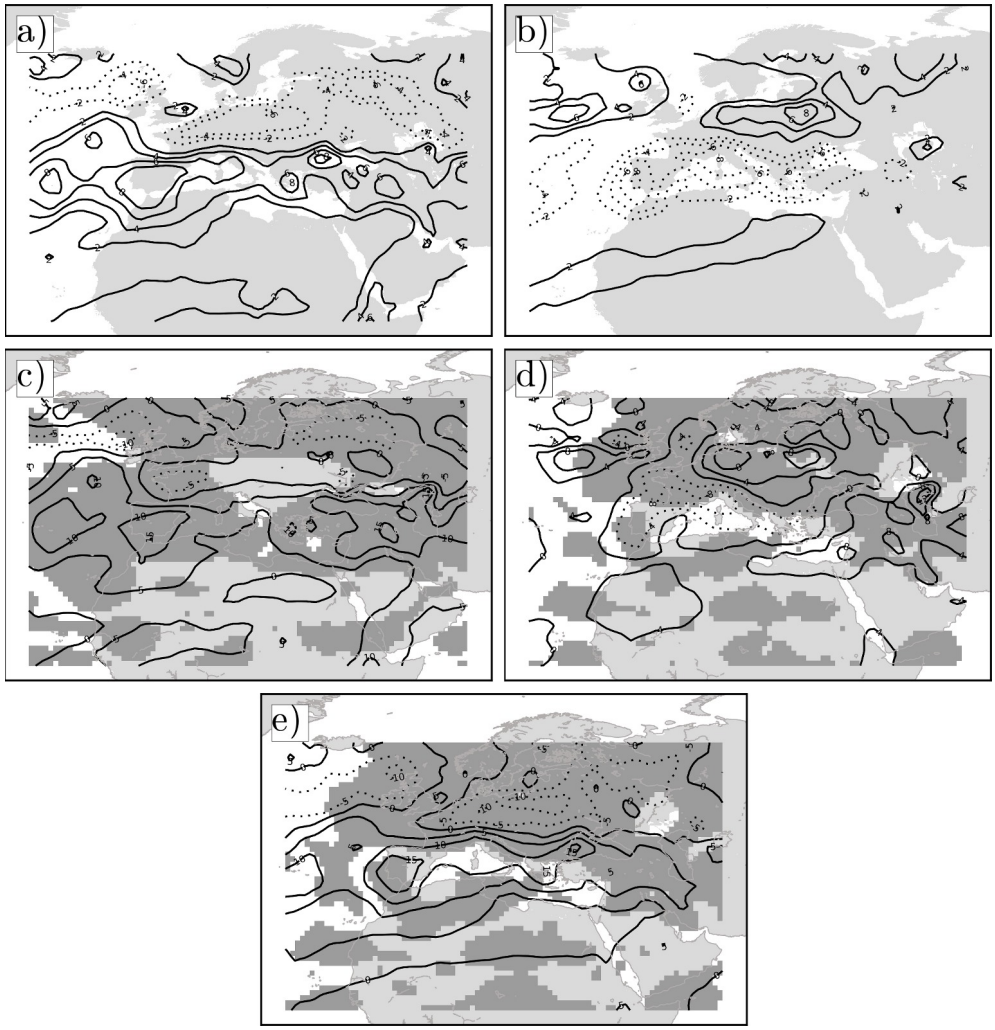


Figure 7.5. Composites of winter season observed solar energy anomalies as a function of the NAO phase. a) During the positive phase (NAO>1). b) during the negative phase (NAO<-1). c) Difference between the positive phase and the normal phase (-1<NAO<1). d) Difference between the negative phase and the normal phase. e) Differences between the positive and negative phase. Data are anomalies in percentage from the long term mean. Continuous line indicates positive or zero anomalies and dotted line indicates negative anomalies. Shading indicates local statistical significance of the difference at 90% confidence level based on a t-test.

that Figa. 7.5c, 7.5d 7.5f represent the spatial patterns of the maximum interannual changes (from one winter to other) that can be expected in the solar energy resources. During positive NAO winters (Fig. 7.5a), the solar energy presents positive anomalies over the whole Mediterranean area and negative anomalies over central Europe and the north of the British Islands. The spatial pattern of anomalies observed during negative NAO winters are similar but of reverse sign (Fig. 7.5b). Both patterns are in agreement with the correlation patterns presented in Fig. 7.5a. When comparing the anomalies during positive NAO and normal NAO winters (Fig. 7.5c), the whole Mediterranean area presents statistically significant positive anomalies. The maximum values (10-15%) are observed over the Iberian Peninsula, Greece and Turkey. In constrast, the north of the British Islands presents the highest negative anomalies (about -10%). The comparison between negative and normal NAO winters (Fig. 7.5d) shows the existence of statistically significant negative anomalies (-4 to -8%) over the Iberian Peninsula, the south of France and over certain areas of Greece and Turkey. In addition, statistically significant positive anomalies (+4 to +8%) are found over eastern and northern Europe. By comparing the anomalies during positive and negative NAO winters (Fig. 7.5d), noticeable interannual changes in the availability of solar energy during the winter season can be expected in certain areas of the study region. In particular, over the Iberian Peninsula, the northern part of Greece and Turkey, central Europe and the British Islands, interannual changes in the solar resources of values up to 15% can be expected associated with interannual changes in the NAO phase.

Similarly to Figs. 7.5 and 7.6 present the solar energy anomalies associated with the NAO phases but on annual basis. In general, the annual spatial patterns of anomalies resemble their winter counterparts but with weaker anomalies. As for the winter case, statistically significant positive anomalies are found over the whole Mediterranean area when comparing positive NAO and normal NAO years (Fig. 7.6c), but anomalies are considerable weaker (about 4% compared to 10% of the winter case). When comparing negative and normal NAO years (Fig. 7.6d) statistically significant negative anomalies (about -3%) are found over the South of France and Italy and positive anomalies (about 2%) over the southeast of the Iberian Peninsula, Tunis and the east of Turkey. The differences between positive and negative NAO years (Fig. 7.5e) show that important interannual changes in the availability of solar energy can be expected in certain areas of the study region, but of a lower magnitude than those observed for the winter case.

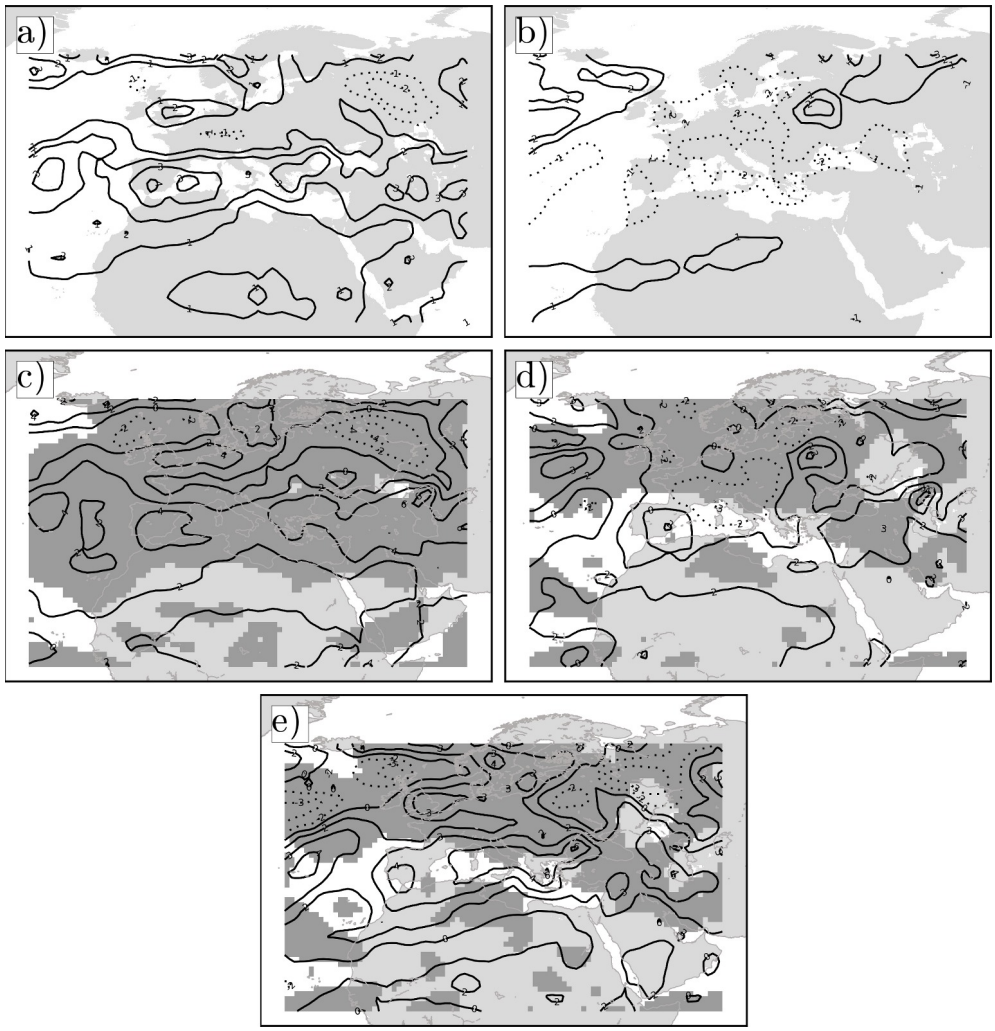


Figure 7.6. As in Figure 5 but for the annual data

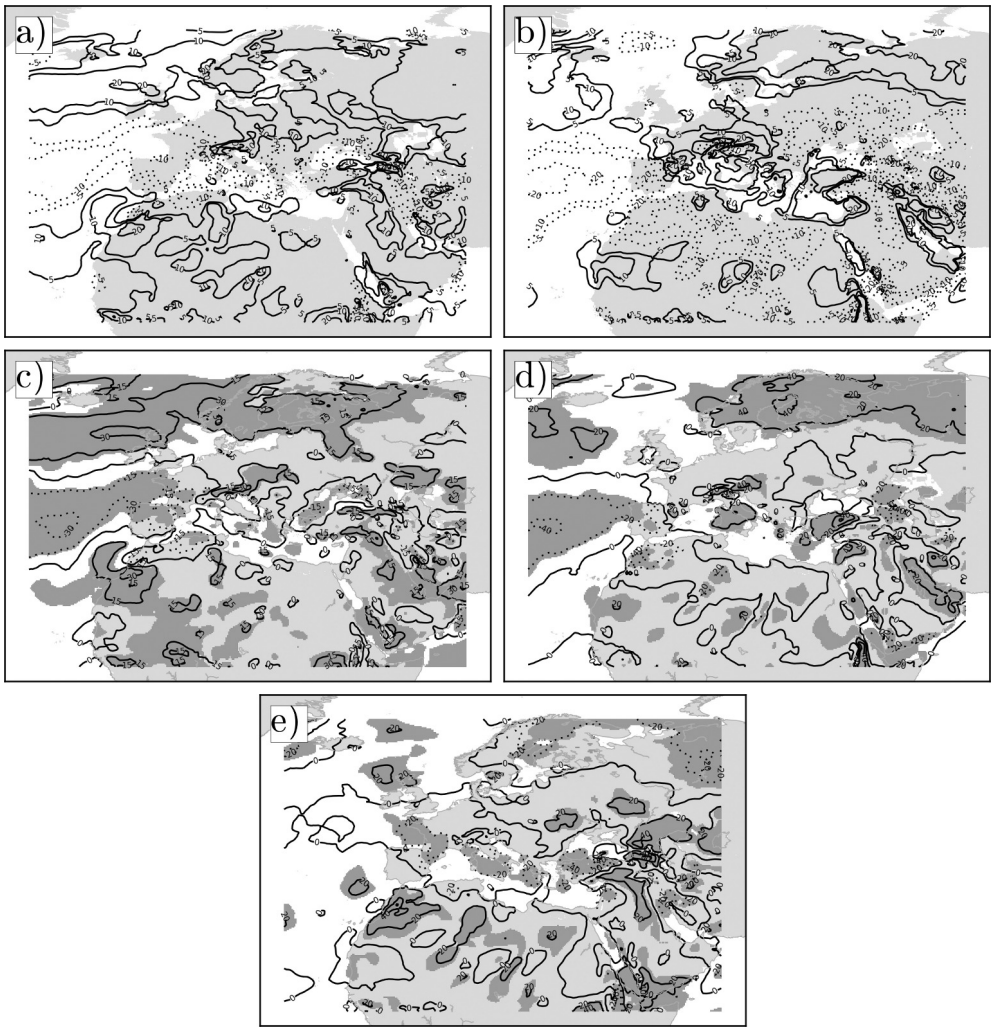


Figure 7.7. As in Figure 5 but for the wind energy anomalies

In particular, in the Mediterranean region, interannual changes of values, between 4 and 8%, can be expected associated with interannual changes in the NAO. Results are in agreement with Lohmann et al. (2006) analysis of the interannual variability of the GHI in the Mediterranean area.

7.3.4 Wind energy composite analysis

As in Fig. 7.5 for the solar energy, Fig. 7.7 presents the composite patterns of wind energy anomalies during the winter associated with the different phases of the NAO. During positive NAO winters (Fig. 7.7a), positive anomalies are observed over the British Isles and the Scandinavian Peninsula, reaching up to 20%. Also positive anomalies but weaker (+10%) are observed over central Europe, the northwest of Morocco/Gibraltar Strait area, the north of Egypt and the eastern of Turkey. In constrast, over the Iberian Peninsula, the central Mediterranean and the Black Sea areas, negative anomalies of values between -5 and -10% are found. When comparing these anomalies with those observed during normal NAO winters (Fig. 7.7c), some interesting features are obtained. In particular, statistically significant and positive values of up to 30% are observed over the British Islands and the Scandinavian area. Positive differences of values between 15 and 30% are observed also over the northwest of Morocco, central Europe and certain areas of the south and north of Turkey. In constrast, statistically significant negative differences (-15 to -30%) are found over the Iberian Peninsula, north of Algeria and the northwest of Turkey. The pattern observed during negative NAO winters (Fig. 7.7b) is not the opposite of that observed during the positive NAO winters. This result is indicative of an important non-linear relationship between the wind energy and the NAO in the study area during the winter. In particular, during negative NAO winters, positive anomalies are observed over the whole Mediterranean basin (10-20%) and the Scandinavian area (about 20%), while negative anomalies are observed over the Iberian Peninsula (-10 to -20%). When comparing these anomalies with those found during normal winters (Fig. 7.7d), statistically significant positive differences are observed over Italy, Greece and Turkey (+20%) and over the Scandinavian area (+40%). In contrast, negative differences are observed over the Iberian Peninsula and the north of Morocco (-20 to -40%). Finally, the patterns in Fig. 7.7e indicate that interannual changes in the winter NAO from positive to negative phase (or vice-versa) may lead to important changes in the wind resources availability. In particular, over the central Mediterranean expected changes from one winter to other can reach about 20%, while over Turkey and the northwest of Morocco these changes can reach up 40%. Remarkably, and as a consequence of the non-linear influence of the NAO on the wind resource, anomalies observed in Fig. 7.7e in the Mediterranean area are of the same order of magnitude than Figs. 7.7c and 7.7d. Therefore, it can be concluded that in many areas

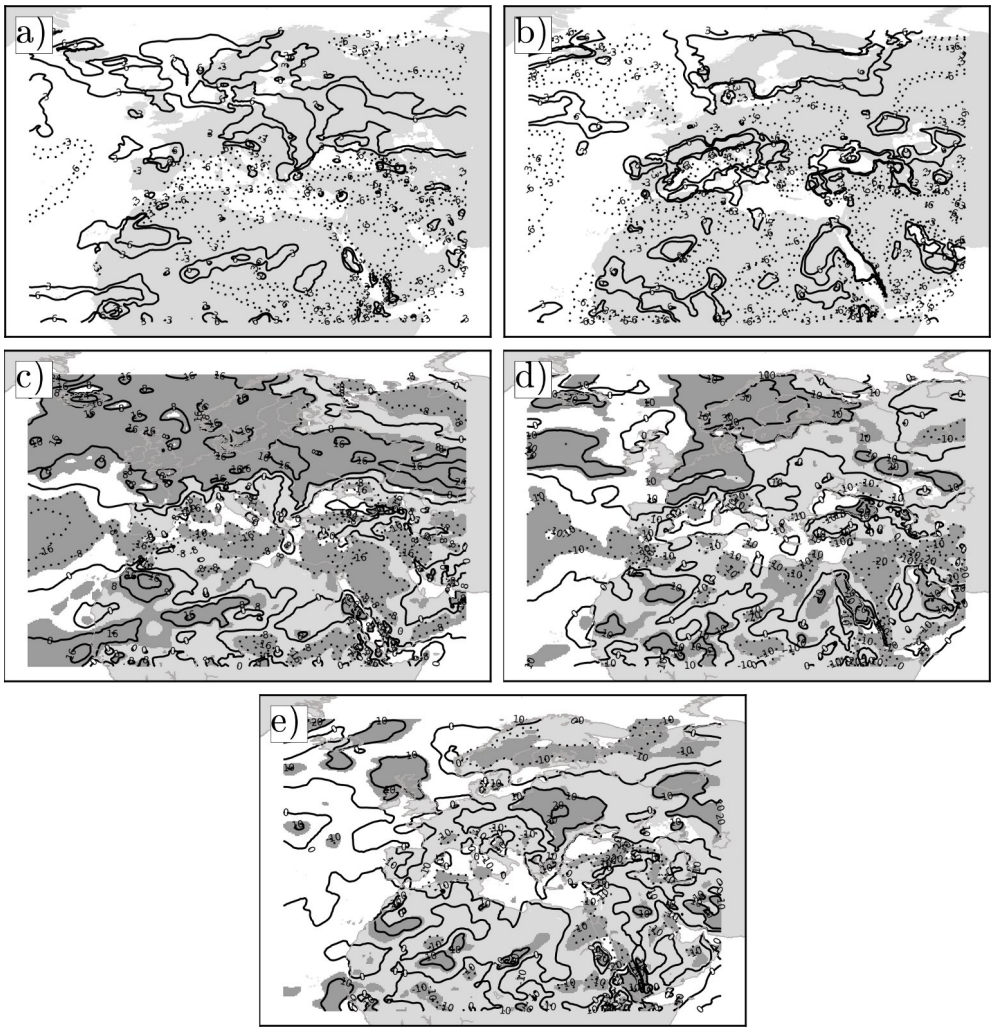


Figure 7.8. As in Fig. 7 but for the annual data

of this region, as Turkey, Greece or the northwest of Morocco, interannual variability of the wind resources from one winter to other can be really high.

This reflects the marked interannual variability of the NAO and because over these areas, wind resources experiment noticeable changes from one winter to another. This happens not only when the NAO changes from the positive to the negative phase, but also when the NAO changes from a positive or negative phase to a normal phase or vice-versa (Figs. from 7.7c to 7.7e). The composite anomaly patterns for the annual case (Fig. 7.8)

are similar to their winter counterparts but displaced south-eastward and with weaker anomalies. In particular, as for the winter case, and as may be expected from Fig. 7.4b, the annual case also presents an important non-linear relationship between the NAO and the wind energy resources. Notably, Figs. 7.8a and 7.8b do not present opposite patterns. Statistically significant negative anomalies (about -8%) are found over the central Mediterranean area when comparing positive NAO and normal NAO years (Fig. 7.8c). Positive anomalies are observed over central and northern Europe and over the Iberian Peninsula, with values in the order of 8%. When comparing negative and normal NAO years (Fig. 7.8d) statistically significant and positive differences (with values about 10%) are found over the central and eastern Mediterranean areas, the north of the Iberian Peninsula and some areas in central and northern Europe.

Moreover, statistically significant negative differences are observed over the south of the Iberian Peninsula and the north of Morocco and Algeria. Finally, Fig. 7.8f indicates the existence of an important interannual variability of the windresources in the study region associated with interannual changes in the NAO from positive to negative phase (or vice-versa). In particular, in the central and eastern part of Mediterranean region, over the Gibraltar Strait area and over the northwest of Morocco, these changes can reach up to 10%. Nevertheless, and as a consequence of the important non-linear relationship between the wind energy resources and the NAO, these changes are of a lower magnitude that the changes observed when the NAO changes from a positive or negative phase to the normal phase (or vice-versa) (Figs. 7.8c and 7.8d). Similarly to the winter analysis, it can be concluded that in certain areas of the Mediterranean (namely the northwest of Morocco, the Gibraltar Strait and Greece), interannual variability of the wind resources can be really high. This situation reflects the fact that wind resources over these areas experiment marked changes from 1 year to other not only when the NAO changes from the positive to the negative phase, but also when the NAO changes from a positive or negative phase to a normal phase or vice-versa (Figs. from 7.8c to 7.8e).

7.3.5 The NAO and the Balancing of the Solar and Wind Energy Resources

The previous sections revealed that the variability of the solar and wind energy resources in the study region associated with the NAO presents considerable spatial differences. Notably, the spatial patterns of the NAO influence on the solar and wind resources reveals in some cases the existence of spatial balancing. For instance, the dipolar pattern of the spatial correlation in Fig. 7.2a indicates the existence of spatial balancing of the solar resources between the central and northern Europe, on one side, and the Mediterranean basin, on the other. Even more, there exists also a weaker but more interesting (because of the availability of the solar resources) balancing between the north of Egypt and the rest of the Mediterranean area. Unfortunately this spatial balancing is not present in the annual analysis (Fig. 7.2b). Regarding the wind, the dipolar pattern in Fig. 7.4a also reveals the existence of spatial balancing between northern Europe and the Mediterranean area as earlier highlighted by Pryor et al. (2006). Compared to the winter solar energy case, the strength of this balancing seems to be weaker. In addition, during winter, there exists also spatial balancing between the western Mediterranean (strait of Gibraltar) and the rest of the Mediterranean region. Regarding the annual case, and unlike the solar resources, the spatial balancing is also present but displaced southwestward (Fig. 7.4b). Finally, the comparison of Figs. 7.2a and 7.4a reveals that the NAO impact on the solar and wind resources over the study area presents a similar north-south dipolar pattern but the sign of the dipoles are just opposite. Therefore, it can be concluded the existence of a notably local balancing between the solar and wind resources almost over the whole study region during winter. Regarding the Mediterranean region, the strength of this balancing seems to be especially high in the central part, over Greece, where correlation between the NAO and the solar energy is higher than 0.6 (Fig. 7.2a) and between the NAO and the wind energy with circa -0.6 (Fig. 7.4a). For the annual case (Figs. 7.2b and 7.4b) the balancing is also present but weaker. Concerning the Mediterranean area, the southwest of the Iberian Peninsula, Greece and Turkey present a remarkable balancing. For instance, over the southwest of Iberian Peninsula the NAO-solar energy correlation reaches about 0.2 while NAO-wind energy correlation is about -0.4.

7.4 Conclusions

The influence of the NAO on the solar and wind energy resources in the Mediterranean area has been explored based on the analysis of 20 years of reanalysis and satellite data. In particular, the role of the NAO cycle in the interannual variability of the solar and wind energy resources was analyzed based on correlation and composite analysis. Although the study is focused on the Mediterranean area, for the sake of completeness, the analysed data covered the whole North Atlantic and Mediterranean area, including the north of Africa. The analysis was carried out twice for the winter and annual periods and aimed to contribute to a better understanding of renewable energy resources in the study region.

Regarding the winter solar energy, a north south dipolar pattern of correlation was found, with the positive centre of the dipole over the Mediterranean and the negative over central and northern Europe. Correlation coefficient over the whole Mediterranean area reached values above 0.6, with the highest value (0.8) over the Iberian Peninsula. The annual case presented a correlation map resembling the winter case but displaced north-eastward and with weaker values. A similar analysis for the cloud cover instead of for the solar energy was able to explain the former results. In any case, the NAO-cloud cover correlation was found, both for the winter and annual case, to be weaker than those obtained for the solar energy. The composite analysis revealed some additional features of the NAO-solar energy relationship.

On the one hand, positive anomalies (10-15%) were found over the Iberian Peninsula, Greece and Turkey associated with the positive phase NAO winters. On the other hand, during negative NAO winters, negative anomalies (-4 to -8%) were found over the Iberian Peninsula, the south of France, Greece and Turkey. As a consequence, over these areas, interannual changes in the winter solar energy resources of values of up to 15% can be expected associated with interannual changes in the NAO phase. Regarding the annual analysis, the composite analysis showed similar results but anomalies were considerable weaker. For instance, the positive NAO years were found associated with positive anomalies (4%) over the whole Mediterranean area. Negative NAO years were found associated with negative anomalies over the South of France and Italy (-3%) and positive anomalies (2%) over the southeast of the Iberian Peninsula, Tunis and the east

of Turkey. As a consequence, for the entire Mediterranean region, interannual changes of values between 4 and 8% were found associated with interannual changes in the NAO phase.

The NAO-wind energy relationship was found to be considerably more complex than the NAO-solar energy one. In particular, the winter correlation analysis proved the existence of north-south dipolar pattern, with positive values over central and northern Europe and negative values over the Mediterranean area. For the latter area, negative correlation values (-0.4 to -0.6) were observed, except over the Gibraltar Strait area, where positive correlation values were found. The annual correlation analysis showed a similar pattern, but shifted south-eastward. Thus over the Mediterranean area, the maximum negative values were observed over Greece (-0.6) in the winter case and over Algeria (-0.6) in the annual case. Noteworthy, in general the correlations were weaker than for the solar energy case, indicating a weaker linear relationship between the NAO and the wind energy. The composite analysis revealed additional features regarding the complex relationship between the NAO and the wind energy in the study area. For instance, the winter analysis proved the existence of positive anomalies (15-30%) over the northwest of Morocco and the south and north of Turkey, and negative anomalies (-15 to -30%) over the Iberian Peninsula, north of Algeria and the northwest of Turkey associated with the positive phase of the NAO. The composite pattern observed during negative NAO winters was not the opposite of the observed during the positive NAO winters. In particular, the main features during this negative phase were the presence of positive anomalies (+20%) over Italy, Greece and Turkey and negative anomalies (-20 to -40%) over the Iberian Peninsula and the north of Morocco. As a consequence, notable interannual changes in the winter wind energy resources associated with interannual changes in the NAO phase were found over the central Mediterranean (20%), Turkey and the northwest of Morocco (+40%). The annual composite patterns showed to be similar to their winter counterparts but the patterns were displaced south-eastward and the anomalies were weaker. In particular, over the central Mediterranean, negative anomalies (-8%) were found associated with the positive phase of the NAO. During the negative phase, positive anomalies (10%) were found over the central and eastern Mediterranean area and the north of the Iberian Peninsula, while negative anomalies (-10%) were found over the south of the Iberian Peninsula and the north of Morocco and Algeria. Consequently, interannual changes in the annual wind resources of values over 10% were found in the

central and eastern part of Mediterranean region, over the Gibraltar Strait area and over the northwest of Morocco associated with interannual changes in the NAO phase.

Finally, the analysis of the spatial patterns of the NAO influence on the solar and wind energy resources revealed the existence of spatial and local balancing. Among others, the dipolar pattern of the spatial correlation obtained for the solar energy during winter indicated the existence of spatial balancing of the solar resources between the central and northern Europe and the Mediterranean. However, it should be noted that this spatial balancing was not present in the annual analysis. The dipolar pattern of the winter NAO-wind energy relationship also revealed the existence of spatial balancing between northern Europe and the Mediterranean area for the wind energy. Nevertheless, compared to the winter solar energy case, the strength of this balancing was found to be weaker. In addition, during winter, spatial balancing between the western Mediterranean (strait of Gibraltar) and the rest of the Mediterranean region was also found. Regarding the annual case, and unlike the solar resources, the spatial balancing was also present but displaced south-westward. In addition to the spatial balancing found for the wind and the solar energy, a significant local balancing between the solar and wind resources almost over the whole study region was found associated with the NAO cycle. Regarding the Mediterranean region and during winter, the strength of this balancing was found to be especially high in the central section. In the annual case the most important local balancing were found over the southwest of the Iberian Peninsula, Greece and Turkey, although the magnitude was weaker than in the winter case.

The authors believe that the results above summarized are of interest regarding the solar and wind energy resources evaluation in the Mediterranean area. In this regard we would like to emphasise that, in the light of results obtained here, a more in depth assessments of solar and wind resources should be required and that measuring solar and wind data covering only a few years should be avoided. This will provide a better estimation of the expected interannual variability of the renewable resources and, therefore, of the plant production interannual variability.

CHAPTER 8

CONCLUDING REMARKS AND FUTURE RESEARCH

An analysis of the spatiotemporal balancing of the wind energy resource alone and between the solar and wind energy resources in the Andalusia (Southern Iberian Peninsula), and its implication for attaining a reduction in wind and solar power fluctuations, has been conducted in this work. Notably, we have investigated whether the existence of balancing patterns leads regional solar and wind energy resources to provide more stable (even baseload) power. The study of the spatial balancing of wind energy alone was assessed in Chapter 4. The balancing between wind energy and the solar energy associated with Global Horizontal Irradinace (GHI) (for photovoltaic PV technology) was studied in Chapter 5. In Chapter 6, the spatiotemporal balancing between the wind energy and the solar energy associated with the Direct Normal Irradiance (DNI) (for concentrating solar power CSP technology) was studied. Data employed in these analyses were obtained based on a dynamical downscaling methodology using the Weather Research and Forecasting (WRF) numerical prediction model. Finally, in Chapter 7, the existence of balancing between the solar and wind energy resources in the whole Mediterranean area associated with the North Atlantic Oscillation (NAO) cycle is analyzed. In the course of this research, a couple of studies (Chapters 2 and 3), not directly related to the balancing issue but of relevance for the dynamical downscaling application in the study region, were also conducted. Remarkably, in these two studies the reliability of the WRF model wind speed and direction estimates in the study region was assessed and the best set up of this model for this region attained.

8.1 Sensitivity of wind estimates to parameterization choice, terrain and surface representation

Given the varied and complex topography of the study region, and considering its relevant influence on wind speed variability, the reliability of WRF model regional wind estimates was evaluated prior to the balancing analysis. In this preliminary evaluation, the first objective was to assess the relative roles of parameterization choice, terrain representation, and surface properties in WRF, as related to regional wind resource assessment. The second and more important objective was to achieve an optimal WRF model set up, for obtaining the most accurate wind and solar estimates used in the balancing analysis. Chapters 2 and 3 are focused on these objectives.

Main conclusions from these two chapters are summarized as follows:

- Wind speed estimates proved to be sensitive mainly to the PBL parameterization choice. Differences between 3% and 8% were observed in the wind speed RMSE values, depending on the PBL parameterization and the station. Sensitivity of the wind speed RMSE values to other parameterizations was not significant. Nevertheless, some combinations of schemes (experiments) performed better than others. In particular, the YSU PBL scheme proved to be better than the MYNN PBL scheme. The ME values of wind speed showed significant dependence on the station and choice of PBL parameterization. Values ranged from -15% to 10%, depending on the station and experiment.
- The combination of YSU scheme for PBL, Morrison-2M for Microphysics, Grell-3D for Cumulus, RRTG for shortwave radiation, and RRTM for longwave radiation parameterizations outperformed all physical configurations, and was used for the setup of the model.
- The accuracy of the terrain representation in the model showed to be especially relevant for the reliability of the wind speed estimates. Notably, the misrepresentation of the station elevation led to higher RMSE and ME (absolute) values. Notably, the overestimation/underestimation of the station elevations led to positive/negative ME values.

- Overall, lower wind speed RMSEs were associated with higher spatial resolutions of WRF. Differences ranged from 0.2 to 1 ms^{-1} when comparing 9 km and 1 km spatial resolution WRF wind estimates.

- Wind speed ME values showed to be remarkably sensitive to the model spatial resolution. This mainly because higher resolution improves the representation of terrain elevation. The sign of the bias depended on terrain morphology and the spatial resolution, but absolute values tended to be much higher with coarser spatial resolution (9 km). An overall positive bias in WRF wind speed estimates was found.

- Physical configuration showed little impact on wind direction distribution estimates. These estimates proved more sensitive to the representation of terrain morphology around the station than to the model spatial resolution. We observed a significant relationship between RMSE and ACC (an accuracy parameter which evaluates the ability of the model to estimate the wind direction with an error below 30°) dependence on the spatial resolution. Smaller RMSEs of the wind speed estimates and better representations of wind direction were observed in areas where wind direction is clearly constrained by terrain morphology, providing this morphology is properly represented.

- The representation of surface properties, especially the roughness length was found to play an important role in the reliability of modeled wind estimates. This influence was mainly observed in the wind speed ME values and, to a lower extent, in the wind speed RMSE values.

- The performance of two land-use maps was assessed: the CORINE and GLCC. In both datasets, the roughness length was better represented in summer than in winter. As a consequence, the ME values were lower in summer than in winter.

- The CORINE land-use dataset provided lower ME (in general) and RMSE values during winter and the GLCC during summer. These results were explained based on the accuracy of roughness length representation provided by both dataset during the former seasons.

- A problem related with the WRF representation of the roughness length was observed. Notably, the WRF Preprocessing System selects the category for each

cell of the modeled domain using the nearest neighbor interpolation technique and based on the land-use data set spatial resolution (1 km spatial resolution for GLCC and 100 m for CORINE). However, the selected category could not be representative for the point of interest, for instance, when the point of interest has a land surface coverage substantially different from the surrounding area.

- It was found that the use of daily updating SST during the WRF integrations improved the wind speed ME values in summer and in autumn, especially at coastal stations.

- Finally, the WRF model was found to be a suitable tool for regional wind resources assessment in the study region, as derived from the evaluation of the model estimates. Notably, using the best set up and terrain representation, the WRF model was able to provide wind speed and direction estimates with RMSE values ranging from 2 to 2.5 ms^{-1}, ME values ranging from -0.5 to 0.3 ms^{-1} and ACC values ranging from 55% to 80%, depending on the topographic complexity of the study area.

8.2 Analysis of the spatio-temporal balancing between solar and wind energy resources

An analysis of the spatiotemporal balancing of the wind energy resource alone (Chapter 4) and between the solar and wind energy resources (Chapters 5 and 6) in the Southern Iberian Peninsula, and its implication for a reduction in wind and solar power fluctuations, was conducted. The analysis included the investigation of whether the existence of balancing patterns permits regional solar and wind energy to provide more stable (even baseload) power. The method consisted on two steps. In the first, a Principal Component Analysis (PCA) or Canonical Correlation Analysis (CCA) is accomplished, and resulting spatiotemporal patterns were examined. The analysis type depended on whether the evaluation implies one resource (wind energy, Chapter 4) or both (wind and solar energy, Chapters 5 and 6). At this step, mesoscale atmospheric conditions associated with each PCA or CCA pattern were analyzed, to explain the observed balancing patterns from a physical standpoint. In the second step, based on the former

analysis, the optimum locations for wind farms (Chapter 4), combinations of PV plants and wind farms (Chapter 5), and combinations of CSP plants and wind farms(Chapter 6), for stable production were assessed. Notably, using a reference wind farm and PV or CSP plant models, the hourly capacity factor (and its standard deviation) of these facilities, operating alone or interconnected, were evaluated at these locations, allowing the analysis of the eventual contribution of these renewable technologies to stable power.

The main conclusions derived from the three above mentioned studies are summarized as follows:

8.2.1 Balancing of wind energy resources alone

- Results showed the existence of valuable spatial balancing of wind energy resources over the study region, but with marked seasonality.
- The most important spatial balancing pattern was found between resources in the east of Andalusia and near the Strait of Gibraltar area. This pattern was most pronounced in the annual and winter analyses, but was also evident in the other seasons.
- The second most important spatial balancing pattern was between the resource in the south, mainly on Mediterranean coast, and in the western area. This pattern was second in importance within the annual and winter analyses, but was also apparent in the other seasons.
- Both spatial balancing patterns were discovered to result from the interaction of mesoscale zonal flow with topographic features in the region.
- Results show that siting of wind farms across the region can be optimized by taking advantage of the aforementioned spatial balancing patterns. Such siting can substantially reduce wind power output fluctuations and, in some cases, produce firm capacity, thereby contributing to baseload power.
- It was observed that the standard deviation of the capacity factor decreased substantially when the wind farms are interconnected. The reduction was highly dependent on season and which sites were interconnected, but an overall standard

deviation decrease of about one third resulted with interconnection of both offshore and onshore sites. This reduction has important consequences for wind energy grid integration. First, other generators within the power system can take advantage of this smoother fluctuation to compensate deviations, allowing time to ramp up or down. Second, since standard deviation is a measure of the reserves necessary for wind energy grid integration, interconnection appears to significantly diminish these necessities.

- Results showed that availability of the power provided by the combination of wind farms when taking advantage of the PCA balancing patterns, can be close to availability provided fossil-fuel based power plants and, therefore, close to be considered baseload power (firm capacity).

- Notably, it was found in all analyzed periods that the interconnection of wind farms creates firm capacity. Values were highly dependent on the season and interconnected sites. Higher values were found for winter (11%) and lowest for summer (8%).

8.2.2 Wind and GHI-derived solar energy resources balancing

- Results show the existence of valuable balancing between the GHI-derived solar and wind energy resources in the region, but with a marked seasonality. That is, coupling between wind and solar energy resources varied considerably in strength, sign and spatial coverage through the year.

- During winter, a noteworthy balancing was observed between the solar energy resources over almost the entire study region and the wind energy resources near the strait of Gibraltar. An important balancing pattern was found in summer between the solar energy over almost the entire region and wind energy in the south and east. Finally, the autumn season turned out to have the most important balancing effect. During this season, balancing between the solar and wind energy resources extended over the entire region, although it was more important in the southwestern and southeastern areas.

- Atmospheric circulations associated with these coupled patterns showed a marked seasonal dependence. Synoptic scale variability greatly influenced the balancing, but so did topography, especially near the strait of Gibraltar.

- When locating reference wind farms and PV plants according to the balancing patterns, their combined power production showed substantially lower variability than production of wind farms and PV plants separately, and combined production achieved by any other locations.

8.2.3 Wind and DNI-derived solar energy resources balancing

- First of all, the results showed the existence of valuable balancing between the DNI-derived solar and wind energy resources over the study region for the all the analyzed periods.

- Although the balancing pattern differed among seasons, there were some common features across seasons that are reflected in the annual analysis. The most important spatial balancing pattern was found to be between the solar energy resources in the whole region and the wind energy resources in all the study area except the western part of the Strait of Gibraltar zone. This balancing pattern was the leading one for the winter, spring and the annual analysis. During autumn this balancing between the solar and wind energy resources even extended over the whole study region, including the strait of Gibraltar area. The former balancing pattern was explained based on zonal circulation and their interaction with the topography over the study area.

- The leading summer mode showed to be different, accounting for a balancing between the solar energy in the whole study region and the wind energy in the southeastern part of the study area.

- The second most important balancing mode was found to be between the solar energy resources at the south and the wind energy resources in the half west of the study region. This pattern was the second mode for the spring, autumn and annual analysis and was explained based on meriodional circulation and their interaction with the topography over the study area.

- The analysis of the power generation of CSP plant and wind turbines located taking advantage of the aforementioned spatial balancing patterns showed some interesting results. Firstly, the capacity factor availability of the aggregated CSP plant and wind farm showed a significant increment compared to those of the individual CSP plant and wind farm.

- For the winter leading mode, a non-zero value for the capacity factor was found around 65% of the time (10% for the CSP and 45% for the wind farm individually), with values above 0.5 (i.e., equivalent to capacity factor 1 for the CSP plant or the wind farm) close to 25% of the time.

- The leading spring mode showed, probably, the most interesting results: a non-zero value for the CSP capacity factor 85% of the time (40% for the CSP and 70% for the wind farm individually), with values above 0.5 around 40% of the time.

- The leading summer mode showed also notable results: a non-zero value for the CSP capacity factor around 75% of the time (45% for the CSP and 50% for the wind farm individually), with values above 0.5 around 30% of the time.

- Also the leading autumn mode provided notable results: a non-zero value for the CSP capacity factor was found around 75% of the time (45% for the CSP and 50% for the wind farm individually), with values above 0.5 around 30% of the time.

- Finally, the leading annual mode showed similar results: a non-zero value for the CSP capacity factor was found near 80% of the time (30% for the CSP and 65% for the wind farm individually), with values above 0.5 around 30% of the time.

- The analysis of the mean daily cycle of the hourly wind, CSP and combined CSP+WF capacity factor time series for the leading CCA modes showed some interesting features. Notably, the minimum wind power capacity factors were observed along the central part of the day, when the CSP capacity factors shows the maximum values. In addition, for all the seasonal analysis, a lag of about 8 hours was observed between the CSP plant (about midday) and the wind farm (about 20:00 h) maximum power production time. For the annual analysis, this lag reduced to 5 hours.

- To sum up, results showed that availability of the power provided by the combination of CSP plant and the wind farm, when taking advantage of the CCA

balancing pattern, can be close to availability provided fossil-fuel based power plants and, therefore, close to be considered baseload power. In addition, the use of the energy storage capabilities of the CSP plants, not considered here, by taking into account the results of the hourly mean capacity factor analysis, may results in a considerable increment in the power availability. This analysis will be attempted in a future work.

8.3 Balancing between the solar and wind energy associated with the NAO cycle

The influence of the NAO on the solar and wind energy resources in the Mediterranean area has been explored based on the analysis of 20 years of reanalysis and satellite data. Particularly, the role of the NAO cycle in the interannual variability of the solar and wind energy resources was analyzed based on correlation and composite analysis. Although the study is focused on the Mediterranean area, for the sake of completeness, the analysed data covered the whole North Atlantic and Mediterranean area, including the north of Africa. The analysis was carried out for the winter and annual periods and aimed to contribute to a better understanding of renewable energy resources in the study region.

The main conclusions derived from this study are summarized as follows:

- A remarkably north south dipolar pattern of correlation between the winter NAO index and the winter solar energy resources in Europe, with the positive centre of the dipole over the Mediterranean and the negative over central and northern Europe, was found.

- The highest correlation values (over 0.8) were found over the Iberian Peninsula.

- The annual case presented a correlation map resembling the winter case but displaced north-eastward and with weaker values.

- A composite analysis revealed some additional features of the NAO-solar energy relationship. Particularly, positive anomalies (10% to 15%) were found over the Iberian Peninsula, Greece and Turkey associated with the positive phase NAO winters. On the other hand, during negative NAO winters, negative anomalies (-4% to -8%) were found over the Iberian Peninsula, the south of France, Greece and Turkey. As a consequence, over these areas, interannual changes in the winter solar energy resources of values of up to 15% can be expected associated with interannual changes in the NAO phase. Regarding the annual analysis, the composite analysis showed similar results but anomalies were considerable weaker.

- The NAO-wind energy relationship was found to be considerably more complex than the NAO-solar energy one. Particularly, the winter correlation analysis proved the existence of north-south dipolar pattern, with positive values over central and northern Europe and negative values over the Mediterranean area. Over this late area, negative correlation values (-0.4 to -0.6) were observed, except for the strait of Gibraltar area, where positive correlation values were found. The annual correlation analysis showed a similar pattern, but shifted south-eastward. Noteworthy, in general the correlations were weaker than for the solar energy case, indicating a weaker linear relationship between the NAO and the wind energy.

- A composite analysis revealed additional features regarding the complex relationship between the NAO and the wind energy in the study area. For instance, the winter analysis proved the existence of positive anomalies (15% to 30%) over the northwest of Morocco and the south and north of Turkey, and negative anomalies (-15% to -30%) over the Iberian Peninsula, north of Algeria and the northwest of Turkey associated with the positive phase of the NAO.

- The composite pattern observed during negative NAO winters was not the opposite of the observed during the positive NAO winters. Particularly, the main features during this negative phase were the presence of positive anomalies (+20%) over Italy, Greece and Turkey and negative anomalies (-20% to -40%) over the Iberian Peninsula and the north of Morocco. As a consequence, notable interannual changes in the winter wind energy resources associated with interannual changes in the NAO phase were found over the central Mediterranean (20%), Turkey and the northwest of Morocco (+40%).

- The annual composite patterns showed to be similar to their winter counterparts but the patterns were displaced south-eastward and the anomalies were weaker.
- Finally, the analysis of the spatial patterns of the NAO influence on the solar and wind energy resources revealed the existence of spatial and local balancing. Particularly, the dipolar pattern of the spatial correlation obtained for the solar energy during winter indicated the existence of spatial balancing of the solar resources between the central and northern Europe and the Mediterranean.
- The dipolar pattern of the winter NAO-wind energy relationship also revealed the existence of spatial balancing between northern Europe and the Mediterranean area for the wind energy. Compared to the winter solar energy case, the strength of this balancing was found to be weaker.
- In addition to the spatial balancing found for the wind and the solar energy, a significant local balancing between the solar and wind resources almost over the whole study region was found associated with the NAO cycle. Regarding the Mediterranean region and during winter, the strength of this balancing was found to be especially high in the central part. In the annual case the most important local balancing was found over the southwest of the Iberian Peninsula, Greece and Turkey, although the magnitude was weaker than in the winter case.

8.4 Future Research

Regarding the use of the dynamical downscaling based on the WRF model for obtaining wind and solar energy resources, it has been here reported the importance of the adequate representation of topography, morphology and the land use for obtaining accurate estimates of wind speed and direction. As a consequence we plan to incorporate a regional Digital Elevation Model (DEM) with higher resolution (100 m) to compare the representation of topography and morphology with the 1 km experiments conducted in this work.

Regarding the balancing studies, the methodology presented in this thesis can be useful in renewable energy integration studies. In these studies, the modeled power production

of existing and future renewable energy-based power plants, are analyzed in order to obtain the optimal mix regarding a stable, and correlated to the demand, renewable power production. In the future, we plan to extend the here presented balancing studies by:

- Increasing the analysis period, in order to test the stability of its results against the interannual climate variability in the study region.
- Including an important dependence in the analysis: the electrical demand.
- Including the energy storage capabilities of the CSP plants and, to a lower extent, of the PV and Wind farms.

Our procedure can be easily applied to areas of arbitrary size, to optimize the grid power output. The method facilitates planning of the location of future wind and solar energy plants across a region, so that total electricity production (solar plus wind) will have smaller fluctuations. Currently, renewable projects are developed in locations with either maximum wind or sun. In the future, in our view, project locations should also take into account the fluctuation of power supply from each renewable. This may result in greater use of wind and solar energy as reliable, baseload electric power.

BIBLIOGRAPHY

AEA, Andalusian Energy Agency. 2009. Wind Energy resources in Andalusia (Spain). Technical report. Andalusian Regional Goverment, Spain.

Alsamamra H., J. Ruiz-Arias, D. Pozo-Vázquez, and J. Tovar-Pescador. 2009. A comparative study of ordinary and residual kriging techniques for mapping global solar radiation over southern Spain. Agricultural and Forest meteorology; 149: 1343-1357.

Alsamamra H., D. Pozo-Vázquez, F.J. Santos-Alamillos, J.A. Ruiz-Arias, V. Lara-Fanego, and J. Tovar-Pescador. 2011. A geostatistical approach for mapping surface wind speed in Andalusia (southern Spain). Manuscript submitted to Meteorological Applications.

Anderson R., Tatham, and WC. Black. 1998. Multivariate Data Analysis. J.F. Hair and E. Rolph, Eds., Prentice Hall, Inc.

Arakawa A. 2004. The Cumulus Parametrization Problem: Past, Present, and Future. Journal of Climate; 17: 2493-2525.

Archer C. and M. Jacobson. 2003. Spatial and temporal distributions of us winds and wind power at 80 m derived from measurements. Journal of Geophysical Research; 108, 1-20.

Archer C, and M. Jacobson M. 2007. Supplying base load power and reducing transmission requirements by interconnecting wind farms. Journal of Applied Meteorology and Climatology; 46: 1701-1717.

Argüeso, D. J. Hidalgo-Muñoz, S. Gámiz-Fortis, M. Esteban-Parra, J. Dudhia, and Y. Castro-Díez. 2011. Evaluation of WRF Parameterizations for climate studies over Southern Spain using a multistep regionalization. Journal of Climate; 24: 5633-5651.

Arya, S. 2001. Introduction to micrometeorology. Academic Pr.

AUSLIG, Australian Surveying and Land Information Group. 1990. Atlas of Australian Resources: Vegetation, Commonwealth of Australia, Canberra, ACT, 64 pp.

Badger, J., X.G. Larsén, N.G. Mortensen, A.N. Hahmann, J.C. Hansen, and H.J. Ejsing. 2010. A universal mesoscale to microscale modelling interface tool. 2010 European Wind Energy Conference and Exhibition. Warsaw, Poland.

Bao J.W., and R.M. Errico. 1997. An adjoint examination of a nudging method for data assimilation. Monthly weather review; 125(6): 1355-1573.

Barbour P., and S. Walker. 2008. Wind resource evaluation: Eola Hills. Technical report, Energy Resources Research Laboratory, Department of Mechanical Engineering, Oregon State University, Corvallis, OR.

Barna M., and B. Lamb. 2000. Improving ozone modeling in region of complex terrain using observational nudging in a prognostic meteorological model. Journal of Atmospheric Environment; 34: 4889-4906.

Barnett, T. and R. Preisendorfer. 1987. Origins and levels of monthly and seasonal forecast skill for united states surface air temperatures determined by canonical correlation analysis. Monthly Weather Review; 115: 1825-1850.

Bartholome E., A.S. Belward, F. Achard, S. Bartalev, C. Carmona-Moreno, H. Eva, S. Fritz, J.M. Gregoire, P. Mayaux, and H.J. Stibig. 2002. GLC 2000 Global Land Cover Mapping for the Year 2000. Project status report. European Commission Joint Research Centre: Italy.

Bartlett M.S. 1941. The Statistical Significance of Canonical Correlations. Biometrika; 32: 29-38.

Beljaars A., R. Brown, and N. Wood. 2004. A new parametrization of turbulent orographic form drag. Quart. J. Roy. Meteor. Soc; 130, 1327-1347.

Berge, E., R.E. Bredesen, and K. Mollestad. 2007. Combining WAsP with WRF mesoscale model: Evaluation of Wind Resource Assessment for three Norwegian Wind Farm Areas. In Proceedings of EWEC2007, Milano, Italy.

Borge R., V. Alexandrov, J Del Vas, J. Lumbreras, and E. Rodríguez. A comprehensive sensitivity analysis of the WRF model for air quality applications over the Iberian Peninsula. Atmospheric Environment; 42: 8560-8574.

Boyle G. 2008. Renewable electricity and the grid: the challenge of variability. Earthscan/James & James

Bretherton, C., C. Smith, and J. Wallace. 1992. An intercomparison of methods for finding coupled patterns in climate data. Journal of Climate; 5: 541-560.

Burlando M. 2009. The synoptic-scale surface wind climate regimes of the Mediterranean Sea according to the cluster analysis of ERA-40 wind fields. Theor Appl Climatol; 96: 69-83.

Byrkjedal Ø, and E. Berge. 2008. The use of WRF for wind resource mapping in Norway. 9th Annual WRF User's Workshop.

Cassola F., M. Burlando, M. Antonelli, and C. Ratto. 2008. Optimization of the regional spatial distribution of wind power plants to minimize the variability of wind energy input into power supply systems. Journal of Applied Meteorology and Climatology; 47: 3099-3116.

Castro-Díez Y., D. Pozo-Vázquez, F. Rodrigo, and M. Esteban-Parra. 2002. NAO and winter temperature variability in southern Europe. Geophysical research letters; 29, 1160.

Chen F. 2007. The Noah Land Surface Model in WRF: A short tutorial. NCAR, LSM group meeting, 30 pp.

Chen F., J. Dudhia. 2001. Coupling an advanced Land surface-Hydrology model with the Penn State-NCAR MM5 modeling system. Part I: model implementation and sensitivity. Monthly Weather Review; 129: 569-585.

Chou, M. and M. Suarez. 1994. An efficient thermal infrared radiation parametrization for use in general circulation models. NASA Tech. Report, 85.

Chiacchio M., and M. Wild. 2010. Influence of NAO and clouds on long-term seasonal variations of surface solar radiation in Europe. J Geophys Res; 115: D00D22.

Cohen C. 2002. A comparison of cumulus parametrizations in idealized sea-breeze simulations. Monthly weather review; 130(11): 2554-2571.

Coopers, P.W.C.P. 2010. 100% Renewable electricity: a roadmap to 2050 for Europe and North Africa. Price Water House Coopers, London.

DESERTEC 2010. Rd paper. An overview of the DESERTEC concept. DESERTEC organization. http://www.desertec.org/

DLR. 2007. TRANS-CSP. DLR-ITT technical report, K oln, Germany

Dudhia J. 1989. Numerical study of convection observed during the winter monsoon experiment using a mesoscale two-dimensional model. Journal of the Atmospheric Sciences; 46: 3077-3107.

EEAA, European Environment Agency. 2000. CORINE Land Cover. Land cover information package.

Energy Efficiency and Renewable Energy (EERE). 1997. Renewable Energy Technology Characterizations. Topical Report TR-109496, Energy Efficiency and Renewable Energy (EERE). US Department of Energy.

Esteban-Parra MJ, R. Rodrigo, and Y. Castro-Díez. 1998. Spatial and temporal patterns of precipitation in Spain for the period 1880-1992. International Journal of climatology; 18: 1557-1574.

Ezber Y., O.L. Sen, T. Kindap, and M. Karaca. 2007. Climatic effects of urbanization in Istanbul: a statistical and modeling analysis. International Journal Climatology; 27: 667â€“679.

Fernández J, Montávez JP, Sáenz J, González-Rouco J, Zorita E. Sensitivity of the MM5 mesoscale model to physical parameterizations for regional climate studies: Annual cycle. Journal of geophysical research 2007; 112: D04 101.

Fichaux N, Wilkes J. Oceans of Opportunity: Harnessing Europe Largest Domestic Energy Resource. European Wind Energy Association: Brussels, Belgium. 2009.

Fitzgerald R.W., and B.G. Lees. 1994. Assessing the classification accuracy of multi-sources remote sensing data. Remote Sensing of Environment; 47: 362-368.

Foody G.M. 2002. Status of land cover classification accuracy assessment. Remote Sensing of Environment; 80: 185-201.

Frank, H.P. O. Rathmann, N.G. Mortensen, and L. Landberg. 2001. The numerical wind atlas-the KAMM/WasP method. Technical Note. Risoe, Denmark.

Gámiz-Fortis, S., D. Pozo-Vázquez, R. Trigo, and Y. Castro-Díez, 2008: Quantifying the predictability of winter river flow in Iberia. part I: Interannual predictability. Journal of Climate, 21, 2484-2502.

GE. 2010. Western Wind and Solar Integration Study. Tech. Report. NREL/SR-550-47434. National Renewable Energy Laboratory (NREL), Golden, CO.

Giebel G. Wind power has a capacity credit - A catalogue of 50 supporting studies. Technical report. Risoe National Laboratory, 2005.

Giebel G. 2007. A variance analysis of the capacity displaced by Wind Energy in Europe. Wind Energy; 10: 69-79.

Gilman P, Cameron C. Solar Advisor Model User Guide for Version 2.0. NREL Technical Report NREL/TP-670-43704. 2008.

Gómez A, Zubizarreta J, Dopazo C and Fueyo N. 2010. Spanish energy roadmap to 2020: Socioeconomic implications of renewable targets. *Energy*, 36: 1973-1985.

Gower J.C. 1971. A general coefficient of similarity and its properties. Biometrics; 27: 857â€“871.

Gravdahl H., and K. Harstveit. 2000. WindSim–Flow simulations in complex terrain, Assessment of wind resources along the Norwegian coast. DEWEK.

Gross R., P. Heptonstall, M. Leach, J. Skea, and D. Anderson. 2008. The UK Energy Research Centre Review of the Costs and Impacts of Interminttency. In: Renewable 786 electricity and the grid: the challenge of variability. 73-93. Edited by Boyle G. Earthscan/James and James.

Gueymard, C. and S. Wilcox, 2011: Assessment of spatial and temporal variability in the US solar resource from radiometric measurements and predictions from models using ground based or satellite data. Solar Energy; 85: 1068-1084.

GWEC (Global Wind Energy Council). 2007. Global wind energy council report.

Hahmann A, D. Rostkier-Edelstein, F. Vandenberghe, Y. Liu, S. Swerdlin, T. Warner and R. Babarsky. 2010. A reanalysis system for the generation of mesoscale climatographies. Journal of Applied Meteorology and Climatology; 40(5): 954-972.

Hansen M., B.C. Reed. 2000. A comparison of the IGBP DISCover and University of Maryland global land cover products. International Journal of Remote Sensing; 21: 1365-1374.

Hartmann D.L. 1994. Global Physical Climatology. Academic Press: San Diego, California, USA.

Heide D, Von Bremen L, Greiner M, Hoffmann C, Speckmann M, and Bonger S. Seasonal optimal mix of wind and solar power in a future, highly renewable Europe. Renewable energy 2010; 35: 2483-2489.

Heide D, Von Bremen L and Hoffmann C. 2011. Reduced storage and balancing needs in a fully renewable European power system with excess wind and solar power generation. Renewable Energy. 35: 2483-2489.

Holttinen H. Hourly wind power variations in the Nordic countries. Wind Energy, 2005; 8(2): 173-95.

Hong S, Noh Y, Dudhia J. A new vertical diffusion package with an explicit treatment of entrainment processes. Monthly Weather Review 2006; 134: 2318-2341.

Huaxing LU. 2008. Modelling terrain complexity. In: Advances in digital terrain analysis. Springer, Berlin, pp 159-176.

Trigo, R., T. Osborn, J. Corte-Real et al., 2002: The north Atlantic oscillation influence on Europe: climate impacts and associated physical mechanisms. Climate Research, 20, 9-17.

Hutchinson, M., J. Kalma, and M. Johnson, 1984: Monthly estimates of wind speed and wind run for Australia. International Journal of Climatology, 4, 311-324.

International Energy Agency. 2008. World energy outlook. Paris, France: OECD publication service, OECD.

International Energy Agency. 2009. Technology roadmap. Wind energy. Paris, France: OECD publication service, OECD.

International Energy Agency. 2010 Technology roadmap. Concentrating Solar Power. Paris, France: OECD publication service, OECD.

International Energy Agency. 2010.Rechnology roadmap. Solar Photovoltaic Energy. Paris, France: OECD publication service, OECD.

Climate Change 2007: Synthesis Report. Contribution of Working Groups I, II and III to the Fourth Assessment Report of the Intergovernmental Panel on Climate Change. Core Writing Team, R.K. Pachauri, and A. Reisinger (eds.), Cambridge University Press, 104 pp.

IPCC (2007b). Summary for policymakers. In: Climate Change 2007: The Physical Science Basis. Contribution of Working Group I to the Fourth Assessment Report of the Intergovernmental Panel on Climate Change. S. Solomon, D. Qin, M. Manning, Z. Chen, M. Marquis, K.B. Averyt, M. Tignor, and H.L. Miller (eds.), Cambridge University Press, pp. 1-18.

Intergovernmental Panel on Climate Change, 2007b. *Contribution of Working Group III to the Fourth Assessment Report of the Intergovernmental Panel on Climate Change*. Metz, O.R. Davidson, P.R. Bosch, R. Dave, L.A. Meyer (eds) Cambridge University Press, Cambridge, United Kingdom and New York, NY, USA.

Intergovernmental Panel on Climate Change, 2011. IPCC Special Report on Renewable Energy Sources and Climate Change Mitigation. Prepared by Working Group III of the Intergovernmental Panel on Climate Change. Cambridge University Press, Cambridge, United Kingdom and New York, NY, USA, 1075 pp.

Isaaks, E.H. and Srivastava, R.M. 1989. An introduction to applied geostatistics. Oxford University Press New York.

Jacobson MZ and Delucchi MA. 2011. Providing all global energy with wind, water and solar power, Part I: Technologies, energy resources, quantities and areas of infrastructure, and materials. *Energy Policy*, 39: 1154-1169.

Jammalamadaka S and A. Sengupta. 2001. Topics in circular statistics. World ScientificPub Co Inc.

Janjic Z. 2002. Nonsingular implementation of the Mellor-Yamada level 2.5 scheme in the NCEP Meso model. NCEP Office Note, 437, 61.

Jiménez B, F. Durante, B. Lange, T. Kreutzer, J. Tambke. 2007. Offore wind resource assessment with WAsP and MM5: Comparative study for the German Bight. Wind Energy; 10:121-134.

Jiménez, P.A. and González-Rouco, J.F. and Navarro, J. and Montávez, J.P. and García-Bustamante, E. 2010. Quality assurance of surface wind observations from automated weather stations; 27(7): 1101-1122.

Jiménez, P.A., and J. Dudhia. 2012. Improving the representation of resolved and unresolved topographic effects on surface wind in the WRF model. Journal of applied meteorology and climatology; 51(2).

Kahn E. The reliability of distributed wind generators. Electric Power Systems Research 1979; 2: 1-14.

Kain J, Fritsch J. Convective parameterization for mesoscale models: The Kain-Fritsch scheme, the representation of cumulus convection in numerical models, 246 pp. Am. Meteorol. Soc., Boston, Mass. 1993.

Kanamitsu M., and H. Kanamaru. 2007. Fifty-seven-year California reanalysis downscaling at 10 km (CaRD10). Part I: System detail and validation with observations. Journal of Climate; 20 (22): 5553-5571.

Kankam, S., and E. Boon. 2009. Energy delivery and utilization for rural development: Lessons from Northern Ghana. Energy for Sustainable Development; 13(3): 212-218.

Kariniotakis G. Next generation short-term forecasting of wind power: Overview of the ANEMOS project. Proc. EWEC 2006, Athens, Greece, European Wind Energy Association, 10.

Kaya S., E. Sertel, D.Z. Seker, and A. Tanik. 2008. Multi-temporal analysis and mapping of coastal erosion caused by open mining areas. Environmental Forensics; 9(2): 271â€“276.

Kearny D, Price H. 2004. Recent advances in parabolic trough solar power plant technology. Journal of solar Energy Engineering. 124(2): 109-125.

Kempton W, Pimenta F, Veron D, Colle B. Electric power from offshore wind via synoptic-scale interconnection. Proceedings of the National Academy of Sciences 2010; 107.

Kim Y., J.H. Jeong, J.H. Bae, S.K. Song and J.W.Seo. 2005. Study on planetary boundary layer schemes suitable for simulation of sea surface wind in the southeastern coastal area. Korea Environ Sci; 456 14 (5): 1015-1026.

Kotroni V., and K. Lagouvardos. 2001. Precipitation forecast skill of different convective parametrization and microphysical schemes: application for the cold season over Greece. Geophys. Res. Let; 28 (10): 1977-1980.

Krajacic G, Duic N and Calvalho MdG. 2011. How to achieve a 100% RES electricity supply for Portugal. *Applied Energy*, 88: 508-517.

Kwun J., Y. Kim, J. Seo, J. Jeong, and S. You. 2009. Sensitivity of MM5 and WRF mesoscale model predictions of surface winds in a typhoon to planetary boundary layer parametrizations. Natural Hazards; 51 (1), 63-77.

Landberg L. The availability and variability of the European wind resource. International Journal of Sustainable Energy 1997; 18: 313-320.

Landberg L., L. Myllerup, O. Rathmann, E. Petersen, B. JÃ¸rgensen, J. Badger, and N. Mortensen. 2003. Wind resource estimation an overview. Wind Energy; 6 (3): 261-271.

Landis J.R., and G.C. Koch. 1987. The measurement of observer agreement for categorical data. Biometric; 33: 159-179.

Lara-Fanego V, Ruiz-Arias JA, Pozo-Vázquez D, Santos-Alamillos FJ, Tovar- Pescador J. Evaluation of the WRF model solar irradiance forecasts in Andalusia (southern Spain). Solar Energy 2011. In Press.

Lavagnini A, A. Sempreviva, C. Transerici, C. Accadia, M. Casaioli, S. Mariani, and A. Speranza. 2006. Offshore wind climatology over the Mediterranean basin. Wind Energy; 9 (3), 251-266.

Li X., S.Zhong, X. Blan, and W.E. Hellman. 2010. Climate and climate variability of the wind power resources in the Great Lakes region of the United States. J Geophys Res; 115: D18107.

Lohmann S., C. Schillings, B. Mayer, R. Meyer. 2006. Long-term variability of solar direct and global radiation derived from ISCCP data and comparison with reanalysis data. Solar Energy 80: 1390-1401.

Lorenz E, Scheidsteger T, Hurka J, Heinemann D, Kurz C. Regional PV power prediction for improved grid integration. Progress in Photovoltaics: Research and Applications 2010: doi: 10.1002/pip.1033.

Loveland T.R., B.C. Reed, J.F. Brown, D.O. Ohlen, J. Zhu, L. Yang, and J.W. Merchant. 2000. Development of a global land cover characteristics database and IGBP DISCover from 1-km AVHRR data. International Journal of Remote Sensing; 21: 1303-1330.

Lund H. 2005. Large-scale integration of wind power into different energy systems. *Energy*, 30: 2402-12.

Lund H. 2006. Large-scale integration of optimal combinations of PV, wind and wave power into the electricity supply. *Renewable Energy*, 31: 503-515.

Lund H. 2007. Renewable energy strategies for sustainable development. *Energy*, 32: 912-919.

Lynn B., L. Druyan, C. Hogrefe, J. Dudhia, C. Rosenzweig, R. Goldberg, D. Rind, R. Healy, J. Rosenthal, and P. Kinney. 2004. Sensitivity of present and future surface temperatures to precipitation characteristics. Clim Res; 28: 53-65.

Mason J.E., and C.L. Archer. 2012. Baseload electricity from wind via compressed air energy storage (CAES). Renewable and Sustainable Energy Reviews; 16: 1099-1109.

Mathiesen BV, Lund H and Karlsson K. 2001. 100% Renewable energy systems, climate mitigation and economic growth. *Applied Energy*, 88: 488-501.

McVicar T., T. Van Niel, L. LiangTao, M. Hutchinson, M. XinMing, and L. ZhiHong. 2007. Spatially distributing monthly reference evapotranspiration and pan evaporation considering topographic influences. Journal of Hidroloy; 338: 196-220.

McVicar, T., T. Van Niel, L. Li, M. Roderick, D. Rayner, L. Ricciardulli, and R. Donohue, 2008: Wind speed climatology and trends for Australia, 1975-2006: capturing the stilling phenomenon and comparison with near-surface reanalysis output. Geophysical Research Letters, 35, L20 403.

Miao J., D. Chen, K. Wyser, K. Borne, J. Lindgren, M. Strandevall, S. Thorsson, C. Achberger, E. Almkvist. 2008. Evaluation of MM5 mesoscale model at local scale

for air quality applications over the Swedish west coast: Influence of PBL and LSM parametrizations. Meteorology and Atmospheric Physics; 99 (1): 77-103.

Mills A and Wiser R. 2010. Implication of wide-area geographic diversity for short-term variability of solar power. Lawrence Berkeley National Laboratory Technical Report LBNL-3884E.

Milborrow L. Wind power on the Grid. Pag. 31-49. In Renewable electricity and the grid: the challenge of variability. Edited by Boyle G. Earthscan-James 2008.

Mlawer E, Taubman S, Brown P, Iacono M, Clough S. Radiative transfer for inhomogeneous atmospheres: RRTM, a validated correlated-k model for the longwave. Journal of Geophysical Research 1997; 102:16 663.

Moomaw, W., F. Yamba, M. Kamimoto, L. Maurice, J. Nyboer, K. Urama, and T. Weir, 2011. Introduction. In IPCC Special Report on Renewable Energy Sources and Climate Change Mitigation [O. Edenhofer, R. Pichs-Madruga, Y. Sokona, K. Seyboth, P. Matschoss, S. Kadner, T. Zwickel, P. Eickemeier, G. Hansen, S. Schl omer, C.von Stechow (eds)], Cambridge University Press, Cambridge, United Kingdom and New York, NY, USA.

Morrison H. and A. Gettelman. 2008. A new two-moment bulk stratiform cloud microphysics scheme in the Community Atmosphere Model, version 3 (CAM3). Part I: Description and numerical tests. Journal of Climate; 21 (15): 3642-3659.

Mortensen, N.G., L. Landberg, I. Troen, and E.L. Petersen. 1993. Wind atlas analysis and application program (WAsP). Technical report. Riso National Laboratory, Roskilde, Denmark.

Mortensen, N.G., and E.L. Petersen. 1998. Influence of topographical input data on the accuracy of wind flow modeling in complex terrain. Proceedings of the 1997 European Wind Energy Conference Mortensen, N.G. and E.L. Petersen (1998). and Exhibition, Dublin, Ireland, October 6-9, 317-320.

Muller H, Dumas F, Blanke F, Mariette V. High-resolution atmospheric forcing for regional oceanic model: the Iroise Sea. Ocean Dynamics 2007; 57(4-5): 375-400.

Nfah, E., J. Ngundam, and R. Tchinda. 2007. Modelling of solar/diesel/battery hybrid power systems for far-north Cameroon. Renewable Energy; 32(5): 832-844.

Nikolakakis T., and V. Fthenakis. 2011. The optimum mix of electricity from wind- and solar-sources in conventional power systems: Evaluating the case for New York State. Energy Policy; 39: 6972:6980.

NOAA. 2010. Trends in Carbon Dioxide. National Oceanic and Atmospheric Administration Earth Systems Research Laboratory, Washington, D.C, USA.

Ostergaard PA. Geographic aggregation and wind power output variance in Denmark. Energy 2008; 33: 1453-1460.

Oswald J, Raine M, Ashraf-Ball H. Will British weather provide reliable electricit?. Energy Policy 2008; 36: 3212-3225.

Otte TL. The Impact of Nudging in the Meteorological Model for Retrospective Air Quality Simulations. Part II: Evaluating Collocated Meteorological and Air Quatily Observations. Journal of Applied Meteorology and Climatology 2007; 47: 1868-1887.

Palomino I. and F. Martin. 1995. A simple method for spatial interpolation of the wind in complex terrain. Journal of Applied Meteorology; 34: 1679-1693.

Papadimas, C., A. Fotiadi, N. Hatzianastassiou, I. Vardavas, and A. Bartzokas, 2010: Regional co-variability and teleconnection patterns in surface solar radiation on a planetary scale. International Journal of Climatology, 30, 2314-2329.

PASENER, 2007. El plan Andaluz de Sostenibilidad Energética 2007-2013. Tech. Report. 67, Andalusian Administration, 305 pp.

Pelland S., and I. Abboud. 2008. Comparing photovoltaic capacity value metrics: case study for the City of Toronto. Progress in Photovoltaics, 16(8), pp. 715-724.

Pérez-Landa G., P. Ciais, M. Sanz, B. Gioli, F. Miglietta, J. Palau, G. Gangoiti, and M. Millán. 2007. Mesoscale circulations over complex terrain in the Valencia coastal region, Spain. Part 1: Simulation of diurnal circulation regimes. Atmospheric Chemistry and Physics; 7:1835-1849.

Pielke R.A., R.l. Walko, L.T. Steyaert, P.L. Vidale, G.E. Liston, W.A. Lyons, and T.N. Chase. 1999. The influence of anthropogenic landscape changes on weather in south Florida. Monthly Weather Review; 127: 1663-1673.

Pineda N., O. Jorga, J. Jorge, and J.M. Baldasano. 2004. Using NOAA AVHRR and SPOT VGT data to estimate surface parameters: application to a mesoscale meteorological model. Int. J. Remote Sensing; 25(10): 129-143.

Pitman AJ. 2003. The evolution of, and revolution in, land surface schemes designed for climate models. International Journal of Climatology: 23: 479-510.

Pozo-Vázquez, A., M. Esteban-Parra, F. Rodrigo, and Y. Castro-Díez, 2000: An analysis of the variability of the north Atlantic oscillation in the time and the frequency domains. International Journal of Climatology, 20, 1675-1692.

Pozo-Vázquez, D., M. Esteban-Parra, F. Rodrigo, and Y. Castro-Díez, 2001: A study of NAO variability and its possible non-linear influences on European surface temperature. Climate Dynamics, 17, 701-715.

Pozo-Vázquez, D., J. Tovar-Pescador, S. Gámiz-Fortis, M. Esteban-Parra, and Y. Castro-Díez, 2004: NAO and solar radiation variability in the European north Atlantic region. Geophysical research letters, 31, L05 201.

Pozo-Vázquez, D., F. Santos-Alamillos, V. Lara-Fanego, J. Ruiz-Arias, and J. Tovar-Pescador, 2011: The Impact of the NAO on the Solar and Wind Energy Resources in the Mediterranean Area. Hydrological, Socioeconomic and Ecological Impacts of the North Atlantic Oscillation in the Mediterranean Region. Vicente-Serrano, Sergio. and Trigo, Ricardo. Springer, 18 pp.

Preisendorfer R.W. 1998. Principal component analysis in meteorology and oceanography. Elsevier. 425pp.

Pryor S., R. Barthelmie, and J.T. Shoof. 2006. Inter-annual variability of wind indices across Europe. Wind Energy; 9: 27-38.

Rajeevan M., A. Kesarkar, S. Thampi, T. Rao, B. Radhakrishna, and M. Rajasekhar. 2010. Sensitivity of WRF cloud microphysics to simulations of a severe thunderstorm event over Southeast India. Ann. Geophys; 28: 603-619.

Ramos-Calzado, P., J. Gómez-Camacho, F. Pérez-Bernal, and M. Pita-López, 2008: A novel approach to precipitation series completion in climatological datasets: application to Andalusia. International Journal of Climatology, 28, 1525-1534.

Ran L., J. E. Pleim, and R. C. Gilliam. 2010. Impact of high resolution land-use data in meteorology and air quality modeling systems. Chapter 1 in Air Pollution Modeling and its Applications. 3-7.

REE, Red Eléctrica de España. 2010. Red Eléctrica de España (REE) Annual Report. Spain.

Reynolds RW, Rayner NA, Smith TM, Stokes DC, Wang W. An improved in situ and satellite SST analysis for climate. Journal of Climate 2002; 15: 1609-1625.

Roques F, Hiroux C, Saguan M. Optimal wind power deployment in Europe- A portfolio approach. Energy Policy 2010; 38: 3245-3256.

Rodriguez-Puebla C., A.H. Encinas, S. Nieto, and J.Garmendia. 1998. Spatial and temporal patterns of annual precipitation variability over the Iberian Peninsula. International Journal of Climatology; 18(3): 299-316.

Romero, R., J. Guijarro, C. Ramis, and S. Alonso, 1998: A 30-year (1964-1993) daily rainfall data base for the Spanish Mediterranean regions: First exploratory study. International Journal of Climatology, 18, 541-560.

Ruiz-Arias JA, Pozo-Vázquez D, Sánchez-Sánchez N, Montávez J, Hayas-Barrú A, Tovar-Pescador J. Evaluation of two MM5-PBL parameterizations for solar radiation and temperature estimation in the South-Eastern area of the Iberian Peninsula. Il Nuovo Cimento 2008; 31: 825-842.

Ruiz-Arias J.A., J. Tovar-Pescador, D. Pozo-Vázquez, and H. Alsamamra. 2009. A comparative analysis of DEM-based models to estimate the solar radiation in mountainous terrain. International Journal of Geographical Information Science; 23(8): 1049-1076.

Ruiz-Arias J.A., Tovar-Pescador J, Pozo-Vázquez D, Alsamamra H. 2010. Proposal of a new regresive model for the hourly diffuse solar radiation under all sky conditions. Energy Conversion and management. 51: 881-893.

Ruiz-Arias J.A., D. Pozo-Vázquez, F.J. Santos-Alamillos, V. Lara-Fanego, and J. Tovar-Pescador. 2011. A topographic geostatistical approach for mapping monthly mean values of daily global solar radiation: A case study in southern Spain. Agricultural and Forest Meteorology.

Ruiz-Arias J.A., D. Pozo-VÃ¡zquez, V. Lara-Fanego, F.J. Santos-Alamillos, and J. Tovar-Pescador. 2012. A High-Resolution Topographic Correction Method for Clear-Sky Solar Irradiance Derived with a Numerical Weather Prediction Model. Journal of Applied Meteorology and Climatology; 50: 2460-2472.

Ruiz-Arias J.A., J. Terrados, P. Pérez-Higueras, D. Pozo-VÁzquez, and G. Almonacid. 2012. Assessment of the renewable energies potential for intensive electricity production in the province of Jaén, southern Spain. Renewable and Sustainable Energy Reviews; 16(5): 2994-3001.

Saha S, Moorthi S, Pan JL, Wu X, Wang J, Dadiga S et al. The NCEP climate forecast system reanalysis. Bulletin of the American Meteorological Society 2010; 90(8): 1015-1057.

Saintcross J, Piwko R, Bai X and Clara K. The Effects of Integrating Wind Power on Transmission System Planning, Reliability, and Operations. 2005; The New York State Energy Research and Development Authority, Albany, New York, USA.

Sanchez-Lorenzo A., J. Calbó, and J. Martin-Vide. 2008. Spatial and temporal trends in sunshine duration over Western Europe (1938-2004). Journal of climate; 21: 6089-6098

Sanchez-Lorenzo A., J. Calbó, M. Brunetti, and C. Deser. 2009. Dimmingbrightening over the Iberian Peninsula: trends in sunshine duration and cloud cover and their relations with atmospheric circulation. Journal of Geophysical Research; 114: D00D09.

Santos-Alamillos FJ, Pozo-Vázquez D, Ruiz-Arias JA, Lara-Fanego V, Tovar-Pescador J. 2011. Analysis of spatiotemporal balancing between wind and solar energy resources in the southern Iberian Peninsula. Submitted to *Journal of Applied Meteorology and Climatology*.

Santos-Alamillos FJ, Pozo-Vázquez D, Ruiz-Arias J.A., Lara-Fanego V and Tovar-Pescador J. 2012. A methodology for evaluating the potential contribution of wind energy to baselad power: A case estudy in Andalusia (Southern Spain). Manuscript in preparation

Santos-Alamillos F.J., D. Pozo-Vázquez, J.A. Ruiz-Arias, V. Lara-Fanego, and J. Tovar-Pescador J. 2012. Analysis of WRF model wind estimate sensitivity to

parameterization choice and terrain representation in Andalusia (Southern Spain). Manuscript submitted to Journal of Applied Meteorology and Climatology. In revision.

Sargent and Lundy LLC Consulting Group. 2003. Assessment of parabolic trough and power tower solar technology cost and performance forecast. NREL/SR-550-34440.

Schweiger E.W., D.W. Bolgrien, T.R. Angradi, and J.R. Kelly. 2005. Environmental monitoring and assessment of a great river ecosystem: the upper missouri river pilot. Environmental Monitoring and Assessment; 103: 21-40.

Seaman NL. Meteorological modeling for air-quality assessments. Journal of Atmospheric Environment 2000; 34: 2231-2259.

Sempreviva A., R. Barthelmie and S. Pryor. 2008. Review of methodologies for offshore wind resource assessment in European seas. Surveys in Geophysics; 29 (6):471-497.

Sertel E., N. Findik, S. Kaya, D.Z. Seker, and A. Samsunlu. 2008. Assessment of landscape changes in the Kizilirmak delta, Turkey, using remotely sensed data and GIS. Environ Eng Sci 25:353-361.

Shimada S., and T. Oshawa. 2011. Accuracy and Characteristics of Offshore Wind Speeds Simulated by WRF. SOLA; 7: 21-24.

Simmons A., S. Uppala, D. Dee, and S. Kobayashi. 2007. ERA-I: new ECMWF reanalysis products from 1989 onwards. ECMWF Newsletter 110:25-35.

Skamarock WC, Kemp JB, Dudhia J, Gill DO, Barker DM, Duda MG, Huang XY et al. A Description of the Advanced Research WRF Version 3, NCAR/TN-475+STR. Mesoscale and Microscale Meteorology Division, National Centre for Atmospheric Research, Boulder, USA. 2008.

Stensrud D. 2007. Parametrization schemes: keys to understanding numerical weather prediction models. Cambridge Univ Pr.

Thompson G, Rasmussen R, Manning K. Explicit forecasts of winter precipitation using an improved bulk microphysics scheme. Part I: Description and sensitivity analysis. Monthly Weather Review 2010; 132: 519-542.

Todt O., M. González, and B. Estévez. 2010. Conflict in the Sea of Trafalgar: offshore wind energy and its context. Wind energy.

Tovar-Pescador J., D. Pozo-Vázquez, J.A. Ruiz-Arias, J. Batlles, G. López, and J.L. Bosch. 2006. On the use of the digial elevation model to estimate the solar radiation in areas of complex topography. Meteorological Applications; 13(6): 279-287.

Trieb, F., Viebahn, P, Kabariti, M., Bennouma, A., and coauthors. Concentrating solar power for the Mediterranean region. Technical report. German Aerospace Center (DLR) Institute of Technical Thermodynamics, Section Systems Analysis and Technology Assessment. Stuttgart, Germany.

Trigo, R. and C. DaCamara, 2000: Circulation weather types and their impact on the precipitation regime in Portugal. International Journal of Climatology, 20, 1559-1581.

Trigo, R., T. Osborn, J. Corte-Real et al., 2002: The north Atlantic oscillation influence on Europe: climate impacts and associated physical mechanisms. Climate Research, 20, 9-17.

Trigo, R., D. Pozo-Vázquez, T. Osborn, Y. Castro-Díez, S. Gámiz-Fortis, and M. Esteban-Parra, 2004: North Atlantic oscillation influence on precipitation, river flow and water resources in the Iberian Peninsula. International Journal of Climatology, 24, 925-944.

Troen I., and E.L. Petersen. 1989. European Wind Atlas. ISBN 87-550-1482-8. Risoe National Laboratory, Roskilde. 656 pp.

Tröster E, Kuwahata R and Ackermann T. 2011. European grid study 2030-2050. Technical Report. Energynautics GmbH.

Uppala S, Dee D, Kobayashi S, Berrisford P, Simmons A. Towards a climate data assimilation system: Status update of ERA-Interim. ECMWF newsletter 2008; 115.

Usaola J. 2011. Smooth Integration of CSP Plants in Power Systems. Preliminary program of the first International Workshop on the Integration of Solar Power into Power Systems. Aarhus. Denmark.

UNESA, Spanish electrical industry association. Annual spanish electrical industry report. 2010. Madrid, Spain.

Undheim O. 2005. The non-linear micro-scale flow solver 3DWind. Developments and validation. Doctoral Thesis at the Norwegian Technical University, Trondheim, Norway.

Von Bremen L. 2008 Large-scale variability of weather dependent renewable energy sources. In: Troccoli A (ed) Management of weather and climate risk in the energy industry. Springer

Von Storch, H. and F. Zwiers, 2001: Statistical analysis in climate research. Cambridge Univ Pr.

Watson L., and W. Bauman. 2009. Weather Research and Forecasting Model Wind Sensitivity Study at Edwards Air Force Base, CA. 13th Conference on Integrated Observing and Assimilation Systems for Atmosphere, Oceans, and Land Surface.

Weaver CP, and R. Avissar. 2001. Atmospheric disturbances caused by human modification of the landscape. Bulletin of the American Meteorological Society 82: 269â€“2281.

Weber, R. and M. Furger, 2001: Climatology of near-surface wind patterns over Switzerland. International Journal of Climatology, 21, 809-827.

Weigt H. Germany's wind energy: The potential for fossil capacity replacement and cost saving. Applied Energy 2009; 86: 1857-1863.

Weisser D. and T. Foxon. 2003. Implications of seasonal and diurnal variations of wind velocity for power output estimation of a turbine: a case study of Grenada. Int J Energy Res; 27: 1165-1179.

Widén, J. 2011: Correlations between large-scale solar and wind power in a future scenario for Sweden. IEEE Transactions on sustainable energy, 2.

Wiemken E, Beyer H, Heydenreich W and Kiefer K. 2001. Power characteristics of PV ensembles: experiences from the combined power production of 100 grid connected PV systems distributed over the area of Germany. Solar Energy, 70, 513-518.

Xcell Energy. 2009. An Effective Load Carrying Capability Analysis for Estimating the Capacity Value of Solar Generation Resources on the Public Service Company of Colorado System. Xcel Energy Services, Inc., Denver, CO, USA, 13 pp.

Yang ZL. 2004. Modeling land surface processes in short term weather and climate studies, in Observation, Theory and Modeling of Atmospheric Variability. World Scientific Series on Meteorology of East Asia, World Scientific: New Jersey; 288â€“313.

Zagar N., M. Zagar, M. Cedilnik, C. Gregori, and J. Rakovec. 2006. Validation of mesoscale low-level winds obtained by dynamical downscaling of ERA40 over complex terrain. Tellus A; 58 (4): 445-455.

Zhang Y, Smith S. 2008. Long-term modeling of solar energy: analysis of CSP and PV technologies. Pacific Northwest National Laboratory Report. PNNL-16727.

Zhang D., and W. Zheng. 2004. Diurnal Cycles of Surface Winds and Temperatures as Simulated by Five Boundary Layer Parametrizations. Journal of Applied Meteorology; 43 (1): 157-169.

Zhang Y, Smith S, Page G, Stackhouse P. 2010. Modeling the potential for thermal concentrating solar power technologies. Energy Policy. 38: 7884-7897.